

UNIVERSIDADE FEDERAL DE ITAJUBÁ - UNIFEI  
PROGRAMA DE PÓS-GRADUAÇÃO EM  
ENGENHARIA ELÉTRICA

Implementation of a Low Complexity  
Structure for MIMO-GFDM Receivers Based  
on the Interference Cancellation Technique

**Danilo Simões Gaspar**

Itajubá, Brazil, November 5, 2024

UNIVERSIDADE FEDERAL DE ITAJUBÁ - UNIFEI  
PROGRAMA DE PÓS-GRADUAÇÃO EM  
ENGENHARIA ELÉTRICA

Danilo Simões Gaspar

Implementation of a Low Complexity  
Structure for MIMO-GFDM Receivers Based  
on the Interference Cancellation Technique

Thesis submitted to the Graduate Program in Electrical Engineering as part of the requirements for obtaining the Title of Doctor in Electrical Engineering.

**Concentration Area: Microelectronics**

**Advisor: Prof. Dr. Tales Cléber Pimenta**

**Co-advisor: Prof. Dr. Luciano Leonel Mendes**

**November 5, 2024**

**Itajubá, Brazil**

# Acknowledgements

I would like to express my gratitude for the support provided by the project XGM-AFCCT-2024-2-15-1, hosted by xGMobile. This project was made possible with the assistance of EMBRAPPII (Empresa Brasileira de Pesquisa e Inovação Industrial) and MCTI (Ministério da Ciência, Tecnologia e Inovação).

I also would like to thank the Kokusai Denki Linear, in special Mr. Masao Ichikawa and Mr. Fabio Pina, for supporting my specialization trajectory.

Finally, I dedicate this work to my wife Aline, who has always supported me and kept me motivated throughout these years of study. A special thanks goes out to my sons, Danilo R. and Júlio, to my parents and to my brothers, Adriano, Eduardo, Everaldo, and Ivan.

# Abstract

The emerging mobile communication systems towards an unprecedented evolution in terms of flexibility, data rate, and latency, enabling wireless networks to support applications that are typically backed by wired technologies. The next generation of mobile communication is already being discussed by the scientific community, standardization institutes, and players in the mobile communication market. The foreseen scenarios are already beginning to be outlined, anticipating that they might be even harder to achieve considering the expected increase in flexibility while supporting conflicting requirements across several applications in different verticals, besides higher data rates, broader coverage, wider frequency bands, and extreme low latency. It is clear that future mobile networks cannot rely on a single radio access network to meet all these demands. Different approaches are needed to address all requirements, but SM (*Spatial Multiplexing*)-MIMO (*Multiple-Input Multiple-Output*) schemes represent a key technology for most future wireless systems. SM-MIMO can provide the necessary bandwidth, reducing the frame duration and increasing the robustness for data with a very short life span. Furthermore, integrating SM-MIMO systems with advanced detection schemes, that leverage both diversity and multiplexing gains, can substantially boost throughput and extend coverage area. Usually, MIMO schemes are combined with OFDM (*Orthogonal Frequency Division Multiplexing*) to deal with double-dispersive channels, assuming that the channel coherence time is larger than the duration of the OFDM block and the channel coherence bandwidth is larger than the subcarrier bandwidth. However, OFDM presents limitations that could hinder its applications in future mobile systems. High OOB (*Out-of-Band*) emissions, low flexibility in terms of parameterization, and low spectral and energy efficiencies for channels with large delay profiles are some examples of these restrictions. In this sense, GFDM (*Generalized Frequency Division Multiplexing*) can be considered a feasible alternative. However, a challenge arises when considering non-orthogonal MIMO-GFDM since conventional linear detectors exhibit higher complexity and inferior performance compared to MIMO-OFDM systems. Consequently, there is a compelling need to explore non-conventional detectors that simultaneously reduce complexity while aiming for performance enhancement. For this end, this thesis reviews fundamental concepts in linear estimation and detection techniques, providing a straightforward algorithmic description that enables complexity comparison and performance simulation. This work adapts the low complexity and low latency iterative MMSE (*Minimum Mean Squared Error*)-PIC (*Parallel Interference Cancellation*) introduced in [1], designing and simulating its performance in a practical 6G (*Sixth Generation*) transceiver for the eRAC (*Enhanced Remote Area Communications*) scenario, a challenging task assuming a non-orthogonal GFDM waveform. The final results, presented in this work, show that MIMO-GFDM is an interesting approach to deal with very contrasting and challenging requirements in

mobile networks. As a result, the pragmatic assessment of theoretical concepts, validated through simulations, is interesting to the scientific community, as it demonstrates the potential improvements that the adoption of a new technology can achieve. Furthermore, this work provides a versatile computational model, which is an essential tool and also a reliable reference for hardware development and performance evaluation.

**Key-words:** SM-MIMO, linear estimation, detection, interference cancelation, non-orthogonal waveform, GFDM.

# Resumo

Os sistemas de comunicação móvel emergentes estão evoluindo de forma sem precedentes em termos de flexibilidade, taxa de dados e latência, permitindo que as redes sem fio suportem aplicações que normalmente são sustentadas por tecnologias cabeadas. A próxima geração de comunicação móvel já está sendo discutida pela comunidade científica, institutos de padronização e pelos atores do mercado de comunicação móvel. Os cenários previstos já estão começando a ser delineados, antecipando que podem ser ainda mais difíceis de alcançar, considerando o aumento esperado na flexibilidade, enquanto suportam requisitos conflitantes em várias aplicações e em diferentes setores, além de taxas de dados mais altas, maior cobertura, bandas de frequência mais amplas e latência extremamente baixa. É claro que as futuras redes móveis não podem depender de uma única rede de acesso sem fio para satisfazer a todas essas demandas. Abordagens diferentes são necessárias para atender a todos os requisitos, mas os esquemas SM-MIMO representam uma tecnologia chave para a maioria dos futuros sistemas sem fio. O SM-MIMO pode fornecer a vazão necessária, reduzindo a duração do quadro e aumentando a robustez para informações com uma vida útil muito curta. Além disso, integrar sistemas SM-MIMO com esquemas de detecção avançados, que aproveitam tanto o ganho de diversidade quanto o de multiplexação, pode aumentar substancialmente a taxa de transferência e estender a cobertura da rede móvel. Normalmente, os esquemas MIMO são combinados com OFDM para lidar com canais duplamente dispersivos, assumindo que o tempo de coerência do canal é maior que a duração do bloco OFDM e a largura de banda de coerência do canal é maior que a largura de banda de uma subportadora. No entanto, o OFDM apresenta limitações que podem dificultar suas aplicações em sistemas móveis futuros. Altas emissões fora da banda, baixa flexibilidade em termos de parametrização e baixa eficiência espectral e energética para canais com longos perfis de atraso são alguns exemplos dessas restrições. Nesse sentido, o GFDM pode ser considerado uma alternativa viável. Entretanto, há um grande desafio ao uso do MIMO GFDM não ortogonal uma vez que os detectores lineares convencionais apresentam maior complexidade e desempenho inferior em comparação com os sistemas MIMO OFDM. Como resultado, há uma necessidade premente de explorar detectores não convencionais que reduzam a complexidade ao mesmo tempo em que buscam melhorias de desempenho. Para esse fim, esta tese revisa conceitos fundamentais sobre técnicas de estimação linear e detecção, fornecendo uma descrição algorítmica direta que permite a comparação de complexidade e simulação de desempenho. Este trabalho adapta o MMSE-PIC iterativo de baixa complexidade e baixa latência introduzido em [1], projetando e simulando seu desempenho em um transceptor 6G prático para o cenário eRAC, uma tarefa desafiadora assumindo que a forma de onda GFDM não é ortogonal. Os resultados finais apresentados neste trabalho mostram que o MIMO-GFDM é uma abordagem interessante para lidar com os requisitos contrastantes e

desafiadores das futuras redes móveis. Logo, a avaliação pragmática de conceitos teóricos, validada por meio de simulações, é de interesse da comunidade acadêmica, pois demonstra as potenciais melhorias que a adoção de uma nova tecnologia pode alcançar. Além disso, esta tese fornece um modelo computacional versátil, uma ferramenta essencial, e também uma referência confiável, para o desenvolvimento de hardware e avaliação de desempenho.

# List of Figures

Figure 1 – Evolution of Mobile Networks. . . . .	21
Figure 2 – GFDM block structure and applicable terminology. . . . .	34
Figure 3 – Structure of the modulation matrix $G$ . . . . .	36
Figure 4 – Receiving prototype impulse response and frequency response. . . . .	37
Figure 5 – PSD comparison between GFDM and OFDM. . . . .	38
Figure 6 – Abrupt transitions at the boundaries of the GFDM block. . . . .	39
Figure 7 – GS-GFDM signal and spectrum. . . . .	40
Figure 8 – W-GFDM symbol in the time domain. . . . .	40
Figure 9 – PSD comparison between OFDM and W-GFDM. . . . .	41
Figure 10 – GFDM SER performance in AWGN channel. . . . .	43
Figure 11 – GFDM SER performance in FSC. . . . .	44
Figure 12 – GFDM SER performance in TVC. . . . .	45
Figure 13 – Simplified block diagram of a generic MIMO communication system . . . . .	47
Figure 14 – Transform matrix for the orthogonal system in the TD. . . . .	51
Figure 15 – Transform matrix for the orthogonal system in FD. . . . .	52
Figure 16 – Reorganized structure of the orthogonal system factorization. . . . .	53
Figure 17 – Transform matrix for the non-orthogonal system in the TD. . . . .	54
Figure 18 – Example of a discrete data transform. . . . .	55
Figure 19 – Transform matrix for the non-orthogonal system in FD. . . . .	56
Figure 20 – Reorganized structure of the NO system factorization. . . . .	57
Figure 21 – MF demodulation for the factorized non-orthogonal system. . . . .	57
Figure 22 – ZF demodulation for the factorized non-orthogonal system. . . . .	58
Figure 23 – Linear estimator function block. . . . .	63
Figure 24 – Intensity chart for the complex random variables estimation. . . . .	75
Figure 25 – MSE versus BCRB for the investigated linear estimators. . . . .	75
Figure 26 – FLOP counting for the presented linear estimators. . . . .	76
Figure 27 – Normalized Affine Transform constellations . . . . .	85
Figure 28 – SD comparison of the SM-MIMO BER performance in FSC. . . . .	88
Figure 29 – Block diagram of the ED computation in SD algorithms. . . . .	89
Figure 30 – Monte Carlo simulation of $4 \times 4$ SM-MIMO-OFDM. . . . .	94
Figure 31 – SD complexity analysis for the simulated parameters. . . . .	95
Figure 32 – FLOP complexity comparison for the main evaluated detection methods. . . . .	95
Figure 33 – Iterative MMSE-PIC detector block diagram. . . . .	99
Figure 34 – Frame structure for the SM-MIMO with iterative MMSE-PIC detection. . . . .	106
Figure 35 – SM-MIMO-NO-GFDM employing the iterative MMSE-PIC detector. . . . .	107
Figure 36 – Envisioned wireless backhaul scenario connecting interest remote areas. . . . .	111

# List of Tables

Table 1 – Common matrix algebra computational complexity. . . . .	32
Table 2 – Useful finite sum identities. . . . .	32
Table 3 – Parameters for the GFDM SER simulation. . . . .	42
Table 4 – Channel models for the GFDM SER simulation. . . . .	42
Table 5 – Parameters for the SM-MIMO factorization example. . . . .	50
Table 6 – Generic factorized subsystem dimension. . . . .	60
Table 7 – Proposed cases for the estimation analysis. . . . .	74
Table 8 – Linear estimation example summary. . . . .	74
Table 9 – Parameters used in SD simulation. . . . .	88
Table 10 – Estimated resource utilization of the SD-ATM ED computation. . . . .	89
Table 11 – Power delay profile of 3GPP ETU channel. . . . .	105
Table 12 – Simulation parameters. . . . .	106
Table 13 – Complexity order summary for OFDM and NO-GFDM detection. . . . .	108
Table 14 – 6G transceiver frame parameters. . . . .	115
Table 15 – 6G transceiver simulation parameters. . . . .	115
Table 16 – 6G transceiver FEC simulation parameters. . . . .	116
Table 17 – 6G transceiver SM-MIMO simulation parameters. . . . .	116

# List of abbreviations and acronyms

1G	<i>First Generation</i>
2G	<i>Second Generation</i>
3G	<i>Third Generation</i>
3GPP	<i>3rd Generation Partnership Project</i>
4G	<i>Fourth Generation</i>
5G	<i>Fifth Generation</i>
5G-NR	<i>5G New Radio</i>
5G-RANGE	<i>Remote Area Access Network for the 5th Generation</i>
6G	<i>Sixth Generation</i>
AI	<i>Artificial Intelligence</i>
ALM	<i>Adaptive Logic Module</i>
ALUT	<i>Adaptive Look-up Table</i>
AMPS	<i>Advanced Mobile Phone System</i>
APP	<i>A-Posteriori Probability</i>
AT	<i>Affine Transform</i>
ATM	<i>Affine Transform Modulation</i>
AWGN	<i>Additive White Gaussian Noise</i>
B2B	<i>Business-to-Business</i>
BCJR	<i>Bahl-Cocke-Jelinek-Raviv</i>
BCRB	<i>Bayesian Cramer-Rao Bound</i>
BER	<i>Bit Error Rate</i>
BFIM	<i>Bayesian Fisher Information Matrix</i>
BLAST	<i>Bell Laboratories Layer Space-Time</i>
BS	<i>Base Station</i>
BW	<i>Bandwidth</i>
CA-SCL	<i>Cyclic Redundancy Check (CRC)-Aided Successive Cancellation List (SCL)</i>
CC	<i>Convolutional Code</i>
CDL	<i>Clustered Delay Line</i>
CDMA	<i>Coded Division Multiple Access</i>
CFLOP	<i>Complex Float-Point Operation</i>
CFmMIMO	<i>cell-free massive MIMO</i>
CFR	<i>Channel Frequency Response</i>
CG	<i>Conjugate Gradient</i>
CIR	<i>Channel Impulse Response</i>

CNR	<i>Carrier to Noise Ratio</i>
CP	<i>Cyclic Prefix</i>
CRC	<i>Cyclic Redundancy Check</i>
CS	<i>Cyclic Suffix</i>
CSI	<i>Channel State Information</i>
CSIR	<i>Channel State Information at the Receiver</i>
CWCU	<i>Component-Wise Conditionally Unbiased</i>
DFT	<i>Discrete Fourier Transform</i>
DLR	<i>Dedicated Logic Register</i>
DSP	<i>Digital Signal Processing</i>
DTV	<i>Digital Television</i>
ED	<i>Euclidean Distance</i>
EDGE	<i>Enhanced Data GSM Evolution</i>
eMBB	<i>Enhanced Mobile Broadband</i>
eRAC	<i>Enhanced Remote Area Communications</i>
ETU	<i>Extended Typical Urban</i>
FD	<i>Frequency Domain</i>
FDD	<i>Frequency-Division Duplex</i>
FDE	<i>Frequency-Domain Equalization</i>
FDMA	<i>Frequency Division Multiple Access</i>
FEC	<i>Forward Error Correction</i>
FER	<i>Frame Error Rate</i>
FLOP	<i>Float-Point Operation</i>
FP	<i>Float Point</i>
FPGA	<i>Field Programmable Gate Array</i>
FSC	<i>Frequency-Selective Channel</i>
FWA	<i>Fixed Wireless Access</i>
FXP18	<i>18-bit Signed Fixed Point</i>
GAD	<i>Genie-Aided Detector</i>
GFDM	<i>Generalized Frequency Division Multiplexing</i>
GPRS	<i>General Packet Radio Service</i>
GPS	<i>Global Positioning System</i>
GS	<i>Guard-Symbol</i>
GSM	<i>Global System for Mobile</i>
HDL	<i>Hardware Description Language</i>
HQR	<i>Householder QR Factorization</i>
IAI	<i>Inter-Antenna Interference</i>
IBI	<i>Inter-Block Interference</i>
ICI	<i>Inter-carrier Interference</i>

IDFT	<i>Inverse Discrete Fourier Transform</i>
IFPI	<i>Interference Free Pilot Insertion</i>
iid	<i>independent and identically distributed</i>
IMT	<i>International Mobile Telephone</i>
IoT	<i>Internet of Things</i>
IP	<i>Internet Protocol</i>
ISI	<i>Inter-Symbol Interference</i>
ITU	<i>International Telecommunication Union</i>
KPI	<i>key performance indicator</i>
LDPC	<i>Low-Density Parity-Check</i>
LLPD	<i>Low-Density Parity-Check (LDPC)-like Polar Decoder</i>
LLR	<i>Log-Likelihood Ratio</i>
LMMSE	<i>Linear Minimum Mean Square Error</i>
LoS	<i>line-of-sight</i>
LTE	<i>Long-Term Evolution</i>
MAP	<i>Maximum a Posteriori</i>
MF	<i>Matched Filter</i>
MIMO	<i>Multiple-Input Multiple-Output</i>
ML	<i>Maximum Likelihood</i>
MLD	<i>Maximum Likelihood Detector</i>
mMIMO	<i>massive MIMO</i>
MMSE	<i>Minimum Mean Squared Error</i>
mMTC	<i>Massive Machine Type Communications</i>
mmWave	<i>millimeter Wave</i>
MSE	<i>Mean Squared Error</i>
NEF	<i>Noise Enhancement Factor</i>
NO	<i>Non Orthogonal</i>
NR	<i>New Radio</i>
OFDM	<i>Orthogonal Frequency Division Multiplexing</i>
OFDMA	<i>Orthogonal Frequency Division Multiple Access</i>
OOB	<i>Out-of-Band</i>
PC	<i>Polar Code</i>
PDF	<i>Probability Density Function</i>
PDP	<i>Power Delay Profile</i>
PHY	<i>Physical Layer</i>
PIC	<i>Parallel Interference Cancelation</i>
PRB	<i>Physical Resource Block</i>
PSD	<i>Power Spectrum Density</i>
QAM	<i>Quadrature Amplitude Modulation</i>

RAN	<i>Radio Access Network</i>
RB	<i>Resource Block</i>
RC	<i>Raised Cosine</i>
RE	<i>Resource Element</i>
RF	<i>Radio Frequency</i>
RIS	<i>Reconfigurable Intelligent Surfaces</i>
ROF	<i>Roll-off Factor</i>
RRC	<i>Root Raised Cosine</i>
RV	<i>Random Variable</i>
SD	<i>Sphere Detector</i>
SDR	<i>Software-Defined Radio</i>
SER	<i>Symbol Error Rate</i>
SIC	<i>Successive Interference Cancellation</i>
SISO	<i>Soft-Input, Soft-Output</i>
SM	<i>Spatial Multiplexing</i>
SMS	<i>Short Message Service</i>
SNR	<i>Signal-to-Noise Ratio</i>
STC	<i>Space Time Code</i>
STPD	<i>Steepest-Descent</i>
TD	<i>Time Domain</i>
TDD	<i>Time-Division Duplex</i>
TDMA	<i>Time Division Multiple Access</i>
TVC	<i>Time-Variant Channel</i>
TVWS	<i>TV White Space</i>
UE	<i>User Equipment</i>
UHF	<i>Ultra High Frequency</i>
URLLC	<i>Ultra-Reliable and Low Latency Communications</i>
V2V	<i>Vehicle-to-Vehicle</i>
W-CDMA	<i>Wideband Coded Division Multiple Access</i>
W-GFDM	<i>Windowed-GFDM</i>
WiFi	<i>Wireless Fidelity</i>
WLAN	<i>wireless Local Area Network</i>
ZF	<i>Zero-Forcing</i>

# List of symbols

$B$	Bandwidth
$E_s$	Average data symbol constellation energy
$K$	Number of available subcarrier resources
$K_{\text{on}}$	Number of active subcarrier resources
$L$	Discrete equivalent base band channel impulse length
$M$	Number of available subsymbol resources
$M_c$	Number of discrete elements in a modulating constellation
$M_{\text{on}}$	Number of active subsymbol resources
$N$	Number of samples per block symbol
$N_0$	Noise spectral density
$N_{\text{CP}}$	Number of samples of cyclic prefix
$N_{\text{CS}}$	Number of samples of cyclic suffix
$N_{\text{R}}$	Number of receiving antennas
$N_{\text{T}}$	Number of transmitting antennas
$N_f$	Number of samples per frame
$N_{\text{off}}$	Number of inactive resources
$N_{\text{on}}$	Number of active resources
$N_s$	Number of block symbols per frame
$N_t$	Total number of samples per block symbol
$N_{\varpi}$	Time window length
$R_b$	Useful data rate in bits/s
$\alpha$	Roll-off factor of the prototype pulse frequency response
$\bar{\mathbf{G}}$	Extended generic modulation matrix
$\bar{\mathbf{U}}$	Extended M-Point DFT matrix
$\Theta$	Linear estimation function
$\circ$	Element-wise multiplication operator
$\otimes$	Circular convolution operator
$\delta$	Positive real step-size parameter
$\ell$	Layer index in a lattice or spanning tree structure
$\epsilon$	Efficiency variable for general purpose
$\eta_{\text{GS}}$	Reduction in the spectral efficiency of the GS-GFDM system
$\eta_{\varpi}$	Reduction in the spectral efficiency of the W-GFDM system
$\iota$	Integer variable for general purpose
$\kappa$	Hypothesis index
$\mathbf{A}$	General purpose matrix

<b>F</b>	Discrete Fourier Transform Matrix
<b>G</b>	Generic modulation matrix
<b>H</b>	Linear Transformation Matrix
<b>H<sub>f</sub></b>	Linear Transformation Matrix in frequency domain
<b>I</b>	Identity matrix with sub-scripted dimension
<b>M</b>	General purpose sub-matrix
<b>P</b>	Data permutation matrix
<b>P<sub>R</sub></b>	System permutation matrix for the receiving side
<b>P<sub>T</sub></b>	System permutation matrix for the receiving side
<b>Q</b>	Resulting <b>Q</b> matrix from QR decomposition
<b>R</b>	Resulting matrix <b>R</b> from QR decomposition
<b>S</b>	Sparse binary selection matrix
<b>T</b>	Affine Transform Modulation matrix
<b>V</b>	Generic demodulation matrix
<b>W</b>	Coefficient matrix used in MMSE-based estimators
<b>Σ</b>	random data covariance matrix
<b>C</b>	Finite discrete constellation set
$\mathcal{F}_N$	N-Point Discrete Fourier Transform Function
$\mathcal{F}_N^{-1}$	N-Point Inverse Discrete Fourier Transform Function
<b>H</b>	Hadamard matrix
<b>M</b>	bits-to-QAM function
<b>O</b>	Complexity involving the execution of a subscripted method
<b>Π</b>	bits-to-QAM function
<b>Ĥ</b>	Circular convolution channel matrix
$\mu$	Number of bits per data symbol
$\oslash$	Element-wise division operator
$\otimes$	Kronecker product operator
$\rho$	Reference code word distance used in MLD and SD
$\sigma_w^2$	Noise variance of the AWGN channel
$\sigma_l^2$	Average power at channel tap $l$
$\tau$	Number of nodes in a lattice or spanning tree structure
<b>j</b>	Complex constant $\sqrt{-1}$
<b>H̃</b>	Data symbol transformation matrix
$\varpi_{\text{fall}}$	Falling transition of the W-GFDM time window
$\varpi_{\text{rise}}$	Rising transition of the W-GFDM time window
$\varrho$	Euclidean distance in a multi-dimensional space
$\vec{\mu}$	vector of expected values of random variables
$\vec{X}$	Independent random variable
$\vec{Y}$	Dependent random variable

$\vec{\eta}$	CWCU-LMMSE weighting vector
$\vec{\lambda}$	Log-likelihood ratio vector
$\vec{\mathbf{b}}$	General purpose vector
$\vec{\mathbf{d}}$	Complex data sequence
$\vec{\mathbf{d}}_f$	Complex data sequence in frequency domain
$\vec{\mathbf{g}}$	GFDM transmitting prototype pulse
$\vec{\mathbf{h}}$	Channel impulse response
$\vec{\mathbf{h}}_f$	Channel frequency response
$\vec{\mathbf{v}}$	GFDM receiving prototype pulse
$\vec{\mathbf{v}}_f$	Frequency response of the GFDM receiving prototype pulse
$\vec{\mathbf{w}}$	Additive White Gaussian Noise
$\vec{\mathbf{w}}_f$	Additive White Gaussian Noise in the frequency domain
$\vec{\mathbf{x}}$	Non-observable random data sequence
$\vec{\mathbf{x}}_f$	Unknown random data sequence in the frequency domain
$\vec{\mathbf{y}}$	Observable random data sequence
$\vec{\mathbf{y}}_f$	Observed random data sequence in the frequency domain
$\vec{\mathbf{z}}$	Offset vector
$\xi$	Noise enhancement factor
$b$	Binary digit or subscript bit index
$d_{k,m}$	Data symbol carried by the $k$ th subcarrier and $m$ th subsymbol
$f_s$	Sampling frequency
$i$	Receiving antenna index
$j$	Transmitting antenna index
$k$	GFDM subcarrier index, $k = 0, 1, \dots, K - 1$
$l$	Integer variable for general purpose
$m$	GFDM subsymbol index, $m = 0, 1, \dots, M - 1$
$n$	GFDM sample index, $n = 0, 1, \dots, N - 1$
$n_l$	Number of nonzero lower diagonals in a banded matrix
$n_u$	Number of nonzero upper diagonals in a banded matrix
$p$	Integer variable for general purpose
$q$	Integer variable for general purpose
$r$	Coding rate
$s$	Integer variable for general purpose
$t$	Iteration index
$z$	Integer variable for general purpose

# Contents

<b>1</b>	<b>INTRODUCTION</b>	<b>20</b>
1.1	Mobile Communication Systems	21
1.2	MIMO Communication Techniques	24
1.3	GFDM as a 6G Waveform Candidate	25
1.4	Motivation and Related Works	26
1.5	Contributions	28
1.6	About this Thesis	30
1.7	Notation	31
1.8	Definitions on Complexity Evaluation	31
<b>2</b>	<b>GFDM BACKGROUND</b>	<b>33</b>
2.1	GFDM Waveform	33
2.2	Matrix Notation	35
2.3	Out of Band Emission	38
2.4	GS-GFDM	39
2.5	W-GFDM	40
2.6	Analysis of GFDM Symbol Error Rate Performance	41
2.6.1	GFDM SER in AWGN Channel	42
2.6.2	GFDM SER performance in FSC	43
2.6.3	GFDM SER performance in TVC	44
2.7	Summary	45
<b>3</b>	<b>SYSTEM MODEL FOR THE MIMO COMMUNICATION PHY</b>	<b>47</b>
3.1	Generic MIMO Linear Model	48
3.2	SM-MIMO Factorization	50
3.2.1	Orthogonal Multicarrier SM-MIMO Factorization	50
3.2.2	Non-Orthogonal Multicarrier MIMO Factorization	54
3.3	GFDM Factorized SM-MIMO Model	58
3.3.1	Generic Factorized Linear Model	60
3.4	Summary	60
<b>4</b>	<b>FUNDAMENTALS ON LINEAR ESTIMATION</b>	<b>62</b>
4.1	Linear Estimation Function	62
4.2	LMMSE Estimator	63
4.3	Steepest Descent Estimator	64
4.4	CWCU-LMMSE Estimator	66

4.4.1	Low Complexity CWCU-LMMSE Estimator . . . . .	66
4.4.2	Band-diagonal Low Complexity CWCU-LMMSE Estimator . . . . .	67
4.4.3	CG-based Low Complexity CWCU-LMMSE Estimator . . . . .	69
<b>4.5</b>	<b>Maximum a Posteriori Estimator . . . . .</b>	<b>71</b>
<b>4.6</b>	<b>Bayesian Cramer-Rao Bound . . . . .</b>	<b>73</b>
<b>4.7</b>	<b>Analysis on Linear Estimators . . . . .</b>	<b>73</b>
<b>4.8</b>	<b>Summary . . . . .</b>	<b>77</b>
<b>5</b>	<b>DETECTION TECHNIQUES . . . . .</b>	<b>78</b>
<b>5.1</b>	<b>Maximum Likelihood Detector . . . . .</b>	<b>79</b>
5.1.1	Genie-aided Detector . . . . .	80
<b>5.2</b>	<b>Sphere Detector . . . . .</b>	<b>81</b>
5.2.1	Low Complexity SD-ATM . . . . .	83
5.2.2	Comparison of the SD Algorithms . . . . .	87
<b>5.3</b>	<b>MMSE-SIC Detector . . . . .</b>	<b>90</b>
<b>5.4</b>	<b>MMSE-PIC Detector . . . . .</b>	<b>91</b>
<b>5.5</b>	<b>Detectors Comparison . . . . .</b>	<b>93</b>
<b>5.6</b>	<b>Summary . . . . .</b>	<b>96</b>
<b>6</b>	<b>ITERATIVE MMSE-PIC DETECTOR . . . . .</b>	<b>97</b>
<b>6.1</b>	<b>Fundamentals on Iterative MMSE-PIC . . . . .</b>	<b>97</b>
<b>6.2</b>	<b>Analysis on Iterative MMSE-PIC Detection Technique . . . . .</b>	<b>105</b>
<b>6.3</b>	<b>Summary . . . . .</b>	<b>108</b>
<b>7</b>	<b>LOW-COMPLEXITY 6G TRANSCEIVER FOR REMOTE AREAS . . . . .</b>	<b>110</b>
<b>7.1</b>	<b>Remote and Rural Areas Use Case Scenario . . . . .</b>	<b>110</b>
<b>7.2</b>	<b>Implementation Characteristics . . . . .</b>	<b>112</b>
<b>7.3</b>	<b>Performance evaluation . . . . .</b>	<b>113</b>
<b>7.4</b>	<b>Summary . . . . .</b>	<b>118</b>
<b>8</b>	<b>CONCLUSION . . . . .</b>	<b>119</b>
	<b>APPENDIX . . . . .</b>	<b>122</b>
	<b>APPENDIX A – LMMSE DERIVATION . . . . .</b>	<b>123</b>
	<b>APPENDIX B – STPD DERIVATION . . . . .</b>	<b>126</b>
	<b>APPENDIX C – CWCU LMMSE DERIVATION . . . . .</b>	<b>129</b>

**REFERENCES . . . . . 133**

# 1 Introduction

Mobile communications networks have revolutionized the way the society communicates and, nowadays, cell phones and smartphones are essential items in modern routines. A few decades ago, before the advent of mobile cellular networks, we used to make phone calls directed to places, not towards people. Phone calls were conditioned and restricted to places once the presence of the intended interlocutor at the called location was a requirement to establish a conversation. During the 1980s, this reality began to change with the deployment of the first mobile communication system. Although offering costly subscription and limited coverage, supporting only voice traffic and based on insecure analog frequency modulation scheme, while employing clumsy and inefficient mobile devices, the **1G** (*First Generation*) [2] was indeed a disruptive technology, triggering a revolution in the way we communicate.

In the 90's, the **2G** (*Second Generation*) [3] increased the system capacity due to voice digitalization, voice compression and digital communication techniques, which significantly increased the spectrum and energy efficiencies. Moreover, it introduced a new text based communication service, named **SMS** (*Short Message Service*) [4]. Next, the **3G** (*Third Generation*) [5] and the **4G** (*Fourth Generation*) [6] were deployed, in 2000 and 2010, respectively. Both of them were developed to provide higher user capacity, worldwide roaming and support to an increasing demand for mobile broadband Internet access, this last one being effectively addressed with the consolidation of the **4G** [7]. During the last decade, the scientific community discussed and planned the **5G** (*Fifth Generation*) [8] to go beyond high data rates and larger user capacity. The **5G** was conceived to expand the mobile network and also to create new business opportunities, where four use case scenarios were considered [9]: **eMBB** (*Enhanced Mobile Broadband*), mainly characterized by high throughput connections up to 10 Gbps; **eRAC**, for wide coverage in remote and rural areas; the **URLLC** (*Ultra-Reliable and Low Latency Communications*), offering low latency and high reliability communication mainly for Industry 4.0 [10] and **V2V** (*Vehicle-to-Vehicle*) [11]; and the **mMTC** (*Massive Machine Type Communications*), encompassing a massive number of connected devices as envisioned by the **IoT** (*Internet of Things*) [12, 13] concept.

Since the **1G**, cellular networks have evolved in terms of coverage and user capacity. By the end of 2021, according to [14], the mobile communication network reached a record of 110 subscriptions per 100 inhabitants, equivalent to 8.662 billion devices worldwide. In order to sustain the competitive edge of mobile networks, the industry and the scientific community have already initiated to envisage what could be the next **6G** [15], anticipating improvements that should surpass the forthcoming difficulties that the current generation

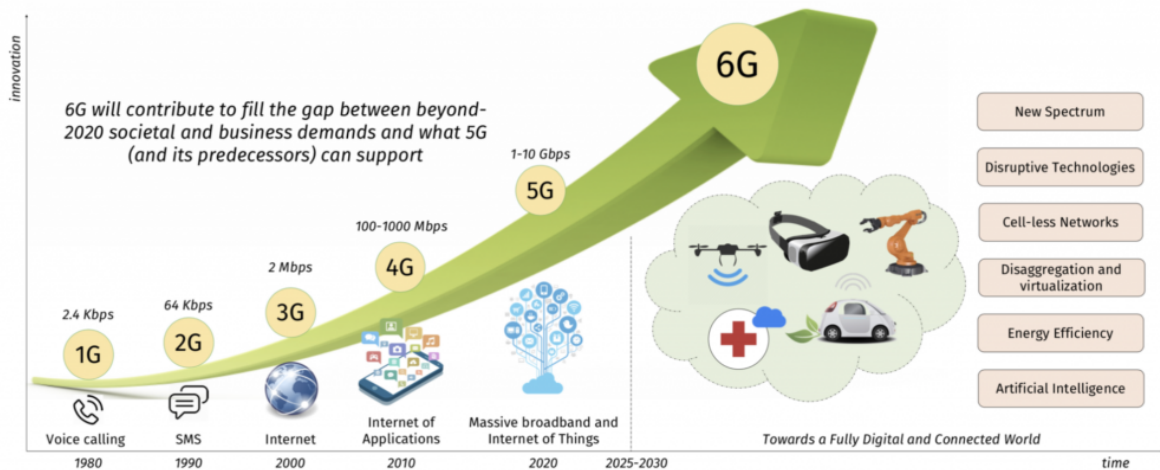


Figure 1 – Evolution of Mobile Networks from 1G to upcoming 6G [16].

may face, besides, of course, keeping the constant evolution history along the successive generations. Figure 1 summarizes the key aspects introduced by each generation of mobile networks.

Aligned with these premises, Section 1.1 briefly presents the main technical aspects related to each mobile network generation. Next, on section 1.2, a short review on MIMO [17] techniques is described, followed by a brief introduction to GFDM [18] as a 6G waveform candidate. Section 1.4 shows the related works, while the main contribution of this thesis is described in section 1.5, highlighting a prominent technique, not adopted in the current 5G, that might become a requirement in future wireless networks, the SM of NO (*Non Orthogonal*) waveforms [19, 20]. Section 1.6 describes the structure of this work, while Section 1.7 presents the notations used in the next chapters and Section 1.8 brings the main concepts to evaluate the complexity of the algorithms discussed in this thesis.

## 1.1 Mobile Communication Systems

In this section, a brief description of the key technical aspects of each mobile generation is presented [21, 22].

The 1G, more specifically the AMPS (*Advanced Mobile Phone System*), was designed to operate within the band between 800 to 900 MHz, with two sub-bands of 12.5 MHz, divided in 416 channels of 30 kHz each, where 21 of them were used for control and the remaining 395 channels were used for analog voice transmission employing frequency modulation. The multi-user access technology was FDMA (*Frequency Division Multiple Access*), allocating a pair of channels per calling. Known limitations of the 1G were insecure communication, unsupported roaming between similar systems, limited number of

users, cell coverage and high power consumption of the handheld devices.

The **2G** inaugurated the digital communication era in mobile networks and overcome several restrictions of the **1G**. The main multi-user access technologies were **CDMA** (*Coded Division Multiple Access*) and **TDMA** (*Time Division Multiple Access*), with the first used in IS-95 networks [23] and the second being used in **GSM** (*Global System for Mobile*) [24] and IS-136 networks [25]. The assigned frequency operation bands were 900 and 1800 MHz. The channel bandwidth in the IS-95 systems was 1.25MHz, supporting up to 64 users per resource and a maximum data rate of 8 kbps for voice transmission. In **GSM**, a 200 kHz channel supported up to 8 users per available resource. IS-136 employed 30 kHz channels, which were shared by up to 6 users. The maximum data rates for voice and data transmission were 13 kbps and 64 kbps, respectively. Both mentioned systems offer secure communication through encrypted encoding, roaming support and multimedia data transmission services as **SMS**. In order to offer higher data rates and provide rudimentary internet access, the **GPRS** (*General Packet Radio Service*), known as 2.5G, and the **EDGE** (*Enhanced Data GSM Evolution*), called 2.75G, both supporting packet switching, were introduced and successfully deployed as evolved transition technologies that coexisted with the **3G** during the 2000s.

In the beginning of the 21st century, the **3G** was launched with the challenging task of defining a common framework under which all different **2G** available networks could evolve and satisfy market demands for global roaming, service portability and multimedia. In this sense, the **ITU** (*International Telecommunication Union*) formulated a plan to implement a global frequency band in the 2000 MHz range, seeking to support a single and ubiquitous wireless communication standard for all countries throughout the world, known as **IMT** (*International Mobile Telephone*) 2000 standard. The main multi-user access technologies used were **TDMA**, **FDMA** and **W-CDMA** (*Wideband Coded Division Multiple Access*), achieving higher network capacity through improved spectral efficiency. The maximum data rates were increased up to 3.6 Mbps and later extended to 8 Mbps. Moreover, a layered network architecture allowed operators to offer a wider range of more advanced services for the users, such as video conference service, broadband wireless data, enhanced audio and video streaming. After the introduction of **3G** mobile communication system, smartphones became popular across the globe. Specific applications were developed for smartphones which handles multimedia chat, email, video calls, games, social media, **GPS** (*Global Positioning System*) assisted location tracking, navigation and maps.

The **4G** is an enhanced version of the **3G** networks, whose requirements were defined by the **ITU** according to the **IMT** Advanced specification [26]. The **4G LTE** (*Long-Term Evolution*) [27] was developed by the academic community and R&D institutes, headed by the **3GPP** (*3rd Generation Partnership Project*) work groups. The main features of **LTE** are the **IP** (*Internet Protocol*)-based architecture [28], **OFDMA** (*Ortho-*

gonal Frequency Division Multiple Access) [29] supporting TDD (*Time-Division Duplex*) or FDD (*Frequency-Division Duplex*), SM-MIMO in the uplink and downlink, different modulation and channel coding schemes, besides improved resource allocation based on achievable link capacity. The LTE increased the system user capacity and throughput to 100 Mbps in high mobility scenarios, at speeds around 60 km/h, and up to 1 Gbps in FWA (*Fixed Wireless Access*). The last LTE release, named Advanced Pro, achieves downlink rates up to 3 Gbps. High definition streaming and low latency game experience are realities in 4G. The LTE is now the most popular mobile network technology off all times and should coexist with the 5G along the forthcoming years while being gradually replaced.

5G technology is expected to expand mobile network connectivity, enhancing user experiences and creating new verticals to serve industries and agribusinesses through innovative operational modes, targeting B2B (*Business-to-Business*) markets. The requirements of IMT 2020 [30] embraces a diverse variety of use case scenarios, such as high downlink data rates up to 20 Gbps with peak spectral efficiency of 30 bps/Hz, latency as low as 1 ms and high connection density, up to 1.000.000 devices/km<sup>2</sup> [31]. The key technologies in the scope of the mobile network companies encompass usage of frequency bands above 28 GHz, massive MIMO antenna arrays at the base station, beam forming MIMO [32], more efficient scheduling and interference management [33].

The 5G technology has recently begun to be deployed in smaller cities, following its initial roll-out in capitals and highly populated centers. Nonetheless, in face of its scope, there is still many challenges to bring broadband connectivity to the rural and remote regions. Particularly in Brazil, a big digital gap between urban and rural areas remains. The urban sector have a typical coverage around 65% while the rural penetration is just 34% [34]. In order to meet this demand, the 5G-RANGE (*Remote Area Access Network for the 5th Generation*) project, a Brazil-Europe bilateral project, was proposed to provide reliable long-range and cost-effective connection in these regions. It also incorporates a cognitive engine allowing local and rural operators to exploit vacant TV channels, also known as TVWS (*TV White Space*), as secondary network in an opportunistic approach [35]. As a result, a practical transceiver, encompassing frame structure and support for diversity MIMO was designed and evaluated in real field operation [36], opening opportunities for new solutions and operating modes for future mobile networks [37].

The academic community and the industry have jointly started the discussions around the requirements and definitions of 6G networks [38]. Up to now, the main goal is to go beyond increasing mobile environment capacity, aiming to improve human quality of life in several aspects, inspired by the United Nations Sustainable Development Goals [39]. The 6G will require new enabling technologies to provide cloud-based architecture and flexible networks of networks, integration of AI (*Artificial Intelligence*) algorithms into the

RAN (*Radio Access Network*) for enhanced network performance, virtual world connectivity, extremely high capacity and data rate as well as highly accurate joint communication and sensing. Some of these advancements in wireless communications are quantum technologies, satellite communication, visual light communication, higher carrier frequencies in the upper mmWave (*millimeter Wave*) band (100-300 GHz), RIS (*Reconfigurable Intelligent Surfaces*) [40] and SM-MIMO systems employing NO waveforms [1, 41]. This last one might become a feasible requirement since SM-MIMO and NO-GFDM, jointly, could lead to a system capacity improvement, benefited by higher spectral efficiency with low OOB emission, besides harvesting multiplexing and extra diversity gain at the same time. These achievements are essential for a mobile network designed for remote areas since low OOB emissions are mandatory for coexistence with legacy technologies, higher data rates are needed, for example, to cover the requirements for imaging and real-time positioning in agribusiness, and robustness is a requirement for increasing coverage and reliability.

In [1], Matthé et al. propose an ingenious low complexity and low latency parallel detection scheme employing NO-GFDM, where the aforementioned multiplexing and diversity gains are demonstrated through simulations. Nevertheless, a practical implementation and evaluation of this scheme, considering a real hardware and its inherently impairments, are still pending. In this context, the present work aims to contribute with a flexible simulation model that formulates the intricate concepts involving this resourceful detection technique. The resulting set of algorithms is an essential reference design for enabling hardware implementation and experimental analysis of this innovative detection scheme across different applications. The system parametrization to be used in real world application is also another important challenge that is addressed by this thesis.

## 1.2 MIMO Communication Techniques

A fundamental aspect for any modern wireless communication system is the use of multi-antennas techniques in order to improve the communications performance by either combating or exploiting multipath scattering of the communication channel [17]. Indeed, the MIMO integration has become a crucial requirement for every emerging waveform, since recent wireless systems are commonly adopting MIMO support as a standard feature. Among them, there are the WLAN (*wireless Local Area Network*), with IEEE 802.11be, also known as WiFi (*Wireless Fidelity*) 7 [42], DTV (*Digital Television*) ATSC 3.0 [43] and newly standards as LTE Railway [44] and 5G NR (*New Radio*) [45]. Undoubtedly, MIMO schemes play a central role for most recent wireless systems as it might bring significant improvements on link reliability or spectral efficiency.

MIMO techniques that attempts to improve link reliability are designed to harvest diversity gain, making use of some sort of diverseness resource, i.e. time-frequency

diversity, polarization diversity and spatial diversity, while transmitting replicas of the same information through independent fading channels. As the channels are independent, it is unlikely that a severe fading affects all of them simultaneously, yielding to an improvement on link robustness after properly combining the received replicas. Time and frequency diversity explore temporal and spectral dynamic of the wireless channel, transmitting the information replicas in distinct time or frequency resources, implying a proportional reduction on gross data rate. On the other hand, spatial diversity allows to make use of independent fading channels without the penalty on data rate, at the cost of a more complex receiving scheme in order to coherently combine the received replicas. Different **MIMO** techniques exploiting spatial diversity jointly with time or frequency diversity are amply available in literature being, among them, the notorious Alamouti **STC** (*Space Time Code*) [46] and its cyclic-prefixed block variations [47, 48], restrained to a pair of transmitting antennas and capable to achieve full diversity gain with low complexity at the receiver.

Another class of **MIMO** techniques, known as **SM-MIMO**, aims to improve the spectral efficiency of a wireless communication system, achieving multiplexing gain by transmitting distinct data streams over the same time and frequency resources, resulting in a data rate improvement, without increasing the required bandwidth. This assumption is true since the receiver is able to correctly decouple and retrieve the transmitted information. The multiplexing gain is proportional to the number of transmitting antennas if the number of receiving antennas at least matches the number of transmitting antennas, while the involved complexity follows, in general, a non-linear growth rate. Considering sub-optimal or even optimal-achievable receivers, the computational cost is polynomial in average and, in the case of an optimal receiver, i.e. **ML** (*Maximum Likelihood*), the complexity grows exponentially with the number of transmitting antennas.

Since these topics are widely studied, the number of different techniques available in the literature can be overwhelming. Hence, this thesis focuses in a practical **SM-MIMO** implementation, considering **NO** waveforms, more specifically the **GFDM**, in order to evaluate the theoretical results presented in [1] but adapted to fulfill the requirements of the **eRAC** scenario in **6G** networks.

### 1.3 GFDM as a 6G Waveform Candidate

The **GFDM** was initially introduced in 2009 [18] as a new waveform employing multiple **NO** sub-carriers. During the initial studies related to the **5G** in the last decade, **GFDM** was appointed as an alternative for the implementation of the **PHY** (*Physical Layer*) [49] thanks to its flexibility and low spurious emission. Although **GFDM** was not chosen as the primary waveform for **5G**, it retains valuable features and demonstrates

superior performance in certain aspects [50, 51], particularly in terms of low OOB emissions. These attributes make GFDM a viable alternative in ongoing discussions about the potential 6G network among the scientific community, standardization institutes and industry stakeholders.

As stated in Section 1.1, the emerging 5G is driving mobile communication systems towards an unprecedented evolution in terms of flexibility, data rate and latency, enabling wireless networks to support applications that are typically backed by wired technologies. The scenarios for the 6G are even harder to achieve considering the foreseen increase in flexibility, while supporting conflicting requirements for several applications in different verticals, besides higher data rates, higher coverage, higher frequency bands and extreme low latency. It is clear that future mobile networks cannot rely on a single radio access network to fulfill all these requirements. Different approaches are needed to address all requirements, but SM-MIMO schemes are a key technology for all future broadband wireless systems. For example, in the agribusiness scenario, high data rates are necessary to transmit multi-spectral videos in infrared, ultraviolet and visible light in real time from drone to the cloud. In industry 4.0, very low latency is necessary for controlling robots and synchronizing autonomous actions with humans on the plant floor. SM-MIMO can provide the necessary bandwidth, reducing the frame duration and increasing the robustness for data with a very short life span. SM-MIMO systems with detection schemes that can harvest diversity and multiplexing gains can improve the throughput and increase coverage. In this sense, GFDM can be considered as a feasible alternative, particularly where OFDM waveforms might experience unfavorable conditions. For example, dynamic spectrum allocation of vacant channels requires low OOB emission, dictated by critical emission masks in order to achieve precise energy sensing. On low latency applications, the GFDM exhibit smaller CP (*Cyclic Prefix*) overhead and, consequently, a better block efficiency. Moreover, prototype pulse format and its ROF (*Roll-off Factor*) allows to control ISI (*Inter-Symbol Interference*) and ICI (*Inter-carrier Interference*), seeking to harvest extra diversity gain when compared with orthogonal waveforms. These are the main advantages that might justify the GFDM as a feasible waveform candidate for 6G networks.

## 1.4 Motivation and Related Works

Providing broadband connectivity and support for IoT devices in remote and rural areas presents a significant challenge for countries like Brazil, characterized by expansive territories and sparse population distribution. Overcoming these challenges would yield substantial social and economic benefits. However, current 5G networks face difficulties in meeting the communication requirements in remote regions due to limited coverage

range, high costs associated with frequency spectrum licenses, and expensive equipment, installation, operation, and maintenance [52]. To address these challenges, the Brazil-Europe bilateral cooperation project has developed the **5G-RANGE** transceiver, aimed at providing connectivity in remote and rural areas [35]. This network opportunistically uses idle **UHF (Ultra High Frequency)** channels in remote regions to establish connectivity, employing TV channels in a secondary manner through cognitive radio. This approach allows local providers to offer Internet access services without the need for spectrum licenses.

The **TVWS** approach provides the necessary conditions to achieve long-range and high data capacity in remote areas once it intends to use vacant TV channels, a valuable resource commonly available in these regions. This requirement indicates that **SM-MIMO** is an ideal solution compared to **mMIMO (massive MIMO)** [53], **CFmMIMO (cell-free massive MIMO)** [54], and **RIS** [40]. **mMIMO** and **CFmMIMO** present impractical aspects at sub-1 GHz frequencies due to large antenna sizes, mutual coupling issues, and the fact that channel hardening is used primarily to improve reliability through diversity gain. The **CFmMIMO** also faces challenges such as complex spectrum management and high deployment costs. Although innovative, **RIS** encounters difficulties with large element sizes, mutual coupling issues, and regulatory constraints, particularly in dynamic environments. In summary, considering the constraints imposed by **TVWS** operation and the challenges presented by other prominent technologies, **SM-MIMO** emerges as a more practical solution.

The **5G-RANGE** network was designed to operate in **TVWS** regime and employs the **GFDM** waveform [55] in its **PHY** core, offering greater flexibility compared to **OFDM**, which is commonly used in current wireless communication standards. **GFDM** enables the selection of a shaping filter for each subcarrier, effectively restricting **OOB** emissions and eliminating the need for a **RF (Radio Frequency)** filter in the transmitter, thereby ensuring spectral agility. Consequently, if a primary user begins using a channel occupied by a secondary network, the latter can detect the incumbent's presence and switch the operating frequency without requiring human intervention. Furthermore, the **PHY** of this access network incorporates a robust error correction code, coupled with a hybrid **MIMO** scheme [17, 56], providing spatial diversity for users in challenging channel conditions and **SM** for users in favorable situations. As a result, this access network can cover larger areas than those designed for operation in urban centers.

Despite significant progress, several challenges remain to ensure effective connectivity in remote and rural areas through the proposed network. One primary obstacle is the development of high-performance, low-complexity **MIMO** detection scheme. In the current **5G-RANGE** transceiver version, the **GFDM** waveform supports only orthogonal pulses, which restricts the reduction in **OOB** emission. Moreover, the **SM-MIMO** detec-

tor relies on the *ZF (Zero-Forcing)* technique, where performance is strongly influenced by noise enhancement and by the rank of the channel matrix between the transmitting and receiving antennas [57]. Frequently, in many scenarios, the propagation environment introduces strong correlation among multipaths, leading to lower-rank channel matrices and consequent degradation in system performance. Furthermore, linear *MIMO* detectors are unable to capture signal diversity and exhibit low performance when *NO* pulses are employed. To fully exploit the flexibility of the communication system designed for the *eRAC* scenario, it is essential to implement a nonlinear *MIMO* detector that offers both high performance and low complexity. In this context, a comprehensive analysis of the estimation and detection algorithms for the next generations of mobile communications is crucial [58, 59]. Within the *NO-GFDM-SM-MIMO* framework, the *MMSE-PIC* detector, proposed in [1], stands out for addressing the detection challenge through an ingenious factorization of the system in the frequency domain. Its primary objective is to simultaneously exploit multiplexing and diversity gains, thereby enabling an affordable low-latency, and low-complexity implementation [60, 61]. Nevertheless, a systematic method to factorize and organize problems of any dimension remains an unsolved challenge.

## 1.5 Contributions

Aiming to continue the *5G-RANGE* evolutionary trajectory and align with the academic discussions surrounding *6G* mobile networks, this thesis proposes the use of *SM-MIMO* technique combined with the *NO-GFDM* waveform, to achieve higher spectral efficiency and high robustness with low *OOB* emission. This approach also enables the harnessing of multiplexing and additional diversity gain while employing a low-complexity *MMSE-PIC* detector [1]. The objective is to implement, through simulations, a real *6G* transceiver capable of addressing the bottleneck challenges in various applications within the *eRAC* scenario. These achievements are crucial for mobile networks designed for remote areas, where low *OOB* emissions are imperative for coexistence with legacy technologies, higher data rates are necessary to fulfill the requirements for imaging and real-time positioning in agribusiness applications, where robustness is essential for enhancing coverage and reliability. Indeed, practical evaluation of theoretic concepts proven correct through computational simulation, are valuable in the sense that these results are essential for the selection, implementation and advancement of any new innovative technologies, including *RIS* [40], and novel waveforms [51].

Specifically, the main contributions of this work are:

- introduction of a generic and simplified linear model to describe the digital *MIMO* communication *PHY* and, afterwards, the basic concepts involving the *GFDM* wa-

veform;

- recapitulation of fundamental concepts on linear estimation and detection techniques, widely employed along this thesis;
- proposal of a reduced complexity *SD (Sphere Detector)* based on *ATM (Affine Transform Modulation)*;
- a comprehensive review of the intricate theory behind the *SM-MIMO MMSE-PIC* algorithm, suitable, but not restricted, to detect multiple data streams transmitted by *NO* waveforms, accompanied by an extended block diagram of the entire detection process;
- mathematical deduction of the system's permutation matrices, crucial to factorize the problem order, where relies the algorithm complexity reduction;
- review of recent procedures in order to adapt the *5G-RANGE* radio to support *NO GFDM* waveform, which involves the application of *IFPI (Interference Free Pilot Insertion)*, as described in [62], and the *LLPD (Low-Density Parity-Check (LDPC)-like Polar Decoder)* based on [63];
- simulation of the low complexity and low latency *MMSE-PIC* detector, aiming to provide a valuable reference design for a future practical evaluation of the *NO-GFDM-SM-MIMO* transceiver implementation;
- detailed overview of the simulation parameters, intended to support readers who wish to replicate the results;
- analysis of *FER (Frame Error Rate)* performance compared to optimal *ML* detector curves, approximated from a *GAD (Genie-Aided Detector)*.
- graphical analysis of the algorithm convergence behavior, a valuable method to optimize the number of required *PIC* iterations.

The research on mobile communication techniques, including novel and recent waveforms, continues to gather the attention of the scientific community, seeking to investigate and propose solutions for the challenging requirements and constant evolution of forthcoming wireless systems. In this extent, practical evaluation of theoretic concepts, proven correct through computational simulation, are indeed valuable in the sense that experimental results are essential for selecting new technologies and serve as a guide for further improvements and implementation approaches.

## 1.6 About this Thesis

Chapter 2 reviews the background concepts involving the GFDM system, including waveform generation and its key characteristics. It revisits the main GFDM demodulation methods, analyzing the advantages and drawbacks compared to the established OFDM, based on their SER (*Symbol Error Rate*) performance across different channels.

In Chapter 3, a simplified generic model to linearly describe the MIMO communication PHY is described, more specifically, the SM-MIMO multi-resource baseband equivalent model, considering a dispersive and FSC (*Frequency-Selective Channel*). Moreover, it describes the factorization of an orthogonal system and explain why a NO waveform typically requires a full system solution. This challenge is the motivation behind the original proposal of a mathematical expression to decompose the entire system into independent sub-problems.

Chapter 4 covers the fundamentals on linear estimation, including the classical estimators like LMMSE (*Linear Minimum Mean Square Error*), STPD (*Steepest-Descent*) and CWCU (*Component-Wise Conditionally Unbiased*)-LMMSE, among others.

Chapter 5 recapitulates relevant detection algorithms, such as MLD (*Maximum Likelihood Detector*), SD and the SIC (*Successive Interference Cancellation*).

Chapter 6 dedicates a special attention to the resourceful MMSE-PIC detector, proposed in [1], designed to solve the NO-SM-MIMO-GFDM detection problem through an ingenious system factorization in the FD (*Frequency Domain*). This chapter is supplemented with detailed block diagrams and algorithms, aiming to establish a safe guidance for practical implementation. To prove the correctness of the method, the results from the aforementioned reference were reproduced, along with a complexity comparison.

Chapter 7 focuses on adapting the MMSE-PIC detector to serve as the receiver PHY core in the Brazil 6G project. This project aims to deploy an innovative transceiver to meet the requirements of rural and remote areas [35], an usual scenario in countries with continental dimensions. The propose relies on the use of recent channel coding and pilot insertion techniques to support the parameters adopted in the transceiver proposal, mainly based on 5G-RANGE radio numerology. This chapter further presents the evaluation of the designed detector within the NO-SM-MIMO-GFDM transceiver, comparing the resulting FER with the ML lower bound performance.

Finally, Chapter 8 summarizes the achievements of this work and propose future research opportunities in this topic.

## 1.7 Notation

Matrices and vectors are written in boldface uppercase and arrowed lowercase as  $\mathbf{X}$  and  $\vec{x}$ , respectively. Matrix element indexing, row or column sectioning, as also as vector indexing, is made through subscript indexes or enclosed by square brackets. A random variable observation is represented as a lowercase  $x_i$  or by  $x[i]$ . The notation  $\mathbb{E}\{\cdot\}$  is the expected value of a given random entity. The exponent  $(\cdot)^H$  is the transpose and conjugate (Hermitian) operator while  $(\cdot)^T$  means only transposition. The mean and the covariance of a given random vector, e.g.  $\vec{x}$ , are defined as  $\vec{\mu}_{\vec{x}} = \mathbb{E}\{\vec{x}\}$  and  $\Sigma_{\vec{x}} = \mathbb{E}\{\vec{x}\vec{x}^H\} - \vec{\mu}_{\vec{x}}\vec{\mu}_{\vec{x}}^H$ , respectively. The operator  $\text{diag}(\cdot)$  gives the diagonal of a square matrix or, when the argument is a vector, it returns a square matrix whose diagonal is populated with the vector elements. The operators  $\circ$  and  $\oslash$  are the element-wise multiplication and division, respectively. The Frobenius norm of a generic matrix  $\mathbf{A}$  is defined by  $\|\mathbf{A}\|^2 \triangleq \sum_{i,j} |A_{ij}|^2$ , with  $A_{ij}$  being the elements of such matrix. The operation  $\lceil x \rceil_2$  denotes the smallest power-of-two that is greater than or equal to  $x$ . The set of binary, real and complex numbers are denoted by  $\mathbb{B}^{p \times q}$ ,  $\mathbb{R}^{p \times q}$  and  $\mathbb{C}^{p \times q}$ , respectively, where  $p$  and  $q$  are the dimension size of the numerical structure.

## 1.8 Definitions on Complexity Evaluation

Before delving into the specifics of linear estimation and detection schemes, it is necessary to first provide a brief review of the foundational principles of complexity analysis. This review aims to establish a clear framework for evaluating and comparing the efficiency and performance of various techniques and algorithms, ensuring that subsequent analyses are both thorough and equitable.

Table 1 summarizes the amount of **FLOPs** (*Float-Point Operations*) demanded on common matrix algebra [64], optimized algorithms for banded matrices [65] and the implicit **HQR** (*Householder QR Factorization*) [66]. In this context,  $\vec{\phi} \in \mathbb{C}^{p \times 1}$  and  $\vec{\psi} \in \mathbb{C}^{q \times 1}$  are generic vectors,  $F \in \mathbb{C}^{q \times p}$ ,  $\Psi \in \mathbb{C}^{q \times p}$  and  $\Phi \in \mathbb{C}^{p \times s}$  are arbitrary matrices, while  $\Omega \in \mathbb{C}^{p \times p}$  is a diagonal matrix,  $\Lambda \in \mathbb{C}^{p \times p}$  is a positive definite matrix and  $\Pi \in \mathbb{C}^{q \times q}$  is a band-diagonal matrix, with single-side bandwidth  $s$  such that  $q=zs$ . For the **HQR**, we consider  $\Gamma \in \mathbb{C}^{p \times q}$  with  $p \geq q$ . The **FLOP** account for the **CFLOP** (*Complex Float-Point Operation*) in [64] considers that a complex summation consists of only 2 **FLOPs** (2 real summations), a complex multiplication requires 6 **FLOPs** (4 real multiplications and 2 real summations), a complex square takes 3 **FLOPs** (2 real multiplications and 1 real summation), a complex square root [67] demands 10 **FLOPs** (2 real multiplications, 2 real divisions, 3 real summations and 3 real square roots) and a complex division takes 11 **FLOPs** (6 real multiplications, 2 real divisions and 3 real summations).

Table 1 – Common matrix algebra computational complexity.

Index	Description	Notation	FLOPs
1	Matrix-Vector Prod.	$\Psi^{q \times p} \vec{\phi}^{p \times 1}$	$8qp - 2q$
2	Matrix-Matrix Prod.	$\Psi^{q \times p} \Phi^{p \times s}$	$8qps - 2qs$
3	Matrix-Diagonal Prod.	$\Psi^{q \times p} \Omega^{p \times p}$	$6qp$
4	Matrix Inversion	$(\Lambda^{p \times p})^{-1}$	$4p^3 + 8p^2 + 10p$
5	Banded Matrix-Vector Prod.	$\Pi_{ q=zs}^{q \times q} \vec{\psi}^{q \times 1}$	$8s^2z - 2sz$
6	Banded Matrix-Matrix Prod.	$\Pi_{ q=zs}^{q \times q} F^{q \times p}$	$8ps^2z - 2psz$
7	Banded Gram Matrix	$(\Pi_{ q=zs}^{q \times q})^H (\Pi_{ q=zs}^{q \times q})$	$8s^3z - 2s^2z$
8	Banded LU factorization	$\mathbf{LU} = \mathbf{LU}(\Pi_{ q=zs}^{q \times q})$	$32s^3z - 16s^2z$
9	Banded Linear System Solution	$F^{q \times p} = (\Pi_{ q=zs}^{q \times q})^{-1} \Psi^{q \times p}$	$48s^2zp - 24szp$
10	$p$ -Point DFT	$\vec{\phi}_f^{p \times 1} = \mathbf{F}_p \vec{\phi}^{p \times 1}$	$p \log(p)$
11	HQR factorization	$\mathbf{QR} = \text{HQR}(\Gamma^{p \times q})$	$2q^2p - 2q^3/3$

Additionally, Table 2 presents some useful finite sum identities [68], which are widely applied in the complexity formulation of the investigated techniques.

Table 2 – Useful finite sum identities.

Index	Expression	Identity
1	$\sum_{p=1}^q c$	$qc$
2	$\sum_{p=\ell}^q c$	$c(q - \ell + 1)$
3	$\sum_{p=1}^q p$	$\frac{q(q+1)}{2}$
4	$\sum_{p=1}^q p^2$	$\frac{q(q+1)(2q+1)}{6}$
5	$\sum_{p=\ell}^q p$	$\sum_{p=1}^q p - \sum_{p=1}^{\ell-1} p = \frac{q(q+1) - \ell(\ell-1)}{2}$

Finite sum identities are mathematical expressions that give exact solutions for the sum of a sequence of terms. These identities are especially useful in fields like computer science, physics, and engineering, as they simplify complex summations and help in analyzing algorithms.

## 2 GFDM Background

GFDM is a flexible multicarrier modulation scheme capable of generating modulated block symbols with variable duration independently of the subcarrier spacing [55]. Basically, GFDM employs filters circularly shifted in the time and frequency domains for spectral formatting of individual subcarriers, responsible for transporting the data symbols in subsequent instants of time. Different from OFDM, where for each block one subcarrier carries only one data symbol, each subcarrier of GFDM symbol can carry multiples data symbols, resulting in multiple subsymbols within the GFDM block.

This section presents a brief introduction, mainly based on [69], regarding the GFDM waveform generation and detection processes, as well as an analysis of its more relevant characteristics.

### 2.1 GFDM Waveform

GFDM can be described as a multicarrier modulation scheme where each subcarrier transports data symbols at successive instants of time, named subsymbols. Each GFDM block carries up to  $N$  data symbols, with  $N=MK$ , where  $M$  and  $K$  denote, respectively, the number of available subsymbols and subcarriers. In this sense, the data symbols, denoted by  $d_{k,m}$ , with  $k = 0, 1, \dots, K-1$  being the subcarrier index and  $m = 0, 1, \dots, M-1$  the subsymbol index, are all organized in a time-frequency grid as illustrated by Figure 2.

Each subcarrier is then filtered according to a prototype pulse  $\vec{\mathbf{g}}_{k,m}$ , shifted both in time and frequency, whose elements are given by

$$\vec{\mathbf{g}}_{k,m}[n] = \vec{\mathbf{g}}[\langle n - mK \rangle_N] e^{j\frac{2\pi}{K}kn}, \quad (2.1)$$

where  $n = 0, 1, \dots, N-1$  is the sample index of the resulting pulse. The operator  $\langle C \rangle_D$  represents the modulo operation or the remainder of the division of  $C$  by  $D$ .

Circular convolution is employed to modulate the prototype pulse according to the corresponding data symbol, hence, the GFDM block symbol is self-contained in  $N$  samples length and expressed by [69]

$$\begin{aligned} \vec{\mathbf{x}}[n] &= \sum_{k=0}^{K-1} \sum_{m=0}^{M-1} d_{k,m} \delta[\langle n - mK \rangle_N] \otimes \vec{\mathbf{g}}[n] e^{j\frac{2\pi}{K}kn} \\ &= \sum_{k=0}^{K-1} \sum_{m=0}^{M-1} d_{k,m} \vec{\mathbf{g}}_{k,m}[n], \end{aligned} \quad (2.2)$$

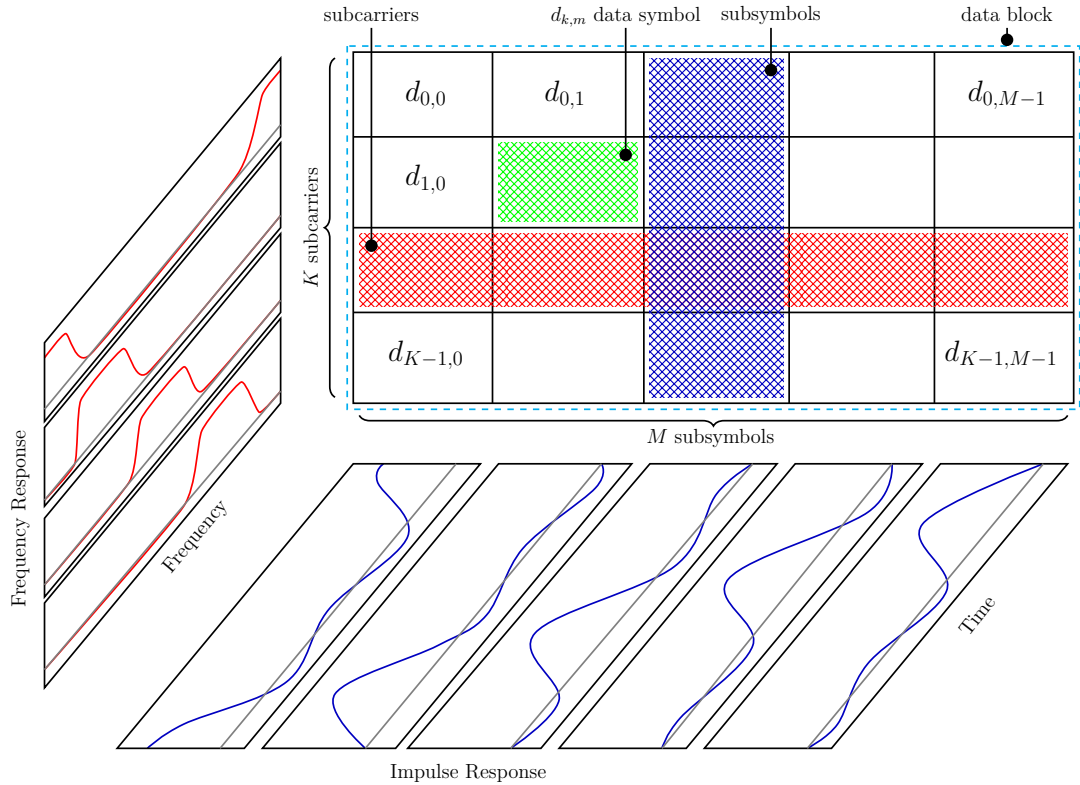


Figure 2 – GFDM block structure [70] and applicable terminology.

where the operator  $\circledast$  denotes circular convolution and  $\delta[n]$  is the discrete Dirac impulse function. This review admits a single-input and single-output system and omits any antenna sub-scripted index for notation simplicity.

In order to protect the  $M$  subsymbols from IBI (*Inter-Block Interference*) introduced by the dispersive communication channel, a CP is appended to the GFDM block. It is worth to highlight the improved frame efficiency of the GFDM where an unique CP protects the entire symbol containing  $M \times K$  resources and, on the contrary, the OFDM requires one CP per  $K \times 1$  symbol block. It is also worth to mention that choosing a RC (*Raised Cosine*) prototype pulse with  $\alpha=0$  and  $M=1$ , the resulting GFDM waveform is identical to OFDM.

Assuming perfect synchronization and CSIR (*Channel State Information at the Receiver*), after the CP removal, the received signal is

$$\vec{\mathbf{y}}[n] = \vec{\mathbf{x}}[n] \circledast \vec{\mathbf{h}}[n] + \vec{\mathbf{w}}[n]. \quad (2.3)$$

Note that the circular convolution in (2.3) occurs upon  $N$  samples of the effective GFDM symbol and still benefits from FDE (*Frequency-Domain Equalization*), which can be performed by

$$\hat{\vec{\mathbf{y}}} = \mathcal{F}_N^{-1} \left( \mathcal{F}_N(\vec{\mathbf{y}}) \oslash \mathcal{F}_N(\vec{\mathbf{h}}) \right), \quad (2.4)$$

where  $\oslash$  is the element-wise division operator,  $\vec{\mathbf{h}}$  is the equivalent base band CIR (*Channel*

*Impulse Response*) while  $\mathcal{F}_N$  and  $\mathcal{F}_N^{-1}$  represents, respectively, the  $N$ -point DFT (*Discrete Fourier Transform*) and IDFT (*Inverse Discrete Fourier Transform*).

After equalization, the transmitted symbols can be retrieved employing a receiving prototype pulse,  $\vec{\mathbf{v}}$ , properly shifted in time and frequency [69], yielding to

$$\begin{aligned}\hat{d}_{k,m} &= \sum_{n=0}^{N-1} \hat{\mathbf{y}}[n] \vec{\mathbf{v}}[\langle n - mK \rangle_N] e^{-j \frac{2\pi kn}{K}} \\ &= \sum_{n=0}^{N-1} \hat{\mathbf{y}}[n] \vec{\mathbf{v}}_{k,m}[n].\end{aligned}\quad (2.5)$$

The transmitting prototype pulse used to filter the subcarriers can be designed to achieve specific goals [71], such as low self-interference and low OOB emission. In general,  $\vec{\mathbf{g}}[n]$  results in a set of non-orthogonal filters that introduce IBI and ICI, hence, the receiver needs to handle the system self-interference. In the next section, an useful matrix notation for the GFDM system is presented, besides a brief description on the design of linear demodulators and its characteristics.

## 2.2 Matrix Notation

The GFDM modulation and demodulation processes can be easily represented through matrix operations, which is convenient to design linear demodulators. The data block grid, illustrated by Figure 2 and organized in a structure of  $K \times M$  elements, can be arranged in a vector  $\vec{\mathbf{d}}$  containing  $N$  elements, grouped by subsymbols,

$$\vec{\mathbf{d}} = \text{vec} \left( \begin{bmatrix} d_{0,0} & \dots & d_{0,M-1} \\ d_{1,0} & \dots & d_{1,M-1} \\ \vdots & \ddots & \vdots \\ d_{K-1,0} & \dots & d_{K-1,M-1} \end{bmatrix} \right) = [d_{0,0} \ \dots \ d_{K-1,0} \ \dots \ d_{0,M-1} \ \dots \ d_{K-1,M-1}]^T. \quad (2.6)$$

All shifted versions of  $\vec{\mathbf{g}}$  can also be organized in a generic modulation matrix  $\mathbf{G}$ . Thus, grouping the columns by subsymbols, results

$$\mathbf{G} = [\vec{\mathbf{g}}_{0,0} \ \dots \ \vec{\mathbf{g}}_{K-1,0} \ \dots \ \vec{\mathbf{g}}_{0,M-1} \ \dots \ \vec{\mathbf{g}}_{K-1,M-1}]. \quad (2.7)$$

In systems employing  $N_{\text{on}}$  active resources out of a total available  $N$ , (2.6) and (2.7) must be adjusted to remove the corresponding  $N_{\text{off}} = N - N_{\text{on}}$  elements from  $\vec{\mathbf{d}}$  and the related  $N_{\text{off}}$  columns of  $\mathbf{G}$ .

Figure 3 shows the structure of the modulation matrix for a given RRC (*Root Raised Cosine*) prototype filter. Each column of  $\mathbf{G}$  is a shifted time-frequency version of the prototype pulse.

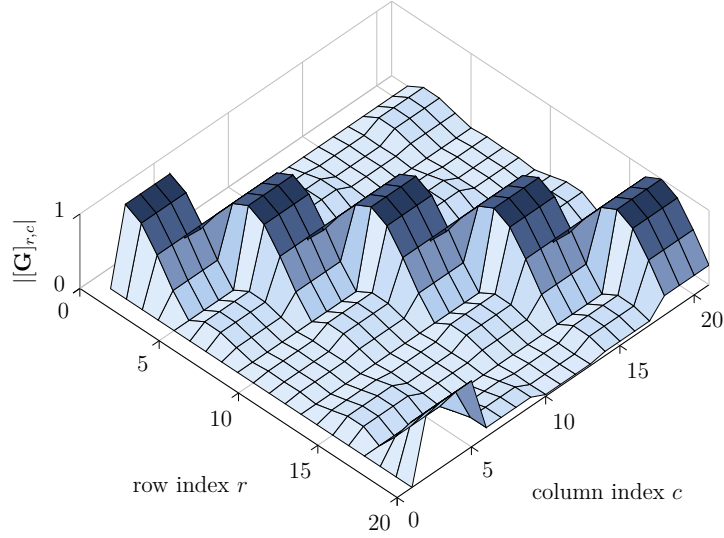


Figure 3 – Structure of the modulation matrix  $\mathbf{G}$  for  $M = 5$ ,  $K = 4$ , RRC filter with  $\alpha = 0.5$ .

The GFDM transmission symbol can now be obtained by

$$\vec{\mathbf{x}} = \mathbf{G}\vec{\mathbf{d}}. \quad (2.8)$$

Again, prior to transmission in a dispersive channel, the GFDM symbol is protected by a CP in such manner that, considering perfect synchronization and CSIR, after CP removal, the received symbol is

$$\vec{\mathbf{y}} = \mathbf{H}\vec{\mathbf{x}} + \vec{\mathbf{w}}. \quad (2.9)$$

Here,  $\mathbf{H}$  is the circulant channel matrix  $\hat{\mathbf{H}}$ . The received signal in the FD is

$$\begin{aligned} \vec{\mathbf{y}}_f &= \mathbf{F}_N \vec{\mathbf{y}} = \mathbf{F}_N \mathbf{H} \vec{\mathbf{x}} + \mathbf{F}_N \vec{\mathbf{w}} \\ &= \mathbf{F}_N \mathbf{H} \mathbf{F}_N^H \mathbf{F}_N \vec{\mathbf{x}} + \vec{\mathbf{w}}_f \\ &= \mathbf{F}_N \mathbf{H} \mathbf{F}_N^H \vec{\mathbf{x}}_f + \vec{\mathbf{w}}_f, \end{aligned} \quad (2.10)$$

where  $\mathbf{F}_N$  is a  $N$ -point DFT matrix,  $\vec{\mathbf{y}}_f$ ,  $\vec{\mathbf{x}}_f$  and  $\vec{\mathbf{w}}_f$  are, respectively, the received signal, the transmitted symbol and the noise signal, all in the frequency domain. Note that  $\mathbf{F}_N \mathbf{H} \mathbf{F}_N^H$  results in a diagonal matrix containing the CFR (*Channel Frequency Response*). Applying the FDE yields to

$$\hat{\vec{\mathbf{y}}}_f = \left( \mathbf{F}_N \mathbf{H} \mathbf{F}_N^H \right)^{-1} \vec{\mathbf{y}}_f = \vec{\mathbf{x}}_f + \left( \mathbf{F}_N \mathbf{H} \mathbf{F}_N^H \right)^{-1} \vec{\mathbf{w}}_f. \quad (2.11)$$

The received and equalized signal, in the TD (*Time Domain*) is given by

$$\begin{aligned} \hat{\vec{\mathbf{y}}} &= \mathbf{F}_N^H \hat{\vec{\mathbf{y}}}_f = \mathbf{F}_N^H \vec{\mathbf{x}}_f + \mathbf{F}_N^H \left( \mathbf{F}_N \mathbf{H} \mathbf{F}_N^H \right)^{-1} \vec{\mathbf{w}}_f \\ &= \vec{\mathbf{x}} + \mathbf{F}_N^H \left( \mathbf{F}_N \mathbf{H} \mathbf{F}_N^H \right)^{-1} \mathbf{F}_N \vec{\mathbf{w}}. \end{aligned} \quad (2.12)$$

Accordingly, the estimated data symbol vector can be retrieved from (2.12) considering a generic demodulation matrix  $\mathbf{V}$ . Thus,

$$\begin{aligned}\hat{\vec{\mathbf{d}}} &= \mathbf{V}\hat{\vec{\mathbf{y}}} = \mathbf{V}\vec{\mathbf{x}} + \mathbf{V}\mathbf{F}_N^H(\mathbf{F}_N\mathbf{H}\mathbf{F}_N^H)^{-1}\mathbf{F}_N\vec{\mathbf{w}} \\ &= \mathbf{V}\mathbf{G}\vec{\mathbf{d}} + \mathbf{V}\mathbf{F}_N^H(\mathbf{F}_N\mathbf{H}\mathbf{F}_N^H)^{-1}\mathbf{F}_N\vec{\mathbf{w}}.\end{aligned}\quad (2.13)$$

Different demodulation matrices can be used to recover the transmitted data symbols. A trivial solution to (2.13) is to find  $\mathbf{V}$  s.t.  $\mathbf{V}\mathbf{G}=\mathbf{I}_N$ , resulting, in this case, in the **ZF** solution

$$\mathbf{V}_{\text{ZF}} = \mathbf{G}^{-1}.\quad (2.14)$$

The **ZF** demodulator eliminates the self-interference introduced by non-orthogonal transmission filters. The disadvantage of this approach resides in the fact that the frequency response of the **ZF** receiving filter spreads over the adjacent subcarriers, which means that the noise outside the range of interest is collected, as shown in Figure 4, resulting in noise power enhancement and performance degradation when the transmission filter is non-orthogonal.

Another possibility for the demodulation matrix resides in the **MF** (*Matched Filter*) approach, defined as

$$\mathbf{V}_{\text{MF}} = \mathbf{G}^H,\quad (2.15)$$

The **MF** demodulation matrix maximizes the **SNR** (*Signal-to-Noise Ratio*) once its frequency response matches the corresponding subcarrier band. In this case, noise enhancement is avoided. However, the **MF** demodulator exhibits a loss on performance caused by the system self-interference, when the matrix product  $\mathbf{V}_{\text{MF}}\mathbf{G}$  is non-diagonal, imposing an error floor on **SER** due to **IBI** and **ICI** among the demodulated data symbols [72].

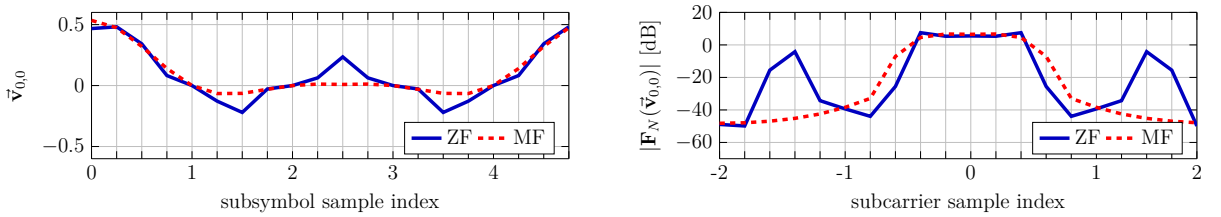


Figure 4 – Receiving prototype impulse response and frequency response.

Finally, the **MMSE** demodulator presents a trade-off between the noise enhancement and self-interference mitigation. When the **CNR** (*Carrier to Noise Ratio*) is low, this demodulator behaves similarly to the **MF**, reducing the influence of the noise over the demodulated data symbols. For high **CNR** conditions, the **MMSE** approaches the **ZF** demodulator, eliminating the self-interference. Assuming  $E_s = \mathbb{E}\{\vec{\mathbf{d}}\vec{\mathbf{d}}^H\} = \mathbf{I}_N$ , the **MMSE** demodulation matrix is given by

$$\mathbf{V}_{\text{MMSE}} = \left(\sigma_{\vec{\mathbf{w}}}^2\mathbf{I}_N + \mathbf{G}^H\mathbf{H}^H\mathbf{H}\mathbf{G}\right)^{-1}\mathbf{G}^H\mathbf{H}^H,\quad (2.16)$$

where  $\sigma_{\mathbf{w}}^2$  is the noise variance of the *AWGN (Additive White Gaussian Noise)*.

It is worth to point out that  $\mathbf{V}_{\text{MMSE}}$  equalizes and demodulates the received vector  $\bar{\mathbf{y}}$  simultaneously once the equivalent channel matrix is already considered in (2.16). Thus, the prior equalization of the received signal is not necessary when the *MMSE* demodulation is employed. Note that the *MMSE* is a biased estimator. Hence, it is necessary to scale the amplitude of the demodulated symbols considering the main diagonal of  $\mathbf{V}_{\text{MMSE}}\mathbf{G}$  (see Section 4.1). The main drawback of the *MMSE* demodulator relies on its increased complexity related to noise variance estimation and demodulation matrix update whenever the *CIR* or the *AWGN* variance changes.

## 2.3 Out of Band Emission

The subcarrier filtering employed in the *GFDM* generation can reduce the *OOB* emission when compared to *OFDM*, as illustrated by the *PSD (Power Spectrum Density)* depicted in Figure 5.

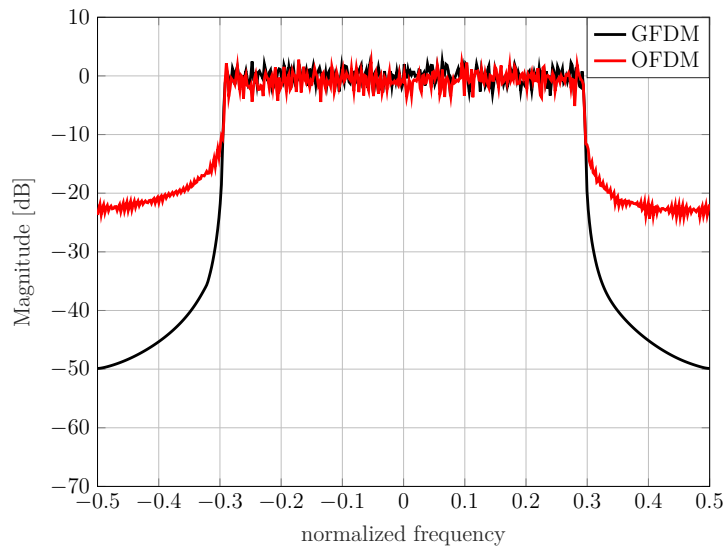


Figure 5 – PSD comparison between GFDM and OFDM. Common parameters are  $K = 128$  and  $K_{\text{on}} = 75$ . Additional GFDM parameters are  $M = 7$  employing a RC filter with  $\alpha = 0.5$ .

Nevertheless, the abrupt transition at the edge between consecutive *GFDM* blocks, shown in Figure 6, imposes a severe limit to the potential *OOB* reduction.

A concise reduction on *OOB* emission can be achieved employing a guard subsymbol between block boundaries or by applying a windowing for each *GFDM* block. These two approaches are described in the following sections.

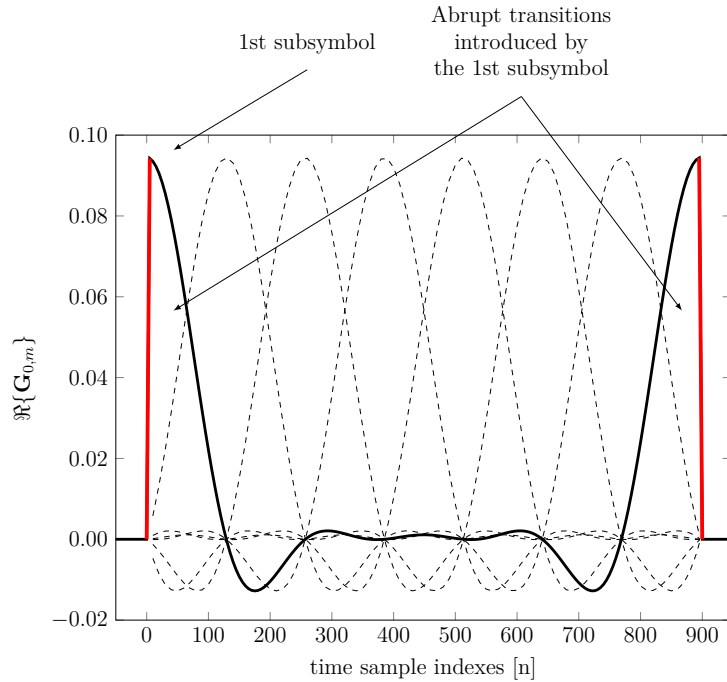


Figure 6 – Abrupt transitions at the boundaries of the GFDM block.

## 2.4 GS-GFDM

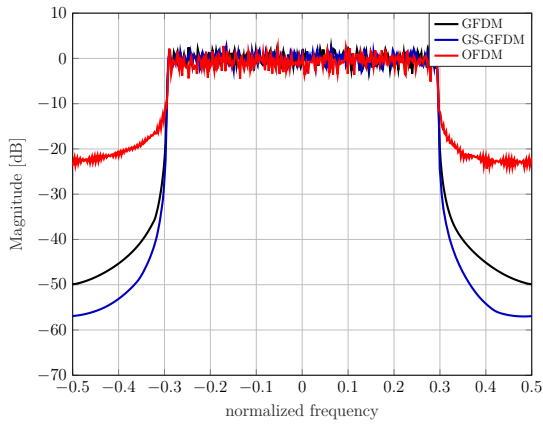
In order to further reduce the **GFDM OOB** emission, it is necessary to avoid abrupt transitions at the block boundaries introduced by usual rectangular window edges. Retrieving the circular nature of the subsymbols in time domain, it is possible to employ a simple approach to reduce the discontinuities between adjacent blocks. As illustrated by Figure 6, the first subsymbol contains the most significant abrupt transition.

Turning off the first subsymbol introduces a guard subsymbol that smooths the transition between consecutive blocks. This technique is named **GS (Guard-Symbol)-GFDM**, whose main characteristics are illustrated by Figure 7. The **PSD** is depicted by Figure 7a and the signal in **TD** that emphasizes the boundaries of two consecutive **GFDM** symbols is detailed by Figure 7b.

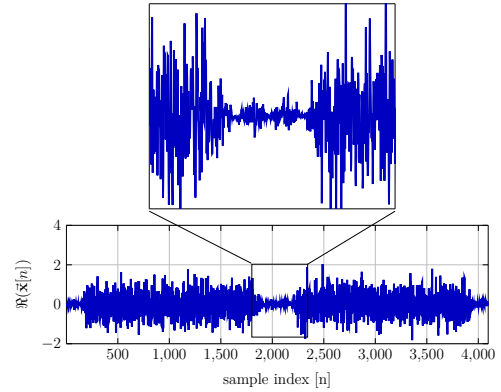
Appending a **CP** would reintroduce discontinuities between consecutive **GFDM** blocks. A possible solution to avoid this problem is to also turn-off the last subsymbol besides adopting  $N_{\text{CP}}=K$ . The drawback of this approach relies in the lower spectrum efficiency, which can be evaluated by

$$\eta_{\text{GS}} = \frac{M-2}{M} \frac{MK}{MK+K} \frac{N}{N+N_{\text{CP}}} = \frac{M-2}{M+1} \frac{N}{N+N_{\text{CP}}}. \quad (2.17)$$

From (2.17), we conclude that this approach becomes interesting for scenarios where  $M$  is large.



(a) PSD comparison between GS-GFDM and OFDM.



(b) Real part of the GS-GFDM signal, emphasizing the smoothed transitions.

Figure 7 – GS-GFDM signal and spectrum.

## 2.5 W-GFDM

The *W-GFDM (Windowed-GFDM)* technique employs a time window over *CP* and *CS (Cyclic Suffix)* to smooth the transitions between block symbols as shown in Figure 8.

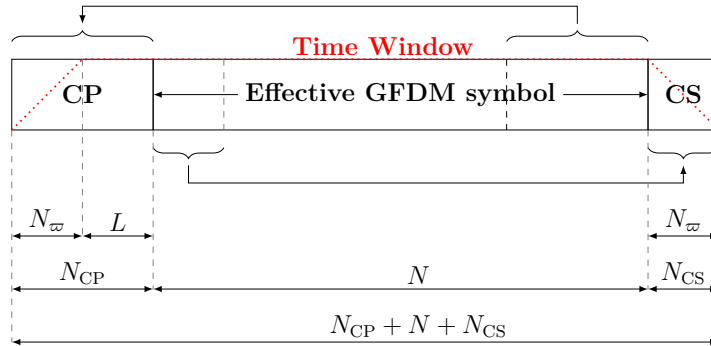


Figure 8 – W-GFDM symbol in the time domain.

It is important to note that the *CP* must cover the channel length and the window length. The *CP* length is chosen in order to obtain  $N_{CP} = N_w + L$  and the *CS* with size  $N_{CS} = N_w$ , where  $N_w$  is the length of the time window transition. The *CS* is a copy of the first  $N_{CS}$  samples of the effective *GFDM* symbol, appended to its end, as presented in Figure 8. The time window is defined by

$$\varpi[n] = \begin{cases} \varpi_{\text{rise}}[n] & \text{if } 0 \leq n < N_w \\ 1 & \text{if } N_w \leq n \leq N_{CP} + N \\ \varpi_{\text{fall}}[n] & \text{if } N_{CP} + N < n < N_{CP} + N + N_w \end{cases}, \quad (2.18)$$

where  $\varpi_{\text{rise}}$  and  $\varpi_{\text{fall}}$  are the rising and falling time window transitions, respectively. The ramp-up and ramp-down segments can assume different shapes. The most common

options are linear, cosine, RC or 4th order RC [55]. Figure 9 shows the PSD achieved by the W-GFDM employing linear and RC windowing with 32 samples each. It is clear that the OOB emission varies according to the ramp-up and ramp-down format. Sequences that introduces few inflection points in its derivative presents low OOB emission.

The W-GFDM can be used to reduce the OOB emission and still achieve a high spectral efficiency, even for  $M$  assuming small values. The loss on system spectrum efficiency caused by the introduction of windowing transition and the CP can be obtained by

$$\eta_{\varpi} = \frac{N}{N + N_{\text{CP}} + 2N_{\varpi}}. \quad (2.19)$$

Once  $N_{\text{CP}}$  is defined according to the CIR spread, this parameter affects the spectral efficiency of both GS-GFDM and W-GFDM. As the length of the rising and falling time window sequences are smaller than the effective GFDM symbol,  $\eta_{\varpi}$  is typically greater than  $\eta_{\text{GS}}$ . From Figures 7a and 9, we can conclude that both techniques reduces the OOB emission when compared to OFDM with the W-GFDM standing as a promising solution for systems with high spectral efficiency and low OOB emission.

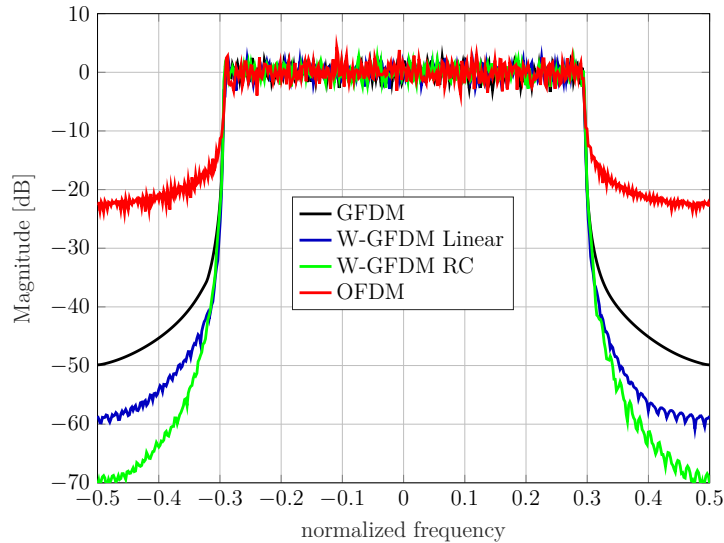


Figure 9 – PSD comparison between OFDM and W-GFDM employing linear and RC time windows.

## 2.6 Analysis of GFDM Symbol Error Rate Performance

NO waveforms are affected by ICI and IBI, thus, they must be considered at the receiver in the system design. In this section, the GFDM SER performance is simulated assuming different channel models for the ZF, MF and MMSE demodulators. Table 3 describes the parameters used in the Monte Carlo simulation while Table 4 summarizes

each channel model. Three models are considered: 1) **AWGN** channel; 2) **FSC**, whose equivalent base band **CIR** is 16 samples long, varying linearly from 0 to -10 dB and; 3) **TVC** (*Time-Variant Channel*), which is a block fading channel given by a normal complex scaling factor.

Table 3 – Parameters for the GFDM SER simulation.

Parameter	GFDM	OFDM
Mapping	4-QAM	4-QAM
Prototype filter	<b>RC</b>	Rectangular
Roll-off factor ( $\alpha$ )	0 and 0.9	0
Subcarriers ( $K$ )	64	64
Subsymbols ( $M$ )	9	1
Cyclic Prefix ( $N_{\text{CP}}$ )	16	16

Table 4 – Channel models for the GFDM SER simulation.

Channel Model	Impulse Response
<b>AWGN</b>	$\vec{\mathbf{h}}_{\text{AWGN}} = [1]$
<b>FSC</b>	$\vec{\mathbf{h}}_{\text{FSC}} = (10^{-\frac{2}{3}i})_{i=0, \dots, 15}^T$
<b>TVC</b>	$\vec{\mathbf{h}}_{\text{TVC}} = [h], h \sim \mathcal{CN}(0, 1)$

### 2.6.1 GFDM SER in AWGN Channel

The **GFDM SER** performance depends on the chosen demodulator used to retrieve the transmitted data symbols. A theoretical reference for the symbol error probability can be obtained assuming the **ZF** demodulator. In this case, the self-interference is eliminated during the demodulation process. However, due to the frequency response shape of the reception pulse, the noise out of the interested band is collected yielding to a noise enhancement. We can define a **NEF** (*Noise Enhancement Factor*) as

$$\xi = \sum_{n=0}^{N-1} |\vec{\mathbf{v}}_{\text{ZF}}[n]|^2, \quad (2.20)$$

where  $\vec{\mathbf{v}}_{\text{ZF}}$  is the reception prototype filter considering the **ZF** demodulator, whose symbol error probability is

$$p_{\text{AWGN}}(e) = 2 \left( \frac{\iota - 1}{\iota} \right) \text{erfc}(\sqrt[2]{\varrho}) - \left( \frac{\iota - 1}{\iota} \right)^2 \text{erfc}^2(\sqrt[2]{\varrho}), \quad (2.21)$$

with  $\iota = \sqrt[2]{2^\mu}$ ,  $\mu$  is the number of bits per data symbol and

$$\varrho = \frac{3R_{\text{T}}}{2(\iota^2 - 1)} \cdot \frac{E_{\text{s}}}{\xi N_0}, \quad (2.22)$$

s.t.  $E_{\text{s}}$  is the average constellation energy,  $N_0$  is the **AWGN** spectrum density and

$$R_{\text{T}} = \frac{N}{N_{\text{CP}} + N + N_{\text{CS}}} \quad (2.23)$$

represents the equivalent SNR reduction caused by introducing the CP and the CS.

The performance loss caused by the NEF depends on the chosen transmission prototype filter. Typically, as higher the system self-interference to be eliminated, more accentuated is the NEF. This means that, when the RC filter is employed, a high roll-off factor results in a higher NEF. Figure 10 compares the performance of different linear demodulators, taking the OFDM SER as a reference. Figures 10a and 10b illustrate the SER for  $\alpha=0$  and  $\alpha=0.9$ , in this order.

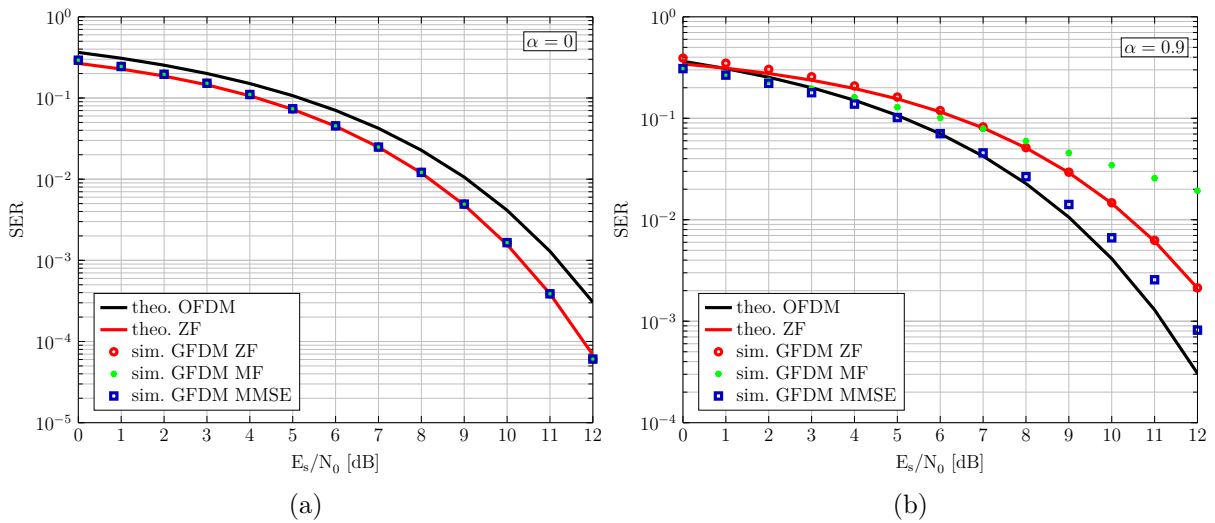


Figure 10 – GFDM SER performance in AWGN channel. (a) RC filter with  $\alpha=0$ . (b) RC filter with  $\alpha=0.9$ .

Figure 10a shows that the GFDM outperforms the OFDM by a more efficient CP usage. Also, the three demodulators present the same performance, since the RC filter with  $\alpha=0$  is the Dirichlet pulse, resulting in an orthogonal GFDM. In Figure 10b, the self-interference imposes a high error floor when the MF demodulator is used. The NEF reduces the ZF performance while the MMSE demodulator results in a trade-off between the ZF and the MF. For low SNR, the MMSE demodulator behaves similarly to the MF, reducing the NEF effects. For high SNR values, the MMSE approaches the ZF performance, eliminating the self-interference.

## 2.6.2 GFDM SER performance in FSC

In frequency selective channels, the effects of the NEF depends on both frequency responses of the prototype reception filter and the channel, which means that the SER for each subcarrier may differ among themselves. Thus, the symbol error probability of the GFDM considering the FSC can be obtained as an average approximated by [69]

$$p_{\text{FSC}}(e) = 2 \left( \frac{\iota - 1}{\iota K} \right) \sum_{k=0}^{K-1} \text{erfc}(\sqrt[2]{\varrho_k}) - \frac{1}{K} \left( \frac{\iota - 1}{\iota} \right)^2 \sum_{k=0}^{K-1} \text{erfc}^2(\sqrt[2]{\varrho_k}), \quad (2.24)$$

where

$$\varrho_k = \frac{3R_T}{2(\iota^2 - 1)} \cdot \frac{E_s}{\xi_k N_0} \quad (2.25)$$

and

$$\xi_k = \frac{1}{N} \sum_{n=0}^{N-1} \left| \frac{\vec{\mathbf{v}}_{f_{k,0}}[-n]}{\vec{\mathbf{h}}_f[n]} \right|^2, \quad (2.26)$$

with  $\vec{\mathbf{v}}_{f_{k,0}}[n]$  being the frequency response of the receiving prototype pulse for the  $k$ th subcarrier of the first subsymbol and  $\xi_k$  is the corresponding NEF at that subcarrier. The selective channel frequency response is  $\vec{\mathbf{h}}_f = \text{diag}(\mathbf{F}_N \mathring{\mathbf{H}} \mathbf{F}_N^H)$ , with  $\mathring{\mathbf{H}}$  as a circular convolution matrix obtained from  $\vec{\mathbf{h}}_{\text{FSC}}$ . It is worth to highlight that the noise enhancement is the same for all subsymbols, however, the channel selective frequency response yields to different NEF according to the pulse position in the frequency domain. Figure 11 shows the SER performance of the GFDM system for the FSC described in Table 4.

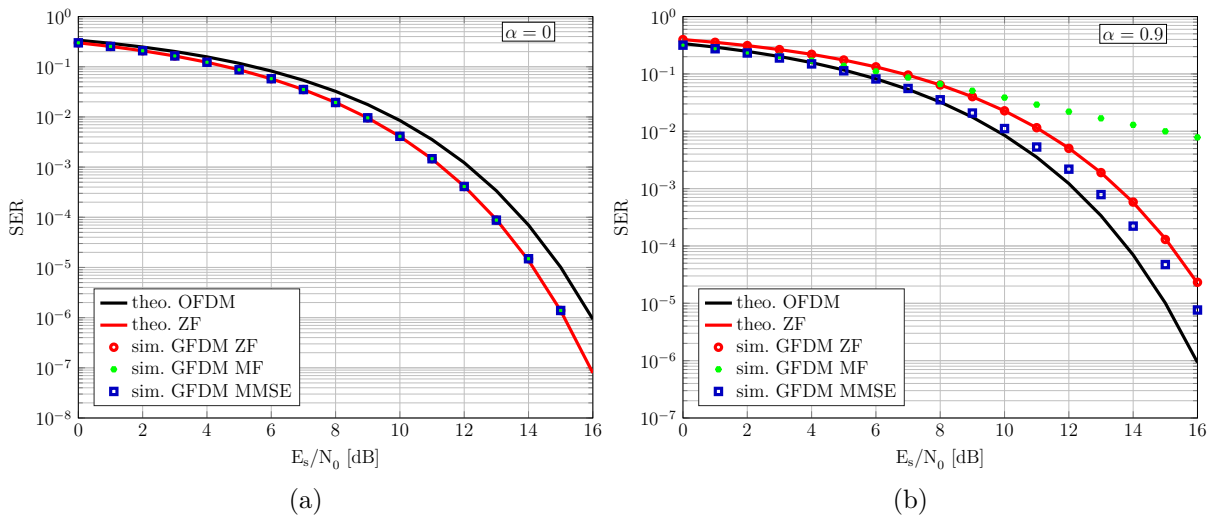


Figure 11 – GFDM SER performance in FSC. (a) RC filter with  $\alpha=0$ . (b) RC filter with  $\alpha=0.9$ .

As depicted in Figure 11a, all demodulators performs equally when the transmission pulse is orthogonal. Again, GFDM overperforms OFDM due to more efficient CP usage. Figure 11b reveals that both IBI and ICI severally impact the MF demodulator performance, resulting in a pronounced error floor. As expected, the ZF demodulator presents a performance degradation caused by the NEF in comparison with the orthogonal case. Finally, the MMSE minimizes the impact of the NEF for low SNR scenarios.

### 2.6.3 GFDM SER performance in TVC

The theoretical SER performance of the GFDM in a TVC considering the ZF demodulator can be obtained assuming that the channel coherence time is greater than

one block symbol period. In this case, the symbol error probability is given by [69]

$$p_{\text{TVC}}(e) = 2 \left( \frac{\iota - 1}{\iota} \right) \left( 1 - \sqrt{\frac{\varrho}{1 + \varrho}} \right) - \left( \frac{\iota - 1}{\iota} \right)^2 \left[ 1 - \frac{4}{\pi} \sqrt{\frac{\varrho}{1 + \varrho}} \arctan \left( \sqrt{\frac{1 + \varrho}{\varrho}} \right) \right], \quad (2.27)$$

where

$$\varrho = \frac{3R_T E_s}{\iota^2 - 1 \xi N_0}. \quad (2.28)$$

Figure 12 shows the GFDM SER performance assuming the TVC described in Table 4, for the presented linear demodulators. Once again, the OFDM theoretical curve is taken as a reference.

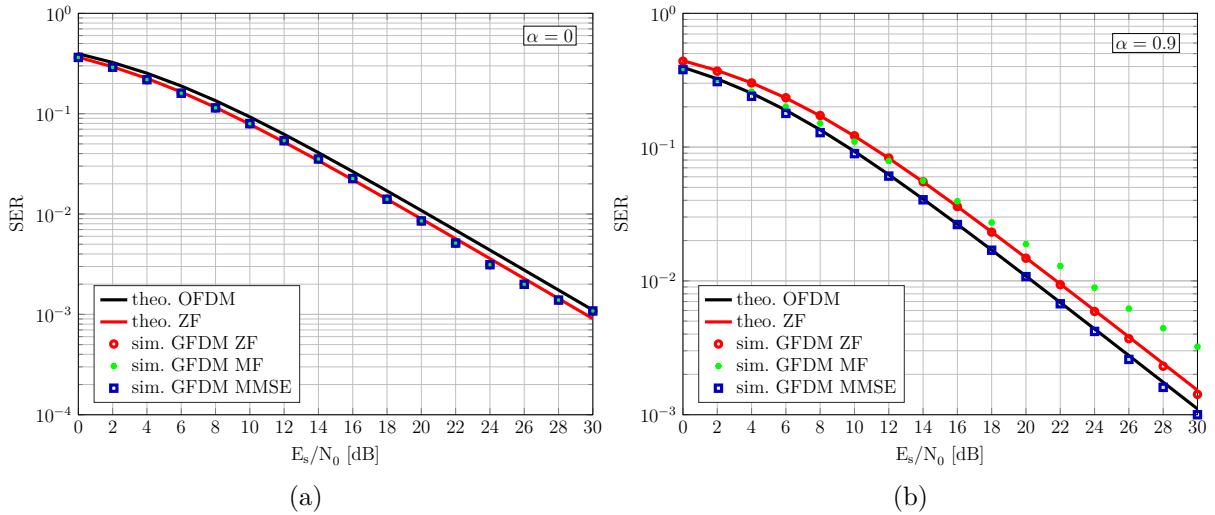


Figure 12 – GFDM SER performance in TVC. (a) RC filter with  $\alpha=0$ . (b) RC filter with  $\alpha=0.9$ .

A similar behavior is observed in relation to the previous discussed channels. All linear demodulators present the same performance when the prototype pulse is orthogonal, as shown in Figure 12a, where the left deviation of the GFDM w.r.t the OFDM occurs because of the more efficient CP. When the pulse is non-orthogonal, the MMSE outperforms the MF demodulator, which presents an error floor, and also surpass the ZF demodulator, whose performance is reduced due to the NEF.

## 2.7 Summary

This chapter introduces the fundamentals regarding the GFDM waveform design, matrix notation and different linear demodulators. A brief analysis on OOB emission and SER comparison w.r.t. OFDM were also conducted. GFDM presents some disadvantages when compared to OFDM such as self interference, which may requires additional

interference cancellation techniques [73]; and a more careful management of symbol synchronization to avoid performance degradation [74]. These characteristics might result in higher processing complexity, especially for resource-constrained devices. On the other hand, GFDM also offers several advantages over OFDM, including improved spectral efficiency, better interference mitigation, and greater flexibility in adapting to varying channel conditions. These benefits make GFDM a promising candidate for future wireless communication systems, particularly in scenarios requiring high data rates and low latency.

### 3 System model for the MIMO communication PHY

This chapter introduces the concept of a multicarrier digital **MIMO** communication **PHY**, represented by a linear model, widely used along this thesis. In a broad sense, a digital communication **PHY** is responsible for: a) adapting the digital information to a waveform that is transmitted to one or more receivers through a communication channel, and; b) for retrieving the information on the receiver side from the distorted and noisy version of the transmitted signal. Both transmitter and receiver are designed based on the communication channel characteristics, such as noise and fading statistics, average scattering pattern, coherence time, coherence bandwidth and the impairments introduced by the transmitter's and receiver's **RF** front-end, among others. Specifically for a modern mobile communication system, the **PHY** must deal with double-dispersive **MIMO** channels, where each path between one transmitting and one receiving antenna is modeled as a time-variant and time-dispersive impulse response.

We consider an arrangement employing  $N_T$  transmitting antennas and  $N_R$  receiving antennas as a generalization of the mobile communication system, since it also embraces more simplified structures, e.g., the usual single-input single-output when  $N_R=N_T=1$ . It is worth to mention that, assuming a **SM-MIMO** case, when  $N_R=N_T \geq 2$ , **IAI** (*Inter-Antenna Interference*) takes place once each receiving antenna collects signals from more than one transmitting antenna. In this case, the detection method should be carefully chosen taking into account the trade-off between performance and complexity. Figure 13 illustrates a simplified wireless communication system assuming this scenario.

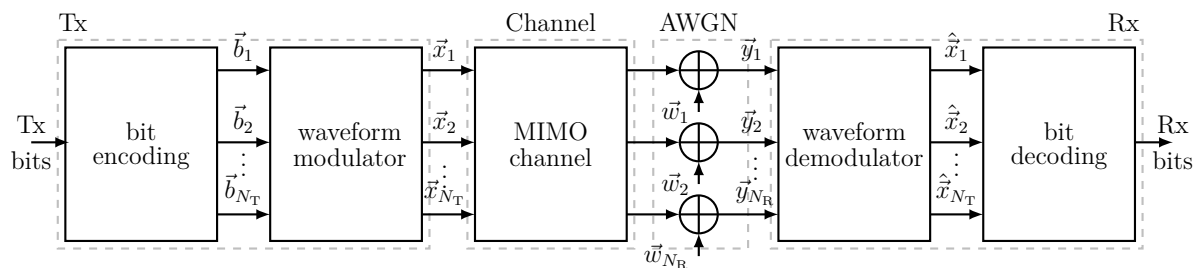


Figure 13 – Simplified block diagram of a generic MIMO communication system.

At the transmitter side, the bit encoding block receives the data bit sequence and protects them by applying different coding techniques such as randomization, **FEC** (*Forward Error Correction*) and interleaving, aiming to increase the system robustness against the adverse effects of the mobile channel. The resulting coded bits are then fed to the waveform modulator block, where different techniques may be used, e.g., symbol

modulation and multicarrier techniques, as GFDM, leading to specific waveforms, tailored for mobile MIMO channels. The MIMO channel introduces time and frequency fading, combining the transmitted signals at each receiving antenna. The AWGN block represents the thermal noise added at each receiver. On the receiver side, the waveform demodulation block is responsible for performing the time and frequency synchronization, waveform demodulation, antenna decoupling and symbol to bit recovery, while the bit decoding block is responsible for correcting the errors that might be introduced by the channel. The recovered binary sequence is delivered for the data sink (user application).

It is worth to clarify that, despite of its importance in the communication research field, the availability of studies involving channel coding techniques are widely available in literature and this subject is beyond the scope of this work. This work exploits algorithms available in [75, 76, 77], such as PCs (*Polar Codes*), CCs (*Convolutional Codes*) and APP (*A-Posteriori Probability*) decoding for performance evaluation, when needed.

Next section describes the matricial representation of the MIMO channel considering a CP protected multicarrier scheme, one of the most popular solution for the air interface in mobile communication systems.

### 3.1 Generic MIMO Linear Model

Consider that a multi-resource modulation scheme, where the term resource, here, refers to an allocated time and/or frequency interval, which is used to transmit  $N_T$  parallel streams containing  $N_{on}=M_{on}K_{on}$  complex data symbols per block, where  $M_{on}$  and  $K_{on}$  are, respectively, the number of active time and frequency resources out of a total available  $M$  and  $K$ , in the same order. Each stream, defined as  $\vec{\mathbf{d}}_j \in \mathbb{C}^{N_{on} \times 1}$ , is mapped into  $N_{on}$  active resources of a block symbol with  $N$  samples length. Let  $\vec{\mathbf{x}}_j \in \mathbb{C}^{N \times 1}$  be the modulated signal in time domain, transmitted by the  $j$ th transmitting antenna, with  $j = 1, 2, \dots, N_T$  and  $N_{on} \leq N$ . Assuming a generic modulation matrix  $\mathbf{G} \in \mathbb{C}^{N \times N_{on}}$ , the modulation process for an individual transmitter as the linear transformation of the  $j$ th data stream is given by

$$\vec{\mathbf{x}}_j = \mathbf{G}\vec{\mathbf{d}}_j. \quad (3.1)$$

Note that each element of  $\vec{\mathbf{d}}_j$  is obtained by mapping a set of  $\mu = \log_2(M_c)$  bits into a corresponding data symbol from a finite set of  $M_c$  distinct elements, arranged in a complex plane that employs the normalised sine and cosine functions as orthonormal bases. Vertically stacking the complex data streams in  $\vec{\mathbf{d}} \in \mathbb{C}^{N_T N_{on} \times 1}$  and defining an extended generic modulation matrix  $\bar{\mathbf{G}} \in \mathbb{C}^{N_T N \times N_T N_{on}}$  as

$$\bar{\mathbf{G}} = \mathbf{I}_{N_T} \otimes \mathbf{G}, \quad (3.2)$$

where  $\mathbf{I}_{N_T}$  is an identity matrix with dimension  $N_T$  and the operator  $\otimes$  represents the Kronecker product, allows to define the modulated signal for the overall system  $\vec{\mathbf{x}} \in \mathbb{C}^{N_T N \times 1}$  given by

$$\underbrace{\begin{bmatrix} \vec{\mathbf{x}}_1 \\ \vdots \\ \vec{\mathbf{x}}_j \\ \vdots \\ \vec{\mathbf{x}}_{N_T} \end{bmatrix}}_{\vec{\mathbf{x}}} = \underbrace{\begin{bmatrix} \mathbf{G} & \mathbf{0} & \dots & \mathbf{0} \\ \mathbf{0} & \mathbf{G} & \dots & \mathbf{0} \\ \vdots & \vdots & \ddots & \vdots \\ \mathbf{0} & \mathbf{0} & \dots & \mathbf{G} \end{bmatrix}}_{\mathbf{G}} \underbrace{\begin{bmatrix} \vec{\mathbf{d}}_1 \\ \vdots \\ \vec{\mathbf{d}}_j \\ \vdots \\ \vec{\mathbf{d}}_{N_T} \end{bmatrix}}_{\vec{\mathbf{d}}}. \quad (3.3)$$

Where the equivalent baseband CIR between the  $j$ th transmitting antenna and the  $i$ th receiving antenna is considered being a finite discrete sequence of  $L$  taps represented by  $\vec{\mathbf{h}}_{i,j} \in \mathbb{C}^{L \times 1}$ , with  $i = 1, 2, \dots, N_R$ . Thus, in order to protect the transmission signal from the dispersive effects of the channel, the last  $N_{CP}$  samples of each  $\vec{\mathbf{x}}_j$  is appended to its beginning as a CP with  $N_{CP} \geq L-1$ . Then, the transmission signal is obtained by vertically stacking all CP protected symbols.

Assuming perfect synchronization, CSIR and after CP removal,  $\vec{\mathbf{y}}_i \in \mathbb{C}^{N \times 1}$  is the received block symbol at  $i$ th receiving antenna and  $\vec{\mathbf{y}}$  represents all received signals, vertically stacked and described by

$$\underbrace{\begin{bmatrix} \vec{\mathbf{y}}_1 \\ \vdots \\ \vec{\mathbf{y}}_i \\ \vdots \\ \vec{\mathbf{y}}_{N_R} \end{bmatrix}}_{\vec{\mathbf{y}}} = \underbrace{\begin{bmatrix} \mathring{\mathbf{H}}_{1,1} & \dots & \mathring{\mathbf{H}}_{1,j} & \dots & \mathring{\mathbf{H}}_{1,N_T} \\ \vdots & \ddots & \vdots & \ddots & \vdots \\ \mathring{\mathbf{H}}_{i,1} & \dots & \mathring{\mathbf{H}}_{i,j} & \dots & \mathring{\mathbf{H}}_{i,N_T} \\ \vdots & \ddots & \vdots & \ddots & \vdots \\ \mathring{\mathbf{H}}_{N_R,1} & \dots & \mathring{\mathbf{H}}_{N_R,j} & \dots & \mathring{\mathbf{H}}_{N_R,N_T} \end{bmatrix}}_{\mathbf{H}} \underbrace{\begin{bmatrix} \vec{\mathbf{x}}_1 \\ \vdots \\ \vec{\mathbf{x}}_j \\ \vdots \\ \vec{\mathbf{x}}_{N_T} \end{bmatrix}}_{\vec{\mathbf{x}}} + \underbrace{\begin{bmatrix} \vec{\mathbf{w}}_1 \\ \vdots \\ \vec{\mathbf{w}}_j \\ \vdots \\ \vec{\mathbf{w}}_{N_R} \end{bmatrix}}_{\vec{\mathbf{w}}}, \quad (3.4)$$

where  $\mathbf{H} \in \mathbb{C}^{N_R N \times N_T N}$  is a structured linear transformation matrix whose elements, denoted by the sub-scripted  $\mathring{\mathbf{H}}_{i,j} \in \mathbb{C}^{N \times N}$  entries, are the equivalent circulant matrix obtained from the CIR between the  $j$ th and  $i$ th transmitting-receiving antennas, respectively. The vector  $\vec{\mathbf{w}} \in \mathbb{C}^{N_R N \times 1}$  represents the AWGN for all receiving antennas, vertically stacked. Equation (3.4) is the generic form of the MIMO linear model, widely used in the linear estimation and detection processes. Inserting (3.3) into (3.4) allows one to rewrite

$$\vec{\mathbf{y}} = \tilde{\mathbf{H}} \vec{\mathbf{d}} + \vec{\mathbf{w}}, \quad (3.5)$$

where  $\tilde{\mathbf{H}} \in \mathbb{C}^{N_R N \times N_T N_{on}}$  encompass both transform matrices: the generic modulation

matrix and the circular convolution channel matrix, whose structure is given by

$$\tilde{\mathbf{H}} = \begin{bmatrix} \mathring{\mathbf{H}}_{1,1} \mathbf{G} & \dots & \mathring{\mathbf{H}}_{1,j} \mathbf{G} & \dots & \mathring{\mathbf{H}}_{1,N_T} \mathbf{G} \\ \vdots & \ddots & \vdots & \ddots & \vdots \\ \mathring{\mathbf{H}}_{i,1} \mathbf{G} & \dots & \mathring{\mathbf{H}}_{i,j} \mathbf{G} & \dots & \mathring{\mathbf{H}}_{i,N_T} \mathbf{G} \\ \vdots & \ddots & \vdots & \ddots & \vdots \\ \mathring{\mathbf{H}}_{N_R,1} \mathbf{G} & \dots & \mathring{\mathbf{H}}_{N_R,j} \mathbf{G} & \dots & \mathring{\mathbf{H}}_{N_R,N_T} \mathbf{G} \end{bmatrix} = \mathbf{H} \bar{\mathbf{G}}. \quad (3.6)$$

Next section provides a detailed analysis of the system transform matrix  $\tilde{\mathbf{H}}$  and its factorization. This approach aims to reduce complexity by dividing it into smaller subsystems, applicable to both orthogonal and **NO** cases.

## 3.2 SM-MIMO Factorization

System factorization is a crucial step in any solution algorithm, as it simplifies complexity by breaking it down into smaller, independent problems. This approach is particularly useful in numerical linear algebra and parallel computing. The resulting subproblems can be individually manipulated and processed simultaneously, enhancing computational efficiency. The following subsections discuss two types of block factorization: the orthogonal case, widely used in systems such as **OFDM**, and an original proposal for the non-orthogonal case, suitable for the **GFDM** waveform. The system parameters for both cases are given by Table 5.

Parameter	Orthogonal	Non-orthogonal
$N_T = N_R$	2	2
$M$	1	3
$K = K_{\text{on}}$	12	4
$N = N_{\text{on}}$	12	12
$\alpha$	0	1
pulse	RC	RC
$N_{\text{CP}} \geq L - 1$	$L = 3$	$L = 3$

Table 5 – Parameters for the SM-MIMO factorization example.

### 3.2.1 Orthogonal Multicarrier SM-MIMO Factorization

Prior to start the analysis of the **NO-SM-MIMO**, it is essential to clearly understand the orthogonal case and how it can be factorized into smaller subsystems, making the solution of this problem more tractable while enlightening the path on solving more complex arrangements.

As mentioned in Section 2.2, GFDM can be parameterized to obtain an orthogonal multicarrier scheme. Defining  $M$  unitary and  $\vec{g}$  as a RC pulse with  $\alpha=0$ , leads to an OFDM system. Retrieving the generic modulation matrix  $\mathbf{G}$ , we assume  $\mathbf{G} = \mathbf{F}_{K_{\text{on}}}^H$ ,  $M=1$  and  $K_{\text{on}}$  active subcarriers, resulting in  $N=N_{\text{on}}=K_{\text{on}}$ . In order to graphically visualize such orthogonal SM-MIMO, consider the noiseless case from (3.5). This example assumes the orthogonal case parameters from Table 5:  $N_T=N_R=2$ ,  $M=1$ ,  $K=K_{\text{on}}=12$ , RC pulse with  $\alpha=0$ ,  $N_{\text{CP}} \geq L-1$ ,  $L=3$  samples and  $\vec{h} \sim \mathcal{CN}(\vec{0}, \mathbf{I}_L)$ , resulting in a dispersive channel with coherence time greater than one block symbol period. In fact, solving the proposed system in the TD would involve a costly full matrix inversion, as illustrated in Figure 14 by the color map graph, relative to the magnitude of  $\tilde{\mathbf{H}}$ .

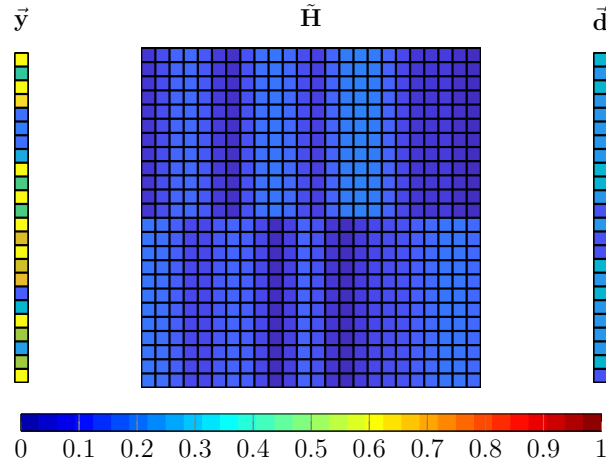


Figure 14 – Transform matrix structure for the orthogonal multicarrier MIMO system in the TD.

Recalling (3.2) and (3.6) into (3.5), it is advantageous to demodulate the orthogonal multicarrier MIMO in the FD, thus

$$\begin{aligned} \vec{y}_f &= (\mathbf{I}_{N_R} \otimes \mathbf{F}_K) \mathbf{H} (\mathbf{I}_{N_T} \otimes \mathbf{G}) \vec{d} \\ &= \underbrace{(\mathbf{I}_{N_R} \otimes \mathbf{F}_K) \mathbf{H} (\mathbf{I}_{N_T} \otimes \mathbf{F}_K^H)}_{\mathbf{H}_f} \vec{d}. \end{aligned} \quad (3.7)$$

Here,  $\mathbf{H}_f \in \mathbb{C}^{N_R N \times N_T N_{\text{on}}}$  results in a very especial structured matrix containing the equivalent CFR in the main diagonals of each  $N_R \times N_T$  sub-matrices with dimension  $N \times N_{\text{on}}$ . This concept can be visualized in Figure 15.

The resulting  $\vec{y}_f$  allows to further define the orthogonal received signal for each

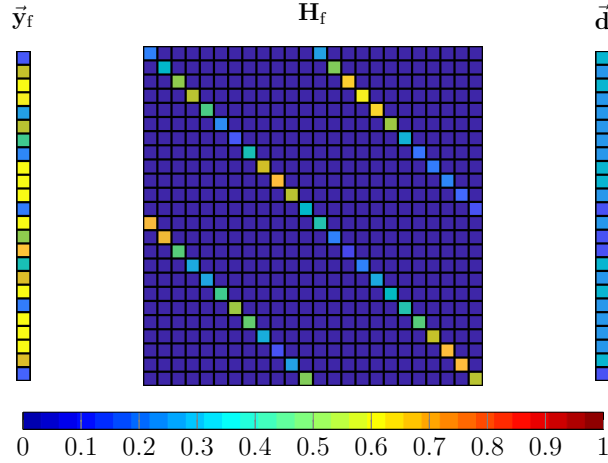


Figure 15 – Transform matrix structure for the orthogonal multicarrier MIMO system in FD.

subcarrier considering all transmitting and receiving antennas. Hence,

$$\underbrace{\begin{bmatrix} \vec{y}_{f_1}[k] \\ \vdots \\ \vec{y}_{f_{N_R}}[k] \end{bmatrix}}_{\vec{y}_f[k]} = \underbrace{\begin{bmatrix} \mathbf{H}_{f_{1,1}}[k] & \dots & \mathbf{H}_{f_{1,N_T}}[k] \\ \vdots & \ddots & \vdots \\ \mathbf{H}_{f_{N_R,1}}[k] & \dots & \mathbf{H}_{f_{N_R,N_T}}[k] \end{bmatrix}}_{\mathbf{H}_f[k]} \underbrace{\begin{bmatrix} \vec{d}_1[k] \\ \vdots \\ \vec{d}_{N_T}[k] \end{bmatrix}}_{\vec{d}[k]}.$$

where the elements of the corresponding  $N_R \times N_T$  matrix structure  $\mathbf{H}_f[k]$  are the equivalent flat Rayleigh channel between each antenna pair at the  $k$ th subcarrier. Suppressing the subcarrier index, for notation simplicity, yields to a noiseless factorized linear model representation of the orthogonal multicarrier SM-MIMO for an arbitrary subcarrier, holding a great potential for parallel computation.

It is clear that, thanks to the structure of  $\mathbf{H}_f$ , the orthogonal multicarrier detection problem can be divided into  $K_{on}$  subsystems with dimension  $N_R \times N_T$ . With the help of specific permutation matrices, designed to group coincident resources from each antenna close next to each other, the system can be reorganized to hold its individual subsystems in a more convenient structure for storage and parallel computation. In this sense, the elements of such permutation matrices, named  $\mathbf{P}_R$  and  $\mathbf{P}_T$ , are defined by

$$P_{R,p,q} = \begin{cases} 1 & \text{for } p = 0, \dots, N_R N - 1 \text{ and} \\ & q = \left\langle pN + \left\langle \frac{M(pN - \langle pN \rangle_{N_R N})}{N_R N} \right\rangle_N \right\rangle_{N_R N} + \frac{p - \langle p \rangle_{N_R K}}{N_R K}, \\ 0 & \text{otherwise,} \end{cases} \quad (3.8)$$

and

$$P_{T,p,q} = \begin{cases} 1 & \text{for } p = 0, \dots, N_T N_{\text{on}} - 1 \text{ and} \\ & q = \left\langle p N_{\text{on}} + \left\langle \frac{M(p N_{\text{on}} - \langle p N_{\text{on}} \rangle_{N_T N_{\text{on}}})}{N_T N_{\text{on}}} \right\rangle_{N_{\text{on}}} \right\rangle_{N_T N_{\text{on}}} + \frac{p - \langle p \rangle_{N_T K_{\text{on}}}}{N_T K_{\text{on}}}, \quad (3.9) \\ 0 & \text{otherwise,} \end{cases}$$

where  $\mathbf{P}_R \in \mathbb{B}^{N_R N \times N_R N}$  and  $\mathbf{P}_T \in \mathbb{B}^{N_T N_{\text{on}} \times N_T N_{\text{on}}}$  are, respectively, the permutation matrices applied in the receiving and transmitting side of the system. Moreover, these matrices have useful properties, e.g., they are orthonormal and left multiplying a given matrix permutes its rows while right multiplication by its transpose yields to column permutation. Note that  $\mathbf{P}_T$  can also be obtained considering all active subcarriers then resized to  $N_T N_{\text{on}}$  when  $K_{\text{on}} < K$  by removing specific rows and columns, corresponding to the inactive subcarriers position. For the example described in Table 5, the resulting non-zero column indexes are

$$q = [0, 12, 1, 13, 2, 14, 3, 15, 4, 16, 5, 17, 6, 18, 7, 19, 8, 20, 9, 21, 10, 22, 11, 23]^T.$$

Applying these permutation matrices in the received signal  $\vec{y}_f$  allows for collecting and reorganizing each factorized subsystem, as illustrated in Figure 16, which brings advantages in practical implementation aspects, such as parallel solving and system order reduction by resource disabling, i.e. when  $K_{\text{on}} < K$ .

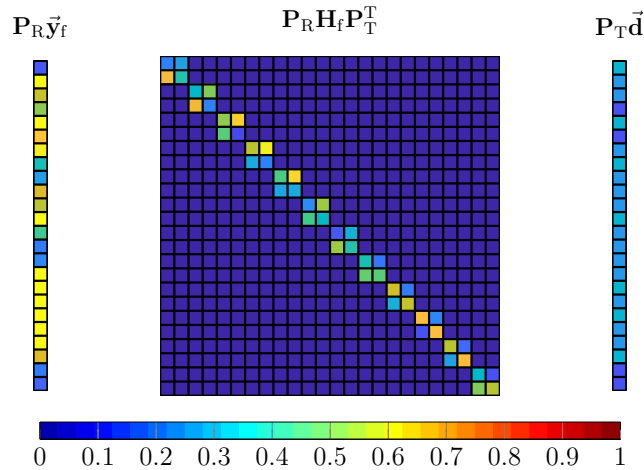


Figure 16 – Reorganized structure of the orthogonal multicarrier MIMO system factorization.

In general, for linear estimators employing matrix inversion, the expected complexity order is  $K_{\text{on}} N_T^3$ . It is easy to note that, for high order MIMO applications, where dozens or even hundreds of antennas are used, not only solving the entire system may

requires prohibitive computational cost but also other challenging aspects arise, e.g. high signaling coordination on MIMO channel estimation, considering each transmitting antenna.

### 3.2.2 Non-Orthogonal Multicarrier MIMO Factorization

In this section, we describe the NO waveform SM-MIMO factorization concepts proposed in [1]. We follow a similar approach to that used in Section 3.2.1, contributing with a formal mathematical representation to decompose the system. Additionally, we provide visual analysis based on a given example.

Retrieving the definitions for the GFDM from Section 2.2, we parameterize the system to obtain a NO multicarrier waveform with  $M > 1$  employing a prototype pulse with non-orthogonal characteristics in both time and frequency domains. To better understand such system, we consider, again, the noiseless case from (3.5). From Table 5  $N_T=N_R=2$ ,  $CP \geq L-1$ ,  $L=3$  samples and  $\vec{\mathbf{h}} \sim \mathcal{CN}(\vec{\mathbf{0}}, \mathbf{I}_L)$ , while choosing RC pulse with  $\alpha=1$ ,  $M=3$  and  $K=K_{\text{on}}=4$  (leading to  $N=12$ , the same number of resources used in the orthogonal case), results in a simple example of a NO-SM-MIMO system based on GFDM, graphically represented in the TD by Figure 17.

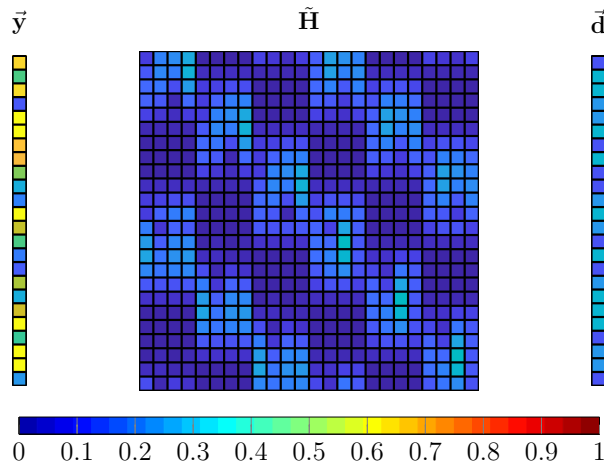


Figure 17 – Transform matrix structure for the non-orthogonal multicarrier MIMO system in the TD.

It is obvious that a solution in the TD involves an undesired and even prohibitive  $N_R N \times N_T N_{\text{on}}$  matrix inversion for the entire transformation matrix  $\tilde{\mathbf{H}}$ . Similarly to the orthogonal case, it is advantageous to represent this system in the frequency domain.

Thus, recalling (3.6) and (3.5), we can redefine  $\vec{y}_f$  for the NO waveform as

$$\begin{aligned}\vec{y}_f &= (\mathbf{I}_{N_R} \otimes \mathbf{F}_N) \mathbf{H} \bar{\mathbf{G}} \vec{d} \\ &= \underbrace{(\mathbf{I}_{N_R} \otimes \mathbf{F}_N) \mathbf{H} \bar{\mathbf{G}} \bar{\mathbf{U}}^H}_{\mathbf{H}_f} \underbrace{\bar{\mathbf{U}} \vec{d}}_{\vec{d}_f}.\end{aligned}\quad (3.10)$$

Here,  $\bar{\mathbf{U}} \in \mathbb{C}^{N_T N_{\text{on}} \times N_T N_{\text{on}}}$  is a specific orthonormal matrix, designed to organize the elements of  $\vec{d}$  in groups of subcarriers followed by an  $M$ -point DFT operation over each subcarrier group. The matrix  $\bar{\mathbf{U}}$  is given by

$$\bar{\mathbf{U}} = \{\mathbf{I}_{N_T} \otimes [(\mathbf{I}_{K_{\text{on}}} \otimes \mathbf{F}_M) \mathbf{P}]\}, \quad (3.11)$$

where  $\mathbf{F}_M$  is an  $M$ -point DFT matrix and  $\mathbf{P} \in \mathbb{B}^{N_{\text{on}} \times N_{\text{on}}}$  is an orthonormal data permutation matrix, responsible for reorganizing the data symbols in groups of subcarriers. Figure 18 exemplifies the relationship between  $\vec{d}$  and  $\vec{d}_f$  and the aspect of the data transform matrix  $\bar{\mathbf{U}}$ .

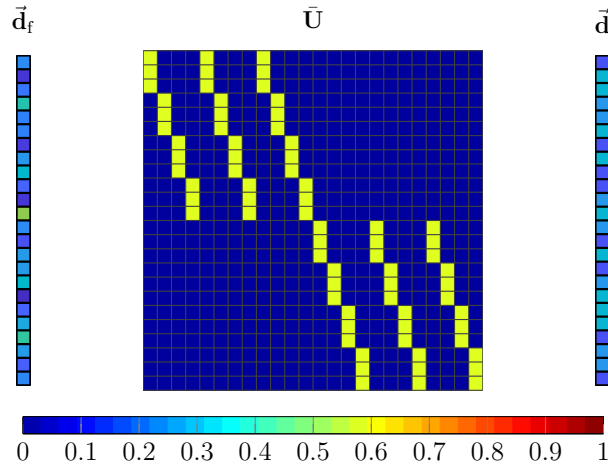


Figure 18 – Example of a discrete data transform employing the extended matrix  $\bar{\mathbf{U}}$ , responsible for reorganizing the data sequence and domain conversion.

The elements of  $\mathbf{P}$  are obtained as

$$P_{p,q} = \begin{cases} 1 & \text{for } p = 0, \dots, N_{\text{on}} - 1, m = \langle p \rangle_M \text{ and } q = \frac{\langle p-m \rangle_{N_{\text{on}}}}{M} + mK_{\text{on}}, \\ 0 & \text{otherwise.} \end{cases} \quad (3.12)$$

Left multiplying a general matrix by  $\mathbf{P}$  leads to row permutation, equivalent to grouping data symbols by subcarrier. Right multiplying a general matrix by  $\mathbf{P}$  transpose implies in column permutation or grouping by subsymbols. For the parameters used as example



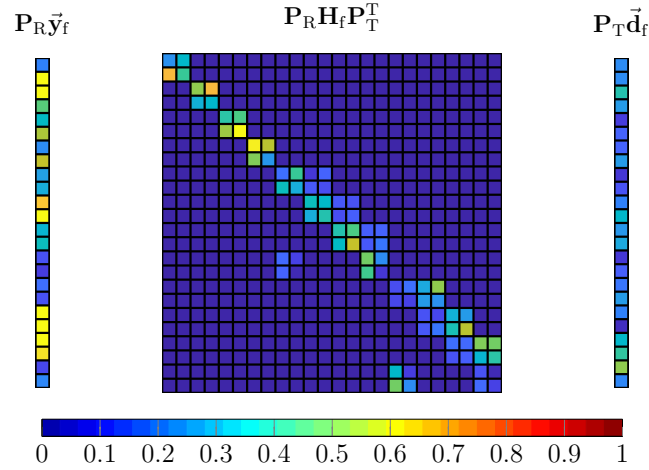


Figure 20 – Reorganized structure of the NO multicarrier MIMO system factorization.

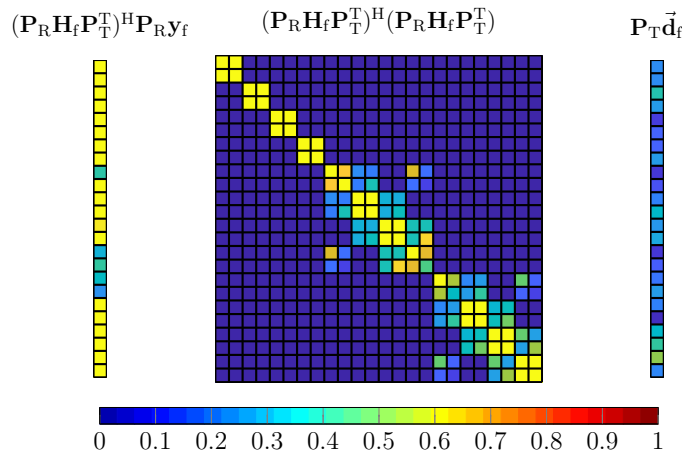


Figure 21 – MF demodulation for the factorized non-orthogonal multicarrier MIMO system.

contrary, it is possible to approximate the Gram matrix to this ending by annulling non-zero off-band-diagonals. As also stated in Chapter 2, the MF solution  $(\mathbf{P}_R \mathbf{H}_f \mathbf{P}_T^T)^H (\mathbf{P}_R \vec{\mathbf{y}}_f)$  is unable to deal with the intrinsic system interference.

Recalling the ZF solution, which, in this specific noiseless example case, coincides with the MMSE approach, it precisely recovers the permuted FD data  $\mathbf{P}_T \vec{\mathbf{d}}_f$ , shown in Figure 22. At a first glance, solving each system would require at least a full subsystem matrix inversion, on the order of  $(N_T K_{on})^3$ , which remains undesirable and insufficient for a reasonable complexity reduction.

It is notable that the factorization procedure proposed in [1] indeed results in a new system representation, more adapted for storage and parallel computation with a great

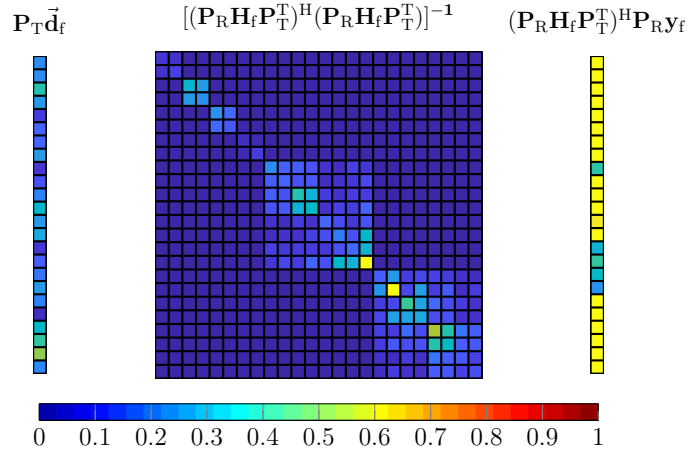


Figure 22 – ZF demodulation for the factorized non-orthogonal multicarrier MIMO system.

potential to achieve a substantial complexity reduction when employing a NO waveform based on GFDM. In [78], an algorithm is proposed to estimate the diagonal of an inverse matrix without explicitly calculating this inverse by exploring its band-diagonal structure [60]. Without going into details here, it is possible to reduce the complexity from cubic order on dimension to linear in number of active subcarriers, and cubic only on the single-side bandwidth length of the band-diagonal matrix. It would be more effective to address this subject in the next chapter.

### 3.3 GFDM Factorized SM-MIMO Model

This section explains how each factorized sub-system can be constructed using the introduced permutation matrices and proper indexation. This process results in independent and reduced problems that are well-suited for parallel computing. Resembling the system in the form of (3.5), reproduced here for convenience,

$$\vec{y} = \tilde{\mathbf{H}}\vec{d} + \vec{w} = \mathbf{H}\bar{\mathbf{G}}\vec{d} + \vec{w}, \quad (3.13)$$

which describes the linear relation between the received signal  $\vec{y}$  and the transmitted data sequence  $\vec{d}$ , where  $\tilde{\mathbf{H}}$  is a  $N_R N \times N_T N_{\text{on}}$  transform matrix. Last sections demonstrate graphical examples of the factorization procedure based on [1], illustrated by Figures 16 and 20. Although slightly different, both cases can be represented by

$$\mathbf{P}_R \vec{y}_f = \mathbf{P}_R \mathbf{H}_f \mathbf{P}_T^T \mathbf{P}_T \vec{d}_f + \mathbf{P}_R \vec{w}_f, \quad (3.14)$$

where the received signal in FD equals to

$$\mathbf{P}_R \vec{y}_f = \mathbf{P}_R (\mathbf{I}_{N_R} \otimes \mathbf{F}_N) \vec{y}, \quad (3.15)$$

the entire system transformation matrix, also in **FD**, expands to

$$\begin{aligned}\mathbf{P}_R \mathbf{H}_f \mathbf{P}_T^T &= \mathbf{P}_R (\mathbf{I}_{N_R} \otimes \mathbf{F}_N) \mathbf{H} \bar{\mathbf{G}} \bar{\mathbf{U}}^H \mathbf{P}_T^T \\ &= \mathbf{P}_R (\mathbf{I}_{N_R} \otimes \mathbf{F}_N) \mathbf{H} (\mathbf{I}_{N_T} \otimes \mathbf{G}) \{ \mathbf{I}_{N_T} \otimes [(\mathbf{I}_{K_{\text{on}}} \otimes \mathbf{F}_M) \mathbf{P}] \}^H \mathbf{P}_T^T,\end{aligned}\quad (3.16)$$

the transmitted information and the receiver additive noise, both in **FD**, are respectively given by

$$\mathbf{P}_T \vec{\mathbf{d}}_f = \mathbf{P}_T \bar{\mathbf{U}} \vec{\mathbf{d}} = \mathbf{P}_T \{ \mathbf{I}_{N_T} \otimes [(\mathbf{I}_{K_{\text{on}}} \otimes \mathbf{F}_M) \mathbf{P}] \} \vec{\mathbf{d}}, \quad (3.17)$$

and

$$\mathbf{P}_R \vec{\mathbf{w}}_f = \mathbf{P}_R (\mathbf{I}_{N_R} \otimes \mathbf{F}_N) \vec{\mathbf{w}}. \quad (3.18)$$

With the help of suitable row and column indexes

$$\vec{\mathbf{p}} = [mN_R K + 1 : (m+1)N_R K] \text{ and } \vec{\mathbf{q}} = [mN_T K_{\text{on}} + 1 : (m+1)N_T K_{\text{on}}], \quad (3.19)$$

equation (3.14) can be rewritten as  $M$  linear subsystems, each one carrying  $N_T K_{\text{on}}$  data symbols amid system-interference and additive noise, explicit given by

$$\vec{\mathbf{y}}_s[m] = (\mathbf{P}_R \vec{\mathbf{y}}_f)[\vec{\mathbf{p}}], \quad (3.20)$$

$$\mathbf{H}_s[m] = (\mathbf{P}_R \mathbf{H}_f \mathbf{P}_T^T)[\vec{\mathbf{p}}, \vec{\mathbf{q}}] \quad (3.21)$$

$$\vec{\mathbf{d}}_s[m] = (\mathbf{P}_T \bar{\mathbf{U}} \vec{\mathbf{d}})[\vec{\mathbf{q}}] \quad (3.22)$$

$$\vec{\mathbf{w}}_s[m] = (\mathbf{P}_R \vec{\mathbf{w}}_f)[\vec{\mathbf{p}}]. \quad (3.23)$$

Omitting all indexes for notation simplicity, the **GFDM** linear subsystem representation is given by

$$\vec{\mathbf{y}}_s = \mathbf{H}_s \vec{\mathbf{d}}_s + \vec{\mathbf{w}}_s, \quad (3.24)$$

where subscript (s) refers to the corresponding factorized subsystems in the frequency domain s.t.  $\vec{\mathbf{y}}_s \in \mathbb{C}^{N_R K \times 1}$  being the observable vector and  $\mathbf{H}_s \in \mathbb{C}^{N_R K \times N_T K_{\text{on}}}$  being the equivalent system transform matrix, including **MIMO** channel and multi-resource modulation. For the discrete random vector  $\vec{\mathbf{d}}$ , built from a finite alphabet  $\mathcal{C} \in \mathbb{C}^{M_c \times 1}$ , with  $M_c$  distinct members, it is reasonable to assume  $\vec{\mathbf{d}}_s \in \mathbb{C}^{N_T K_{\text{on}} \times 1}$  being a continuous gaussian random vector after the **FD** analysis of the corresponding  $m$ th subsymbol. The **AWGN** is represented by  $\vec{\mathbf{w}}_s \in \mathbb{C}^{N_R K \times 1}$ . The original data sequence can be obtained performing

$$\hat{\vec{\mathbf{d}}} = \bar{\mathbf{U}}^H \mathbf{P}_T^T [\hat{\vec{\mathbf{d}}}_{s_0}; \dots; \hat{\vec{\mathbf{d}}}_{s_m}; \dots; \hat{\vec{\mathbf{d}}}_{s_{M-1}}]. \quad (3.25)$$

### 3.3.1 Generic Factorized Linear Model

In order to obtain a generic factorized linear model in **FD**, we can rewrite (3.24) from the subsystem perspective while omitting the subscript (s), yielding to

$$\vec{y} = \mathbf{H}\vec{d} + \vec{w}. \quad (3.26)$$

The dimensions of the subsystem can be generally defined as shown in Table 6. For  $M = 1$ , the system can be decomposed according to subsection 3.2.1, when the **GFDM** is parameterized to mimic the **OFDM**. On other cases, it is necessary to proceed according to 3.2.2. This approach simplifies the description of the linear estimation process and detection techniques, allowing for an analysis of complexity that is independent of the waveform nature, whether orthogonal or not.

It is worth mentioning that, if the elements of  $\vec{d}$  are continuous Gaussian *RVs* (*Random Variables*) in the factorized domain, it might be necessary to employ suitable linear transformations for domain conversion, from discrete to factorized domain and vice-versa. These transforms are useful when the estimation or detection method depends solely on discrete data sequence from the constellation set  $\mathcal{C}$ . This is a common requirement for lattice-based detectors since they are exclusively built as a finite lattice whose nodes are discrete hypotheses. In such cases, it is possible to incorporate the domain conversion transform into  $\mathbf{H}$ . For example, when the factorization occurs in **FD**, it might be necessary to incorporate  $\mathbf{F}_q$  into  $\mathbf{H}$  in order to accept discrete data sequences in **TD** as input argument.

Table 6 – Generic factorized subsystem dimension as a function of parameter  $M$ .

Parameter	subsystem dimension		
	$M=1$	$M>1$	Generic
$\vec{y}$	$N_R \times 1$	$N_R K \times 1$	$p \times 1$
$\mathbf{H}$	$N_R \times N_T$	$N_R K \times N_T K_{\text{on}}$	$p \times q$
$\vec{d}$	$N_T \times 1$	$N_T K_{\text{on}} \times 1$	$q \times 1$
$\vec{w}$	$N_R \times 1$	$N_R K \times 1$	$p \times 1$
#subsystems	$K_{\text{on}}$	$M$	$s$

Following chapters will repeatedly reference this model. Note that, in order to benefit from system factorization, we must be able to estimate or detect all discrete information sequences in any domain, preferably in a parallel approach.

## 3.4 Summary

This chapter presented the **MIMO** principles employing a linear model through a transformation matrix encompassing the **MIMO** transmission channel and a generic mo-

dulation matrix, in line with the **GFDM** proposal. Further, we described the **SM-MIMO** system factorization for the orthogonal and **NO GFDM** waveforms, which can be considered as a key requirement to succeed on the practical implementation of a **SM-MIMO-GFDM** system. Next chapters review linear estimation and detection techniques suitable for retrieving the transmitted data, aiming to achieve both diversity and multiplexing gains when employing the **NO GFDM** waveform.

## 4 Fundamentals on Linear Estimation

Within digital communications, the estimation process requires selecting a hypothesis from an infinite set of possibilities, based on specific predefined criteria. Channel estimation serves as a prime example in communication systems, where the receiver must estimate the channel impulse response or frequency response, aiming to minimize the *MSE (Mean Squared Error)*. This chapter examines data linear estimation algorithms, discussing their derivations and estimated complexity based on the definitions presented in Section 1.8. These estimators are useful for data recovering when multiple transmit and receive antennas are employed to achieve *SM* gain. They work by estimating the channel state information *CSI (Channel State Information)*, which is essential for decoding the received signals accurately. This process involves complex algorithms that can handle the interference and noise present in the communication channel. Although the estimation techniques are widely used in *CSI* recovery, only data estimation problem is addressed, making several assumptions about the *MIMO* transmission channel: it is considered to be an uncorrelated frequency-selective and time-variant channel, perfectly known by the receiver, and the coherence time is larger than the symbol block length. Additionally, it is assumed perfect time and frequency synchronization among the transmitters and receivers. This chapter concludes with an analysis of the energy efficiency and complexity of the reviewed estimators.

### 4.1 Linear Estimation Function

As presented in Chapter 3, the digital communication system admits different linear representations depending on the analysis domain and the structure under investigation. From the estimator perspective, few parameters are sufficient to describe a certain linear system in the form of (3.4): an observable random vector  $\vec{\mathbf{y}} \in \mathbb{C}^{p \times 1}$ , a known linear transformation matrix  $\mathbf{H} \in \mathbb{C}^{p \times q}$  and the non-observable random vector  $\vec{\mathbf{x}} \in \mathbb{C}^{q \times 1}$ , whose elements are assumed to be continuous Gaussian random variables, for which an estimate is desired amid the presence of the noise vector  $\vec{\mathbf{w}} \in \mathbb{C}^{p \times 1}$ . Hence, considering the generic description above, the linear system used along this section is

$$\vec{\mathbf{y}} = \mathbf{H}\vec{\mathbf{x}} + \vec{\mathbf{w}}. \quad (4.1)$$

Following a similar notation as in [1], the estimation function  $\Theta$  is given by

$$(\vec{\mu}_{\vec{\mathbf{x}}}^p, \Sigma_{\vec{\mathbf{x}}}^p) = \Theta \left[ \vec{\mathbf{y}} = \mathbf{H}\vec{\mathbf{x}} + \vec{\mathbf{w}}, \mathcal{CN}(\vec{\mu}_{\vec{\mathbf{x}}}^a, \Sigma_{\vec{\mathbf{x}}}^a), \mathcal{CN}(\vec{\mathbf{0}}, \Sigma_{\vec{\mathbf{w}}}^a) \right] \quad (4.2)$$

where  $\vec{\mu}_{\vec{x}} \in \mathbb{C}^{q \times 1}$ ,  $\Sigma_{\vec{x}} \in \mathbb{C}^{q \times q}$  and  $\Sigma_{\vec{w}} \in \mathbb{C}^{p \times p}$  are, respectively, the expected value and the covariance of the corresponding subscripted random data, while the superscripts a and p means a-priory and posterior information, in this order. The parameter  $\Sigma_{\vec{x}}$  can also be interpreted as the uncertainty on the expected value of  $\vec{x}$ .

In function (4.2), three input arguments are utilized. The first argument represents the linear system model, while the second and third describe the prior distribution characteristics of the non-observable data vector and the additive noise process, respectively. The output arguments are the posterior or the refined expectation and covariance of the estimated data. The estimate can also be represented as a linear equalizer

$$\vec{\mu}_{\vec{x}} = \mathbf{W}\vec{y} + \vec{z}, \quad (4.3)$$

where  $\mathbf{W}$  and  $\vec{z}$  are, respectively, the coefficient matrix and an offset vector, properly designed to achieve MMSE for given constraints. The dimension of involved parameters are implicit obtained by the input arguments parser and stored in the integer variables, i.e.  $p$  and  $q$ . Figure 23 illustrates a block diagram representation of (4.2) where different estimation techniques are identified according to  $\Theta$  function subscript.

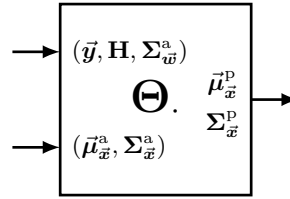


Figure 23 – Linear estimator function block.

Following sections intend to present different techniques to estimate the transmitted data taking each subsystem from the factorized structure, described in Section 3.2.2, as the input argument for the linear model.

## 4.2 LMMSE Estimator

The LMMSE [79, 59] refers to a simplified implementation of the classic MMSE estimator, constrained to be linear, yielding to sub-optimal performance. Basically, this estimator seeks to minimize the MSE  $E\{(\vec{x} - \vec{\mu}_{\vec{x}})(\vec{x} - \vec{\mu}_{\vec{x}})^H\}$  of the estimate in (4.3) for the linear system given by (4.1). Addressing (4.2),  $\Theta_1$  is obtained performing

$$\vec{\mu}_{\vec{x}}^p = \Sigma_{\vec{x}}^a \mathbf{H}^H \left( \mathbf{H} \Sigma_{\vec{x}}^a \mathbf{H}^H + \Sigma_{\vec{w}}^a \right)^{-1} (\vec{y} - \mathbf{H} \vec{\mu}_{\vec{x}}^a) + \vec{\mu}_{\vec{x}}^a \quad (4.4)$$

and

$$\Sigma_{\vec{x}}^p = \Sigma_{\vec{x}}^a - \Sigma_{\vec{x}}^a \mathbf{H}^H \left( \mathbf{H} \Sigma_{\vec{x}}^a \mathbf{H}^H + \Sigma_{\vec{w}}^a \right)^{-1} \mathbf{H} \Sigma_{\vec{x}}^a. \quad (4.5)$$

A complete derivation of these expressions is available in Appendix A. The LMMSE estimator is globally unbiased once  $\mathbf{E}\{\vec{\mu}_{\vec{x}}^p\} = \mathbf{E}\{\vec{x}\}$ , where the global attribute indicates that the unbiasedness condition only occurs for the whole observations of  $\vec{x}$  w.r.t. the true parameter value  $\vec{\mu}_{\vec{x}}$ .

---

**Algorithm 1** LMMSE
 

---

- 1:  $\Sigma_{\vec{x}}^a \mathbf{H}^H$
  - 2:  $(\mathbf{H} \Sigma_{\vec{x}}^a \mathbf{H}^H + \Sigma_{\vec{w}}^a)^{-1}$
  - 3:  $(\vec{y} - \mathbf{H} \vec{\mu}_{\vec{x}}^a)$
  - 4:  $\vec{\mu}_{\vec{x}}^p = \Sigma_{\vec{x}}^a \mathbf{H}^H (\mathbf{H} \Sigma_{\vec{x}}^a \mathbf{H}^H + \Sigma_{\vec{w}}^a)^{-1} (\vec{y} - \mathbf{H} \vec{\mu}_{\vec{x}}^a) + \vec{\mu}_{\vec{x}}^a$
  - 5:  $\Sigma_{\vec{x}}^p = \Sigma_{\vec{x}}^a - \Sigma_{\vec{x}}^a \mathbf{H}^H (\mathbf{H} \Sigma_{\vec{x}}^a \mathbf{H}^H + \Sigma_{\vec{w}}^a)^{-1} (\Sigma_{\vec{x}}^a \mathbf{H}^H)^H$
- Return:**  $(\vec{\mu}_{\vec{x}}^p, \Sigma_{\vec{x}}^p)$
- 

With the help of Table 1, it is possible to evaluate the associated computational complexity in Algorithm 1, in terms of FLOPs, which is given by

$$\mathcal{O}_1(4p^3 + 24p^2q + 16q^2p + 8p^2 + 10pq + 10p). \quad (4.6)$$

The LMMSE complexity is mainly dictated by the  $p \times p$  matrix inversion with cubic complexity order on  $p$ .

### 4.3 Steepest Descent Estimator

The STPD is an iterative procedure that can be applied to LMMSE and other estimators, not limited solely to MMSE performance criteria. In particular, applying the STPD procedure to linear estimation problem may allow, under certain convergence conditions, to reduce its overall complexity once no matrix inversion is necessary. As a result, the STPD scheme can achieve the same MSE performance as the LMMSE. Consider the STPD linear estimate in the form of (4.3). The coefficient matrix  $\mathbf{W} \in \mathbb{C}^{q \times p}$  can be approximated in an interactive fashion by

$$\mathbf{W}_t = \mathbf{W}_{t-1} + \delta \left[ \Sigma_{\vec{x}}^a \mathbf{H}^H - \mathbf{W}_{t-1} (\mathbf{H} \Sigma_{\vec{x}}^a \mathbf{H}^H + \Sigma_{\vec{w}}^a) \right], \quad (4.7)$$

where  $t$  is an iteration index and  $\delta$  is the step-size parameter with an important role on algorithm convergence. This is a crucial parameter and should be chosen carefully or designed to ensure a reasonable trade-off between convergence speed and stability [80]. It is important to notice that the STPD performs successive step searches in the opposite gradient direction for all random variables at once, possibly leading to small misdirection perturbation, impacting the convergence behavior. The STPD estimator function  $\Theta_{\text{stpd}}$  is evaluated at iteration  $t$  by

$$\vec{\mu}_{\vec{x}}^p = \mathbf{W}_t (\vec{y}_t - \mathbf{H} \vec{\mu}_{\vec{x}}^a) + \vec{\mu}_{\vec{x}}^a, \quad (4.8)$$

$$\Sigma_{\vec{x}}^p = \Sigma_{\vec{x}}^a - \left[ (\Sigma_{\vec{x}}^a \mathbf{H}^H \mathbf{W}_t^H)^H + \Sigma_{\vec{x}}^a \mathbf{H}^H \mathbf{W}_t^H \right] + \mathbf{W}_t (\mathbf{H} \Sigma_{\vec{x}}^a \mathbf{H}^H + \Sigma_{\vec{w}}^a) \mathbf{W}_t^H. \quad (4.9)$$

As  $\mathbf{W}_t$  converges, (4.9) approaches the final LMMSE. It is worth to mention that (4.8) do not employ matrix inversion. Instead, a certain amount of iterations must be considered to achieve convergence. Furthermore, prior knowledge of the signal statistics are required and, at  $t=0$ ,  $\mathbf{W}_{-1}$  might be initialized as a null matrix. The derivation of (4.7), (4.8) and (4.9) is described in Appendix B. Algorithm 2 summarizes the STPD estimator.

---

**Algorithm 2** STPD
 

---

**Initialize:**

- 1:  $\mathbf{W}_{-1} = \mathbf{0}$
- 2:  $t = 0$

**Update Statistics:**

- 3:  $\Sigma_{\vec{\mathbf{x}}}^{\mathbf{a}} \mathbf{H}^{\mathbf{H}}$
- 4:  $(\mathbf{H} \Sigma_{\vec{\mathbf{x}}}^{\mathbf{a}} \mathbf{H}^{\mathbf{H}} + \Sigma_{\vec{\mathbf{w}}}^{\mathbf{a}})$

**Iterate:**

- 5:  $\mathbf{W}_t = \mathbf{W}_{t-1} + \delta \left[ \Sigma_{\vec{\mathbf{x}}}^{\mathbf{a}} \mathbf{H}^{\mathbf{H}} - \mathbf{W}_{t-1} \left( \mathbf{H} \Sigma_{\vec{\mathbf{x}}}^{\mathbf{a}} \mathbf{H}^{\mathbf{H}} + \Sigma_{\vec{\mathbf{w}}}^{\mathbf{a}} \right) \right]$  % complexity:  $8p^2q + 2pq + 2$

**Estimate:**

- 6:  $\Sigma_{\vec{\mathbf{x}}}^{\mathbf{a}} \mathbf{H}^{\mathbf{H}} \mathbf{W}_t^{\mathbf{H}}$
- 7:  $\vec{\boldsymbol{\mu}}_{\vec{\mathbf{x}}}^{\mathbf{p}} = \mathbf{W}_t (\vec{\mathbf{y}}_t - \mathbf{H} \vec{\boldsymbol{\mu}}_{\vec{\mathbf{x}}}^{\mathbf{a}}) + \vec{\boldsymbol{\mu}}_{\vec{\mathbf{x}}}^{\mathbf{a}}$
- 8:  $\Sigma_{\vec{\mathbf{x}}}^{\mathbf{p}} = \Sigma_{\vec{\mathbf{x}}}^{\mathbf{a}} - \left[ (\Sigma_{\vec{\mathbf{x}}}^{\mathbf{a}} \mathbf{H}^{\mathbf{H}} \mathbf{W}_t^{\mathbf{H}})^{\mathbf{H}} + \Sigma_{\vec{\mathbf{x}}}^{\mathbf{a}} \mathbf{H}^{\mathbf{H}} \mathbf{W}_t^{\mathbf{H}} \right] + \mathbf{W}_t \left( \mathbf{H} \Sigma_{\vec{\mathbf{x}}}^{\mathbf{a}} \mathbf{H}^{\mathbf{H}} + \Sigma_{\vec{\mathbf{w}}}^{\mathbf{a}} \right) \mathbf{W}_t^{\mathbf{H}}$
- 9:  $t = t + 1$

**Return:**  $(\vec{\boldsymbol{\mu}}_{\vec{\mathbf{x}}}^{\mathbf{p}}, \Sigma_{\vec{\mathbf{x}}}^{\mathbf{p}})$ 


---

Algorithm 2 is partitioned in four segments, enabling the optimization of execution complexity. For instance, if the statistics remain unchanged, it is more efficient to iterate through only line 5 before estimation. On the other hand, if intermediary estimates are needed while a-priori information may vary, an option is to execute the entire algorithm except the initialization. The overall complexity for Algorithm 2, considering non-sparse transform matrices and  $t$  iterations, is given by

$$\mathcal{O}_s \left( 16p^2q + 24q^2p + 2q^2 + 12pq + t(8p^2q + 2qp + 2) \right). \quad (4.10)$$

Notice that  $\mathcal{O}_s$  refers to the computational effort per iteration. If we only consider the steps necessary for expectation estimate of  $\vec{\boldsymbol{\mu}}_{\vec{\mathbf{x}}}^{\mathbf{p}}$  and not its associated variance  $\Sigma_{\vec{\mathbf{x}}}^{\mathbf{p}}$ , the complexity is more restrained than LMMSE. For both parameters estimation, STPD is even more complex, which reduces the appeal to use this estimator. Commonly, when  $p = q$ , the complexity is still cubic on system dimension, which is insufficient for computational savings.

Both LMMSE and STPD result in biased estimation since the effective channel matrix after filtering, i.e.  $\Sigma_{\vec{\mathbf{x}}}^{\mathbf{a}} \mathbf{H}^{\mathbf{H}} \left( \mathbf{H} \Sigma_{\vec{\mathbf{x}}}^{\mathbf{a}} \mathbf{H}^{\mathbf{H}} + \Sigma_{\vec{\mathbf{w}}}^{\mathbf{a}} \right)^{-1} \mathbf{H}$ , from (4.5), does not have a unit diagonal. Next section briefly analyzes an unbiased LMMSE estimator known as CWCU-LMMSE.

## 4.4 CWCU-LMMSE Estimator

The **CWCU-LMMSE** is a constrained linear and conditionally unbiased version of **MMSE** estimator, where the conditional expectation of each estimated component  $\hat{x}$  is individually forced to be equivalent to its associated indirect observable random variable  $x$  [59]. As the **CWCU-LMMSE** performs unbiased estimation, it can not outperform the **LMMSE** estimator in a **MSE** criteria, since it seeks to minimize the estimation error under the additional constraint  $\mathbb{E}\{\hat{x}|x\} = x$ . The corresponding estimator function  $\Theta_c$  is

$$\vec{\mu}_{\vec{x}}^p = \vec{\eta} \circ \mathbf{H}^H \left( \mathbf{H} \Sigma_{\vec{x}}^a \mathbf{H}^H + \Sigma_{\vec{w}}^a \right)^{-1} (\vec{y} - \mathbf{H} \vec{\mu}_{\vec{x}}^a) + \vec{\mu}_{\vec{x}}^a, \quad (4.11)$$

$$\text{diag}(\Sigma_{\vec{x}}^p) = \vec{\eta} - \text{diag}(\Sigma_{\vec{x}}^a), \quad (4.12)$$

where, in the context of Section 4.1,  $\vec{\eta} \in \mathbb{R}^{q \times 1}$  is a weighting vector given by

$$\vec{\eta} = \vec{\mathbf{1}} \oslash \text{diag} \left( \mathbf{H}^H \left( \mathbf{H} \Sigma_{\vec{x}}^a \mathbf{H}^H + \Sigma_{\vec{w}}^a \right)^{-1} \mathbf{H} \right). \quad (4.13)$$

A detailed derivation of these expressions is available in Appendix C. Equation (4.11) is closed related to **LMMSE** estimator in (4.4), except by the weighting vector product instead of a matrix-matrix multiplication. Moreover, the estimate variance (4.12) is obtained with less operations. Hence, the **CWCU-LMMSE** procedure can be complemented by including (4.13) according to Algorithm 3.

---

### Algorithm 3 CWCU-LMMSE

---

- 1:  $\Sigma_{\vec{x}}^a \mathbf{H}^H$
- 2:  $(\mathbf{H} \Sigma_{\vec{x}}^a \mathbf{H}^H + \Sigma_{\vec{w}}^a)^{-1}$
- 3:  $(\vec{y} - \mathbf{H} \vec{\mu}_{\vec{x}}^a)$
- 4:  $\vec{\eta} = \vec{\mathbf{1}} \oslash \text{diag} \left( \mathbf{H}^H \left( \mathbf{H} \Sigma_{\vec{x}}^a \mathbf{H}^H + \Sigma_{\vec{w}}^a \right)^{-1} \mathbf{H} \right)$
- 5:  $\vec{\mu}_{\vec{x}}^p = \vec{\eta} \circ \mathbf{H}^H \left( \mathbf{H} \Sigma_{\vec{x}}^a \mathbf{H}^H + \Sigma_{\vec{w}}^a \right)^{-1} (\vec{y} - \mathbf{H} \vec{\mu}_{\vec{x}}^a) + \vec{\mu}_{\vec{x}}^a$
- 6:  $\text{diag}(\Sigma_{\vec{x}}^p) = \vec{\eta} - \text{diag}(\Sigma_{\vec{x}}^a)$

**Return:**  $(\vec{\mu}_{\vec{x}}^p, \Sigma_{\vec{x}}^p)$

---

The resulting complexity executing Algorithm 3 is

$$\mathcal{O}_c \left( 4p^3 + 16p^2q + 8q^2p + 8p^2 + 14pq + 10p + 4q \right), \quad (4.14)$$

again, mainly dictated by the  $p \times p$  matrix inversion with cubic complexity order on  $p$  and other matrices product.

### 4.4.1 Low Complexity CWCU-LMMSE Estimator

In order to avoid redundant computations, the **CWCU-LMMSE** estimator can be modified, as referenced in [61], computing the Gram matrix  $\mathbf{H}^H \mathbf{H} \in \mathbb{C}^{q \times q}$  and the

matched-filter output  $\vec{\mathbf{y}}_{\text{MF}} = \mathbf{H}^H \vec{\mathbf{y}}$  prior to iterative detection. In every iteration, the estimation is performed based only on the previous computation of these parameters, which roughly halves the number of complex multiplications. The resulting low-complexity  $\Theta_{\text{lc}}$  estimator is obtained rewriting (4.11) and (4.13), yielding to

$$\vec{\boldsymbol{\mu}}_{\vec{\mathbf{x}}}^{\text{p}} = \vec{\boldsymbol{\eta}} \circ \left( \mathbf{H}^H \mathbf{H} \boldsymbol{\Sigma}_{\vec{\mathbf{x}}}^{\text{a}} + \boldsymbol{\Sigma}_{\vec{\mathbf{w}}}^{\text{a}} \right)^{-1} \left( \mathbf{H}^H \vec{\mathbf{y}} - \mathbf{H}^H \mathbf{H} \vec{\boldsymbol{\mu}}_{\vec{\mathbf{x}}}^{\text{a}} \right) + \vec{\boldsymbol{\mu}}_{\vec{\mathbf{x}}}^{\text{a}} \quad (4.15)$$

and

$$\vec{\boldsymbol{\eta}} = \vec{\mathbf{1}} \oslash \text{diag} \left( \left( \mathbf{H}^H \mathbf{H} \boldsymbol{\Sigma}_{\vec{\mathbf{x}}}^{\text{a}} + \boldsymbol{\Sigma}_{\vec{\mathbf{w}}}^{\text{a}} \right)^{-1} \mathbf{H}^H \mathbf{H} \right), \quad (4.16)$$

while reusing (4.12) to obtain the estimate variance. This procedure is summarized in Algorithm 4.

---

**Algorithm 4** Low Complexity CWCU-LMMSE
 

---

**Initialize:**

- 1:  $\mathbf{H}^H \mathbf{H}$
- 2:  $\vec{\mathbf{y}}_{\text{MF}} = \mathbf{H}^H \vec{\mathbf{y}}$
- 3:  $\boldsymbol{\Sigma}_{\vec{\mathbf{w}}}^{\text{a}} = \sigma_{\vec{\mathbf{w}}}^2 \mathbf{I}$
- 4:  $\vec{\boldsymbol{\mu}}_{\vec{\mathbf{x}}}^{\text{a}} = \vec{\mathbf{0}}, \boldsymbol{\Sigma}_{\vec{\mathbf{x}}}^{\text{a}} = \mathbf{I}, \boldsymbol{\Sigma}_{\vec{\mathbf{x}}}^{\text{p}} = \mathbf{I}$

**Iterate:**

- 5:  $\left( \mathbf{H}^H \mathbf{H} \boldsymbol{\Sigma}_{\vec{\mathbf{x}}}^{\text{a}} + \boldsymbol{\Sigma}_{\vec{\mathbf{w}}}^{\text{a}} \right)^{-1}$
- 6:  $\left( \vec{\mathbf{y}}_{\text{MF}} - \mathbf{H}^H \mathbf{H} \vec{\boldsymbol{\mu}}_{\vec{\mathbf{x}}}^{\text{a}} \right)$
- 7:  $\vec{\boldsymbol{\eta}} = \vec{\mathbf{1}} \oslash \text{diag} \left( \left( \mathbf{H}^H \mathbf{H} \boldsymbol{\Sigma}_{\vec{\mathbf{x}}}^{\text{a}} + \boldsymbol{\Sigma}_{\vec{\mathbf{w}}}^{\text{a}} \right)^{-1} \mathbf{H}^H \mathbf{H} \right)$
- 8:  $\vec{\boldsymbol{\mu}}_{\vec{\mathbf{x}}}^{\text{p}} = \vec{\boldsymbol{\eta}} \circ \left( \mathbf{H}^H \mathbf{H} \boldsymbol{\Sigma}_{\vec{\mathbf{x}}}^{\text{a}} + \boldsymbol{\Sigma}_{\vec{\mathbf{w}}}^{\text{a}} \right)^{-1} \left( \vec{\mathbf{y}}_{\text{MF}} - \mathbf{H}^H \mathbf{H} \vec{\boldsymbol{\mu}}_{\vec{\mathbf{x}}}^{\text{a}} \right) + \vec{\boldsymbol{\mu}}_{\vec{\mathbf{x}}}^{\text{a}}$
- 9:  $\text{diag} \left( \boldsymbol{\Sigma}_{\vec{\mathbf{x}}}^{\text{p}} \right) = \vec{\boldsymbol{\eta}} - \text{diag} \left( \boldsymbol{\Sigma}_{\vec{\mathbf{x}}}^{\text{a}} \right)$

**Return:**  $(\vec{\boldsymbol{\mu}}_{\vec{\mathbf{x}}}^{\text{p}}, \boldsymbol{\Sigma}_{\vec{\mathbf{x}}}^{\text{p}})$

---

Algorithm 4 is an interesting option for the orthogonal detection case, depending on system order, where the PIC procedure is decomposed into  $K_{\text{on}}$  subsystems with non-sparse transform matrices of dimension  $N_{\text{R}} \times N_{\text{T}}$ . The Algorithm 4 complexity is

$$\mathcal{O}_{\text{lc}} \left( 12q^3 + 30q^2 + 14q \right). \quad (4.17)$$

Next subsection briefly reviews an approximation for the CWCU-LMMSE estimator exploiting band-diagonal systems with noticeable complexity reduction.

#### 4.4.2 Band-diagonal Low Complexity CWCU-LMMSE Estimator

In [60], the authors propose an algorithm that can exploit the structure of a band-diagonal transform matrix  $\mathbf{H} \in \mathbb{C}^{p \times q}$  for an iterative implementation of a CWCU-LMMSE estimator with reduced complexity, denominated here as  $\Theta_{\text{lc|}}$ . Hence, assuming  $\boldsymbol{\Sigma}_{\vec{\mathbf{x}}}$  strictly diagonal, the estimate outputs are given by

$$\vec{\boldsymbol{\mu}}_{\vec{\mathbf{x}}}^{\text{p}} = \vec{\boldsymbol{\xi}} \oslash \vec{\boldsymbol{\gamma}} + \vec{\boldsymbol{\mu}}_{\vec{\mathbf{x}}}^{\text{a}}, \quad (4.18)$$

$$\text{diag}(\boldsymbol{\Sigma}_{\bar{\mathbf{x}}}^p) = \vec{\mathbf{1}} \circ \vec{\gamma} - \text{diag}(\boldsymbol{\Sigma}_{\bar{\mathbf{x}}}^a), \quad (4.19)$$

where

$$\vec{\boldsymbol{\xi}} = \mathbf{W}^{-1} (\vec{\mathbf{y}}_{\text{MF}} - \mathbf{H}^H \mathbf{H} \vec{\boldsymbol{\mu}}_{\bar{\mathbf{x}}}^a), \quad (4.20)$$

$$\vec{\gamma} = \text{diag}(\mathbf{W}^{-1} \mathbf{H}^H \mathbf{H}), \quad (4.21)$$

with

$$\vec{\mathbf{y}}_{\text{MF}} = \mathbf{H}^H \vec{\mathbf{y}} = \mathbf{H}^H \mathbf{H} \vec{\mathbf{x}} + \mathbf{H}^H \vec{\mathbf{w}}, \quad (4.22)$$

$$\mathbf{W} = \mathbf{H}^H \mathbf{H} \boldsymbol{\Sigma}_{\bar{\mathbf{x}}}^a + \sigma_{\vec{\mathbf{w}}}^2 \mathbf{I}_q \quad (4.23)$$

and  $\mathbf{H}^H \mathbf{H} \in \mathbb{C}^{q \times q}$  being a square band-diagonal Gram matrix with dimension  $q = zs$ , single-side bandwidth  $s$  and  $2s - 1$  upper and lower diagonals. The noise variance can be obtained by  $\sigma_{\vec{\mathbf{w}}}^2 = \text{tr}(\boldsymbol{\Sigma}_{\vec{\mathbf{w}}}^a)/p$ .

Instead of directly inverting (4.23) to obtain (4.18) and (4.19), it is preferable to define two linear systems,

$$\mathbf{W} \vec{\boldsymbol{\xi}} = \vec{\mathbf{y}}_{\text{MF}} - \mathbf{H}^H \mathbf{H} \vec{\boldsymbol{\mu}}_{\bar{\mathbf{x}}}^a \quad (4.24)$$

and

$$\mathbf{W} \boldsymbol{\Upsilon} = \mathbf{H}^H \mathbf{H} \mathbf{M}, \quad (4.25)$$

where  $\mathbf{M} \in \mathbb{R}^{q \times 2\lceil s \rceil_2}$  is an arbitrary real matrix, i.e.  $\mathbf{M} = \mathcal{H}^T [1 : q, 1 : \lceil 2s \rceil_2]$ , or the first  $q$  rows and first  $\lceil 2s \rceil_2$  columns of the transposed Hadamard matrix  $\mathcal{H}$  with dimension  $\lceil q \rceil_2$ , s.t. the off-diagonal elements of  $\mathbf{M} \mathbf{M}^T$  are zero where  $\mathbf{W}^{-1} \mathbf{H}^H \mathbf{H}$  is non-zero [60, 78].

Then, solving the banded linear systems (4.24) and (4.25) employing specific optimized algorithms [65, Functions *zgbtrf*, *zgbtrs*], leads to

$$\vec{\gamma} \approx (\mathbf{M} \circ \boldsymbol{\Upsilon}) \vec{\mathbf{1}} \circ (\mathbf{M} \circ \mathbf{M}) \vec{\mathbf{1}}. \quad (4.26)$$

Algorithm 5 summarizes the low complexity **CWCU-LMMSE** procedure when the transform matrix is banded. Note that, at first interaction, in case of a-priori information is not available, line 8 initializes these parameters. Without entering in details now, the idea behind this algorithm is refining estimates after soft demodulation and decoding. Soft bits are then mapped into soft symbols and fed back as a-priori information for next interaction. This recursive behavior takes place as much as necessary in a tentative to approach a required **BER** (*Bit Error Rate*) target. This concept is known as iterative detection and it is addressed with further details in Chapter 6.

**Algorithm 5** Band-diagonal Low Complexity CWCU-LMMSE**Initialize:**

- 1:  $\mathbf{H}^H \mathbf{H}$
- 2:  $\sigma_{\mathbf{w}}^2 = \text{tr}(\Sigma_{\mathbf{w}}^a)/p$
- 3:  $\mathcal{H} = \text{Hadamard}(\lceil q \rceil_2)$
- 4:  $\mathbf{M} = \mathcal{H}^T [1 : q, 1 : \lceil 2s \rceil_2]$
- 5:  $\mathbf{H}^H \mathbf{H} \mathbf{M}$
- 6:  $(\mathbf{M} \circ \mathbf{M}) \vec{\mathbf{1}}$
- 7:  $\vec{\mathbf{y}}_{\text{MF}} = \mathbf{H}^H \vec{\mathbf{y}}$
- 8:  $\vec{\boldsymbol{\mu}}_{\mathbf{x}}^a = \vec{\mathbf{0}}, \Sigma_{\mathbf{x}}^a = \mathbf{I}, \Sigma_{\mathbf{x}}^p = \mathbf{I}$

**Iterate:**

- 9:  $\mathbf{W} = \mathbf{H}^H \mathbf{H} \Sigma_{\mathbf{x}}^a + \sigma_{\mathbf{w}}^2 \mathbf{I}_q$
- 10:  $\mathbf{LU} = \text{LU}(\mathbf{W})$  % zgbtrf function
- 11:  $\vec{\boldsymbol{\xi}} = \mathbf{LU}^{-1} (\vec{\mathbf{y}}_{\text{MF}} - \mathbf{H}^H \mathbf{H} \vec{\boldsymbol{\mu}}_{\mathbf{x}}^a)$  % solve (4.24) via zgbtrs function
- 12:  $\mathbf{Y} = \mathbf{LU}^{-1} \mathbf{H}^H \mathbf{H} \mathbf{M}$  % solve (4.25) via zgbtrs function
- 13:  $\vec{\boldsymbol{\gamma}} \approx (\mathbf{M} \circ \mathbf{Y}) \vec{\mathbf{1}} \oslash (\mathbf{M} \circ \mathbf{M}) \vec{\mathbf{1}}$
- 14:  $\vec{\boldsymbol{\mu}}_{\mathbf{x}}^p = \vec{\boldsymbol{\xi}} \oslash \vec{\boldsymbol{\gamma}} + \vec{\boldsymbol{\mu}}_{\mathbf{x}}^a$
- 15:  $\text{diag}(\Sigma_{\mathbf{x}}^p) = \vec{\mathbf{1}} \oslash \vec{\boldsymbol{\gamma}} - \text{diag}(\Sigma_{\mathbf{x}}^a)$

**Return:**  $(\vec{\boldsymbol{\mu}}_{\mathbf{x}}^p, \Sigma_{\mathbf{x}}^p)$ 

Only initialization process counts  $8s^3z + 2s^2z(4\lceil 2s \rceil_2 + 3) - 2sz\lceil 2s \rceil_2 + 1$  FLOPs while the overall complexity on every iteration of Algorithm 5 is given by

$$\mathcal{O}_{\text{icl}} \left( 32s^3z + 56s^2z\lceil 2s \rceil_2 - 42sz\lceil 2s \rceil_2 + 48s^2z - 9sz \right), \quad (4.27)$$

mainly governed by lines 10 to 12, with cubic complexity order only on  $s$ , though limited to a band-diagonal linear system.

Next subsection shortly revisits a low complexity CWCU-LMMSE approximation based on CG (*Conjugate Gradient*) with applications in time-to-frequency conversion estimates and vice-versa.

#### 4.4.3 CG-based Low Complexity CWCU-LMMSE Estimator

According to [60], an algorithm suitable for a specific application of interest is resorted to. Recall from Section 3.2 that the system factorization takes place in the frequency domain. Therefore, it is essential to execute efficient conversions between the time and frequency domains, especially when employing iterative detection methods. In this sense, assuming  $\mathbf{H} = \mathbf{F}_q$  for the specific case of time-domain data estimation based on frequency-domain observation, where  $\mathbf{H}$  holds the normalized unitary property s.t.  $\mathbf{H}\mathbf{H}^H = \mathbf{I}$  and  $\mathbf{H}^H = \mathbf{H}^{-1}$ , allows to rewrite (4.11) and (4.13) as

$$\vec{\boldsymbol{\mu}}_{\mathbf{x}}^p = \vec{\boldsymbol{\eta}} \circ \left( \Sigma_{\mathbf{x}}^a + \mathbf{H}^H \Sigma_{\mathbf{w}}^a \mathbf{H} \right)^{-1} \left( \mathbf{H}^H \vec{\mathbf{y}} - \vec{\boldsymbol{\mu}}_{\mathbf{x}}^a \right) + \vec{\boldsymbol{\mu}}_{\mathbf{x}}^a, \quad (4.28)$$

and

$$\vec{\eta} = \vec{\mathbf{I}} \circ \text{diag} \left( \left( \Sigma_{\vec{x}}^a + \mathbf{H}^H \Sigma_{\vec{w}}^a \mathbf{H} \right)^{-1} \right). \quad (4.29)$$

The central idea of the algorithm is to avoid the matrix inversion in (4.28) by estimating

$$\hat{\vec{x}} = \mathbf{A}^{-1} \vec{\mathbf{b}} = \left( \Sigma_{\vec{x}}^a + \mathbf{H}^H \Sigma_{\vec{w}}^a \mathbf{H} \right)^{-1} \left( \mathbf{H}^H \vec{\mathbf{y}} - \vec{\mu}_{\vec{x}}^a \right), \quad (4.30)$$

for the linear model  $\mathbf{A}\vec{x} = \vec{\mathbf{b}}$ , with the right-hand side  $\vec{\mathbf{b}} = (\mathbf{H}^H \vec{\mathbf{y}} - \vec{\mu}_{\vec{x}}^a)$  when  $\mathbf{A}$  is a highly structured matrix by being the sum of a positive definite diagonal and a circulant matrix. This is exactly the case when  $\mathbf{H}$  is a  $q$ -point DFT kind matrix and  $\Sigma$  parameters are approximately diagonal in (4.30). To this end, CG is considered for the estimator function  $\Theta_{\text{cg}}$ . This iterative procedure is capable to converge in a finite number of iterations with relative low complexity [81]. The solution is refined interactively and the step-search is performed in the conjugate direction with a movement towards the best solution [79]. As the CG method requires an initial starting point to determine the step size and the direction prior to update the solution, [60] suggests using the following approximation

$$\text{diag} \left( \mathbf{A}^{-1} \right) \approx \vec{\mathbf{I}} \circ \text{diag} \left( \Sigma_{\vec{x}}^a + \frac{1}{q} \text{tr} \left( \Sigma_{\vec{w}}^a \right) \mathbf{I} \right). \quad (4.31)$$

Algorithm 6 describes the CG procedure adopting usual nomenclature identification for the local variables. With exception of the initialization steps, targeted to address (4.30) under the aforementioned assumptions, this algorithm can be used to solve general system of equations when  $\mathbf{A}$  is a positive-definite matrix. In line 5, the starting point is defined following the approximation in (4.31), allowing to initialize the residual error and the search direction at line 6, in this order. In iterative section, line 9 updates the step-size s.t. the residual error be orthogonal w.r.t. current searching line and immediately refines the solution. The residual error is updated at line 11. In CG, each new residual error is made orthogonal to all previous residual and search directions. If the resulting error is greater than or equal to the MSE target and not all search directions have been iterated, lines 13 and 14 ideally ensure that current and next search directions are conjugate or  $\mathbf{A}$ -orthogonal [81]. On the contrary, CG has already achieved convergence and low complexity CWCU-LMMSE is obtained executing steps 19 to 21. This avoids a division by zero after convergence, when the residual error approaches zero. The overall complexity on Algorithm 6, considering  $t$  iterations, is

$$\mathcal{O}_{\text{cg}} \left( 20q^2 + 11q + 2q \log(q) + t(16q^2 + 37q - 1) + 1 \right). \quad (4.32)$$

Further details on applications of the CG-based and the band-diagonal low complexity CWCU-LMMSE estimators are available in Chapter 6.

**Algorithm 6** CG-based Low Complexity CWCU-LMMSE**Initialize:**

- 1:  $\Sigma_{\vec{x}}^p = \mathbf{I}$
- 2:  $\mathbf{A} = (\Sigma_{\vec{x}}^a + \mathbf{H}^H \Sigma_{\vec{w}}^a \mathbf{H})$
- 3:  $\vec{\mathbf{b}} = \mathbf{H}^H \vec{\mathbf{y}} - \vec{\mu}_{\vec{x}}^a$
- 4:  $\text{diag}(\mathbf{A}^{-1}) \approx \vec{\mathbf{1}} \oslash \text{diag}(\Sigma_{\vec{x}}^a + \frac{1}{q} \text{tr}(\Sigma_{\vec{w}}^a) \mathbf{I})$
- 5:  $\hat{\vec{\mathbf{x}}}_0 = \text{diag}(\mathbf{A}^{-1}) \circ \vec{\mathbf{b}}$
- 6:  $\vec{\mathbf{r}}_0 = \vec{\mathbf{b}} - \mathbf{A} \hat{\vec{\mathbf{x}}}_0, \vec{\mathbf{d}}_0 = \vec{\mathbf{r}}_0$
- 7:  $t = 0, e = \text{MSE target}$

**Iterate:**

- 9:  $\alpha_t = \frac{\vec{\mathbf{r}}_t^H \vec{\mathbf{r}}_t}{\vec{\mathbf{d}}_t^H \mathbf{A} \vec{\mathbf{d}}_t}$
- 10:  $\hat{\vec{\mathbf{x}}}_{t+1} = \vec{\mathbf{x}}_t + \alpha_t \vec{\mathbf{d}}_t$
- 11:  $\vec{\mathbf{r}}_{t+1} = \vec{\mathbf{r}}_t - \alpha_t \mathbf{A} \vec{\mathbf{d}}_t$
- 12: **if**  $\left( \frac{\vec{\mathbf{r}}_{t+1}^H \vec{\mathbf{r}}_{t+1}}{q} \geq e \right)$  **and**  $(t < q - 1)$  **then**
- 13:      $\beta_t = \frac{\vec{\mathbf{r}}_{t+1}^H \vec{\mathbf{r}}_{t+1}}{\vec{\mathbf{r}}_t^H \vec{\mathbf{r}}_t}$
- 14:      $\vec{\mathbf{d}}_{t+1} = \vec{\mathbf{r}}_{t+1} + \beta_t \vec{\mathbf{d}}_t$
- 15:      $t = t + 1$
- 16: **else**
- 17:     **break**
- 18: **end if**

**Estimate:**

- 19:  $\vec{\boldsymbol{\eta}} = \vec{\mathbf{1}} \oslash \text{diag}(\mathbf{A}^{-1})$
- 20:  $\vec{\mu}_{\vec{x}}^p = \vec{\mu}_{\vec{x}}^a + \vec{\boldsymbol{\eta}} \circ \hat{\vec{\mathbf{x}}}_{t+1}$
- 21:  $\text{diag}(\Sigma_{\vec{x}}^p) = \vec{\boldsymbol{\eta}} - \text{diag}(\Sigma_{\vec{w}}^a)$

**Return:**  $(\vec{\mu}_{\vec{x}}^p, \Sigma_{\vec{x}}^p)$ 

## 4.5 Maximum a Posteriori Estimator

The **MAP** (*Maximum a Posteriori*) estimator is an useful approach to incorporate prior information into the data estimation problem. The **MAP** estimator is based on posterior probability maximization and it is close related to **MAP** hypothesis testing [82]. Although the **MAP** estimator could, in some cases, result in optimum estimates, like the **MSE**, it can be cumbersome (or even prohibited) to determine the exactly posterior probability function. In general, the **MAP** estimate of the **RV**  $\vec{\mathbf{X}}$  given the observation  $\vec{\mathbf{Y}} = \vec{\mathbf{y}}$  is

$$\vec{\mu}_{\vec{x}}^p = \underset{\vec{\mathbf{x}}}{\text{argmax}} f_{\vec{\mathbf{X}}|\vec{\mathbf{Y}}}(\vec{\mathbf{x}} | \vec{\mathbf{y}}), \quad (4.33)$$

where  $f_{\vec{\mathbf{X}}|\vec{\mathbf{Y}}}(\vec{\mathbf{x}} | \vec{\mathbf{y}})$  is the conditional distribution function of  $\vec{\mathbf{X}}$  given  $\vec{\mathbf{Y}} = \vec{\mathbf{y}}$ .

Retrieving the definition of the iid (*independent and identically distributed*) complex Gaussian random vectors  $\vec{\mathbf{x}}$  and  $\vec{\mathbf{y}}$  from section 4.1, connected through the linear

model in (4.1), the a-priori cross covariance can be described in terms of the independent RV as

$$\Sigma_{\vec{x}\vec{y}}^a = \Sigma_{\vec{x}}^a \mathbf{H}^H = (\Sigma_{\vec{y}\vec{x}}^a)^H. \quad (4.34)$$

Similarly, the expectancy and covariance are given by

$$\vec{\mu}_{\vec{y}}^a = \mathbf{H} \vec{\mu}_{\vec{x}}^a, \quad (4.35)$$

$$\Sigma_{\vec{y}}^a = \mathbf{H} \Sigma_{\vec{x}}^a \mathbf{H}^H + \Sigma_{\vec{w}}^a. \quad (4.36)$$

These matrices are, in general, part of the linear estimation solution and are also present in the associated error covariance matrix of the estimator, a common parameter used in performance analysis. The conditional PDF (*Probability Density Function*) is given by the bi-variate complex Gaussian distribution [83] as

$$f_{\vec{x}|\vec{y}}(\vec{x} | \vec{y}) = \pi^{-1} \det(\Sigma)^{-1} \exp\left[-(\vec{x} - \tilde{\mu})^H \Sigma^{-1} (\vec{x} - \tilde{\mu})\right] \quad (4.37)$$

where  $\det(\cdot)$  is the determinant operator,

$$\Sigma = \Sigma_{\vec{x}}^a - \Sigma_{\vec{x}\vec{y}}^a (\Sigma_{\vec{y}}^a)^{-1} \Sigma_{\vec{y}\vec{x}}^a \quad (4.38)$$

and

$$\tilde{\mu} = \vec{\mu}_{\vec{x}}^a + \Sigma_{\vec{x}\vec{y}}^a (\Sigma_{\vec{y}}^a)^{-1} (\vec{y} - \vec{\mu}_{\vec{y}}^a). \quad (4.39)$$

Analyzing (4.37), it is clear that its maximum probability occurs when its exponent is null, hence, when  $\vec{x} = \tilde{\mu}$ . This condition yields to

$$\vec{\mu}_{\vec{x}}^p = \vec{\mu}_{\vec{x}}^a + \Sigma_{\vec{x}\vec{y}}^a (\Sigma_{\vec{y}}^a)^{-1} (\vec{y} - \vec{\mu}_{\vec{y}}^a). \quad (4.40)$$

Finally, replacing (4.34), (4.35) and (4.36) in (4.40) leads to

$$\vec{\mu}_{\vec{x}}^p = \vec{\mu}_{\vec{x}}^a + \Sigma_{\vec{x}}^a \mathbf{H}^H \left( \mathbf{H} \Sigma_{\vec{x}}^a \mathbf{H}^H + \Sigma_{\vec{w}}^a \right)^{-1} (\vec{y} - \mathbf{H} \vec{\mu}_{\vec{y}}^a), \quad (4.41)$$

which, in this specific case, resolves to the LMMSE estimator in (4.4) and the estimation procedure describe in algorithm 1. Hence, its computational complexity is equivalent to (4.6),

$$\mathcal{O}_{\text{map}}(4p^3 + 24p^2q + 16q^2p + 8p^2 + 10pq + 10p), \quad (4.42)$$

while the error covariance matrix corresponds to (4.5) and is given by

$$\Sigma_{\vec{x}}^p = \Sigma_{\vec{x}}^a - \Sigma_{\vec{x}}^a \mathbf{H}^H \left( \mathbf{H} \Sigma_{\vec{x}}^a \mathbf{H}^H + \Sigma_{\vec{w}}^a \right)^{-1} \mathbf{H} \Sigma_{\vec{x}}^a. \quad (4.43)$$

## 4.6 Bayesian Cramer-Rao Bound

The **BCRB** (*Bayesian Cramer-Rao Bound*) defines a physical lower bound for **MSE** performance, which is helpful to classify whether a given estimator attains or not this criteria. Since all our information is embodied in the observed data and, eventually, in our prior knowledge about the unknown parameter, the estimation accuracy depends directly on its **PDFs** [84]. The **BCRB** is defined as a lower bound for the **MSE** matrix and it is related to the inverse of the **BFIM** (*Bayesian Fisher Information Matrix*)  $\mathcal{I}_B$  [85] by

$$\mathbf{E}_{\text{BCRB}} \geq \mathcal{I}_B^{-1}, \quad (4.44)$$

where the matrix inequality means that  $\mathbf{E}_{\text{BCRB}} - \mathcal{I}_B^{-1}$  is a non-negative definite matrix. The elements of  $\mathcal{I}_B$ , whose row and column indexes are given by the subscripts  $p$  and  $q$ , respectively, are obtained by

$$[\mathcal{I}_B]_{p,q} = -\mathbf{E} \left\{ \frac{\partial^2 \ln f_{\vec{y}|\vec{x}}}{\partial x_p \partial x_q} \right\} - \mathbf{E} \left\{ \frac{\partial^2 \ln f_{\vec{x}}}{\partial x_p \partial x_q} \right\}. \quad (4.45)$$

From the linear model in (4.1), replacing the corresponding **PDFs**

$$f_{\vec{y}|\vec{x}} = \pi^{-1} \det(\boldsymbol{\Sigma}_{\vec{w}})^{-1} \exp \left[ -(\vec{y} - \mathbf{H}\vec{x})^H \boldsymbol{\Sigma}_{\vec{w}}^{-1} (\vec{y} - \mathbf{H}\vec{x}) \right] \quad (4.46)$$

and

$$f_{\vec{x}} = \pi^{-1} \det(\boldsymbol{\Sigma}_{\vec{x}})^{-1} \exp \left[ -(\vec{x} - \vec{\mu}_{\vec{x}})^H \boldsymbol{\Sigma}_{\vec{x}}^{-1} (\vec{x} - \vec{\mu}_{\vec{x}}) \right] \quad (4.47)$$

in (4.45), allows to define the **BCRB** as

$$\mathbf{E}_{\text{BCRB}} = \left( \boldsymbol{\Sigma}_{\vec{x}}^{-1} + \mathbf{H}^H \boldsymbol{\Sigma}_{\vec{w}}^{-1} \mathbf{H} \right)^{-1}. \quad (4.48)$$

## 4.7 Analysis on Linear Estimators

To showcase the properties of the linear estimators under investigation, we present a numerical example. The objective is to assess and compare the resulting **MSE** in estimating four distinct random variables, each corresponding to a specific scenario. These scenarios have been carefully selected to facilitate a clear visualization of their distinct biases. In this sense, it is sufficient to analyze the **LMMSE** estimator and its unbiased version **CWCU-LMMSE**. The analysis is complemented by a complexity comparison for all presented estimators as a function of their respective cost sensitive parameters.

Consider a linear system as in (4.1) with  $p=q=4$ . The elements of  $\mathbf{H}$ ,  $\vec{x}$  and  $\vec{w}$  are mutually independent,  $\vec{w} \sim \mathcal{CN}(\vec{\mathbf{0}}, \boldsymbol{\Sigma}_{\vec{w}})$ , for  $\text{diag}(\boldsymbol{\Sigma}_{\vec{w}}) = [0.01, 0.01, 0.05, 0.05]$ ,  $\vec{x} = \{e^{j\pi/4}, e^{j3\pi/4}, e^{j5\pi/4}, e^{j7\pi/4}\} + e^{j(2\varphi-1)\pi/4}$ , with variance  $\boldsymbol{\Sigma}_{\vec{x}} = \mathbf{I}$  and  $\varphi = 1, \dots, q$  is a

discrete random variable with uniform distribution. Here,  $\vec{\mathbf{x}}$  was defined in order to position each random variable on different quadrants of a complex plane for an easy visual identification regarding on biasedness property of each estimator. The proposed transformation matrix  $\mathbf{H} = \text{diag}([1, 0.5, 1, 0.5])$  was built in order to allow the investigation of the **MSE** in some specific cases, varying from unitary transform coefficient and lower noise energy to low scaling factor with high noise variance. Table 7 outlines the proposed cases of study.

Table 7 – Proposed cases for the estimation analysis.

Case	Scaling Factor	Noise Energy	Known rv	Est. rv
1	High	Low	$y_1$	$\hat{x}_1$
2	Low	Low	$y_2$	$\hat{x}_2$
3	High	High	$y_3$	$\hat{x}_3$
4	Low	High	$y_4$	$\hat{x}_4$

The **LMMSE** and **CWCU-LMMSE** estimators were simulated for the proposed cases following the instructions presented in Algorithms 1 and 3. Table 8 summarizes the most relevant results for the performance analysis of the estimators considered in this example. Columns 2, 3 and 4 present the diagonal components of the obtained equalization matrix  $\mathbf{W}$ , the offset vector  $\mathbf{z}$  and the diagonal elements of the resulting **MSE** matrix  $\Sigma_{\vec{\mathbf{x}}}^{\text{p}}$ , respectively. Each element corresponds, from left to right, to the proposed cases 1 to 4, in this order.

Table 8 – Linear estimation example summary.

Estimator	$\text{diag}(\mathbf{W})$	$\mathbf{z}$	$\text{diag}(\Sigma_{\vec{\mathbf{x}}}^{\text{p}})$
LMMSE	[0.99, 1.92, 0.95, 1.67]	$[0.01 + 0.01j, -0.05 + 0.05j, -0.07 - 0.07j, 0.24 - 0.24j]^T$	[0.01, 0.04, 0.05, 0.17]
CWCU-LMMSE	[1.00, 2.00, 1.00, 2.00]	$[0.00 + 0.00j, 0.00 + 0.00j, 0.00 + 0.00j, 0.00 + 0.00j]^T$	[0.01, 0.04, 0.05, 0.20]

Figures 24a and 24b illustrate intensity charts of the relative frequencies for each estimates in the complex plane. High incidence values are marked in red, while low occurrences are plotted in blue. The  $\times$  markers indicate possible values assumed by the unknown vector  $\vec{\mathbf{x}}$ . In the top right quadrant, the intensity color plot for the random variable  $x_1$  is shown, corresponding to the proposed case 1 from Table 7 and, in counterclockwise direction, the remaining quadrants illustrate the resulting estimation of  $x_2$ ,  $x_3$  and  $x_4$ , respectively, related to cases 2, 3 and 4, in this order. Figures 24a and 24b reproduce, respectively, the results for the **LMMSE** and **CWCU-LMMSE** estimators.

For the case 1, where the scaling factor equals one and the **SNR** is high, all estimators perform equally in terms of the **MSE**. This result is also observed for cases 2 (low scaling factor and high **SNR**) and case 3 (high scaling factor and low **SNR**). For case 4,

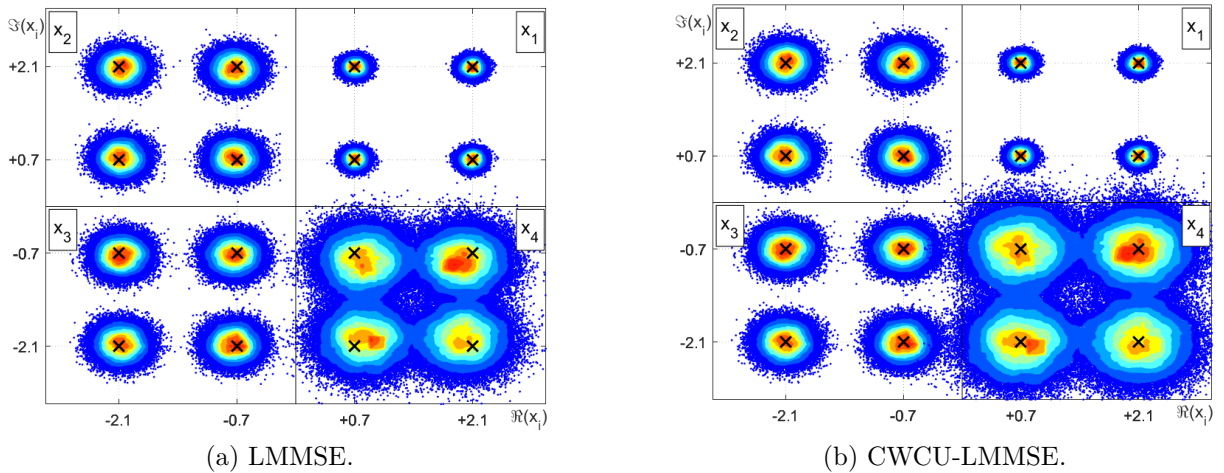


Figure 24 – Intensity chart for the complex random variables estimation.

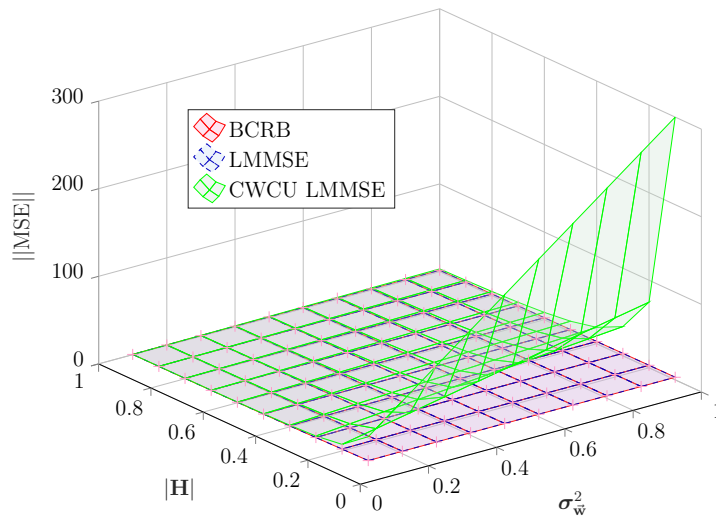


Figure 25 – MSE versus BCRB for the investigated linear estimators.

with low scaling factor and low SNR, the MSE increases in relation to other cases. In this situation, one can observe that the LMMSE estimator, whose restriction relies only on the linearity constraint, achieve the smallest MSE. The CWCU-LMMSE estimator cannot outperform the LMMSE estimator in a MSE sense since it has additional constraints. However, the CWCU-LMMSE estimator features its inherent conditional unbiased property, which is evidenced for study case 4 according to Figure 24b. The CWCU-LMMSE has its estimates centered around the true random variable events, since this estimator holds the unbiased constraint. In contrast, the LMMSE introduce a small bias towards the prior mean, avoiding noise enhancement while attaining the MMSE.

Another form to evaluate the performance of these estimators is comparing their MSE against the BCRB. Figure 25 illustrates this comparison for different values of a scalar channel gain and noise variance.

As expected, the CWCU-LMMSE does not attain the BCRB and shows low per-

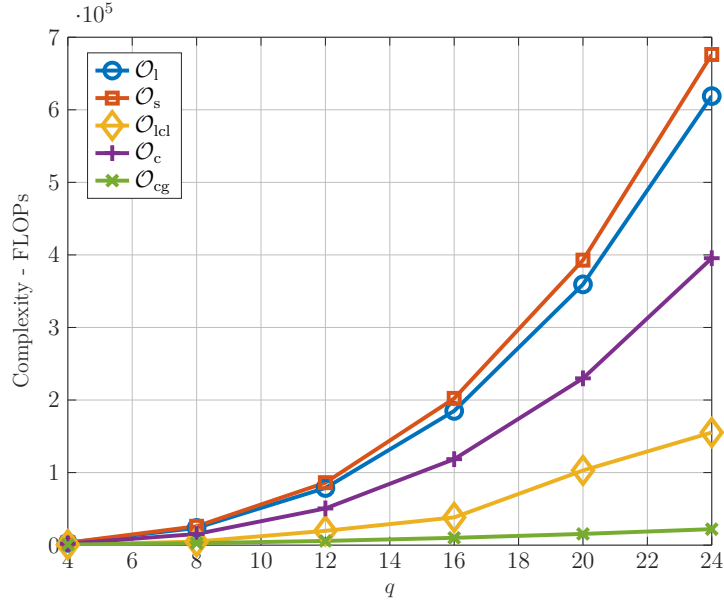


Figure 26 – FLOP counting for the presented linear estimators.

formance in terms of **MSE** under intense noise enhancement (high noise variance and low channel gain). Although the **LMMSE** estimator attains the **BCRB** and are considered optimal in a Bayesian sense, this does not necessarily means that the resulting **BER** on detection applications would be minimized. Actually, in this case, the **CWCU-LMMSE** have an improved performance since this estimator better fits the equalized data to the constellation grid prior the detection [58].

The complexity comparison is performed considering the computational cost of each presented estimator and its low complex variances. It is also considered a linear system in the form of (4.1), whose transform matrix  $\mathbf{H}$  has dimension  $p \times q$ , with  $p=q=zs$ ,  $s=\{1, \dots, 6\}$  and  $z=4$ , holding the special features required by each estimator function.

In Figure 26, we have the **FLOPs** accounting as function of system dimension  $q$ . For iterative methods, a single iteration cost is considered. Figure 26 confirms that estimating both expectation and variance parameters using the **STPD** is inefficient once its complexity  $\mathcal{O}_s$  is dominated by additional inter-matrix products. Both  $\mathcal{O}_l$  and  $\mathcal{O}_c$ , respectively the **LMMSE** and its **CWCU** unbiased version, follow the aforementioned cubic complexity growth with system dimension, although the **CWCU** being more efficient as this method replaces some matrix operations by a real weighting vector. The low complexity procedures indeed achieve a noticeable economy in terms of **FLOPs** when compared to their reference estimators. The Band-diagonal Low Complexity **LMMSE**, given by  $\mathcal{O}_{lcl}$ , achieves a quasi-linear in  $q$  computational cost. The **CG**-based **CWCU-LMMSE** presents an efficient complexity  $\mathcal{O}_{cg}$  for time-frequency conversion estimation assuming that both a-priory and posterior covariance matrices are diagonal. Its is worth to mention that the complexity reduction only takes place if the number of required iterations are kept low. Fortunately, according to [1], no more than a few iterations are

necessary to achieve proper results.

## 4.8 Summary

This section reviewed established linear estimation methods, highlighting the popular **LMMSE** and the **STPD** estimators. Focusing on digital communication, particularly the linear estimation of a discrete **RV** from a finite set of symbols in a mapping constellation, the **CWCU-LMMSE** and its low-complexity variants were detailed. These methods are fundamental for reducing the computational cost of **NO GFDM** detection to levels comparable to **OFDM**. Next chapter introduces effective detection techniques for data recovery in the system described by (3.5) and its equivalent factorized subsystems. Most of these detectors are based on the estimation concepts discussed here and reviewed in [58].

## 5 Detection Techniques

The detection procedure involves making a decision from a countably finite set of hypotheses based on an established criterion. Another interesting example in digital communication system is discrete data detection. In this case, the detector must choose one of the  $M_c$  possible data symbols from a discrete sample space (or constellation) using either the maximum likelihood or minimum distance criteria [86]. Since these topics are widely studied, the number of different techniques available in the literature can be overwhelming. This chapter compiles a list of recent studies and reviews for those interested, as detailed below.

An extensive survey on detection algorithms related to massive MIMO can be found in [87], where well-known linear detectors, including linear equalizers and suitable iterative methods as alternatives to avoid matrix inversion, are characterized according to its performance and complexity profiles. This reference also chronologically lists pertinent publications on MIMO subject. Similarly, in [79], low complexity linear detectors employing different numerical solutions for the large matrix inversion problem are evaluated, comparing its respective estimated computational cost and resource utilization in a system level deployment.

An accessible overview encompassing the state-of-the-art solutions to the detection problem is available in [88]. Prominent linear equalizers and detectors are investigated in [89], presenting BER performance analysis and computational complexity comparison under the assumption of different channel correlation scenarios. In [90], the SD is examined, presenting the respective complexity in terms of the number of visited nodes, culminating in the definition of lower and upper bounds for the computational cost given the channel matrix dimension, constellation size and SNR.

This chapter focuses on a critical task of mobile communication PHY, encompassing detection and non-linear estimator schemes designed to overcome the limitations of linear estimators in specific applications, such as SM-MIMO [91]. The remainder of this chapter describes a detection model for the factorized SM-MIMO system and reviews classical detection processes, including their derivations and estimated complexities. It concludes with a performance analysis and a comparison of these complexities. This review starts describing the MLD, taking it as a reference for performance and complexity analysis. In order to overcome the prohibitive computational cost on realizing the ML procedure, the so called GAD is considered. In sequence, the SD and interference-cancellation-based detectors are formally addressed, including the ordered SIC and PIC. Finally, under the conditions of a hypothetical scenario, this chapter evaluates and com-

compares these detection schemes, taking the [ML](#) lower bound as a reference.

From this point forward, whenever possible and without loss of generality, the generic linear subsystem model from (3.26) is considered, whose dimension is parameterized according with Table 6. However, the full system model in (3.13) can also be adopted, with necessary adjustments to the system dimensions. It is also assumed that  $\vec{\mathbf{d}}$  obeys an equiprobable discrete distribution of the elements in  $\mathcal{C}$ .

## 5.1 Maximum Likelihood Detector

As presented in Chapter 3, the detection task at the receiver is basically a decision process applied on the received signal in order to recover the transmitted message. Assuming a linear system in the form of (3.26), under the common assumption that all code words from  $\mathcal{C}$  are equiprobable, the [ML](#) criteria seeks to minimize the [ED](#) (*Euclidean Distance*) between the observed signal and a given hypothesis [92], thus

$$\hat{\mathbf{d}}_{\text{ML}} = \underset{\vec{\mathbf{d}}_{\kappa}}{\operatorname{argmin}} \|\vec{\mathbf{y}} - \mathbf{H}\vec{\mathbf{d}}_{\kappa}\|^2, \quad (5.1)$$

where  $\vec{\mathbf{d}}_{\kappa} \in \mathcal{C}^q$  is the  $\kappa$ th data sequence hypothesis and  $\kappa = 1, \dots, M_c^q$ , which contains all possible cross combinations of the elements in  $\mathcal{C}$ , taken  $q$  at a time. In general, finding the optimal solution requires an exhaustive search over all  $M_c^q$  hypotheses [93], yielding to a  $q$ -exponential order problem. Each hypothesis contains  $q$  discrete symbols and the [MLD](#) can be seen as a lattice structure consisting of  $qM_c^q$  nodes. When the elements of  $\vec{\mathbf{d}}$  are continuous Gaussian [RVs](#) representing a linear transformation of a discrete data symbol sequence, it is essential to incorporate this transformation matrix into  $\mathbf{H}$ . This ensures that the hypotheses under test are formed only by combinations of the elements from the set  $\mathcal{C}$ . The Algorithm 7 summarizes the [ML](#) detection procedure whose complexity is mainly dictated by the squared [ED](#) computation of each hypothesis at line 3.

---

### Algorithm 7 Maximum Likelihood Detector

---

**Result:**  $\hat{\mathbf{d}}_{\text{ML}}$

- 1:  $\rho^2 = \infty$
  - 2: **for**  $\kappa \leftarrow 1$  to  $M_c^q$  **do**
  - 3:      $\varrho_{\kappa}^2 = \|\vec{\mathbf{y}} - \mathbf{H}\vec{\mathbf{d}}_{\kappa}\|^2$
  - 4:     **if**  $\varrho_{\kappa}^2 < \rho^2$  **then**
  - 5:          $\rho^2 = \varrho_{\kappa}^2$
  - 6:          $\hat{\mathbf{d}}_{\text{ML}} = \vec{\mathbf{d}}_{\kappa}$
  - 7:     **end if**
  - 8: **end for**
-

In Algorithm 7,  $\varrho_{\kappa}^2$  is the squared ED of the  $\kappa$ th hypothesis. The complexity of computing this algorithm is

$$\mathcal{O}_{\text{ML}}(M_c^q(8pq + 3p + 2)). \quad (5.2)$$

Given an alphabet with  $M_c=16$  distinct elements and  $q=8$ , the ML detector needs to verify a total of  $4.29 \times 10^9$  hypotheses in order to retrieve the transmitted data symbol sequence. Although optimal, ML detection often results in prohibitive complexity [93]. The energy efficiency of ML detection is commonly used as a benchmark for evaluating alternative detectors. However, the computational effort required for simulations might be impractical. To overcome this challenge, we can consider employing a hypothetical GAD.

### 5.1.1 Genie-aided Detector

The GAD access additional transmission side information carried to the detector through a non-dispersive and unitary gain parallel channel, representing the genie [94]. In the receiver side, upon decision of the transmitted data, the ED  $\varrho_R$  between the detected information  $\hat{\mathbf{d}}$  and received signal  $\vec{\mathbf{y}}$  is compared with the ED  $\varrho_T$  of the transmitted data  $\vec{\mathbf{d}}$  and  $\vec{\mathbf{y}}$ . If  $\varrho_R < \varrho_T$ , an optimal MLD would also detect the wrong data sequence, leading to a frame error. On the contrary, when  $\varrho_R \geq \varrho_T$ , it is assumed that the MLD would have found the correct data sequence and the detector under analysis not, accumulating a frame error. This procedure overestimates the MLD performance yielding to a lower bound on ML detection [1]. The validity of this bound is a direct consequence of the fact that any composite hypothesis test cannot perform better than the corresponding perfect measurement test [95]. Algorithm 8 is used to evaluate the MLD FER lower bound employing a GAD.

---

#### Algorithm 8 Genie-Aided Detector

---

**Initialize:**

- 1: total\_frames = 0;
- 2: frame\_error = 0;

**For each iteration results:** FER<sub>ML</sub>

- 3: total\_frames = total\_frames + 1;
  - 4:  $\varrho_R = |\vec{\mathbf{y}} - \mathbf{H}\hat{\mathbf{d}}|$
  - 5:  $\varrho_T = |\vec{\mathbf{y}} - \mathbf{H}\vec{\mathbf{d}}|$
  - 6: **if**  $\varrho_R < \varrho_T$  **then**
  - 7:     frame\_error = frame\_error + 1;
  - 8: **end if**
  - 9: FER<sub>ML</sub> =  $\frac{\text{frame\_error}}{\text{total\_frames}}$
- 

Following sections present reduced complexity alternatives for the ML detection, some of them at the expense of sub-optimal performance.

## 5.2 Sphere Detector

The **SD** [96] is an algorithm to address the non deterministic polynomial-time hard integer least squares problem, able to achieve optimal **MLD** performance with an average polynomial complexity [97]. The principle of **SD** is to reduce the exhaustive search procedure over all possible code words carried out by the **MLD**. This is accomplished restricting the search only on hypothesis where the distance from one possible code word are within a predefined radius of a high-dimensional sphere, where each hypothesis can be seen as a path with sequentially interconnected nodes in a finite tree structure. Whenever a path segment reaches a cumulative distance that exceeds the sphere radius, this segment and all subsequent nodes are discarded, yielding to a variable complexity reduction [88].

In this way, depending only on the radius parameter  $\rho$ , a trade off between performance and complexity can be trimmed. If  $\rho$  is chosen sufficiently high and kept constant, all paths might be checked and the **SD** behaves just like the **MLD**. If  $\rho$  is too small, this can result in non eligible paths. In this situation, the procedure can be repeated with an increased radius. A practical approach is to initialize  $\rho = \infty$  or based on a code word given by a low complexity technique [98], e.g. the **ZF** or **MMSE** detectors [99] and update the radius whenever a better hypothesis is found during the search procedure. Just like in the **MLD** method, when the elements of  $\vec{\mathbf{d}}$  are continuous Gaussian **RVs** resulting from the linear transformation of a discrete data symbol sequence, it is crucial to integrate this transformation matrix into  $\mathbf{H}$ . This guarantees that the hypotheses being tested are composed exclusively by the elements from the set  $\mathcal{C}$ .

We start introducing the **HQR** factorization [100] expressed as  $\mathbf{QR} = \text{HQR}(\mathbf{H})$  for the full-rank matrix  $\mathbf{H}$ , where  $\mathbf{Q} \in \mathbb{C}^{p \times p}$  is an orthonormal matrix and  $\mathbf{R} \in \mathbb{C}^{p \times q}$  is an upper-triangular matrix. Left multiplying the received vector from (3.26) by  $\mathbf{Q}^H$  yields to

$$\tilde{\mathbf{y}} = \mathbf{Q}^H(\mathbf{QR}\vec{\mathbf{d}} + \vec{\mathbf{w}}) = \mathbf{R}\vec{\mathbf{d}} + \tilde{\vec{\mathbf{w}}}. \quad (5.3)$$

Since  $\mathbf{Q}$  is orthonormal, the noise distribution of (5.3) is still **AWGN** and the detection problem is equivalent to (5.1), including  $\vec{\mathbf{d}}_\kappa$  definition. Thus, the **SD** procedure yields to

$$\hat{\vec{\mathbf{d}}}_{\text{SD}} = \underset{\vec{\mathbf{d}}_\kappa}{\text{argmin}} \|\tilde{\mathbf{y}} - \mathbf{R}\vec{\mathbf{d}}_\kappa\|^2, \quad (5.4)$$

which can be addressed through a node-sequence search algorithm [101]. This structure resembles a spanning tree, with a root node located at the top layer  $\ell = q$ , spanning to  $M_c$  nodes in the immediately next layer  $\ell = q - 1$ . In this way, each node from an upper layer connects to  $M_c$  nodes in subsequent beneath layer. Each layer connection or path section is defined here as a segment. A series of segments connecting a root node to one of the  $M_c^q$  nodes at the final layer  $\ell = 1$  forms one distinct path among  $M_c^q$  possibilities. The total amount of nodes  $\tau$  in a certain spanning tree structure has a close relation with

the SD complexity and is expressed by

$$\tau = \sum_{\ell=1}^q M_c^\ell. \quad (5.5)$$

The SD executes a top-down search along the tree while computes the squared node distance  $\varrho_\ell^2$  at layer  $\ell$  under analysis. Thus,

$$\varrho_\ell^2 = \left| \tilde{y}_\ell - \sum_{l=\ell}^q \mathbf{R}_{\ell,l} \vec{\mathbf{d}}_{\kappa_l} \right|^2, \quad (5.6)$$

where  $\ell = q, \dots, 1$  is the layer index and  $\vec{\mathbf{d}}_{\kappa_l}$  is the  $l$ th element of the  $\kappa$ th hypothesis, chosen from the set  $\mathcal{C}$ . The scalar  $\mathbf{R}_{\ell,p}$  is one element of matrix  $\mathbf{R}$  and  $\tilde{y}_\ell$  is the corresponding  $\ell$ th element of same vector. When  $\varrho_\ell^2 > \rho^2$ , subsequent layers are pruned, leading the algorithm to move on next segment direction or beginning a new path search. It is worth to mention that, in order to avoid the square root in (5.6), this comparison can be evaluated over the squared distances.

Algorithm 9 describes the SD mechanism to find  $\hat{\mathbf{d}}_{\text{SD}}$  employing a recursive function  $\text{SD}(\ell)$  along the tree search task. For simplicity, the algorithm initializes the parameter  $\rho^2 = \infty$ . Here, the variable  $s = 1, \dots, M_c$  is the segment or constellation symbol index for each node hypothesis test. It is also assumed that, when necessary, some parameters are global accessible inside the algorithm environment.

---

**Algorithm 9** Sphere Detector

---

**Result:**  $\hat{\mathbf{d}}_{\text{SD}}$

```

1:  $\mathbf{QR} = \text{HQR}(\mathbf{H})$ 
2:  $\vec{\mathbf{y}} = \mathbf{Q}^H \vec{\mathbf{y}}$ 
3:  $\rho^2 = \infty$ 
4:  $\ell = q$ 
5: function  $\text{SD}(\ell)$ 
6:   for  $s \leftarrow 1$  to  $M_c$  do
7:      $\vec{\mathbf{d}}_{\kappa_\ell} = \mathcal{C}_s$ 
8:      $\varrho_\ell^2 = \left| \tilde{y}_\ell - \sum_{l=\ell}^q \mathbf{R}_{\ell,l} \vec{\mathbf{d}}_{\kappa_l} \right|^2$ 
9:     if  $(\sum_{l=\ell}^q \varrho_l^2 < \rho^2)$  then
10:      if  $(\ell == 1)$  then
11:         $\hat{\mathbf{d}}_{\text{SD}} = \vec{\mathbf{d}}_{\kappa}$ 
12:         $\rho^2 = \sum_{l=1}^q \varrho_l^2$ 
13:      else
14:         $\text{SD}(\ell - 1)$ 
15:      end if
16:    end if
17:  end for
18: end function

```

---

The task of finding an exact expression for the complexity of the SD is not trivial once it depends not only on the transmission channel matrix dimension but also on the

sphere radius, which is, in turn, a function of the SNR. Indeed, the SD FLOPs account is a random variable with expected polynomial complexity. In the worst case scenario, it can reach exponential complexity [97]. Considering the worst case, where all nodes of every segment are visited, the resulting complexity is given by

$$\mathcal{O}_{\text{SD}} = \mathcal{O}_{\text{HQR}} + \mathcal{O}_{\vec{y}} + M_c^q \sum_{\ell=1}^q \mathcal{O}_{\text{node}}(\ell), \quad (5.7)$$

where  $\mathcal{O}_{\text{HQR}}$  is the complexity of the HQR factorization at line 1 of Algorithm 9, given by Table 1, and the second term refers to the matrix-vector product in line 2. The last term in (5.7) represents the complexity of the recursive function  $\text{SD}(\ell)$ , with  $M_c^q$  segments in the spanning tree structure. The complexity of one node inspection at layer  $\ell$  is given by

$$\mathcal{O}_{\text{node}}(\ell) = \sum_{l=\ell}^q 8(q-l) + 11. \quad (5.8)$$

With the aid of the identities given in Table 2, (5.8) and (5.7) can be solved yielding to a complexity upper bound for the SD algorithm given by

$$\max(\mathcal{O}_{\text{SD}}) = \frac{2q^2(3p-q)}{3} + 2p(4p-1) + \frac{M_c^q(8q^3 + 33q^2 + 25q)}{6}, \quad (5.9)$$

where the last term is the predominant computational cost associated with the recursive  $\text{SD}(\ell)$  function. Thus

$$\mathcal{O}_{\text{SD}} \left( \frac{M_c^q(8q^3 + 33q^2 + 25q)}{6} \right). \quad (5.10)$$

At a first glance, the worst case scenario for the SD algorithm exhibits higher complexity when compared with the MLD. This happens due the fact that every visited node requires the computation of the squared partial distances  $\varrho_\ell^2$ . However, as the SD is able to reduce its complexity to a polynomial degree, thanks to its segment pruning behavior based on partial distances, in practice, the SD complexity is smaller than the MLD, specially at high SNR. Indeed, the MLD exhibits an exponential complexity since all hypotheses are always evaluated.

There are also some slight variants of the SD algorithm that seeks to achieve a reduced [102] or even fixed complexity [88] at the cost of sub-optimal performance. In [103], some suitable approximations and simplifications are admitted, leading to implementations with affordable complexities. Next subsection introduces an ED computation based on affine transform modulation. It shows a reasonable potential to improve the efficiency on practical SD hardware implementation.

### 5.2.1 Low Complexity SD-ATM

This subsection proposes a reduced complexity and widely compliant SD algorithm, suitable to low constellation orders and intermediary SM-MIMO, which is the case

of future networks of autonomous and power restrained devices, e.g., **IoT** applications. The proposed scheme is capable of achieving the **ML** performance in terms of **BER** with practical advantages in hardware synthesis implementation of the **SD** [104].

To this end, the **ATM** concept is considered in order to describe a sequence of **QAM** (*Quadrature Amplitude Modulation*) symbols as the **AT** (*Affine Transform*) of its corresponding bit labels. In this way, the received vector can be seen as a linear transformation of the transmitted binary information plus the receiver noise [105]. The complexity reduction relies on a subtle simplification in the cost dominant inner function of every **SD** algorithm, the **ED** computation at each visited node of the tree search structure.

The proposed detection scheme takes advantage on computing each hypothesis **ED** over groups of bits per symbol, sparing at least one complex multiplication since one of the involved operators is binary. In this sense, when the binary coefficient assumes the digit zero, the result is null, otherwise, when the coefficient is unitary, the result is the proper value of the second operator. Assuming a hardware synthesis, we can exploit the knowledge that one of the operators is binary and replace the complex inner product in the extensively accessed core of the **SD** algorithm by multiplexers and adders. Hence, this proposal reduces the demanded resources in **FPGA** (*Field Programmable Gate Array*) devices, requiring a smaller silicon area and improving the maximum operation frequency when considering the **SD-ATM** implementation.

Usually, there is no linear function, or, to be more precise, a vector scaling factor that could address the bit sequence mapping to the transmitted signal, once the bit-to-**QAM** is a non-linear operation. Nevertheless, an **AT** can, with some restrictions, be employed in this task when the real and imaginary parts vary linearly with the corresponding bit labeling. The **ATM** operates on the input data bit vector  $\vec{\mathbf{b}} \in \mathbb{B}^{\mu q \times 1}$ , vertically stacked with the least significant bit first, performing scaling and translation functions to obtain a sequence of data symbols  $\vec{\mathbf{d}} \in \mathbb{C}^{q \times 1}$  given in general form by

$$\vec{\mathbf{d}} = \mathbf{T}\vec{\mathbf{b}} + \vec{\mathbf{z}}, \quad (5.11)$$

where  $\mathbf{T} \in \mathbb{C}^{q \times \mu q}$  is a sparse matrix,  $\vec{\mathbf{z}} \in \mathbb{C}^{q \times 1}$  is a complex vector and  $q$  is the number of data resources in a factorized **SM-MIMO** subsystem, similar to (3.26). The parameters  $\mathbf{T}$  and  $\vec{\mathbf{z}}$  are defined according to the chosen constellation set, thereby

$$\mathbf{T} = \begin{cases} 2\mathbf{I}, & \text{for } M_c = 2, \\ 2(\mathbf{S}_1 - \mathbf{S}_0\mathbf{j}), & \text{for } M_c = 4, \\ 4\mathbf{S}_2 + 2\mathbf{S}_1 - 2\mathbf{S}_0\mathbf{j}, & \text{for } M_c^{(\text{bin})} = 8, \\ 4\mathbf{S}_2 + 2\mathbf{S}_1 + (2\mathbf{S}_1 - 4\mathbf{S}_0)\mathbf{j}, & \text{for } M_c^{(\text{non-rect})} = 8, \end{cases} \quad (5.12)$$

and

$$\vec{z} = \begin{cases} -\vec{1}, & \text{for } M_c = 2, \\ (-1 + 1j)\vec{1}, & \text{for } M_c = 4, \\ (-3 + 1j)\vec{1}, & \text{for } M_c = 8, \end{cases} \quad (5.13)$$

where the superscripts (bin) identifies a rectangular constellation with binary mapping, while the superscript (non-rect) characterizes a non-rectangular constellation with gray mapping. If the superscript is omitted, gray mapping is considered. Here,  $\mathbf{S}_\iota$  is a sparse binary matrix with dimension  $q \times \mu q$  for  $\iota = 0, \dots, \mu - 1$ , containing an unique unitary entry per row and zeros elsewhere, given by

$$\mathbf{S}_\iota[\ell, s] = \begin{cases} 1 & \text{at } s = \mu(\ell - 1) + \iota + 1, \text{ for } \ell = 1, \dots, q, \\ 0 & \text{otherwise.} \end{cases} \quad (5.14)$$

For example, considering  $q=3$ ,  $\mu=2$  and  $\iota=0$ , the corresponding bit 0 selection matrix is  $\mathbf{S}_0 = \begin{pmatrix} 1 & 0 & 0 & 0 & 0 & 0 \\ 0 & 0 & 1 & 0 & 0 & 0 \\ 0 & 0 & 0 & 0 & 1 & 0 \end{pmatrix}$ . If desired, constellation energy normalization can also be performed dividing (5.12) and (5.13) by  $\sqrt{\frac{\|\mathbf{C}\|^2}{M_c}}$ . Figure 27 illustrates the normalized constellations for  $M_c = \{2, 4, 8\}$  according to the definitions in (5.12) and (5.13).

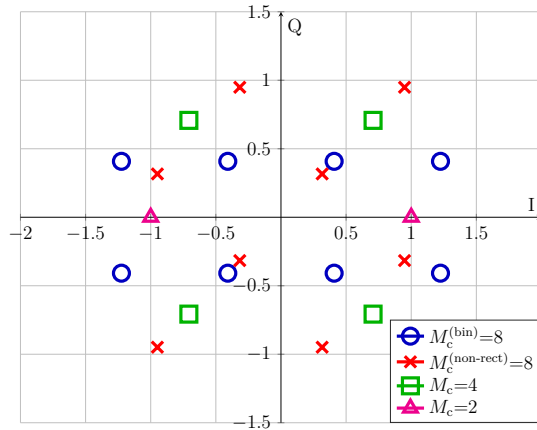


Figure 27 – Normalized Affine Transform constellations according to (5.12) and (5.13).

The complexity associated with the SD procedure given by Algorithm 9 is mainly ruled by the recursive SD( $\ell$ ) function and the internal ED computation at line 8. It is expected that the overall SD complexity can be significantly reduced if the ED computation, intensively accessed by the recursive function, could be simplified. This can be achieved by exploiting the ATM. Replacing (5.11) in (3.26) yields to

$$\vec{y} = \mathbf{H}\vec{z} + \mathbf{H}\mathbf{T}\vec{b} + \vec{w}. \quad (5.15)$$

Defining  $\vec{y}' = \vec{y} - \mathbf{H}\vec{z}$ , yields to a linear function of the transmitted bit sequence

$$\vec{y}' = \mathbf{H}\mathbf{T}\vec{b} + \vec{w}, \quad (5.16)$$

Again, employing the HQR factorization of  $\mathbf{H}$ , then, left multiplying (5.16) by  $\mathbf{Q}^H$  while replacing  $\mathbf{H}=\mathbf{QR}$ , allows one to define  $\mathring{\mathbf{R}} = \mathbf{RT}$ , with  $\mathring{\mathbf{R}} \in \mathbb{C}^{q \times \mu q}$ , leading to

$$\tilde{\mathbf{y}} = \mathbf{Q}^H(\mathbf{QRT}\vec{\mathbf{b}} + \vec{\mathbf{w}}) = \mathring{\mathbf{R}}\vec{\mathbf{b}} + \tilde{\vec{\mathbf{w}}}. \quad (5.17)$$

Since  $\mathbf{Q}$  is orthonormal, the noise distribution of (5.17) is still AWGN and the detection problem is equivalent to (5.3). Hence, the SD-ATM procedure performs

$$\hat{\mathbf{b}}_{\text{SD-ATM}} = \underset{\vec{\mathbf{b}}_\kappa}{\text{argmin}} \|\tilde{\mathbf{y}} - \mathring{\mathbf{R}}\vec{\mathbf{b}}_\kappa\|^2, \quad (5.18)$$

where  $\vec{\mathbf{b}}_\kappa = \mathcal{M}^{-1}(\vec{\mathbf{d}}_\kappa)$ , for  $\kappa = 1, \dots, M_c^q$ ,  $\mathcal{M}^{-1}$  is a function that performs QAM-to-bits demapping, taking  $\vec{\mathbf{d}}_\kappa$  as argument and resulting  $\vec{\mathbf{b}}_\kappa$  as the binary representation of one possible transmitted symbol sequence from the set  $\mathcal{C}^q$ . As  $\mathring{\mathbf{R}}$  still holds its triangular structure, (5.18) can be addressed through a node-sequence search algorithm. Note that  $\mathring{\mathbf{R}}$ , with elements  $\mathring{\mathbf{R}}_{\ell,l}$ , has  $(q+1-\ell)\mu$  non-zero entries at  $\ell$ th row, with  $\ell=1, \dots, q$  and  $l=1, \dots, \mu q$ , meaning that  $\mu$ -tuple bits are jointly detected along the searching procedure. The notation  $\mathring{\mathbf{R}}_{\ell,l|\vec{\mathbf{b}}_{\kappa_l}=1}$  represents the elements of the product  $\mathring{\mathbf{R}}\vec{\mathbf{b}}_\kappa$  whose corresponding coefficient  $\vec{\mathbf{b}}_{\kappa_l}$  is non-zero.

Algorithm 10 synthesizes the proposed detector, where  $\mathcal{C}[s]$  is the  $s$ th QAM symbol from the constellation set  $\mathcal{C}$ .

---

**Algorithm 10** Sphere Detector based on ATM
 

---

**Result:**  $\hat{\mathbf{b}}_{\text{sd}}$

```

1:  $\mathbf{QR} = \text{HQR}(\mathbf{H})$ 
2:  $\tilde{\mathbf{y}} = \mathbf{Q}^H(\vec{\mathbf{y}} - \mathbf{H}\vec{\mathbf{z}})$ 
3:  $\mathring{\mathbf{R}} = \mathbf{RT}$ 
4:  $\rho^2 = \infty$ 
5:  $\ell = q$ 
6: function SD( $\ell$ )
7:   for  $s \leftarrow 1$  to  $M_c$  do
8:      $\vec{\mathbf{b}}_{\kappa_{\mu(\ell-1)+1:\mu\ell}} = \mathcal{M}^{-1}(\mathcal{C}[s])$ 
9:      $\varrho_\ell^2 = \left| \tilde{y}_\ell - \sum_{l=\mu(\ell-1)+1}^{\mu q} \mathring{\mathbf{R}}_{\ell,l|\vec{\mathbf{b}}_{\kappa_l}=1} \right|^2$ 
10:    if  $(\sum_{l=\ell}^q \varrho_l^2 < \rho^2)$  then
11:      if  $(\ell == 1)$  then
12:         $\hat{\mathbf{b}}_{\text{SD-ATM}} = \vec{\mathbf{b}}_\kappa$ 
13:         $\rho^2 = \sum_{l=1}^q \varrho_l^2$ 
14:      else
15:        SD( $\ell - 1$ )
16:      end if
17:    end if
18:  end for
19: end function

```

---

The Algorithm 10 complexity is mainly dictated by the inner recursive function  $\text{SD}(\ell)$ , dominated by the ED computation at line 9, followed by the layer distance summation at line 10, a common step in both conventional and proposed SD algorithms. Hence, the investigation of the node complexity based only on line 9 is sufficient for comparison. Assuming the worst case scenario, where the tree search structure is entirely explored, the complexity follows (5.7) while the computational cost comprising one node inspection at layer  $\ell$  is given by

$$\mathcal{O}_{\text{node}}(\ell) = \sum_{l=\ell}^q 2\mu(q-l) + 3, \quad (5.19)$$

with the aid of some useful summation identities from Table 2, (5.19) can be solved, approximating the complexity upper bound for Algorithm 10 by

$$\mathcal{O}_{\text{SD-ATM}} \left( \frac{M_c^q (2\mu q^3 + (6\mu + 9)q^2 + (4\mu + 9)q)}{6} \right). \quad (5.20)$$

A complexity comparison can be evaluated taking the second derivative of the ratio between (5.20) and (5.10) w.r.t.  $q$ , leading to

$$\epsilon_\mu = \frac{\partial^2(\mathcal{O}_{\text{SD-ATM}}/\mathcal{O}_{\text{SD}})}{\partial^2 q} = \frac{2\mu}{8}. \quad (5.21)$$

For  $\epsilon_\mu < 1$ , this implies that  $1 \leq \mu < 4$ , constraining  $M_c$  for the constellation sets with 2, 4 or 8 symbols, where a corresponding theoretical complexity reduction down to 25%, 50% and 75% are expected for the proposed algorithm, taking the conventional SD as a reference. Following subsection summarizes the performance and complexity comparison between the conventional SD and the proposed SD-ATM.

## 5.2.2 Comparison of the SD Algorithms

In [104], a multi-user uplink scenario employing intermediary order SM-MIMO system with  $N_R=N_T=4$  and  $\mu=\{1, 2, 3\}$  is considered. From Table 6, each factorized orthogonal subsystem has dimension  $p \times q$  s.t.  $p=q=N_T$ . The BER performance and detection complexity of a single transmission resource in a CP-OFDM system is evaluated, assuming perfect synchronization and CSIR. The simulation parameters are given in Table 9.

Figure 28 illustrates the resulting BER Monte Carlo simulation, taking a conventional gray mapping SD as a reference. It is clear that the proposed SD-ATM algorithm presents no measurable performance loss compared to the conventional SD when  $\mu=1$  and 2, while attaining the ML. In these cases, the SD-ATM allows gray mapping constellations. For  $\mu=3$ , we have two distinct results. When the proposed algorithm, for the same

Table 9 – Parameters used in SD simulation.

Parameter	Symbol	Value
CIR length	$L$	16 samples
CP length	$N_{\text{CP}}$	$L$
$k$ th subcarrier frequency response	$\mathbf{H}[k]$	$\mathcal{CN}(\mathbf{0}^{p \times q}, \mathbf{1}^{p \times q})$
Number of subcarriers	$K$	64 subcarriers
bit-symbol energy ratio	$E_b/E_s$	$(K + N_{\text{CP}})/\mu K$

rectangular 8-QAM symbol disposal of the reference but employing binary mapping, a constant performance loss of approximately 0.3 dB is observed. On the contrary, for the SD-ATM employing a custom non-rectangular constellation with gray mapping, as illustrated by Figure 27, no performance loss is observed and both algorithms achieves the MLD BER.

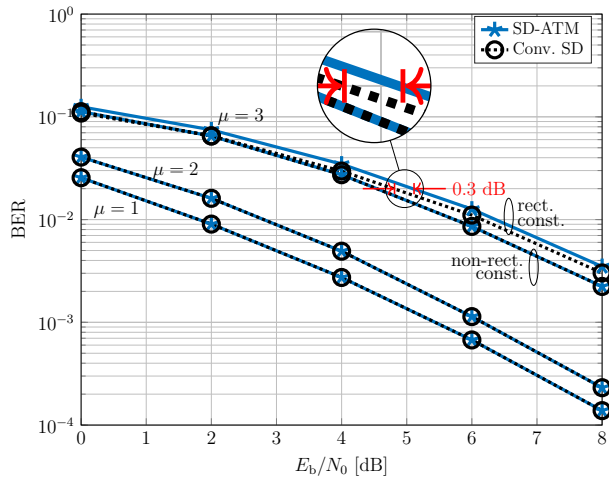


Figure 28 – SD comparison of the SM-MIMO BER performance in FSC.

Figure 29 presents a simplified block diagram of the inner product required by the ED computation for both analyzed algorithms. The proposed structure is targeted to a balanced optimization on area and speed. The inner product for the conventional SD requires an input stage employing parallel multipliers to implement the complex product between the elements of  $\mathbf{R}$  and  $\vec{\mathbf{d}}$ . For the proposed SD-ATM algorithm, it requires only the sequential accumulator stage once the product between the complex entries of  $\mathbf{R}$  by the binary coefficients of  $\vec{\mathbf{b}}_{\kappa}$  can be replaced by a common 2:1 multiplexer that selects between a null result, for  $\vec{\mathbf{b}}_{\kappa_l} = 0$  or the current input entry  $\mathbf{R}_{\ell,l}$  when  $\vec{\mathbf{b}}_{\kappa_l} = 1$ , reducing the complexity on the ED computation as stated in subsection 5.2.1. This is exactly the central point of the proposed algorithm and where relies the main contribution in [104].

In order to analyze and compare the concept illustrated in Figure 29, a functional simulation of the inner product for both algorithms was synthesized and evaluated, employing a HDL (*Hardware Description Language*) with two different numerical repre-

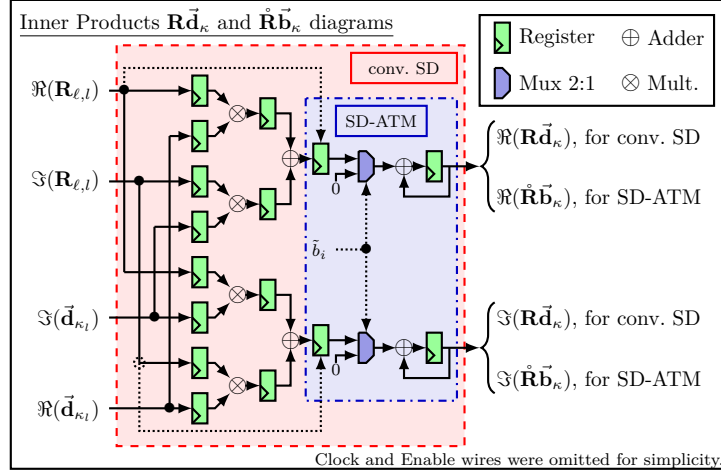


Figure 29 – Block diagram of the inner product in the ED computation for the conventional and proposed SD algorithms.

representations: an **FXP18** (*18-bit Signed Fixed Point*) and the IEEE 754 32-bit **FP** (*Float Point*). It considers an Intel **FPGA** from the family Cyclone V, more specifically the 5CSEMA6F31. Table 10 relates the resource allocation usage for each synthesized entity in terms of the number of **ALMs** (*Adaptive Logic Modules*), **ALUTs** (*Adaptive Look-up Tables*), **DLRs** (*Dedicated Logic Registers*) and **DSPs** (*Digital Signal Processings*). Moreover, the maximum achievable operational frequency  $F_{\max}$  and the number of required clock periods to process the inner product operation were also obtained. These results allows to define the practical complexity reduction  $\hat{\epsilon}_\mu$  as the weighted average of the so called area and latency parameters. Analyzing the obtained results for both fixed and float point approaches, when  $\mu=1, 2$  and  $3$ , taking the theoretical complexity reduction estimates given by (5.21) as a reference, allows one to confirm that the proposed **SD** algorithm based on **ATM** close achieves the theoretical reduction gain for the **FP** implementation and are indeed capable to even surpass in almost two times the foreseen complexity reduction for the **FXP18**. In **FXP18** approach, area and latency are both improved at the same time. On the other hand, in the **FP** implementation, only the theoretical foreseen area reduction occurs once the latency related on **FP** multiplication and addition are quite similar.

Table 10 – Estimated resource utilization of the inner product in the SD-ATM ED computation considering an Intel Cyclone V FPGA 5CSEMA6F31C7.

Inner product entities	Area parameters				Latency parameters		$\hat{\epsilon}_\mu = \frac{1}{2} \frac{(\sum \text{area} \times \text{Latency} / F_{\max})_{\text{SD-ATM}}}{(\sum \text{area} \times \text{Latency} / F_{\max})_{\text{conv. SD}}}$		
	ALMs	ALUTs	DLRs	DSPs	$F_{\max}$ [MHz]	Latency [T <sub>clk</sub> ]	$\mu = 1$	$\mu = 2$	$\mu = 3$
$\mathbf{R}\vec{d}_k$ FXP18 (conv. SD)	677.5 (1.62%)	1182 (1.41%)	261 (0.22%)	0 (0%)	77.975	$4(q - \ell + 1)$			
$\mathbf{R}\vec{b}_k$ FXP18 (SD-ATM)	45.0 (0.11%)	44 (0.05%)	116 (0.01%)	0 (0%)	177.465	$2\mu(q - \ell + 1)$	0.158	0.268	0.378
$\mathbf{R}\vec{d}_k$ FP (conv. SD)	1310.0 (3.12%)	2032 (2.42%)	1014 (0.87%)	4 (3.57%)	71.925	$10(q - \ell + 1)$			
$\mathbf{R}\vec{b}_k$ FP (SD-ATM)	567.5 (1.35%)	876 (1.05%)	377 (0.32%)	0 (0%)	79.430	$4\mu(q - \ell + 1)$	0.390	0.571	0.752

These results demonstrate that the complexity of the cost dominant function in the **SD** reduces to 39%, 57% and 75%, in the **FP** case, for  $\mu=1, 2$  and  $3$ , respectively, when employing the **SD-ATM** approach. In the **FXP18** case, a complexity reduction of

approximately 6 times (16%), 4 times (27%) and 3 times (38%) is observed, in comparison with the regular **ED** computation of the conventional **SD**. This happens because, in fixed point arithmetic, adders are, in general, less expensive than multipliers, from the hardware implementation perspective and are, often, capable of achieving higher operational frequencies. These results suggest that the proposed **SD** algorithm employing the **ATM** is a suitable detection scheme for low order modulation systems.

The following section focuses on **SIC** technique, aiming to reduce even further the detection problem complexity and improve the energy efficiency.

### 5.3 MMSE-SIC Detector

The **MMSE-SIC** is a non-linear estimator that attempts to improve interference cancellation in applications such as **SM-MIMO**, i.e. **BLAST** (*Bell Laboratories Layer Space-Time*) variances [17].

Basically, this method makes partial decisions w.r.t. the transmitted data sequence, then, it performs successive interference cancellation based on already decided symbols along the remaining information detection. Here, the well known sorted **SIC** [106] is considered. This method starts reorganizing the factorized subsystem from (3.26) in ascending order of **SNR**, permuting the rows of received sequence  $\vec{\mathbf{y}}$  and the full-rank transform matrix  $\mathbf{H}$ . Afterwards, starting from the last row, which holds the symbol with highest **SNR**, decides by the most likely transmitted information at layer  $\ell$  through **ML** criterion. The estimated symbol from layer  $\ell=q$  is then used to remove its interference in the foregone layer  $\ell=q-1$ , prior to **ML** detection. This procedure is repeated until all layers have been processed. Finally, original ordering is reestablished undoing the initial sort operation. The idea to reorganize the system according to the estimated signal quality is a tentative to avoid error propagation, a possibility that might occur case the **SIC** algorithm starts at an arbitrary low **SNR** resource [107]. Underneath the common assumption that the constellation alphabet  $\mathcal{C}$  is zero mean with normalized energy and  $\vec{\mathbf{w}}$  is **AWGN**, the estimated **SNR** after equalization is  $(\sigma_{\vec{\mathbf{w}}}^2 \|\mathbf{H}\mathbf{H}^H\|)^{-1}$ . Hereafter, assuming  $\vec{\mathbf{y}}$  and  $\mathbf{H}$  already sorted according to **SNR**, the **SIC** at the  $\ell$ th layer performs interference cancellation then equalization through

$$\hat{\mathbf{d}} = \mathbf{H}_{1:\ell}^H \left( \mathbf{H}_{1:\ell} \mathbf{H}_{1:\ell}^H + \Sigma_{\vec{\mathbf{w}}} \right)^{-1} \left( \vec{\mathbf{y}} - \sum_{\ell+1}^q \hat{\mathbf{d}}_{\text{sic}_{\ell+1}} \mathbf{H}_{\ell+1} \right), \quad (5.22)$$

followed by **ML** detection

$$\hat{\mathbf{d}}_{\text{sic}_{\ell}} = \underset{\mathbf{d}}{\text{argmin}} |\hat{\mathbf{d}}_{\ell} \vec{\mathbf{1}} - \mathcal{C}|^2. \quad (5.23)$$

In (5.22),  $\hat{\mathbf{d}}$  is the transmitted data estimate obtained from the received vector  $\vec{\mathbf{y}}$ , after interference removal from upper layers, followed by equalization considering the first  $\ell$

columns of  $\mathbf{H}$ . The interference cancellation depends on lower layers decision, once it employs the already detected symbols for  $\ell < q$ . Algorithm 11 is proposed for MMSE-SIC implementation.

---

**Algorithm 11** MMSE-SIC Detector
 

---

**Result:**  $\hat{\mathbf{d}}_{\text{sic}}$ 

```

1: for  $\ell \leftarrow q$  to 1 do
2:   if ( $\ell == q$ ) then
3:      $\hat{\mathbf{d}}_{1:\ell} = \mathbf{H}_{1:\ell}^H (\mathbf{H}_{1:\ell} \mathbf{H}_{1:\ell}^H + \Sigma_{\bar{\mathbf{w}}})^{-1} \bar{\mathbf{y}}$ 
4:   else
5:      $\hat{\mathbf{d}}_{1:\ell} = \mathbf{H}_{1:\ell}^H (\mathbf{H}_{1:\ell} \mathbf{H}_{1:\ell}^H + \Sigma_{\bar{\mathbf{w}}})^{-1} (\bar{\mathbf{y}} - \sum_{\ell+1}^q \hat{\mathbf{d}}_{\text{sic}_{\ell+1}} \mathbf{H}_{\ell+1})$ 
6:   end if
7:    $\hat{\mathbf{d}}_{\text{sic}_\ell} = \text{argmin} |\hat{\mathbf{d}}_\ell \bar{\mathbf{1}} - \mathcal{C}|^2$ 
8: end for

```

---

Analyzing algorithm 11 and applying the summation identities from Table 2 for the variable matrix size computations along all  $q$ -layer iterations, the estimated complexity for the MMSE-SIC is

$$\mathcal{O}_{\text{sic}} \left( 4p^3q + 2p^2q^2 + 8p^2q + 4pq^2 + 2p^2 + 6pq + 10M_c - q^2 - q \right). \quad (5.24)$$

Similar to ML-based algorithms, the MMSE-SIC also requires a system in the form of (3.26), but relating the observed signal and a discrete random vector through a known linear transformation. Unlike the exponential complexity in MLD and exponential upper bound in the case of SD, this interference cancellation method exhibits cubic complexity in the system order due to successive matrix inversions. The SNR-ordered SIC, although more robust than simple SIC, it is still affected by error propagation, resulting in sub-optimal performance.

## 5.4 MMSE-PIC Detector

Differently from SIC, where data symbols are individually detected removing the interference caused by already decided symbols, the PIC estimates all data elements sharing the same radio resource jointly. The PIC performs a detection on the  $j$ th element  $d_j$  of  $\bar{\mathbf{d}}$  assuming that all its other elements, denoted by  $\bar{\mathbf{d}}_\chi$ , are interfering terms. Retrieving (3.26) allows to rewrite

$$\bar{\mathbf{y}} = \mathbf{H}_j d_j + \mathbf{H}_\chi \bar{\mathbf{d}}_\chi + \bar{\mathbf{w}}, \quad (5.25)$$

where  $\mathbf{H}_j$  is the  $j$ th column of  $\mathbf{H}$  while  $\mathbf{H}_\chi$  is  $\mathbf{H}$  removing the  $j$ th column. Then, the PIC yields the signal  $\tilde{\mathbf{y}}_j$  given by

$$\tilde{\mathbf{y}}_j = \tilde{\mathbf{y}} - \mathbf{H}_\chi \tilde{\boldsymbol{\mu}}_{\tilde{\mathbf{d}}_\chi} = \mathbf{H}_j d_j + \underbrace{\mathbf{H}_\chi (\tilde{\mathbf{d}}_\chi - \tilde{\boldsymbol{\mu}}_{\tilde{\mathbf{d}}_\chi})}_{\tilde{\mathbf{w}}_j} + \tilde{\mathbf{w}}, \quad (5.26)$$

with  $\tilde{\boldsymbol{\mu}}_{\tilde{\mathbf{d}}_\chi}$  denoting the vector of expectancies  $\tilde{\boldsymbol{\mu}}_{\tilde{\mathbf{d}}}$  removing its  $j$ th element,  $\tilde{\mathbf{w}}_j$  models the noise-plus-interference, with variance  $\mathbf{H}\boldsymbol{\Sigma}_{\tilde{\mathbf{d}}}^a\mathbf{H}^H + \sigma^2\mathbf{I}$ . Based on (5.26), all  $j = 1 \dots q$  elements can be estimated and detect in parallel, employing independent linear estimation processes, whose, in general, require  $q \times q$  matrix inversions for each  $d_j$ , normally yielding to cubic complexity order. In [60], the authors demonstrate that this process is equivalent to a single linear estimation exploring a-priori knowledge about  $\tilde{\mathbf{d}}$ .

Resembling the LMMSE estimator from Section 4.2, the expected value and variance of  $\tilde{\mathbf{d}}$  can be estimated by

$$\tilde{\boldsymbol{\mu}}_{\tilde{\mathbf{d}}}^p = \boldsymbol{\Sigma}_{\tilde{\mathbf{d}}}^a \mathbf{H}^H (\mathbf{H} \boldsymbol{\Sigma}_{\tilde{\mathbf{d}}}^a \mathbf{H}^H + \boldsymbol{\Sigma}_{\tilde{\mathbf{w}}}^a)^{-1} (\tilde{\mathbf{y}} - \mathbf{H} \tilde{\boldsymbol{\mu}}_{\tilde{\mathbf{d}}}^a) + \tilde{\boldsymbol{\mu}}_{\tilde{\mathbf{d}}}^a \quad (5.27)$$

and

$$\boldsymbol{\Sigma}_{\tilde{\mathbf{d}}}^p = \boldsymbol{\Sigma}_{\tilde{\mathbf{d}}}^a - \boldsymbol{\Sigma}_{\tilde{\mathbf{d}}}^a \mathbf{H}^H (\mathbf{H} \boldsymbol{\Sigma}_{\tilde{\mathbf{d}}}^a \mathbf{H}^H + \boldsymbol{\Sigma}_{\tilde{\mathbf{w}}}^a)^{-1} \mathbf{H} \boldsymbol{\Sigma}_{\tilde{\mathbf{d}}}^a. \quad (5.28)$$

where  $\tilde{\boldsymbol{\mu}}_{\tilde{\mathbf{d}}}^p$  can be used solely for hard demodulation, employing, for example, the ML criteria, or in conjunction with  $\boldsymbol{\Sigma}_{\tilde{\mathbf{d}}}^p$  in soft demodulation. If  $\tilde{\boldsymbol{\mu}}_{\tilde{\mathbf{d}}}^p$  is Gaussian in the factorized domain, it is necessary to estimate the equivalents of (5.27) and (5.28) in the discrete domain, as described in Section 3.3.

Algorithm 12 describes a subsystem hard detection method assuming that  $\tilde{\mathbf{d}}$  is a discrete sequence of symbols in the factorized domain. Line 6 performs the minimum distance hard detection of the estimated data sequence in the discrete domain. The term  $\tilde{\mathbf{I}}\mathcal{C}^T$  results in a  $q \times M_c$  matrix and the minimum argument operator is taken along its row direction.

---

**Algorithm 12** MMSE PIC
 

---

- 1:  $\boldsymbol{\Sigma}_{\tilde{\mathbf{d}}}^a \mathbf{H}^H$
- 2:  $(\mathbf{H} \boldsymbol{\Sigma}_{\tilde{\mathbf{d}}}^a \mathbf{H}^H + \boldsymbol{\Sigma}_{\tilde{\mathbf{w}}}^a)^{-1}$
- 3:  $(\tilde{\mathbf{y}} - \mathbf{H} \tilde{\boldsymbol{\mu}}_{\tilde{\mathbf{d}}}^a)$
- 4:  $\tilde{\boldsymbol{\mu}}_{\tilde{\mathbf{d}}}^p = \boldsymbol{\Sigma}_{\tilde{\mathbf{d}}}^a \mathbf{H}^H (\mathbf{H} \boldsymbol{\Sigma}_{\tilde{\mathbf{d}}}^a \mathbf{H}^H + \boldsymbol{\Sigma}_{\tilde{\mathbf{w}}}^a)^{-1} (\tilde{\mathbf{y}} - \mathbf{H} \tilde{\boldsymbol{\mu}}_{\tilde{\mathbf{d}}}^a) + \tilde{\boldsymbol{\mu}}_{\tilde{\mathbf{d}}}^a$
- 5:  $\boldsymbol{\Sigma}_{\tilde{\mathbf{d}}}^p = \boldsymbol{\Sigma}_{\tilde{\mathbf{d}}}^a - \boldsymbol{\Sigma}_{\tilde{\mathbf{d}}}^a \mathbf{H}^H (\mathbf{H} \boldsymbol{\Sigma}_{\tilde{\mathbf{d}}}^a \mathbf{H}^H + \boldsymbol{\Sigma}_{\tilde{\mathbf{w}}}^a)^{-1} (\boldsymbol{\Sigma}_{\tilde{\mathbf{d}}}^a \mathbf{H}^H)$
- 6:  $\hat{\mathbf{d}}_{\text{pic}} = \text{argmin} |\tilde{\boldsymbol{\mu}}_{\tilde{\mathbf{d}}}^p - \tilde{\mathbf{I}}\mathcal{C}^T|^2$

**Return:**  $(\tilde{\boldsymbol{\mu}}_{\tilde{\mathbf{d}}}^p, \boldsymbol{\Sigma}_{\tilde{\mathbf{d}}}^p, \hat{\mathbf{d}}_{\text{pic}})$

---

The associated computational complexity in Algorithm 12 is approximately the same as the LMMSE estimation, and it is given by

$$\mathcal{O}_1(4p^3 + 24p^2q + 16q^2p + 8p^2 + 10pq + 10p). \quad (5.29)$$

It is mainly dictated by the  $p \times p$  matrix inversion with cubic complexity order on  $p$ .

## 5.5 Detectors Comparison

This section explores an orthogonal  $N_T \times N_R$  SM-MIMO digital communication system. The analysis relies on the model described in Section 3.3, which offers a framework for representing factorized and independent subsystems. By examining this model, it is possible to compare and contrast different detectors, highlighting their strengths and weaknesses in the context of SM-MIMO systems. This analysis adopts  $N_T = N_R = 4$  antennas for both the transmitter and receiver, such that  $N_T$  different data streams are transmitted simultaneously. Furthermore, no channel coding neither any kind of precoding are used. The system uses a 16-QAM to map bits into symbols, which are transmitted through a time-varying and frequency selective channel employing an orthogonal multicarrier scheme, i.e. CP protected OFDM. Assuming a symbol length with  $K = 64$  samples, a CP with  $N_{CP} = 16$  samples, which is larger than the maximum channel delay profile. In this case, the channel coherence bandwidth is wider than the bandwidth of a subcarrier and the channel frequency response can be considered to be a flat Rayleigh channel per subcarrier. It is also assumed perfect synchronization and CSIR. The simulation parameters are the same given in Table 9.

Figure 30 illustrates some selected energy efficiency Monte Carlo simulation results. It relates the BER versus the  $E_b/N_0$  ratio for some of the main presented estimation and detection techniques so far. The MMSE process, which involves LMMSE equalization, is applied to the received and demodulated symbols. This method is appropriate here because the system model is linear.

The CWCU-LMMSE method applies diagonal weighting to the LMMSE equalization matrix, as shown in Section 4.4. Immediately after equalization, ML detection is used to identify the most probable transmitted sequence. This example uses the LMMSE equalization matrix to estimate the SNR in the MMSE-SIC, as described in Algorithm 11. Additionally, it serves as the estimator for the MMSE-PIC, as outlined in Algorithm 12. Alongside these detectors, the results for the classical SD, detailed in Algorithm 9, is also included. The MLD, described in Algorithm 7, has also been implemented as a benchmark for the techniques considered in this analysis.

The detector based on CWCU-LMMSE estimation shows a slight improvement in the BER performance when compared with the corresponding LMMSE, which employs

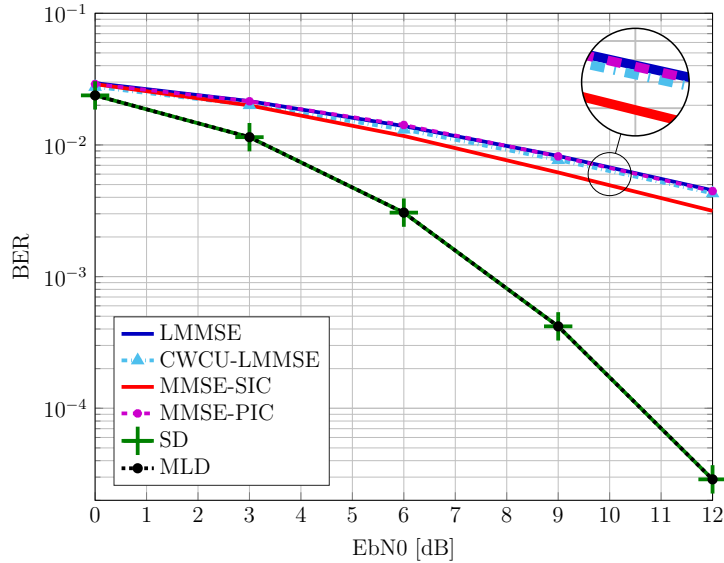


Figure 30 – Monte Carlo simulation of an uncoded 16-QAM employing a  $4 \times 4$  SM-MIMO-OFDM in time-varying and frequency selective channel.

an equalization matrix with unweighted diagonal. This small improvement is a result of a better fitting of the **CWCU-LMMSE** equalized signal on the constellation grid prior to detection. This characteristic holds for the Rayleigh flat-fading channel, where the symbols after **CWCU-LMMSE** equalization remains unbiased, while the symbols equalized by the **LMMSE** tends to introduce a small bias towards the expected value of the discrete **RV** set, which, for a symmetric equiprobable **QAM** constellation, is zero. On the other hand, for **AWGN** channel, both equalizers performs equally in terms of **BER** [108].

The **SD** achieves a performance that is equivalent to the one observed for the **MLD** and over performing all previous detectors. Figure 31 analyzes the **SD** complexity for the proposed example in terms of the average number of visited nodes at each layer. Notice that this parameters is not so dependent on the **SNR** as the average amount of visited nodes slight decays with the  $E_b/N_0$ . Furthermore, bottom layers are more commonly visited once the tree search structure exponentially expands towards the underneath layers.

The average complexity in **FLOPs** is obtained from the average number of visited nodes and (5.8). This is an important parameter once it allows to compare the upper bound of the **SD** complexity, given by (5.10), its average computational cost, and the **MLD** complexity given by (5.2). This behavior can be seen graphically in Figure 32, that brings the complexity growth, in log scale, of the presented detection methods, in terms of **FLOPs** counting as a function of the constellation size  $M_c$ , while assuming  $N_T=N_R$ . Among the presented detectors, the **MMSE-SIC** and the **MMSE-PIC** have the lowest and restrained computational cost since (5.24) and (5.29) follow a cubic expansion rate with the number of receive antennas. Analyzing (5.10) and (5.2), an exponential growth in the worst case scenario for both **SD** and **MLD** can be inferred. The average complexity of **SD**

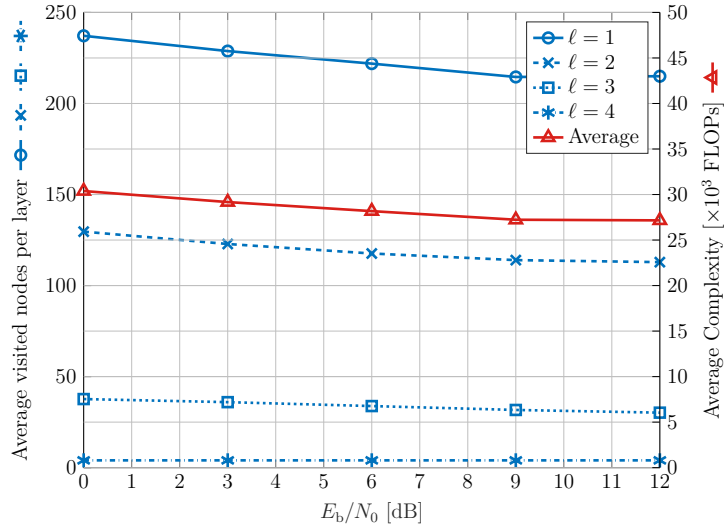


Figure 31 – SD complexity analysis for the simulated parameters.

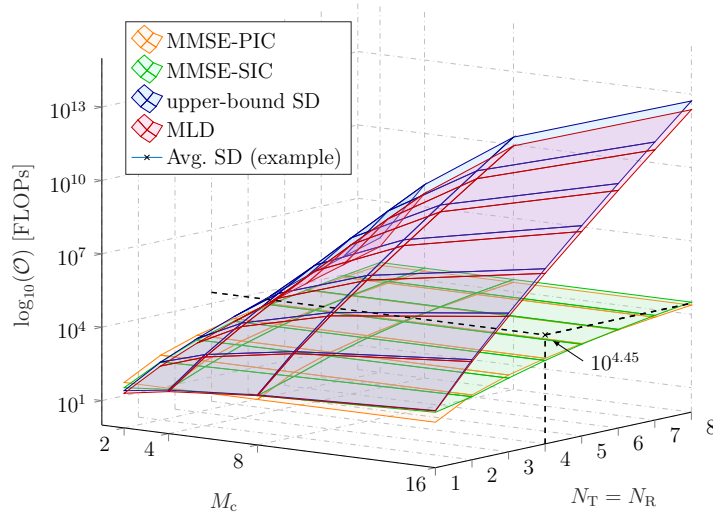


Figure 32 – FLOP complexity comparison for the main evaluated detection methods.

for the proposed example is also marked, confirming that, in average, the **SD** achieves the **MLD** performance at a smaller complexity (approximately  $4x \mathcal{O}_{\text{osic}}$  in this example), although it can still reach exponential computational cost.

It is evident that both **SD** and **MLD** algorithms, while optimal in terms of **BER** performance compared with the **SIC** approach, exhibit prohibitive complexity as the modulation order or the number of antennas increases. This is particularly true for high-order communication systems, such as massive **MIMO** [87]. In such cases, it is important to consider various solutions, which may include slight variations of classical methods mentioned earlier in this chapter, as well as new proposals that may arise.

## 5.6 Summary

This chapter explored detection methods aiming to retrieve all the information simultaneously transmitted in a **SM-MIMO** application. These methods may require intricate detection procedures to manage the intrinsic system interference that arises when employing multiple antennas. These detectors are described in details, supported by practical algorithms and complexity order expressions. While some detectors, such as **MLD** and **SD**, are optimal, they are impractical for implementation due to their high computational cost. Other alternatives, such as the **SNR-ordered SIC** and the **PIC**, although feasible in terms of complexity, remain sub-optimal. The subjects covered in this chapter are original contributions from this thesis which have been published in [58] and [104]. The following chapter details a low-complexity and low-latency iterative **PIC** method capable of achieving optimal performance even for **NO** waveforms [1].

## 6 Iterative MMSE-PIC Detector

Non-orthogonal waveforms pose challenges for data separation and diversity gain, once any previous equalization results in homogeneous flat channel at subcarriers before detection. The use of **ML** detectors for optimal performance in such situations is often intricate and impractical, involving the comparison of the received signal in the time domain with all possible waveforms transmitted over the radio channel. To address the challenges introduced by **NO** waveforms, achieving data separation, **ICI** and **ISI** mitigation, as well as diversity harvesting, the reception process can be carried out through iterative **PIC** techniques.

This chapter provides a detailed description of the iterative **MMSE-PIC** algorithm, supported by a comprehensive block diagram that visualizes the information flow during detection. The entire process is divided into smaller, easily comprehensible parts, each described algorithmically.

### 6.1 Fundamentals on Iterative MMSE-PIC

In [1], Matthé et al. proposes a low complexity and low latency iterative **MMSE-PIC**, suitable for, but not restrained to, **NO-GFDM** detection in **SM-MIMO** applications, aiming for harvesting multiplexing and diversity gains simultaneously. The complexity reduction relies on the equivalence between a **PIC** process and a single **LMMSE** estimation with a-priory knowledge about system parameters [60]. Most important, under the assumption that both inputs and outputs are continuous gaussian random variables, linear estimators becomes an interesting enabler to iterative detection by providing estimates and uncertainties for **SISO** (*Soft-Input, Soft-Output*) demapping and decoding operations. This assumption is crucial in order to employ factorized systems in the form of (3.24), allowing to explore low complexity estimation methods based on their specific band structured matrices.

Figure 33 illustrates the block diagram for the proposed iterative **SISO MMSE-PIC** detector. Its entry point considers, under the premise of perfect synchronization and **CSIR**, the received signal vector  $\vec{y}$ , after **CP** removal, the equivalent **MIMO** channel, as  $\tilde{\mathbf{H}}$ , and the corresponding **AWGN** variance  $\sigma_w^2$ . On sequence, the linear system represented by (3.5) is factorized into  $M$  subsystems with dimension  $N_T K_{on} \times N_T K_{on}$ , according to (3.14) and related equations. Each resulting subsystem at sample-frequency domain refers to (3.24), where an estimate on the expectation and variance of  $\vec{d}_s$  is desired. These parameters are estimated with the help of function  $\Theta_{icl}$  and the available a-priory information

$\vec{\mu}_{\mathbf{d}_s}^a$  and  $\vec{\Sigma}_{\mathbf{d}_s}^a$ . Initially, when no a-priori information is available, these parameters are initialized as a null and unitary vectors, respectively. Note that the uncertainty parameter  $\vec{\Sigma}$  is represented by a vector once the involved covariance matrices are approximately forced to be diagonal. Then, the resulting posterior estimates  $\vec{\mu}_{\mathbf{d}_s}^p$  and  $\vec{\Sigma}_{\mathbf{d}_s}^p$  are reorganized into  $N_T K_{\text{on}}$  subsystems of size  $M \times M$ , used in the sample-frequency to data-time domain estimation employing the function  $\Theta_{\text{cg}}$ . Following this operation, properly concatenation and permutation yields to posterior estimate on the expected transmitted data  $\vec{\mu}_{\mathbf{d}}^p$  and its variance  $\vec{\Sigma}_{\mathbf{d}}^p$ .

Optionally, interleaving symbols and/or bits might be considered in order to improve the robustness against burst errors. In case of random interleaving had been considered in the transmitter side, identified by  $\Pi$ , the corresponding de-interleaving function, denoted as  $\Pi^{-1}$ , must also be considered prior to symbol de-mapping or channel decoding. Afterwards, the same random interleaver operation is performed in the feedback direction. The interleaving is an efficient option in order to improve the correction capacity. If the noise coming into channel decoding is highly correlated, then the convolutional decoder, commonly designed with a short constraint length, is more likely to make a decoding error than if the noise was independent. Since channel decoders are affected by burst errors, the interleaver spreads these errors out, allowing the decoders to operate with relative independent noise from bit to bit [86].

Soft demapping function  $\mathcal{M}_{\text{soft}}^{-1}$  performs individual bit probability estimation for each data symbol, constrained by the constellation set  $\mathcal{C}$ . Assuming uncorrelated noise and dismissing the necessity of previous knowledge about the bit sequence, the approximated LLRs (*Log-Likelihood Ratios*) are efficiently obtained with negligible impact on the overall detection performance [1, 61] by

$$\vec{\lambda}_{e,s,b}^p = \frac{1}{(\vec{\Sigma}_{\mathbf{d}}^p)_s} \left( \min \left| (\vec{\mu}_{\mathbf{d}}^p)_s - \mathcal{C}_b^{(0)} \right|^2 - \min \left| (\vec{\mu}_{\mathbf{d}}^p)_s - \mathcal{C}_b^{(1)} \right|^2 \right) \quad (6.1)$$

where  $\vec{\lambda}_e^p \in \mathbb{R}^{\mu N_T N_{\text{on}} \times 1}$  is the approximated extrinsic LLR vector with  $\mathcal{C}_b^{(0)}$  and  $\mathcal{C}_b^{(1)}$  being the subsets of constellation symbols whose  $b$ th bit is 0 or 1, respectively. It is worth to mention that diverse LLRs sequences are required when considering SM-MIMO systems employing frame structures that carry out integer multiples of a codeword, simultaneously transmitted by  $N_T$  antennas in  $N_s$  block symbols per frame. Thus, after properly gathering and organizing each codeword, soft decoding is the last procedure on every outer PIC iteration.

Soft channel decoding is responsible for recovering the transmitted bit information from demapper estimates, obeying the code constraints. Usually, soft decoding applies algorithms able to exactly compute or approximate the APP of the information bits or, more generally, a reliability measure about each information bit. Hence, soft decoding results decoded LLRs, required in order to output re-encoded LLRs  $\vec{\lambda}_i^a$  for a next ite-

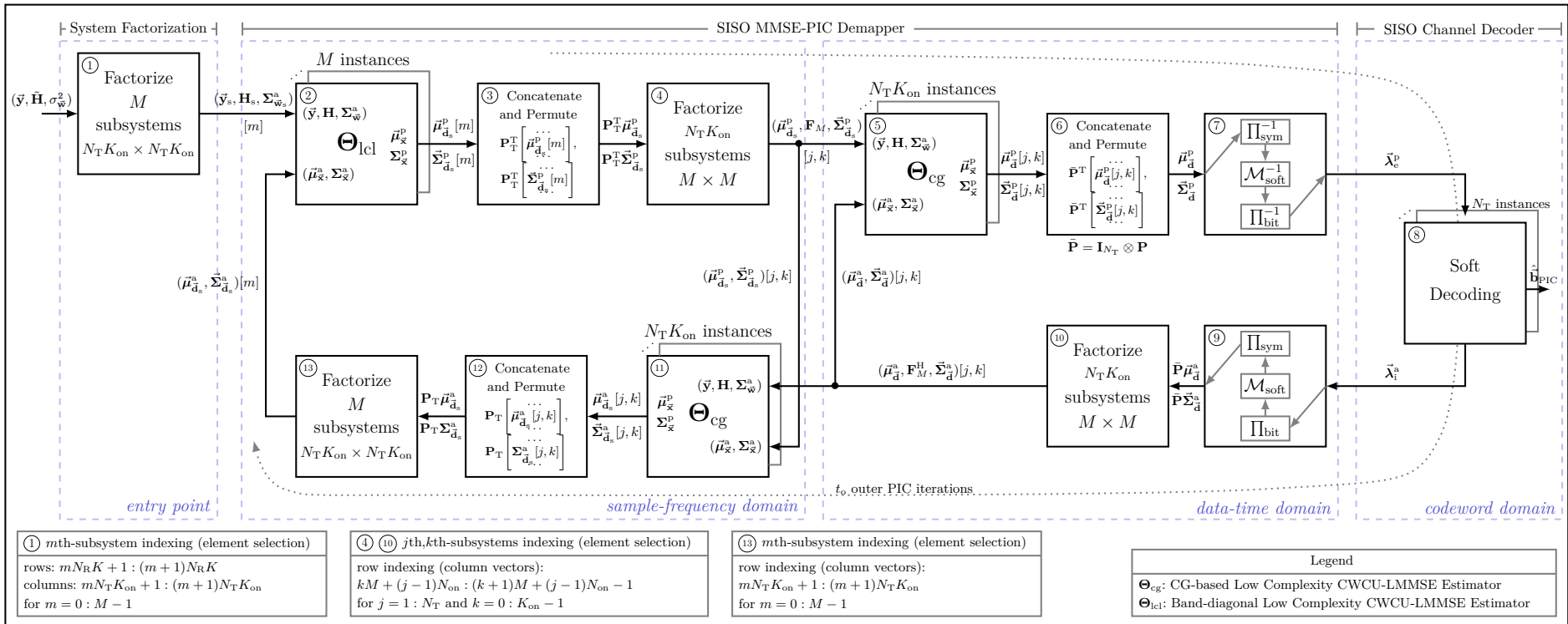


Figure 33 – Iterative MMSE-PIC detector block diagram for SM-MIMO employing NO-GFDM.

ration or by taking a final hard bit decision  $\vec{\mathbf{b}}_{\text{PIC}}$ . According to [1], convolutional codes performed better among the analyzed coding techniques, therefore, max-log BCJR (*Bahl-Cocke-Jelinek-Raviv*) algorithm [109] is also considered as an optimal achievable decoding technique in order to obtain the LLRs for the PIC feedback.

In turbo decoding, both decoders have to be fed with information not originating from themselves in order to improve the correctness of its decisions, corresponding to the so called extrinsic LLRs [110]. As adopted in [61], using the intrinsic a-priory LLRs in the feedback computation of soft symbols instead of extrinsic ones leads, in general, to significantly better error-rate performance of the SISO MMSE-PIC algorithm. In the same manner, the intrinsic a-priory LLRs is considered along this work. Thus, the intrinsic information gained during codeword domain processing, denoted by  $\vec{\lambda}_i^a$ , is soft modulated according to [1, 61]. Defining the  $b$ th bit of the  $s$ th constellation symbol by  $\vec{\mathbf{b}}_{s,b} \in \{0, 1\}$  with probabilities  $\mathcal{P}[\vec{\mathbf{b}}_{s,b} = 1] = [1 + \exp(\vec{\lambda}_i^a)]^{-1}$  and  $\mathcal{P}[\vec{\mathbf{b}}_{s,b} = 0] = 1 - \mathcal{P}[\vec{\mathbf{b}}_{s,b} = 1]$ , the mean and variance of the a-priory constellation symbols are updated performing

$$(\vec{\mu}_{\mathbf{d}}^a)_s = \sum_{d \in \mathcal{C}} \prod_b \mathcal{P}[\vec{\mathbf{b}}_{s,b} = \mathcal{M}^{-1}(d)] d \quad (6.2)$$

and

$$(\vec{\Sigma}_{\mathbf{d}}^a)_s = \sum_{d \in \mathcal{C}} \prod_b \mathcal{P}[\vec{\mathbf{b}}_{s,b} = \mathcal{M}^{-1}(d)] \|d - (\vec{\mu}_{\mathbf{d}}^a)_s\|^2. \quad (6.3)$$

The a-priory probabilities in (6.2) and (6.3) can be obtained by [111]

$$\mathcal{P}[\vec{\mathbf{b}}_{s,b} = \{0, 1\}] = \frac{1}{2} \left[ 1 + (2\vec{\mathbf{b}}_{s,b} - 1) \tanh \left( \frac{1}{2} \vec{\lambda}_i^a [\mu_s + b] \right) \right], \quad (6.4)$$

which shows numerically stability w.r.t.  $\vec{\lambda}_i^a$  and can be efficiently implemented in hardware through look-up tables [61].

In the sequence,  $\vec{\mu}_{\mathbf{d}}^a$  and  $\vec{\Sigma}_{\mathbf{d}}^a$  are conveniently grouped by subcarriers through left multiplication by the augmented permutation matrix  $\bar{\mathbf{P}} = \mathbf{I}_{N_T} \otimes \mathbf{P}$  and factorized into  $M$  subsystems for time to frequency estimation, leading to a-priory estimates on sample-frequency domain, denoted by  $\vec{\mu}_{\mathbf{d}_s}^a$  and  $\vec{\Sigma}_{\mathbf{d}_s}^a$ . This encloses the iterative MMSE-PIC outer loop, allowing to start a new iteration considering the a-priory information gained from soft decoding. Along successive iterations, both demapper and decoder procedures self benefit from exchanged refined information between each other. Algorithm 13 presents a detailed task list necessary to implement the iterative detector for  $t_o$  outer iterations.

In Algorithm 13, except by the processes in lines 9, 10 and 11, where (de)interleave, soft (de)map and decode operations are executed one codeword per transmitting antenna, all other procedures are processed in a block-by-block fashion, for all  $N_s$  block-symbols in a frame. Lines 5, 8 and 14 perform element concatenation and permutation, referring to blocks 3, 6 and 12 in Figure 33, respectively. Soft demapping and mapping functions, from

**Algorithm 13** Iterative MMSE-PIC Detector

---

```

1: Algorithm 13.1: Initialize MMSE-PIC Detector
2: Algorithm 13.2: Factorize into  $M$  subsystems  $N_T K_{\text{on}} \times N_T K_{\text{on}}$  % Block (1)
3: for 1 to  $t_o$  do
4:   Algorithm 13.3: Estimate data in FD % Block (2)
5:   Algorithm 13.4: Concatenate and permute data in FD % Block (3)
6:   Algorithm 13.5: Factorize into  $N_T K_{\text{on}}$  subsystems  $M \times M$  % Block (4)
7:   Algorithm 13.6: Estimate TD data from FD % Block (5)
8:   Algorithm 13.7: Concatenate and permute data in TD % Block (6)
9:   Algorithm 13.8: De-interleaving and soft de-mapping % Block (7)
10:  Algorithm 13.9: Soft decoding % Block (8)
11:  Algorithm 13.10: Interleaving and Soft mapping % Block (9)
12:  Algorithm 13.11: Factorize into  $N_T K_{\text{on}}$  subsystems  $M \times M$  % Block (10)
13:  Algorithm 13.12: Estimate FD data from TD % Block (11)
14:  Algorithm 13.13: Concatenate and permute data in FD % Block (12)
15:  Algorithm 13.14: Factorize into  $M$  subsystems  $N_T K_{\text{on}} \times N_T K_{\text{on}}$  % Block (13)
16: end for
Return:  $\vec{\mathbf{b}}_{\text{PIC}}$ 

```

---

**Algorithm 13.1** Initialize MMSE-PIC Detector

---

```

1:  $\mathbf{P}_R \vec{\mathbf{y}}_f = \mathbf{P}_R (\mathbf{I}_{N_R} \otimes \mathbf{F}_N) \vec{\mathbf{y}}$ 
2:  $\mathbf{P}_R \mathbf{H}_f \mathbf{P}_T^T = \mathbf{P}_R (\mathbf{I}_{N_R} \otimes \mathbf{F}_N) \tilde{\mathbf{H}} \tilde{\mathbf{U}}^H \mathbf{P}_T^T$ 
3:  $\vec{\boldsymbol{\mu}}_{\mathbf{d}_s}^a = \vec{\boldsymbol{\mu}}_{\mathbf{d}}^a = \vec{\mathbf{0}}$ 
4:  $\vec{\boldsymbol{\Sigma}}_{\mathbf{d}_s}^a = \vec{\boldsymbol{\Sigma}}_{\mathbf{d}}^a = \vec{\mathbf{I}}$ 
5:  $\vec{\boldsymbol{\lambda}}_e^a = \vec{\boldsymbol{\lambda}}_e^p = \vec{\mathbf{0}}$ 

```

---

**Return****Algorithm 13.2** Factorize  $\mathbf{P}_R \vec{\mathbf{y}}_f$  and  $\mathbf{P}_R \mathbf{H}_f \mathbf{P}_T^T$  into  $M$  subsystems  $(\vec{\mathbf{y}}_s, \mathbf{H}_s, \boldsymbol{\Sigma}_{\vec{\mathbf{w}}_s}^a)[m]$ 


---

```

1: for  $m = 0$  to  $M - 1$  do
2:    $\vec{\mathbf{p}} = [m N_R K + 1 : (m + 1) N_R K]$ 
3:    $\vec{\mathbf{q}} = [m N_T K_{\text{on}} + 1 : (m + 1) N_T K_{\text{on}}]$ 
4:    $\vec{\mathbf{y}}_s[m] = (\mathbf{P}_R \vec{\mathbf{y}}_f)[\vec{\mathbf{p}}]$ 
5:    $\mathbf{H}_s[m] = (\mathbf{P}_R \mathbf{H}_f \mathbf{P}_T^T)[\vec{\mathbf{p}}, \vec{\mathbf{q}}]$ 
6:    $\boldsymbol{\Sigma}_{\vec{\mathbf{w}}_s}^a[m] = \sigma_{\vec{\mathbf{w}}}^2 \mathbf{I}_{N_T K_{\text{on}}}$ 
7: end for

```

---

**Return:**  $M$  subsystems  $(\vec{\mathbf{y}}_s, \mathbf{H}_s, \boldsymbol{\Sigma}_{\vec{\mathbf{w}}_s}^a)[m]$ **Algorithm 13.3** Estimate data in **FD**


---

```

1: for all  $m$  do %  $M$  parallel instances, suppressed indexes
2:    $(\vec{\boldsymbol{\mu}}_{\mathbf{d}_s}^p, \vec{\boldsymbol{\Sigma}}_{\mathbf{d}_s}^p) = \Theta_{\text{lcl}} [(\vec{\mathbf{y}}_s = \mathbf{H}_s \vec{\mathbf{d}}_s + \vec{\mathbf{w}}_s), \mathcal{CN}(\vec{\boldsymbol{\mu}}_{\mathbf{d}_s}^a, \boldsymbol{\Sigma}_{\mathbf{d}_s}^a), \mathcal{CN}(\vec{\mathbf{0}}, \boldsymbol{\Sigma}_{\vec{\mathbf{w}}_s}^a)]$ 
3: end for

```

---

**Return**

**Algorithm 13.4** Concatenate and permute data in FD

- 1:  $\mathbf{P}_T^T \vec{\boldsymbol{\mu}}_{\mathbf{d}_s}^p = \mathbf{P}_T^T [\vec{\boldsymbol{\mu}}_{\mathbf{d}_s}^p [0]; \dots; \vec{\boldsymbol{\mu}}_{\mathbf{d}_s}^p [m]; \dots; \vec{\boldsymbol{\mu}}_{\mathbf{d}_s}^p [M - 1]]$
- 2:  $\mathbf{P}_T^T \vec{\boldsymbol{\Sigma}}_{\mathbf{d}_s}^p = \mathbf{P}_T^T [\vec{\boldsymbol{\Sigma}}_{\mathbf{d}_s}^p [0]; \dots; \vec{\boldsymbol{\Sigma}}_{\mathbf{d}_s}^p [m]; \dots; \vec{\boldsymbol{\Sigma}}_{\mathbf{d}_s}^p [M - 1]]$

**Return****Algorithm 13.5** Factorize  $\mathbf{P}_T^T \vec{\boldsymbol{\mu}}_{\mathbf{d}_s}^p$  and  $\mathbf{P}_T^T \vec{\boldsymbol{\Sigma}}_{\mathbf{d}_s}^p$  into  $N_T K_{\text{on}}$  subsystems  $(\vec{\boldsymbol{\mu}}_{\mathbf{d}_s}^p, \vec{\boldsymbol{\Sigma}}_{\mathbf{d}_s}^p)[j, k]$ 

- 1: **for**  $j = 1$  to  $N_T$  **do**
- 2:     **for**  $k = 0$  to  $K_{\text{on}} - 1$  **do**
- 3:          $\vec{\mathbf{q}} = [kM + (j - 1)N_{\text{on}} : (k + 1)M + (j - 1)N_{\text{on}} - 1]$
- 4:          $\vec{\boldsymbol{\mu}}_{\mathbf{d}_s}^p [j, k] = (\mathbf{P}_T^T \vec{\boldsymbol{\mu}}_{\mathbf{d}_s}^p)[\vec{\mathbf{q}}]$
- 5:          $\vec{\boldsymbol{\Sigma}}_{\mathbf{d}_s}^p [j, k] = (\mathbf{P}_T^T \vec{\boldsymbol{\Sigma}}_{\mathbf{d}_s}^p)[\vec{\mathbf{q}}]$
- 6:     **end for**
- 7: **end for**

**Return:**  $N_T K_{\text{on}}$  subsystems  $(\vec{\boldsymbol{\mu}}_{\mathbf{d}_s}^p, \vec{\boldsymbol{\Sigma}}_{\mathbf{d}_s}^p)[j, k]$ **Algorithm 13.6** Estimate TD data from FD

- 1: **for all**  $j, k$  **do** %  $N_T K_{\text{on}}$  parallel instances, suppressed indexes
- 2:      $(\vec{\boldsymbol{\mu}}_{\mathbf{d}}^p, \vec{\boldsymbol{\Sigma}}_{\mathbf{d}}^p) = \Theta_{\text{cg}} [(\vec{\mathbf{d}}_s = \mathbf{F}_M \vec{\mathbf{d}} + \vec{\boldsymbol{\sigma}}_{\mathbf{d}_s}^2 \mathbf{I}_M), \mathcal{CN}(\vec{\boldsymbol{\mu}}_{\mathbf{d}}^a, \vec{\boldsymbol{\Sigma}}_{\mathbf{d}}^a), \mathcal{CN}(\vec{\boldsymbol{\mu}}_{\mathbf{d}_s}^a, \boldsymbol{\Sigma}_{\mathbf{d}_s}^a)]$
- 3: **end for**

**Return****Algorithm 13.7** Concatenate and permute data in TD

- 1:  $\vec{\boldsymbol{\mu}}_{\mathbf{d}}^p = \bar{\mathbf{P}}^T [\vec{\boldsymbol{\mu}}_{\mathbf{d}}^p [0, 0]; \dots; \vec{\boldsymbol{\mu}}_{\mathbf{d}}^p [j, k]; \dots; \vec{\boldsymbol{\mu}}_{\mathbf{d}}^p [N_T - 1, K_{\text{on}} - 1]]$
- 2:  $\vec{\boldsymbol{\Sigma}}_{\mathbf{d}}^p = \bar{\mathbf{P}}^T [\vec{\boldsymbol{\Sigma}}_{\mathbf{d}}^p [0, 0]; \dots; \vec{\boldsymbol{\Sigma}}_{\mathbf{d}}^p [j, k]; \dots; \vec{\boldsymbol{\Sigma}}_{\mathbf{d}}^p [N_T - 1, K_{\text{on}} - 1]]$

**Return****Algorithm 13.8** De-interleaving and soft de-mapping

- 1: **function**  $\Pi^{-1}$
- 2:     deinterleaved[permutation\_indexes] = interleaved[linear\_indexes]
- 3: **end function**
- 4: **function**  $\mathcal{M}_{\text{SOFT}}^{-1}$  % according to (6.1)
- 5:      $N_d = \text{length}(\vec{\boldsymbol{\mu}})$
- 6:      $M_c = \text{length}(\mathcal{C})$
- 7:      $\mathcal{C}_2 = \text{binary}(1 : M_c)$
- 8:     **for**  $s \leftarrow 1$  to  $N_d$  **do**
- 9:         **for**  $b \leftarrow 1$  to  $\mu$  **do**
- 10:              $\text{idx} = \mu(s - 1) + b$
- 11:              $\vec{\boldsymbol{\lambda}}[\text{idx}] = -\frac{1}{\vec{\boldsymbol{\Sigma}}[s]} [\min(|\vec{\boldsymbol{\mu}}[s] - \mathcal{C}[\mathcal{C}_2[b] = 0]|^2) - \min(|\vec{\boldsymbol{\mu}}[s] - \mathcal{C}[\mathcal{C}_2[b] = 1]|^2)]$
- 12:         **end for**
- 13:     **end for**
- 14: **end function**
- 15:  $\vec{\boldsymbol{\lambda}}_e^p = \Pi_{\text{bit}}^{-1} \{ \mathcal{M}_{\text{soft}}^{-1} [\Pi_{\text{sym}}^{-1}(\vec{\boldsymbol{\mu}}_{\mathbf{d}}^p), \Pi_{\text{sym}}^{-1}(\vec{\boldsymbol{\Sigma}}_{\mathbf{d}}^p)] \}$

**Return**

**Algorithm 13.9** Soft channel decoding

---

```

1: if  $r > 1/2$  then
2:   De-puncturing( $\vec{\lambda}_e^p$ )
3: end if
4:  $(\vec{\lambda}_i^a, \vec{b}_{\text{PIC}}) = \text{BCJR}(\vec{\lambda}_e^p)$  % Soft decoding according to [109]
5: if  $r > 1/2$  then
6:   Puncturing( $\vec{\lambda}_i^a$ )
7: end if

```

**Return****Algorithm 13.10** Interleaving and soft mapping

---

```

1: function  $\square$ 
2:   interleaved[linear_indexes] = deinterleaved[permutation_indexes]
3: end function
4: function  $\mathcal{M}_{\text{SOFT}}$  % according to (6.2) and (6.3)
5:    $N_d = \text{length}(\vec{\lambda})/\mu$ 
6:    $M_c = \text{length}(\mathcal{C})$ 
7:    $\mathcal{C}_2 = \text{binary}(1 : M_c)$ 
8:   for  $s \leftarrow 1$  to  $N_d$  do
9:      $idx = \mu(s - 1) + 1 : \mu$ 
10:     $\mathcal{P} = \frac{1}{2} \left[ 1 + (2\mathcal{C}_2 - 1) \circ \tanh \left( \frac{1}{2} \vec{\mathbf{1}}(\vec{\lambda}_i^a[idx])^T \right) \right]$ 
11:     $\vec{\mu}[s] = \mathcal{P}^T \mathcal{C}$ 
12:     $\vec{\Sigma}[s] = \mathcal{P}^T |\mathcal{C} - \vec{\mu}[s]|^2$ 
13:   end for
14: end function

```

**Return****Algorithm 13.11** Factorize  $\bar{\mathbf{P}}\vec{\mu}_d^a$  and  $\bar{\mathbf{P}}\vec{\Sigma}_d^a$  into  $N_T K_{\text{on}}$  subsystems  $(\vec{\mu}_d^a, \vec{\Sigma}_d^a)[j, k]$ 


---

```

1: for  $j = 1$  to  $N_T$  do
2:   for  $k = 0$  to  $K_{\text{on}} - 1$  do
3:      $\vec{q} = [kM + (j - 1)N_{\text{on}} : (k + 1)M + (j - 1)N_{\text{on}} - 1]$ 
4:      $\vec{\mu}_d^a[j, k] = (\bar{\mathbf{P}}\vec{\mu}_d^a)[\vec{q}]$ 
5:      $\vec{\Sigma}_d^a[j, k] = (\bar{\mathbf{P}}\vec{\Sigma}_d^a)[\vec{q}]$ 
6:   end for
7: end for

```

**Return:**  $N_T K_{\text{on}}$  subsystems  $(\vec{\mu}_d^a, \vec{\Sigma}_d^a)[j, k]$ **Algorithm 13.12** Estimate FD data from TD

---

```

1: for all  $j, k$  do %  $N_T K_{\text{on}}$  parallel instances, suppressed indexes
2:    $(\vec{\mu}_{d_s}^a, \vec{\Sigma}_{d_s}^a) = \Theta_{\text{cg}} \left[ (\vec{d} = \mathbf{F}_M^H \vec{d}_s + \vec{\sigma}_d^2 \mathbf{I}_M), \mathcal{CN}(\vec{\mu}_{d_s}^p, \vec{\Sigma}_{d_s}^p), \mathcal{CN}(\vec{\mu}_d^a, \Sigma_d^a) \right]$ 
3: end for

```

**Return**

---

**Algorithm 13.13** Concatenate and permute data in **FD**

---

- 1:  $\mathbf{P}_T \vec{\boldsymbol{\mu}}_{\mathbf{d}_s}^a = \mathbf{P}_T [\vec{\boldsymbol{\mu}}_{\mathbf{d}_s}^a [0]; \dots; \vec{\boldsymbol{\mu}}_{\mathbf{d}_s}^a [m]; \dots; \vec{\boldsymbol{\mu}}_{\mathbf{d}_s}^a [M - 1]]$
- 2:  $\mathbf{P}_T \vec{\boldsymbol{\Sigma}}_{\mathbf{d}_s}^a = \mathbf{P}_T [\vec{\boldsymbol{\Sigma}}_{\mathbf{d}_s}^a [0]; \dots; \vec{\boldsymbol{\Sigma}}_{\mathbf{d}_s}^a [m]; \dots; \vec{\boldsymbol{\Sigma}}_{\mathbf{d}_s}^a [M - 1]]$

**Return**

---

**Algorithm 13.14** Factorize  $\mathbf{P}_T \vec{\boldsymbol{\mu}}_{\mathbf{d}_s}^a$  and  $\mathbf{P}_T \vec{\boldsymbol{\Sigma}}_{\mathbf{d}_s}^a$  into  $M$  subsystems  $(\vec{\boldsymbol{\mu}}_{\mathbf{d}_s}^a, \vec{\boldsymbol{\Sigma}}_{\mathbf{d}_s}^a)[m]$

---

- 1: **for**  $m = 0$  to  $M - 1$  **do**
- 2:    $\vec{\mathbf{q}} = [mN_T K_{\text{on}} + 1 : (m + 1)N_T K_{\text{on}}]$
- 3:    $\vec{\boldsymbol{\mu}}_{\mathbf{d}_s}^a [m] = (\mathbf{P}_T \vec{\boldsymbol{\mu}}_{\mathbf{d}_s}^a)[\vec{\mathbf{q}}]$
- 4:    $\vec{\boldsymbol{\Sigma}}_{\mathbf{d}_s}^a [m] = (\mathbf{P}_T \vec{\boldsymbol{\Sigma}}_{\mathbf{d}_s}^a)[\vec{\mathbf{q}}]$
- 5: **end for**

**Return:**  $M$  subsystems  $(\vec{\boldsymbol{\mu}}_{\mathbf{d}_s}^a, \vec{\boldsymbol{\Sigma}}_{\mathbf{d}_s}^a)[m]$

---

lines 9 and 11, assign for blocks 7 and 9. Algorithm 13.2 corresponds to block number 1 in the diagram of Figure 33. It performs system factorization in the **FD**. Algorithms 13.2, 13.5, 13.11 and 13.14 comprehend the factorization procedures identified as block numbers 1, 4, 10 and 13, in this order.

With respect to computational effort comparison, it is reasonable to consider the estimation processes at lines 1, 4, 7 and 13, detaining the majority of overall complexity on executing Algorithm 13. Since demapping and decoding are, in general, common tasks in every digital communication system, it is sufficient to express the **MMSE-PIC** detector complexity by

$$\mathcal{O}_{\text{PIC}} \left( N_R \mathcal{O}(\mathcal{F}_N) + t_o (M \mathcal{O}_{\text{icl}} + 2N_T K_{\text{on}} \mathcal{O}_{\text{cg}}) \right), \quad (6.5)$$

where the first term is the dominant cost in the initialization step, corresponding to the transformation of the received **TD** signal to the **FD** in Algorithm 13.1, assuming that **CFR** estimate is already available. The second term comprehends  $t_o$  **PIC** iterations with three internal linear estimation stages, lines 4, 7 and 13 in Algorithm 13. The first estimation stage employs  $M$  parallel instances of the function  $\Theta_{\text{icl}}$  to solve each  $N_T K_{\text{on}} \times N_T K_{\text{on}}$  band diagonal system with single-side bandwidth  $N_T$ . From (4.27), the complexity involved on refining the sample-frequency domain signal is

$$\mathcal{O}_{\text{icl}} \left( 32N_T^3 K_{\text{on}} + 56N_T^2 K_{\text{on}} [2N_T]_2 + 48N_T^2 K_{\text{on}} - 42N_T K_{\text{on}} [2N_T]_2 - 9N_T K_{\text{on}} \right). \quad (6.6)$$

Second and third stages perform time-frequency conversion s.t. each stage employs  $N_T K_{\text{on}}$  parallel instances of the estimator function  $\Theta_{\text{cg}}$ . Here, the linear transform refers to  $M$ -point **DFT** matrices. Retrieving (4.32) and considering up to  $M$  iterations in the **CG** algorithm, which, according to [1], close achieves the exactly solution, has a computational cost given by

$$\mathcal{O}_{\text{cg}} \left( 16M^3 + 57M^2 + 10M + 2M \log(M) + 1 \right). \quad (6.7)$$

In [1], the author presents the complexity of both OFDM and GFDM in Big- $\mathcal{O}$  notation, restrained to highest order terms only, disregarding their coefficients. Hence, replacing  $\tilde{\mathcal{O}}_{\text{icl}} \approx N_{\text{T}}^3 K_{\text{on}}$  and  $\tilde{\mathcal{O}}_{\text{cg}} \approx M^3$  in (6.5) allows one to write

$$\mathcal{O}_{\text{GFDM}} \left( N_{\text{R}} M K \log(MK) + t_{\text{o}} N_{\text{T}}^3 M K_{\text{on}} + t_{\text{o}} 2 N_{\text{T}} M^2 K_{\text{on}} \right), \quad (6.8)$$

which is the dominant complexity order of the MMSE-PIC detector, considering the NO-GFDM. Just for comparison purpose, and still referring to [1], the equivalent computational order applying the straight-forward implementation of the SISO MMSE-PIC demapping operation for OFDM with symbol length  $MK$ , allocating  $MK_{\text{on}}$  active subcarriers, is approximately given by

$$\mathcal{O}_{\text{OFDM}} \left( N_{\text{R}} M K \log(MK) + t_{\text{o}} N_{\text{T}}^3 M K_{\text{on}} \right). \quad (6.9)$$

Comparing (6.8) and (6.9), both systems exhibit similar order of complexity. Moreover, the MMSE-PIC offers linear computational cost w.r.t. the number of active subcarriers  $K_{\text{on}}$ . By supporting a solution over the factorized system, in the sample-frequency domain, it also admits high-level pipeline and parallel processing.

## 6.2 Analysis on Iterative MMSE-PIC Detection Technique

This section presents the results obtained by a Monte Carlo simulation considering solely the aforementioned iterative MMSE-PIC method, which, according to [58], is the most prominent detection technique for the SM-MIMO application in terms of performance and complexity. The main motivation for this section is to reproduce the final results from [1] as a reference, to validate the accuracy of this work's interpretation. This step is essential before conducting a deeper analysis in a different scenario or any practical implementation.

The reference simulation considers a  $4 \times 4$  MIMO system under practical LTE ETU (*Extended Typical Urban*) channel model defined by 3GPP, with a maximum delay spread of 5  $\mu\text{s}$ . Table 11 shows the PDP (*Power Delay Profile*) and its equivalent base band nearest discrete time indexes, for a sampling frequency of  $f_{\text{s}} = 23.04$  MHz. Coincident indexes have their average power  $\sigma_l^2$  summed. Every simulated CIR between any transmitting and receiving antennas are normalized by  $\sqrt{\sum_{l=0}^{L-1} |h_{i,j}[l]|^2}$ .

Table 11 – Power delay profile of 3GPP ETU channel.

$\tau_l$ [ $\mu\text{s}$ ]	0	50	120	200	230	500	1600	2300	5000
$\text{round}(f_{\text{s}}\tau_l)$	0	1	3	5	5	12	37	53	115
$\sigma_l^2$ [dB]	-1.0	-1.0	-1.0	0.0	0.0	0.0	-3.0	-5.0	-7.0

In [1], the frame structure is briefly described. To complete the set of simulation parameters, this work proposes a practical frame structure that includes pilot-symbol

Table 12 – Simulation parameters.

Description	Symbol/Parameter	Value
Number of antennas	$[N_T, N_R]$	[4, 4]
Bits per symbol and coding rate	$[\mu, r]$	[4, 1/2]
Channel coding	{Convolutional; BCJR}	{7, [171, 133]; Log-MAP}
Code-word length	$N_c$	1008
Channel model	{PDP, CSIR}	{ETU, Perfect}
Blocks per frame	[#Preambles, #Data]	[1, 7]
Allocated subcarriers	$[K_{on}, K]$	[3, 128]
Allocated subsymbols	$[M_{on}, M]$	[12, 12]
Prototype filter and roll-off	$\{g, \alpha\}$	{RC, 1}
CP and time-window samples	$[N_{cp}, N_w]$	[384, 16]
Block and frame duration [ $\mu$ s]	$[T_B, T_F]$	[84.7, 931.4]
Block and frame efficiency [dB]	$[\eta_B, \eta_F]$	[-1.04, -0.58]
SNR	$1/\sigma_w^2$	$\mu r E_b/N_0$

preambles for joint synchronization and channel estimation purposes [112, 113], where all antennas simultaneously transmit orthogonal sequences. Figure 34 depicts the proposed arrangement, where  $N_t$  is the total number of samples including the CP and windowing. The frame length in samples is given by  $N_f$ . Following the preamble,  $N_s = 7$  data blocks are transmitted, carrying  $N_T$  codewords of 1008 bits after coding rate 1/2 convolutional encoding. Data QAM symbol modulation with  $\mu = 4$  bits per symbol are transmitted by each resource element. The channel decoder employs SISO log-MAP BCJR algorithm [109]. In order to meet the low OOB emission, a ramp-up and ramp-down RC time-window is used. To mitigate IBI, the CP duration is 16.7  $\mu$ s.

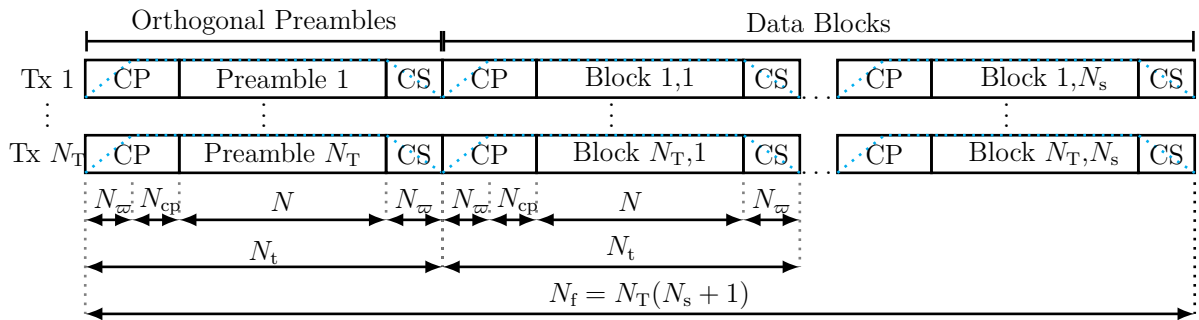


Figure 34 – Proposed frame structure for the SM-MIMO system with iterative MMSE-PIC detection.

Table 12 summarizes the simulated parameters, where the bandwidth of a single GFDM subcarrier equals a PRB (*Physical Resource Block*) of an LTE system.

The relation between symbol and bit energy can be obtained from

$$\frac{E_s}{N_0} = \mu r \frac{E_b}{N_0} \quad (6.10)$$

and the corresponding SNR, considering the proposed frame structure, is given by

$$\text{SNR} = \frac{E_s}{N_0} N_T \frac{R_b}{B} = \mu r \frac{E_b}{N_0} \frac{N N_s}{N_f}, \quad (6.11)$$

where  $r$  is the channel coding rate,  $R_b$  is the useful bit rate in bits/s,  $B = K_{\text{on}} f_s$  is the occupied bandwidth,  $N_f = N_t(N_s + 1)$  and the equivalent base band noise variance is  $\sigma_{\tilde{w}}^2 = N_0$ .

Figure 35 presents the BER and the FER curves of the simulated system. The BER curves represents a 1x1 system used to demonstrate the exactness of noise calibration by comparing the orthogonal case, when  $\alpha = 0$ , with theoretical curves assuming AWGN and flat Rayleigh channels. In the same figure, the FER curve is plotted against the reference curve from [1], showing the preciseness of the MMSE-PIC interpretation for NO waveforms, which simulates the reception of 3 allocated PRB, simultaneously transmitted by  $N_T = 4$  antennas over an ETU channel, assuming constant CIR during the frame period.

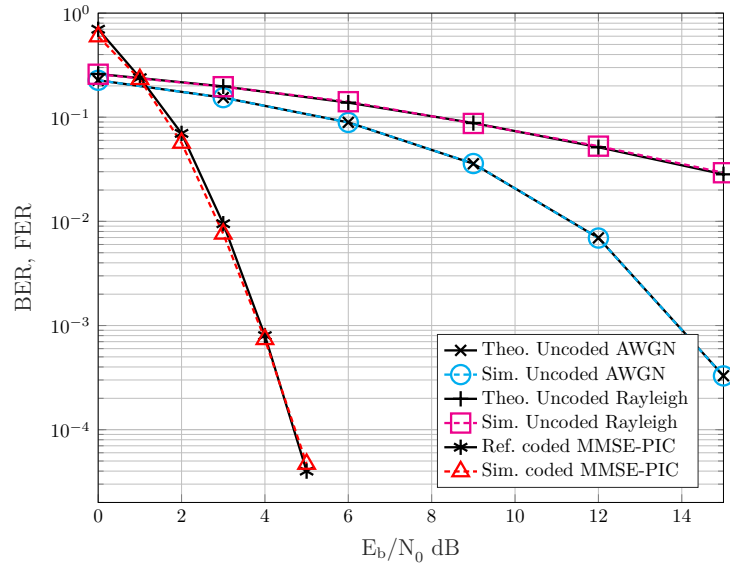


Figure 35 – Uncoded BER of a 1x1 system over AWGN and flat Rayleigh channels besides coded FER of a 4x4 SM-MIMO-NO-GFDM employing the iterative MMSE-PIC detector.

Allocating all 83 available PRB results in an occupied BW (*Bandwidth*) of 15 MHz and a gross bit rate of 120 Mbps, equivalent to a total throughput of approximately 60 Mbps considering the channel coding rate  $r = 1/2$ . In terms of coverage, the CP protection ensures links up to 30 km. These results show that the iterative MMSE-PIC algorithm is indeed a prominent tool capable of achieving the ML lower bound with affordable complexity and low latency. Further improvements might be achieved by improving the efficiency of the coding technique, while a new numerology for the frame structure can also be proposed to improve the coverage.

Table 13 presents a computational cost comparison by summarizing the complexity order taking the principal terms from (5.2), (5.20), (5.24), (6.8) and (6.9), assuming that both OFDM and GFDM have the same number of active resources. It is important to highlight the property of OFDM factorization in the frequency domain, which results in  $K_{\text{on}}$  subsystems with dimension  $N_{\text{R}} \times N_{\text{T}}$ . The expressions have been adjusted accordingly to this scenario.

Table 13 – Complexity order summary for OFDM and NO-GFDM detection.

Detector	OFDM		NO-GFDM	
	System Order	Complexity	System Order	Complexity
MLD	$K_{\text{on}}$	$N_{\text{R}}K \log(K) + K_{\text{on}}M_{\text{c}}^{N_{\text{T}}}$	$M$	$N_{\text{R}}N \log(N) + MM_{\text{c}}^{N_{\text{T}}K_{\text{on}}}$
SD				
MMSE-SIC	Subsystems	$N_{\text{R}}K \log(K) + N_{\text{T}}^3 K_{\text{on}}$	Subsystems	$N_{\text{R}}N \log(N) + MN_{\text{R}}^3 K^3 N_{\text{T}}K_{\text{on}}$
MMSE-PIC	$N_{\text{R}} \times N_{\text{T}}$	$N_{\text{R}}K \log(K) + t_{\text{o}}N_{\text{T}}^3 K_{\text{on}}$	$N_{\text{R}}K \times N_{\text{T}}K_{\text{on}}$	$N_{\text{R}}N \log(N) + t_{\text{o}}N_{\text{T}}^3 N_{\text{on}} + 2t_{\text{o}}MN_{\text{T}}N_{\text{on}}$

An exponential complexity order in  $N_{\text{T}}$  for the OFDM and  $N_{\text{T}}K_{\text{on}}$  for GFDM is characteristic in MLD and it is an upper bound for the SD, making this detectors prohibitive for NO detection, despite of achieving optimal performance. The MMSE-SIC detector presents the smallest cost for OFDM detection but pays a high penalty in terms of BER performance. For the NO-GFDM, the SIC detector follows a quartic complexity growth assuming  $N_{\text{R}}=N_{\text{T}}$  and  $N=N_{\text{on}}$ , which, besides poor performance, makes it unattractive. The iterative MMSE-PIC shows an affordable complexity for both multicarrier modulations, being linear w.r.t. the number of active resources while offering potential to close approach the ML performance. The complexity difference between OFDM and NO-GFDM is a quasi-linear increment caused by the additive term  $2t_{\text{o}}MN_{\text{T}}N_{\text{on}}$ . These facts makes the iterative MMSE-PIC a natural choice for the SM-MIMO implementation employing the NO-GFDM.

### 6.3 Summary

This chapter provides a comprehensive explanation of the iterative MMSE-PIC detector, focusing on NO waveforms as an advanced technique to simultaneously achieve multiplexing and diversity gains. It also examines the frame structure and evaluates the detection performance in terms of energy efficiency, throughput, and cell coverage. By reproducing the FER simulation results from [1], it validates the algorithm's interpretation, which is a crucial step before future hardware implementation. This advanced detector

---

demonstrated near-optimal performance with manageable complexity, making it suitable for SM-MIMO applications including NO waveforms. The topics addressed in this chapter were published in [114]. Next chapter will explore practical aspects and the challenges to adapt the iterative MMSE-PIC detector to meet the requirements of remote areas in the Brazil 6G Project.

## 7 Low-Complexity 6G Transceiver for Remote Areas

Foreseen application scenarios for 6G networks are already under discussion, indicating that achieving the expected increase in flexibility of use cases may present even greater challenges. It is evident that future mobile networks cannot rely solely on a single radio access infrastructure. Instead, they will require the incorporation of enabling technologies to address several scenarios and supporting contrasting requirements. By integrating **SM-MIMO** schemes with detection schemes capable of leveraging diversity and multiplexing gains, alongside **NO** waveforms like **GFDM**, there is significant potential to enhance data transmission rates and expand coverage. These are essential features for some applications envisioned for **6G**, mainly in remote and rural areas.

This chapter outlines the **eRAC** scenario and provides an overview of the proposed **6G** transceiver in the **TVWS** regime, detailing the parameters used in the simulation, with the aim of providing a valuable reference point for future practical evaluation of the proposed transceiver implementation. Performance analysis is performed using Monte Carlo simulations to assess this communication system, designed to offer robust, long-range, and cost-effective connectivity in remote areas.

### 7.1 Remote and Rural Areas Use Case Scenario

The conservative standardization process of **5G-NR** (*5G New Radio*) has limited the application potential of **5G** networks across various verticals [115]. Sectors crucial to the social and economic development of Brazil, as well as other countries—such as agribusiness, logistics, and mining—require connectivity in remote and rural areas, a challenge not easily addressed by **5G-NR**. Particularly in Brazil, a significant digital gap persists between urban and rural areas, with urban coverage at approximately 65%, contrasting with only 34% at rural areas [34]. Remote areas are characterized by low population density and limited services, including restricted Internet access and a scarcity of basic facilities like schools, health centers, and supermarkets. On the other hand, solutions tailored for remote scenarios drive innovation, offering resources such as automated machinery, production traceability, transport logistics, **IoT** connectivity, remote maintenance, livestock monitoring, and other intelligent agricultural services. These solutions also help in reducing digital exclusion in specific communities. This objective aligns with the United Nations' sustainable development goals, aiming to establish resilient infrastructures for inclusive and sustainable industrialization, while promoting global innovation through

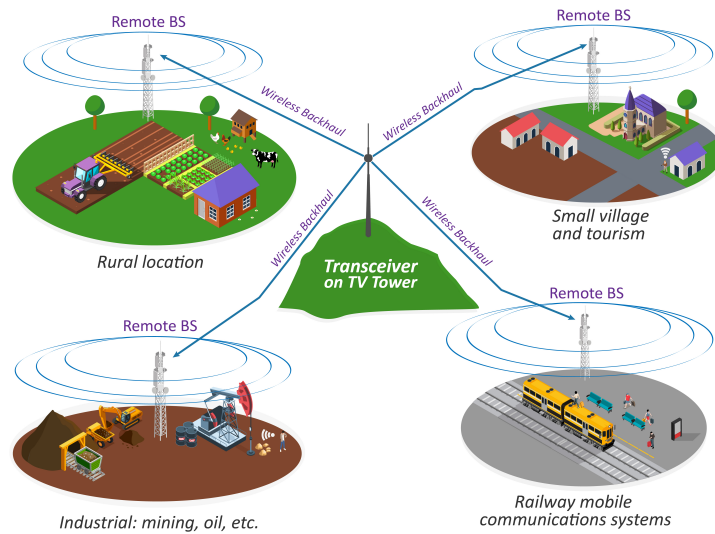


Figure 36 – Envisioned wireless backhaul scenario connecting interest remote areas.

universal Internet access [116]. This emphasizes the need for communication capabilities in remote areas, in which a 6G radio access network must achieve comprehensive coverage in such regions.

Due to conflicting requirements in 6G networks, a single numerology cannot efficiently accommodate all possible demands. Both 5G-NR and 5G-RANGE proposed frames supporting multiple numerologies to cover a large set of use cases, a strategy that will be probably adopted by 6G networks. Particularly, as outlined in [35], the requirements for wireless backhaul and local high-quality connections are met with numerology number 0. This involves facilitating data transport between the core network and specific small cells located in remote areas as illustrates by Fig. 36, a scenario considered here to the proposed transceiver implementation. The wireless backhaul approach holds value for extending coverage to remote regions, like tourist destinations, schools, industrial or agricultural facilities, remote railway stations and mining areas.

The proposed scenario primarily operates the radio access network in the 700 MHz band or below, aiming for extensive coverage with cells of 50 km radius. This strategy leverages TV transmission infrastructure, such as towers and frequency channels, for implementing wireless backhaul in remote areas, where TV coverage is robust and underused, defining it as a TVWS system. By installing the 6G transceiver BSs (*Base Stations*) on TV towers, LoS (*line-of-sight*) links can be established using idle UHF channels directed towards small remote locations. In these areas, other BSs cells are situated in rural zones. This link operates transparently, connecting small cells to the central network infrastructure, enabling mobile users to connect to these remote BSs. To exploit channel vacancies in the TVWS regime, typically with a bandwidth between 6 to 8 MHz, where aggregating multiple channels is not always feasible, high spectral efficiency becomes crucial. High-order modulation may need high transmission power to maintain long-distance cove-

range. Thus, employing SM-MIMO schemes with a moderate number of antennas in both transmitters and receivers proves viable. Also, ensuring low OOB emission is essential to ensure coexistence with incumbents, a feature that is guaranteed by GFDM. Extended link range creates multiple propagation paths, complicating the communication channel and requiring efficient detectors like the iterative MMSE-PIC. Regarding user experience KPIs (*key performance indicators*), each remote BS in the wireless backhaul scenario typically covers a small area with low UE (*User Equipment*) density. It must ensure a high throughput connection of 100 Mbps, utilizing three to four TV channels, equivalent to approximately 24 MHz. The wireless backhaul channel typically exhibits a long-range and doubly dispersive profile [117].

## 7.2 Implementation Characteristics

The 6G transceiver is largely based on 5G-RANGE frame structure, specifically the numerology number 0, with slightly modifications in PHY to support NO waveforms and SISO decoding [37, 35]. The NO-GFDM symbols are protected from the dispersive transmission channel by an additional CP and CS, incorporating a ramp-up and ramp-down RC windowing to meet the required low OOB emission. The system's non-orthogonality occurs with a non-zero  $\alpha$  roll-off factor for the adopted transmission filter, introducing intentional self-interference in the form of controlled ICI, where a suitable detector can benefit from extra frequency diversity. In the transmitter, an orthogonal IFPI approach, as in [62], is used to allocate reference pilot symbols from each transmitting antenna in non-coincident specific bins, far from the interference of data subcarriers as much as possible. This allows settled frequency domain channel estimation methods to be applied by the receiver.

Regarding channel coding, the same PC used in 5G-RANGE is also adopted. However, a countermeasure is needed to address the fact that polar decoding is essentially a hard-output process [75]. Moreover, recent CA-SCL (*Cyclic Redundancy Check (CRC)-Aided Successive Cancellation List (SCL)*) polar decoding still cannot generate soft estimates of the codeword bits [63], which are fundamental for iterative cancellation during the exchange of soft information between the demapper and decoder. To overcome this problem, a LLPD is used to generate re-encoded LLRs for the iterative detection method presented in Chapter 6, illustrated in Fig. 33. Basically, de-mapped LLRs are hard decoded by the CA-SCL polar algorithm, which maintains a list of the most probable codewords throughout the process. The most promising decoded information is re-encoded to update the initial LLRs sign. These updated LLRs are then processed by an LDPC (*Low-Density Parity-Check*) decoding algorithm, employing a sparse parity-check matrix derived from the polar generator matrix [118]. This process produces soft

codewords for subsequent iterations. As an alternative to polar FEC, CC and a BCJR decoders [109] are also considered. According to [1], this combination performs better than LDPC for short-length codewords in a similar schema.

An integer number of codewords carrying 2048 bits are transmitted per sub-frame, depending on the amount of allocated RBs (*Resource Blocks*). Eventually, bit stuffing is used to exactly fit coded bit sequences in the available REs (*Resource Elements*). Bit interleaving is also implemented to spread the information across time, frequency, and space resources, which is an essential feature to improve the robustness against burst errors.

Fig. 37a illustrates the frame structure in time domain jointly with the time-frequency grid in Fig. 37b, detailing the content of the first available RBs. The resource allocation among UEs occurs every 4.6 ms sub-frame period, comprehending two consecutive GFDM block symbols with  $K = 16384$  and  $M = 4$  for  $f_s = 30.72$  MHz sampling frequency. The fragmented spectrum allocation, required for TVWS operation, is achieved by selecting integer number of RBs, each one equivalent to  $K_{\text{on}} = 96$  subcarriers or 180 kHz bandwidth. In total, up to  $N_{\text{RB}} = 132$  or 23.76 MHz can be continuously allocated. In this case, the simulated transceiver achieves up to 72.6 Mbps and 145.2 Mbps throughput for the  $2 \times 2$  and  $4 \times 4$  SM-MIMO systems, respectively.

Fig. 37c allows to visualize the disposal of the IFPI technique alongside data subcarriers for different values of the filter roll-off parameter. For unitary  $\alpha$ , the inserted pilot pair suffers interference from surrounding data subcarriers and should be avoided. Conversely, for  $\alpha \leq 0.9$ , these interference decays rapidly as illustrated. Since the over-sampled rate in frequency domain is governed by the number of subsymbols and, in order to achieve interference free insertion, the number of orthogonal pilots inserted at each GFDM reserved pilot subcarrier is limited to a single pair, once the proposed application defines  $M = 4$ .

Table 14 provides a summary of the key parameters of the radio frame used in the implementation of the proposed 6G transceiver evaluated in this chapter. In view of system dimension, the use of sparse matrices in the frequency domain becomes imperative, as it leads to memory storage saving and speeds up the permutation process through direct index arithmetic operations.

### 7.3 Performance evaluation

Two scenarios are analyzed in this section, a  $2 \times 2$  and a  $4 \times 4$  SM-MIMO, comparing the performance of the MMSE-PIC detector with PC and CC FECs. It considers  $N_{\text{RB}} = 4$  allocated resource blocks, simultaneously transmitted by  $N_{\text{T}} = \{2, 4\}$  antennas. It is also assumed CDL (*Clustered Delay Line*) channel model D [117, 119] with perfect CSIR during



Table 14 – 6G transceiver frame parameters.

Parameter	Description	Value
$M, K$	Available subsymbols and subcarriers	4, 16384
$N$	Available resources (symbol length)	65536
$K_{\text{on}}^{(\text{RB})}$	Active subcarriers per RB	96
$K_{\text{off}}$	Inactive subcarriers (guard band)	3712
$N_{\text{on}}^{(\text{pilot})}, N_{\text{on}}^{(\text{data})}$	Active resources per RB	96, 672
$\text{BW}_{\text{RB}}$	RB bandwidth [kHz]	180
$N_{\text{RBmax}}$	Maximum available RBs	132
$N_{\text{cp}}, N_{\text{cs}}=N_{\text{w}}$	CP and CS length [samples]	3584, 768
$N_{\text{t}}$	Total symbol length	70656
$f_{\text{s}}$	Sampling frequency [MHz]	30.72
$T_{\text{sf}}$	Sub-frame period [ms]	4.6
$R_{\text{s}}$	Symbol rate (all RBs) [MSps]	19.28
OBW	Occupied BW (all RBs) [MHz]	23.76

normalized by its squared root energy. In all cases, each active data RE carries  $\mu = 4$  bits per symbol, mapped in a 16-QAM constellation. Channel code rate is  $r = 1/2$  for the CC FEC, which employs the generator polynomial  $[133, 171]_8$  and encodes 1023 bits per sub-frame. For the PC, the rate is  $r \approx 1/2$ , where 16-bit CRC (*Cyclic Redundancy Check*) is appended to 1024 uncoded bits and produces 2048 coded bits. At the receiver, the CA-SCL LLPD uses a list size of 16, and the LDPC decoder is limited to 200 iterations. Tables 15, 16 and 17 detail the adopted parameters for the simulations.

Table 15 – 6G transceiver simulation parameters.

Parameter	Description	Value
$N_{\text{RB}}$	number of resource blocks	4
$N_{\text{RE}}$	number of resource elements	2688
$\mu$	bits per symbol	4
$r$	FEC rate	$K_{\text{FEC}}/N_{\text{FEC}}$
$N_{\text{cb}}$	number of coded bits	10752
$t_{\text{o}}$	number of PIC iterations	10
$t$	number of CG iterations	4
$f_{\text{s}}$	sampling frequency [MHz]	30.72
OBW	occupied bandwidth [kHz]	720
$\vec{h}_{i,j}$	equivalent base band channel	CDL-D
$L$	number of taps	40
$h_{\text{norm}}$	channel power normalization	$\vec{h}_{i,j}^{\text{H}} \vec{h}_{i,j}$
$\sigma^2$	noise variance	$1/(\mu r E_{\text{b}}/N_0)$
$\vec{g}$	prototype pulse	RC FD
$\alpha$	roll-off factor	0.5

Fig. 38a illustrates the FER performance of the simulated  $2 \times 2$  system, comparing the 5G-RANGE transceiver and the proposed 6G transceiver. For a fair performance comparison, both systems were configured with an orthogonal GFDM waveform (i.e.,

Table 16 – 6G transceiver FEC simulation parameters.

Parameter	Description	Polar	Conv.
$K_{\text{FEC}}$	input message length	1040	1023
$N_{\text{FEC}}$	output message length	2048	2046
$N_{\text{cw}}$	number of codewords	5	5
$N_{\text{sb}}$	number of stuff bits	512	522
$N_{\text{ub}}$	number of uncoded bits	5120	5115
CC	Chanel coding	16-bit CA	[133, 171] <sub>8</sub>
CD	Chanel decoding	CA-SCL-LLPD	BCJR

Table 17 – 6G transceiver SM-MIMO simulation parameters.

Parameter	Description	$2 \times 2$	$4 \times 4$
$R_{\text{b}}$	throughput [Mbps]	2.22	4.44
$\eta$	spectral efficiency	3.089	6.167
$\text{SNR}_{\text{dB}} - (E_{\text{b}}/N_0)_{\text{dB}}$	SNR to $E_{\text{b}}/N_0$ ratio	5.11	8.12

$\alpha = 0$ ) and hard Polar decoding in a non-iterative detection setup, as employed by the **5G-RANGE** transceiver. In the same figure, we also compare the proposed transceiver operating in the **NO** format, with  $\alpha = 0.5$ , arbitrarily chosen, and with iterative **MMSE-PIC** detection for two different **SISO** decoding approaches, the **CA-SCL LLPD** and the **BCJR** decoder. This comparison enables the analysis of both **PC** and **CC** performance. The curve obtained using a **GAD** serves as a **ML** lower bound reference. The **CC** outperforms the **PC**, but exhibits poor performance compared with the **GAD**. This happens as a result of the insufficient diversity of the  $2 \times 2$  system.

Fig. 38b plots the  $4 \times 4$  **FER** performance with the corresponding **GAD**. In both  $2 \times 2$  and  $4 \times 4$  cases, the **CC**, although less powerful, performs better than **PC** in the context of iterative detection. The **GAD** curves are derived from the detector using the **BCJR** decoder. This is because the distance of the detected codeword using **PC** is consistently greater than the distance between the transmitted and received signals, resulting in no frame errors by **GAD**. It is observed that the transceiver with the iterative **MMSE-PIC** detector with **BCJR** exhibits a **FER** closer to the **ML** lower bound compared to the polar-based detector. This behavior is more pronounced in the  $4 \times 4$  **SM-MIMO** system, primarily due to the additional spatial diversity from the increased number of antennas and partly due to the wider spread range of bit interleaving. It should be mentioned that, despite increased system interference according to the number of transmitting antennas, iterative **MMSE-PIC** is capable of addressing the entire system while harvesting diversity and multiplexing gains.

Figure 38c analyzes the convergence behavior of iterative detectors in a  $4 \times 4$  system, specifically comparing **PC** and **CC** performances along successive iterations. This analysis helps determine the optimal number of iterations based on estimated **SNR**. Selecting the optimal number of iterations is a critical task for minimizing computational

costs and latency in the PIC algorithm. Notably, while PC shows diminishing returns beyond 4 iterations, whereas CC consistently improves FER up to 8 iterations.

In Fig. 38d, the MMSE-PIC complexity expressions were evaluated, demonstrating a cubic growth in complexity with the number of antennas, while keeping a linear behavior with respect to the number of active REs, given by  $N_{\text{on}}$ . Additionally, a linear increase in complexity with the number of iterations is observed. In all cases, the detection cost of GFDM is comparable to OFDM, attesting the low-complexity characteristic of the proposed method.

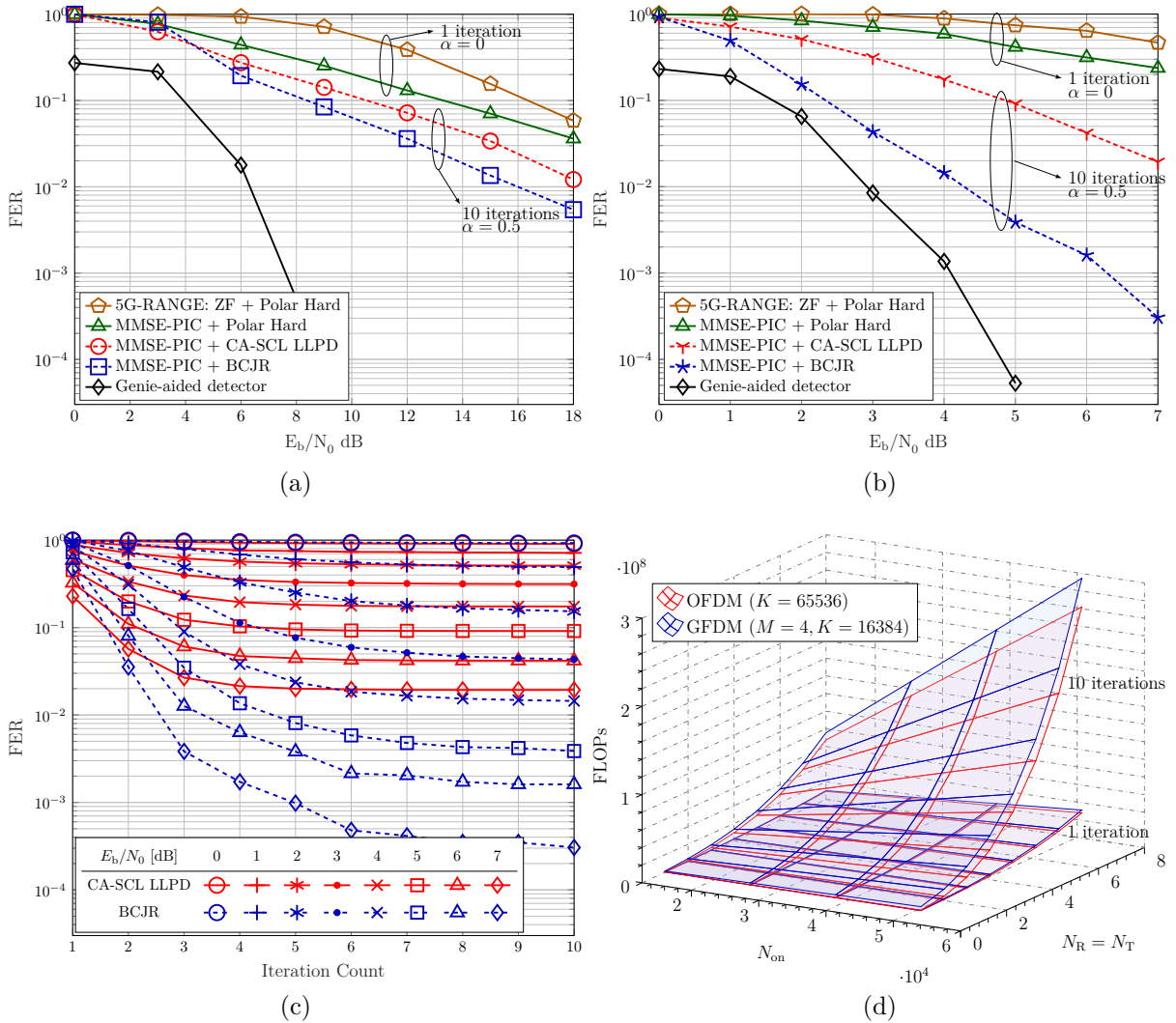


Figure 38 – (a): FER comparison of 5G-RANGE and iterative MMSE-PIC detector for a 2x2 SM-MIMO application in CDL-D channel; (b): FER results for the augmented 4x4 SM-MIMO system and (c): corresponding iterative MMSE-PIC convergence behavioral; (d): Low complexity detection aspect of GFDM, comparable to OFDM.

The FER performance of this scheme were evaluated and compared with the ML lower bound from a GAD, considering the involved aspects for the proposed frame structure. The preliminary simulation results presented herein demonstrate that the transceiver

offers a feasible approach to address the highly diverse and challenging requirements of emerging 6G mobile networks.

## 7.4 Summary

This chapter details the proposed low complexity 6G transceiver based on NO-GFDM-SM-MIMO and the iterative interference cancelation technique for the eRAC scenario. Recent advances were used to support NO-GFDM waveforms within the radio frame based on adopted 5G-RANGE, employing IFPI and SISO LLPD.

The FER results were obtained through Monte Carlo simulations of the iterative MMSE-PIC detector, suitable for the wireless backhaul scenario described in Section 7.1. The radio frame follows the numerology number zero from 5G-RANGE, adapted to support NO waveforms. This set of parameters imposes several challenges to practical implementation using a NO waveform. Countermeasures to overcome these challenges required different advanced techniques. Among them, it is possible to highlight the strictly sparse representation of the entire system, the usage of IFPI for timing recovery and CFR estimation, and SISO decoding employing LLPD. This chapter is based on [121] and supports [122].

## 8 Conclusion

Across all generations of mobile communications, the constant technological evolution is evident. Over the last few decades, each successive generation has supported higher data rates, lower latency, wider coverage, and an increased number of users. Recently, mobile communications have expanded into various scenarios, each with specific and often conflicting requirements. Consequently, flexibility has become a crucial characteristic in designing different radio solutions to meet all these requisites.

The eRAC scenario is critically important, especially for countries with vast continental areas, like Brazil. It aims to promote economic growth and social transformation in isolated regions by improving infrastructure and connectivity. The main requirements for the eRAC are high data rate, long range and low OOB emission. Improved spectral efficiency supports wireless backhaul operation, granting high data rates for users. Low spurious emission ensures compliance with opportunistic vacancy channel usage, a common situation in isolated areas. Long range links are supported by the diversity gain of the MIMO system and by the high efficiency of the CP use presented in GFDM.

In this context, GFDM stands out as a strong candidate to address diverse scenarios due to its ability to jointly offer the necessary flexibility and low OOB. To achieve the required spectral efficiency, SM-MIMO employing NO waveform and iterative MMSE-PIC detection, as introduced in [1], can closely approach optimal performance.

With the aid of detailed algorithms and the factorization expressions proposed in this thesis, the process of adapting the iterative MMSE-PIC to address the eRAC scenario becomes more structured and precise. This adaptation not only results in a feasible reference model for practical implementation but also enhances the overall efficiency and performance of mobile communications in isolated regions, effectively meeting the high data rate, high robustness and low OOB emission requirements.

To this end, this thesis introduced a generic linear model for digital MIMO communication PHY, along with the fundamental concepts of GFDM waveforms. Following this, established linear estimation and detection techniques were revisited, building the necessary background to exploit the iterative MMSE-PIC algorithm. This work provided comprehensive insights into its intricate theory and practical implementation, complete with detailed block diagrams and corresponding algorithms. Understanding the deduction of permutation matrices is crucial for grasping the concept of algorithmic complexity reduction. By leveraging recent advancements, such as IFPI and SISO LLLPD, the NO-GFDM waveform was successfully adapted for use within the adopted 5G-RANGE-based radio frame. This structured approach ensures a robust framework for practical deploy-

ment across diverse and challenging scenarios, particularly in the eRAC case.

The simulation of the proposed low-complexity, low-latency iterative MMSE-PIC detector offers a benchmark for future practical evaluations of NO-GFDM-SM-MIMO transceiver implementations, serving as a reference design for future deployment. Detailed parameters are provided to support the results and serve as a guide for reproduction. The FER performance analysis, taking the GAD ML lower bound as a common reference, allowed settling CC as the best option for the iterative detection. Furthermore, a useful graphical analysis of the algorithm convergence is presented to optimize the number of PIC iterations required for efficient detection.

Finally, in terms of requirements for remote and rural areas, the proposed scheme adheres to the TVWS regime by adopting the same proven radio frame from 5G-RANGE. In terms of transmission capacity, the simulated transceiver achieves up to 72.6 Mbps and 145.2 Mbps throughput for  $2 \times 2$  and  $4 \times 4$  SM-MIMO systems, respectively, considering the allocation of all 132 available RBs, equivalent to 24 MHz.

Future research in this area includes the following possibilities.

- impact analysis of real channel estimation on FER performance;
- new numerology in order to support a higher number of antennas, improving diversity and spectral efficiency;
- study the possibility to apply the iterative MMSE-PIC detection in mMIMO employing NO-GFDM;
- design of an intellectual property library in hardware description language to speed up the linear system solution, i.e., exploiting band diagonal matrices;
- evaluation of real deployments based on this study using FPGA or SDRs (*Software-Defined Radios*).

## List of Recent Publications

58 GASPAR, D.; MENDES, L. L.; PIMENTA, T. C. *A Review on Principles, Performance and Complexity of Linear Estimation and Detection Techniques for MIMO Systems*. *Frontiers in Communications and Networks*, v. 4, 2023. ISSN 2673-530X. Disponível em: <<https://www.frontiersin.org/articles/10.3389/frcmn.2023.968370>>.

104 GASPAR, D.; MENDES, L.; PIMENTA, T. *Sphere Detector with Low Complexity Euclidean Distance Computation Based on Affine Transform Modulation*. *Electronics Letters*, Institution of Engineering and Technology (IET), ago. 2022. Disponível em: <<https://doi.org/10.1049/ell2.12594>>.

114 GASPAR, D. et al. *Spatial Multiplexing MIMO for Remote Areas employing MMSE Parallel Interference Cancellation for Non-Orthogonal GFDM*. In: 2023 International Conference on Microelectronics (ICM). [S.l.: s.n.], 2023. p. 119–124.

121 GASPAR, D. et al. *A Low-Complexity 6G Transceiver Based on the Non-Orthogonal GFDM-MIMO Signal Interference Cancellation Technique for Enhanced Communications in Remote and Rural Areas*. Submitted to IEEE Transactions on Communications. 2024.

122 Danilo Gaspar, Vanessa Mendes Rennó, Luiz Guedes e Luciano Leonel Mendes. *Transceptor para Redes 6G em Áreas Remotas e Rurais*. 2024. BR1020240211715. INPI - Instituto Nacional da Propriedade Industrial.

# Appendix

## Appendix A: LMMSE Derivation

Consider the scalar case for the estimator in (4.3) assuming  $q = 1$

$$\mu_{x_j}^p = \vec{\mathbf{W}}_j^H \vec{\mathbf{y}} + z_j \quad (\text{A.1})$$

where  $\mu_{x_j}^p$  is a random variable dependent on the random vector  $\vec{\mathbf{y}}$ , scaled by the weighting vector  $\vec{\mathbf{W}}_j \in \mathbb{C}^{p \times 1}$ , and on a constant coefficient  $z_j$ . The sub-index  $j = 1 \dots q$  is an element index for the random vector  $\vec{\mathbf{x}}_1$ . Then the equivalent MSE expression for the scalar case is

$$E_j = \mathbb{E}\left\{\left(x_j - \mu_{x_j}^p\right)\left(x_j - \mu_{x_j}^p\right)^H\right\}. \quad (\text{A.2})$$

Introducing (A.1) in (A.2) and expanding the product of differences

$$\begin{aligned} E_j = & \mathbb{E}\{x_j x_j^H\} - \mathbb{E}\{x_j \vec{\mathbf{y}}^H\} \vec{\mathbf{W}}_j - \mathbb{E}\{x_j\} z_j^H \\ & - \vec{\mathbf{W}}_j^H \mathbb{E}\{\vec{\mathbf{y}} x_j^H\} - z_j \mathbb{E}\{x_j^H\} + \vec{\mathbf{W}}_j^H \mathbb{E}\{\vec{\mathbf{y}} \vec{\mathbf{y}}^H\} \vec{\mathbf{W}}_j \\ & + \vec{\mathbf{W}}_j^H \mathbb{E}\{\vec{\mathbf{y}}\} z_j^H + z_j \mathbb{E}\{\vec{\mathbf{y}}^H\} \vec{\mathbf{W}}_j + z_j z_j^H \end{aligned} \quad (\text{A.3})$$

then applying the Complex Gradient rules [80] to the partial derivative of  $\Sigma_j^p$  with respect to  $\vec{\mathbf{W}}_j$  and  $z_j$  leads to

$$\frac{\partial \Sigma_j^p}{\partial \vec{\mathbf{W}}_j} = -\mathbb{E}\{x_j \vec{\mathbf{y}}^H\} + \vec{\mathbf{W}}_j^H \mathbb{E}\{\vec{\mathbf{y}} \vec{\mathbf{y}}^H\} + z_j \mathbb{E}\{\vec{\mathbf{y}}^H\} = 0 \quad (\text{A.4})$$

$$\frac{\partial \Sigma_j^p}{\partial z_j} = -\mathbb{E}\{x_j^H\} + \mathbb{E}\{\vec{\mathbf{y}}^H\} \vec{\mathbf{W}}_j + z_j^H = 0 \quad (\text{A.5})$$

Solving for  $\vec{\mathbf{W}}_j$  and  $z_j$ , results in

$$\vec{\mathbf{W}}_j = \left(\mathbb{E}\{\vec{\mathbf{y}} \vec{\mathbf{y}}^H\} - \mathbb{E}\{\vec{\mathbf{y}}\} \mathbb{E}\{\vec{\mathbf{y}}^H\}\right)^{-1} \left(\mathbb{E}\{\vec{\mathbf{y}} x_j^H\} - \mathbb{E}\{\vec{\mathbf{y}}\} \mathbb{E}\{x_j^H\}\right) \quad (\text{A.6})$$

and

$$z_j = \mathbb{E}\{x_j\} - \vec{\mathbf{W}}_j^H \mathbb{E}\{\vec{\mathbf{y}}\}. \quad (\text{A.7})$$

Employing the generic definitions for the mean and covariance, presented in Section 4.5, (A.6) and (A.7) can be rewritten as

$$\vec{\mathbf{W}}_j = \Sigma_{\vec{\mathbf{y}}}^{-1} \Sigma_{\vec{\mathbf{y}} x_j} \quad (\text{A.8})$$

and

$$z_j = \mu_{x_j}^a - \Sigma_{x_j \vec{y}} \Sigma_{\vec{y}}^{-1} \vec{\mu}_{\vec{y}}. \quad (\text{A.9})$$

Applying (A.8) and (A.9) into (A.1) and (A.3) results in

$$\mu_{x_j}^p = \mu_{x_j}^a + \left( \Sigma_{x_j \vec{y}} \Sigma_{\vec{y}}^{-1} \right) (\vec{y} - \vec{\mu}_{\vec{y}}) \quad (\text{A.10})$$

$$\Sigma_{x_j}^p = \Sigma_{x_j}^a - \Sigma_{x_j \vec{y}} \Sigma_{\vec{y}}^{-1} \Sigma_{\vec{y} x_j} \quad (\text{A.11})$$

From (A.10) and (A.11), it is possible to generalize the complex LMMSE estimator for the vector case ( $q > 1$ ) and its correspondent error co-variance matrix as

$$\vec{\mu}_{\vec{x}}^p = \vec{\mu}_{\vec{x}}^a + \left( \Sigma_{\vec{x} \vec{y}} \Sigma_{\vec{y}}^{-1} \right) (\vec{y} - \vec{\mu}_{\vec{y}}), \quad (\text{A.12})$$

$$\Sigma_{\vec{x}}^p = \Sigma_{\vec{x}}^a - \Sigma_{\vec{x} \vec{y}} \Sigma_{\vec{y}}^{-1} \Sigma_{\vec{y} \vec{x}}, \quad (\text{A.13})$$

where  $\Sigma_{\vec{y}}$  and  $\Sigma_{\vec{x}}^a$  are auto co-variance matrices and  $\Sigma_{\vec{x} \vec{y}} = \Sigma_{\vec{y} \vec{x}}^H$  is the cross co-variance between  $\vec{x}$  and  $\vec{y}$ . Note that (A.11), for  $j = 1 \dots q$ , are the diagonal elements of (A.13). These parameters can be rewritten in terms of the known linear transformation matrix  $\mathbf{H}$  and the a-priori statistics of  $\vec{x}$ , whose elements are mutually independent and uncorrelated with the disturbance vector  $\vec{w}$ . Then,

$$\begin{aligned} \Sigma_{\vec{x} \vec{y}} &= \mathbb{E}\{\vec{x} \vec{y}^H\} - \mathbb{E}\{\vec{x}\} \mathbb{E}\{\vec{y}^H\} \\ &= \mathbb{E}\{\vec{x} (\mathbf{H} \vec{x} + \vec{w})^H\} - \mathbb{E}\{\vec{x}\} \mathbb{E}\{(\mathbf{H} \vec{x} + \vec{w})^H\} \\ &= \Sigma_{\vec{x}}^a \mathbf{H}^H, \end{aligned} \quad (\text{A.14})$$

$$\begin{aligned} \Sigma_{\vec{y}} &= \mathbb{E}\{\vec{y} \vec{y}^H\} - \mathbb{E}\{\vec{y}\} \mathbb{E}\{\vec{y}^H\} \\ &= \mathbf{H} \mathbb{E}\{\vec{x} \vec{x}^H\} \mathbf{H}^H + \mathbb{E}\{\vec{w} \vec{w}^H\} - \mathbf{H} \mathbb{E}\{\vec{x}\} \mathbb{E}\{\vec{x}^H\} \mathbf{H}^H \\ &= \mathbf{H} \Sigma_{\vec{x}}^a \mathbf{H}^H + \Sigma_{\vec{w}}^a \end{aligned} \quad (\text{A.15})$$

and

$$\vec{\mu}_{\vec{y}} = \mathbf{H} \vec{\mu}_{\vec{x}}^a. \quad (\text{A.16})$$

Applying (A.14), (A.15) and (A.16) into (A.12) and (A.13), the final LMMSE expression is obtained as

$$\vec{\mu}_{\vec{x}}^p = \vec{\mu}_{\vec{x}}^a + \Sigma_{\vec{x}}^a \mathbf{H}^H \left( \mathbf{H} \Sigma_{\vec{x}}^a \mathbf{H}^H + \Sigma_{\vec{w}}^a \right)^{-1} (\vec{y} - \mathbf{H} \vec{\mu}_{\vec{x}}^a) \quad (\text{A.17})$$

with co-variance error matrix given by

$$\Sigma_{\vec{x}}^p = \Sigma_{\vec{x}}^a - \Sigma_{\vec{x}}^a \mathbf{H}^H \left( \mathbf{H} \Sigma_{\vec{x}}^a \mathbf{H}^H + \Sigma_{\vec{w}}^a \right)^{-1} \mathbf{H} \Sigma_{\vec{x}}^a. \quad (\text{A.18})$$

In order to express (4.4) in the same form presented in (4.3), the estimator coefficient matrix  $\mathbf{W}$  and the offset vector  $\vec{z}$  are defined by

$$\mathbf{W} = \Sigma_{\vec{x}}^a \mathbf{H}^H \left( \mathbf{H} \Sigma_{\vec{x}}^a \mathbf{H}^H + \Sigma_{\vec{w}}^a \right)^{-1}, \quad (\text{A.19})$$

and

$$\vec{z} = \vec{\mu}_{\vec{x}}^a - \mathbf{W} \mathbf{H} \vec{\mu}_{\vec{x}}^a, \quad (\text{A.20})$$

where  $\mathbf{W} = [\vec{\mathbf{W}}_1^H, \dots, \vec{\mathbf{W}}_q^H]$  and  $\vec{z} = [z_1, \dots, z_q]^T$ .

## Appendix B: STPD Derivation

In the [STPD](#) method, an iterative procedure is proposed in order to search for the optimal coefficient matrix  $\mathbf{W}$  that allows to solve the estimation problem by minimizing the mean squared error. This procedure starts from an initial guess for  $\mathbf{W}_{t-1}$  and improves it in a recursive fashion until eventually converging to the optimal solution, e.g. the [LMMSE](#) closed-form solution presented in [\(A.19\)](#). Consider the following expression,

$$\mathbf{W}_t = \mathbf{W}_{t-1} + \delta \Upsilon, \quad (\text{B.1})$$

where  $\Upsilon$  is a complex update direction matrix with dimension  $q \times p$ , whose elements are scaled by the real positive scalar  $\delta$ . These parameters must be properly chosen to ensure the convergence of  $\mathbf{W}_t$  to the optimal [LMMSE](#). The rule for selecting  $\delta$  and  $\Upsilon$  is to impose that a cost function, in this case the [MMSE](#), to monotonically decrease along iterations.

Retrieving the [LMMSE](#) linear estimator in [\(4.3\)](#) and the closed-form solution for the independent term [\(A.20\)](#), allows to define

$$\vec{\mu}_{\vec{x}}^p = \mathbf{W}\vec{y} + \vec{z}, \quad (\text{B.2})$$

$$\vec{z} = \mathbf{E}\{\vec{x}\} - \mathbf{W}\mathbf{H}\mathbf{E}\{\vec{x}\}, \quad (\text{B.3})$$

and express a quadratic cost function dependent on the coefficient matrix  $\mathbf{W}$  as follows

$$\begin{aligned} \mathbf{E} &= \mathbf{E}\{(\vec{x} - \vec{\mu}_{\vec{x}}^p)(\vec{x} - \vec{\mu}_{\vec{x}}^p)^H\} \\ &= \underbrace{\mathbf{E}\{\vec{x}\vec{x}^H\}}_1 - \underbrace{\mathbf{E}\{\vec{x}\vec{x}^H\}\mathbf{H}^H\mathbf{W}^H}_2 - \underbrace{\mathbf{E}\{\vec{x}\}\mathbf{E}\{\vec{x}\}^H}_3 + \underbrace{\mathbf{E}\{\vec{x}\}\mathbf{E}\{\vec{x}\}^H\mathbf{H}^H\mathbf{W}^H}_4 - \underbrace{\mathbf{W}\mathbf{H}\mathbf{E}\{\vec{x}\vec{x}^H\}}_5 \\ &\quad + \underbrace{\mathbf{W}\mathbf{H}\mathbf{E}\{\vec{x}\vec{x}^H\}\mathbf{H}^H\mathbf{W}^H}_6 + \underbrace{\mathbf{W}\mathbf{H}\mathbf{E}\{\vec{x}\}\mathbf{E}\{\vec{x}\}^H}_7 - \underbrace{\mathbf{W}\mathbf{H}\mathbf{E}\{\vec{x}\}\mathbf{E}\{\vec{x}\}^H\mathbf{H}^H\mathbf{W}^H}_8 + \underbrace{\mathbf{W}\mathbf{E}\{\vec{w}\vec{w}^H\}\mathbf{W}^H}_9 \\ &\quad - \underbrace{\mathbf{E}\{\vec{x}\}\mathbf{E}\{\vec{x}\}^H}_10 + \underbrace{\mathbf{W}\mathbf{H}\mathbf{E}\{\vec{x}\}\mathbf{E}\{\vec{x}\}^H}_11 + \underbrace{\mathbf{E}\{\vec{x}\}\mathbf{E}\{\vec{x}\}^H\mathbf{H}^H\mathbf{W}^H}_12 - \underbrace{\mathbf{W}\mathbf{H}\mathbf{E}\{\vec{x}\}\mathbf{E}\{\vec{x}\}^H\mathbf{H}^H\mathbf{W}^H}_13 \\ &\quad + \underbrace{\mathbf{E}\{\vec{x}\}\mathbf{E}\{\vec{x}\}^H}_14 - \underbrace{\mathbf{E}\{\vec{x}\}\mathbf{E}\{\vec{x}\}^H\mathbf{H}^H\mathbf{W}^H}_15 - \underbrace{\mathbf{W}\mathbf{H}\mathbf{E}\{\vec{x}\}\mathbf{E}\{\vec{x}\}^H}_16 + \underbrace{\mathbf{W}\mathbf{H}\mathbf{E}\{\vec{x}\}\mathbf{E}\{\vec{x}\}^H\mathbf{H}^H\mathbf{W}^H}_17. \end{aligned} \quad (\text{B.4})$$

Analyzing the expression above and enumerating its terms from left to right shows that the pair of terms 1 and 3 equals to  $\Sigma_{\vec{x}}^a$ . The pair of terms 2 and 4 jointly are equivalent to  $-\Sigma_{\vec{x}}^a\mathbf{H}^H\mathbf{W}^H$ . The pair of terms 5 and 7, together, are equivalent to  $-\mathbf{W}\mathbf{H}\Sigma_{\vec{x}}^a$  and the

terms 6 and 8 corresponds to  $\mathbf{W}\mathbf{H}\Sigma_{\bar{\mathbf{x}}}^{\mathbf{a}}\mathbf{H}^{\mathbf{H}}\mathbf{W}^{\mathbf{H}}$ . The 9<sup>th</sup> term is equal to  $\mathbf{W}\Sigma_{\bar{\mathbf{w}}}^{\mathbf{a}}\mathbf{W}^{\mathbf{H}}$  while the pair of terms, 10 and 14, 11 and 16, 12 and 15, 13 and 17, cancels each other. Then all remaining terms together yields to

$$\mathbf{E} = \Sigma_{\bar{\mathbf{x}}}^{\mathbf{a}} - \Sigma_{\bar{\mathbf{x}}}^{\mathbf{a}}\mathbf{H}^{\mathbf{H}}\mathbf{W}^{\mathbf{H}} - \mathbf{W}\mathbf{H}\Sigma_{\bar{\mathbf{x}}}^{\mathbf{a}} + \mathbf{W}\mathbf{H}\Sigma_{\bar{\mathbf{x}}}^{\mathbf{a}}\mathbf{H}^{\mathbf{H}}\mathbf{W}^{\mathbf{H}} + \mathbf{W}\Sigma_{\bar{\mathbf{w}}}^{\mathbf{a}}\mathbf{W}^{\mathbf{H}}, \quad (\text{B.5})$$

whose derivative with respect to  $\mathbf{W}$  is given by

$$\nabla_{\mathbf{W}}\mathbf{E} = \left(\mathbf{H}\Sigma_{\bar{\mathbf{x}}}^{\mathbf{a}}\mathbf{H}^{\mathbf{H}} + \Sigma_{\bar{\mathbf{w}}}^{\mathbf{a}}\right)\mathbf{W}^{\mathbf{H}} - \mathbf{H}\Sigma_{\bar{\mathbf{x}}}^{\mathbf{a}}. \quad (\text{B.6})$$

Evaluating (B.5) for iteration  $t$  and inserting  $\mathbf{W}_t$  from (B.1) leads to

$$\begin{aligned} \mathbf{E}_t &= \Sigma_{\bar{\mathbf{x}}}^{\mathbf{a}} - \Sigma_{\bar{\mathbf{x}}}^{\mathbf{a}}\mathbf{H}^{\mathbf{H}}\left(\mathbf{W}_{t-1}^{\mathbf{H}} + \Upsilon^{\mathbf{H}}\delta^{\mathbf{H}}\right) - \left(\mathbf{W}_{t-1} + \delta\Upsilon\right)\mathbf{H}\Sigma_{\bar{\mathbf{x}}}^{\mathbf{a}} \\ &\quad + \left(\mathbf{W}_{t-1} + \delta\Upsilon\right)\mathbf{H}\Sigma_{\bar{\mathbf{x}}}^{\mathbf{a}}\mathbf{H}^{\mathbf{H}}\left(\mathbf{W}_{t-1}^{\mathbf{H}} + \Upsilon^{\mathbf{H}}\delta^{\mathbf{H}}\right) + \left(\mathbf{W}_{t-1} + \delta\Upsilon\right)\Sigma_{\bar{\mathbf{w}}}^{\mathbf{a}}\left(\mathbf{W}_{t-1}^{\mathbf{H}} + \Upsilon^{\mathbf{H}}\delta^{\mathbf{H}}\right) \\ &= \underbrace{\Sigma_{\bar{\mathbf{x}}}^{\mathbf{a}}}_1 - \underbrace{\Sigma_{\bar{\mathbf{x}}}^{\mathbf{a}}\mathbf{H}^{\mathbf{H}}\mathbf{W}_{t-1}^{\mathbf{H}}}_2 - \underbrace{\Sigma_{\bar{\mathbf{x}}}^{\mathbf{a}}\mathbf{H}^{\mathbf{H}}\Upsilon^{\mathbf{H}}\delta^{\mathbf{H}}}_3 - \underbrace{\mathbf{W}_{t-1}\mathbf{H}\Sigma_{\bar{\mathbf{x}}}^{\mathbf{a}}}_4 - \underbrace{\delta\Upsilon\mathbf{H}\Sigma_{\bar{\mathbf{x}}}^{\mathbf{a}}}_5 \\ &\quad + \underbrace{\mathbf{W}_{t-1}\mathbf{H}\Sigma_{\bar{\mathbf{x}}}^{\mathbf{a}}\mathbf{H}^{\mathbf{H}}\mathbf{W}_{t-1}^{\mathbf{H}}}_6 + \underbrace{\mathbf{W}_{t-1}\mathbf{H}\Sigma_{\bar{\mathbf{x}}}^{\mathbf{a}}\mathbf{H}^{\mathbf{H}}\Upsilon^{\mathbf{H}}\delta^{\mathbf{H}}}_7 + \underbrace{\delta\Upsilon\mathbf{H}\Sigma_{\bar{\mathbf{x}}}^{\mathbf{a}}\mathbf{H}^{\mathbf{H}}\mathbf{W}_{t-1}^{\mathbf{H}}}_8 + \underbrace{\delta\Upsilon\mathbf{H}\Sigma_{\bar{\mathbf{x}}}^{\mathbf{a}}\mathbf{H}^{\mathbf{H}}\Upsilon^{\mathbf{H}}\delta^{\mathbf{H}}}_9 \\ &\quad + \underbrace{\mathbf{W}_{t-1}\Sigma_{\bar{\mathbf{w}}}^{\mathbf{a}}\mathbf{W}_{t-1}^{\mathbf{H}}}_10 + \underbrace{\mathbf{W}_{t-1}\Sigma_{\bar{\mathbf{w}}}^{\mathbf{a}}\Upsilon^{\mathbf{H}}\delta^{\mathbf{H}}}_11 + \underbrace{\delta\Upsilon\Sigma_{\bar{\mathbf{w}}}^{\mathbf{a}}\mathbf{W}_{t-1}^{\mathbf{H}}}_12 + \underbrace{\delta\Upsilon\Sigma_{\bar{\mathbf{w}}}^{\mathbf{a}}\Upsilon^{\mathbf{H}}\delta^{\mathbf{H}}}_13. \end{aligned} \quad (\text{B.7})$$

Equation (B.7) can be rewritten taken into account that terms 1, 2, 4, and 6 equals to  $\mathbf{E}_{t-1}$ . Terms 5, 8 and 12 are equivalent to  $\delta\Upsilon\nabla_{\mathbf{W}_{t-1}}\mathbf{E}_{t-1}$  as well as terms 3, 7 and 11 equals to  $(\nabla_{\mathbf{W}_{t-1}}\mathbf{E}_{t-1})^{\mathbf{H}}\Upsilon^{\mathbf{H}}\delta^{\mathbf{H}}$ . The remaining terms, 9 and 13, together, are  $\delta\Upsilon(\mathbf{H}\Sigma_{\bar{\mathbf{x}}}^{\mathbf{a}}\mathbf{H}^{\mathbf{H}} + \Sigma_{\bar{\mathbf{w}}}^{\mathbf{a}})\Upsilon^{\mathbf{H}}\delta^{\mathbf{H}}$ . Thus,

$$\mathbf{E}_t = \mathbf{E}_{t-1} + 2\delta\Re\left(\Upsilon\nabla_{\mathbf{W}_{t-1}}\mathbf{E}_{t-1}\right) + \delta^2\Upsilon\left(\mathbf{H}\Sigma_{\bar{\mathbf{x}}}^{\mathbf{a}}\mathbf{H}^{\mathbf{H}} + \Sigma_{\bar{\mathbf{w}}}^{\mathbf{a}}\right)\Upsilon^{\mathbf{H}}. \quad (\text{B.8})$$

One condition to meet the monotonically decreasing behavior of the cost function in (B.8) is to ensure that  $\mathbf{E}_t < \mathbf{E}_{t-1}$ , where the matrix inequality means that  $\mathbf{E}_{t-1} - \mathbf{E}_t$  is a non-negative definite matrix.

Since  $\delta^2\Upsilon\left(\mathbf{H}\Sigma_{\bar{\mathbf{x}}}^{\mathbf{a}}\mathbf{H}^{\mathbf{H}} + \Sigma_{\bar{\mathbf{w}}}^{\mathbf{a}}\right)\Upsilon^{\mathbf{H}}$  is positive definite matrix for all nonzero  $\Upsilon$ , as  $\left(\mathbf{H}\Sigma_{\bar{\mathbf{x}}}^{\mathbf{a}}\mathbf{H}^{\mathbf{H}} + \Sigma_{\bar{\mathbf{w}}}^{\mathbf{a}}\right)$  is a non-negative definite matrix, the update direction matrix  $\Upsilon$  must satisfy

$$\Re\left(\Upsilon\nabla_{\mathbf{W}_{t-1}}\mathbf{E}_{t-1}\right) < 0. \quad (\text{B.9})$$

This condition will guarantee that the second term in (B.8) is strictly negative and the choice of  $\Upsilon$  relies on whether  $\nabla_{\mathbf{W}_{t-1}}\mathbf{E}_{t-1}$  is zero or not. If the gradient vector is zero, then  $\mathbf{W}_{t-1}$  already coincides with the optimal solution, the recursion attained its purpose and  $\Upsilon$  should also be zero. On the other hand, if the gradient vector at  $\mathbf{W}_{t-1}$  is nonzero, there are many choices that satisfies (B.9), e.g., all  $\Upsilon = -\mathbf{B}(\nabla_{\mathbf{W}_{t-1}}\mathbf{E}_{t-1})^{\mathbf{H}}$ , for

any positive-definite matrix  $\mathbf{B}$ . This choice also results  $\Upsilon = \mathbf{0}$  whenever  $\nabla_{\mathbf{w}_{t-1}} \mathbf{E}_{t-1} = 0$ , otherwise, the product  $\Upsilon \nabla_{\mathbf{w}_{t-1}} \mathbf{E}_{t-1}$  is negative real-valued and evaluates to

$$\Upsilon \nabla_{\mathbf{w}_{t-1}} \mathbf{E}_{t-1} = -\mathbf{B} \left( \nabla_{\mathbf{w}_{t-1}} \mathbf{E}_{t-1} \right)^{\text{H}} \nabla_{\mathbf{w}_{t-1}} \mathbf{E}_{t-1}. \quad (\text{B.10})$$

A common choice is to define  $\mathbf{B} = \mathbf{I}$  which leads to the update direction matrix

$$\Upsilon = - \left( \nabla_{\mathbf{w}_{t-1}} \mathbf{E}_{t-1} \right)^{\text{H}} = \Sigma_{\mathbf{x}}^{\text{a}} \mathbf{H}^{\text{H}} - \mathbf{W}_{t-1} \left( \mathbf{H} \Sigma_{\mathbf{x}}^{\text{a}} \mathbf{H}^{\text{H}} + \Sigma_{\mathbf{w}}^{\text{a}} \right). \quad (\text{B.11})$$

Note that when  $\mathbf{W}_{t-1}$  achieves the optimal solution from (A.19), then  $\Upsilon = \mathbf{0}$ . Inserting this specific choice for  $\Upsilon$  in (B.1) yields to the final recursion

$$\mathbf{W}_t = \mathbf{W}_{t-1} + \delta \left[ \Sigma_{\mathbf{x}}^{\text{a}} \mathbf{H}^{\text{H}} - \mathbf{W}_{t-1} \left( \mathbf{H} \Sigma_{\mathbf{x}}^{\text{a}} \mathbf{H}^{\text{H}} + \Sigma_{\mathbf{w}}^{\text{a}} \right) \right]. \quad (\text{B.12})$$

Note that  $\mathbf{W}_t$  is updated towards the opposite direction of the conjugate gradient of the cost function by the scaled direction matrix  $\Upsilon$ . The choice of the scale or step-size parameter  $\delta$  is crucial and, if not chosen carefully, it can drives to undesirable results. As a rule, this parameter should be kept small ( $\ll 1$ ), ensuring convergence and, to speed up the process, optimal step-size calculation should be employed.

## Appendix C: CWCU LMMSE Derivation

Consider the  $j$ th component of the estimator

$$\mu_{x_j}^p = \vec{\mathbf{W}}_j^H \vec{\mathbf{y}} + z_j \quad (\text{C.1})$$

where  $\vec{\mathbf{W}}_j^H$  denotes the  $j$ th row of an estimator coefficient matrix. The conditional mean of  $\mu_{x_j}^p$  can be written as

$$\mathbf{E}\{\mu_{x_j}^p \mid x_j\} = \mathbf{E}\{\vec{\mathbf{W}}_j^H \vec{\mathbf{y}} + z_j\} = \vec{\mathbf{W}}_j^H \mathbf{E}\{\vec{\mathbf{y}} \mid x_j\} + z_j. \quad (\text{C.2})$$

The **CWCU-LMMSE** constraint in (C.2) can be satisfied for all  $x_j$  when the conditional mean  $\mathbf{E}\{\mu_{x_j}^p \mid x_j\}$  is a linear function of  $x_j$ . This condition occurs, e.g., when  $\vec{\mathbf{x}}$  and  $\vec{\mathbf{y}}$  are jointly complex Gaussian. In this case, the conditional mean  $\mathbf{E}\{\vec{\mathbf{y}} \mid x_j\}$  can be obtained from the jointly Gaussian **PDF** [82] by

$$\mathbf{E}\{\vec{\mathbf{y}} \mid x_j\} = \mathbf{E}\{\vec{\mathbf{y}}\} + \Sigma_{\vec{\mathbf{y}}x_j}(x_j - \mathbf{E}\{x_j\})(\sigma_{x_j}^2)^{-1}. \quad (\text{C.3})$$

Replacing (C.3) in (C.2) yields to

$$\mathbf{E}\{\mu_{x_j}^p \mid x_j\} = \vec{\mathbf{W}}_j^H \mathbf{E}\{\vec{\mathbf{y}}\} + \vec{\mathbf{W}}_j^H \Sigma_{\vec{\mathbf{y}}x_j} x_j - \vec{\mathbf{W}}_j^H \Sigma_{\vec{\mathbf{y}}x_j} (\sigma_{x_j}^2)^{-1} \mathbf{E}\{x_j\} + z_j. \quad (\text{C.4})$$

Then, from (C.4), the conditions to fulfill the **CWCU-LMMSE** constraint are

$$\vec{\mathbf{W}}_j^H \Sigma_{\vec{\mathbf{y}}x_j} (\sigma_{x_j}^2)^{-1} = 1 \quad (\text{C.5})$$

and

$$\mathbf{E}\{x_j\} - \vec{\mathbf{W}}_j^H \mathbf{E}\{\vec{\mathbf{y}}\} = z_j. \quad (\text{C.6})$$

Inserting (C.1) and (C.6) into the **MSE** function  $\mathbf{E}_j = \mathbf{E}\{(x_j - \mu_{x_j}^p)(x_j - \mu_{x_j}^p)^H\}$  leads to

$$\begin{aligned} \mathbf{E}_j = & \underbrace{\vec{\mathbf{W}}_j^H \mathbf{E}\{\vec{\mathbf{y}}\vec{\mathbf{y}}^H\} \vec{\mathbf{W}}_j}_{1} + \underbrace{\vec{\mathbf{W}}_j^H \mathbf{E}\{\vec{\mathbf{y}}\} \mathbf{E}\{x_j\}^H}_{2} - \underbrace{\vec{\mathbf{W}}_j^H \mathbf{E}\{\vec{\mathbf{y}}\} \mathbf{E}\{\vec{\mathbf{y}}\}^H \vec{\mathbf{W}}_j}_{3} - \underbrace{\vec{\mathbf{W}}_j^H \mathbf{E}\{\vec{\mathbf{y}}x_j^H\}}_{4} \\ & + \underbrace{\mathbf{E}\{x_j\} \mathbf{E}\{\vec{\mathbf{y}}\}^H \vec{\mathbf{W}}_j}_{5} + \underbrace{\mathbf{E}\{x_j\} \mathbf{E}\{x_j\}^H}_{6} - \underbrace{\mathbf{E}\{x_j\} \mathbf{E}\{\vec{\mathbf{y}}\}^H \vec{\mathbf{W}}_j}_{7} - \underbrace{\mathbf{E}\{x_j\} \mathbf{E}\{x_j\}^H}_{8} \\ & - \underbrace{\vec{\mathbf{W}}_j^H \mathbf{E}\{\vec{\mathbf{y}}\} \mathbf{E}\{\vec{\mathbf{y}}\}^H \vec{\mathbf{W}}_j}_{9} - \underbrace{\vec{\mathbf{W}}_j^H \mathbf{E}\{\vec{\mathbf{y}}\} \mathbf{E}\{x_j\}^H}_{10} + \underbrace{\vec{\mathbf{W}}_j^H \mathbf{E}\{\vec{\mathbf{y}}\} \mathbf{E}\{y\}^H \vec{\mathbf{W}}_j}_{11} + \underbrace{\vec{\mathbf{W}}_j^H \mathbf{E}\{\vec{\mathbf{y}}\} \mathbf{E}\{x_j\}^H}_{12} \\ & - \underbrace{\mathbf{E}\{x_j \vec{\mathbf{y}}^H\} \vec{\mathbf{W}}_j}_{1} - \underbrace{\mathbf{E}\{x_j\} \mathbf{E}\{x_j\}^H}_{14} + \underbrace{\mathbf{E}\{x_j\} \mathbf{E}\{\vec{\mathbf{y}}\}^H \vec{\mathbf{W}}_j}_{15} + \underbrace{\mathbf{E}\{x_j x_j^H\}}_{16}. \end{aligned} \quad (\text{C.7})$$

From (C.7), we conclude that the pair of terms 1 and 3, together, are equivalent to  $\vec{\mathbf{W}}_j^H \Sigma_{\vec{\mathbf{y}}} \vec{\mathbf{W}}_j$ . The pair of terms 2 and 4 jointly are equivalent to  $-\vec{\mathbf{W}}_j^H \Sigma_{\vec{\mathbf{y}}x_j}$ . The pairs of terms 5 and 7, 6 and 8, 9 and 11, 10 and 12, cancels each other. The 13<sup>th</sup> term together with the 15<sup>th</sup> are equivalent to  $-\Sigma_{x_j\vec{\mathbf{y}}} \vec{\mathbf{W}}_j$  while the 14<sup>th</sup> term combined with the 16<sup>th</sup> one yield to  $\Sigma_{x_j}^a$ . Thus the expanded MSE function simplifies as

$$\mathbf{E}_j = \vec{\mathbf{W}}_j^H \Sigma_{\vec{\mathbf{y}}} \vec{\mathbf{W}}_j - \vec{\mathbf{W}}_j^H \Sigma_{\vec{\mathbf{y}}x_j} - \Sigma_{x_j\vec{\mathbf{y}}} \vec{\mathbf{W}}_j + \Sigma_{x_j}^a. \quad (\text{C.8})$$

From the constraint stated by (C.5), which establishes that  $\vec{\mathbf{W}}_j^H \Sigma_{\vec{\mathbf{y}}x_j} = \sigma_{x_j}^2$  and also the fact that  $\Sigma_{x_j}^a = \sigma_{x_j}^2$ , the final MSE cost function for the CWCU-LMMSE estimator is

$$\mathbf{E}_j = \vec{\mathbf{W}}_j^H \Sigma_{\vec{\mathbf{y}}} \vec{\mathbf{W}}_j - \sigma_{x_j}^2. \quad (\text{C.9})$$

The solution for  $\vec{\mathbf{W}}_j$  can be obtained minimizing (C.9), which leads to the following constrained optimization problem

$$\underset{\vec{\mathbf{w}}_j}{\operatorname{argmin}} \left( \vec{\mathbf{W}}_j^H \Sigma_{\vec{\mathbf{y}}} \vec{\mathbf{W}}_j - \sigma_{x_j}^2 \right),$$

s.t.  $\vec{\mathbf{W}}_j^H \Sigma_{\vec{\mathbf{y}}x_j} = \sigma_{x_j}^2$ . This optimization problem can be addressed through the Lagrange multiplier method performing

$$\begin{aligned} \mathcal{L} \left( \vec{\mathbf{W}}_j^H \Sigma_{\vec{\mathbf{y}}} \vec{\mathbf{W}}_j - \sigma_{x_j}^2, \vec{\mathbf{W}}_j^H \Sigma_{\vec{\mathbf{y}}x_j} - \sigma_{x_j}^2 \right) &= \frac{\partial (\vec{\mathbf{W}}_j^H \Sigma_{\vec{\mathbf{y}}} \vec{\mathbf{W}}_j - \sigma_{x_j}^2)}{\partial \vec{\mathbf{W}}_j} - \nu \frac{\partial (\vec{\mathbf{W}}_j^H \Sigma_{\vec{\mathbf{y}}x_j} - \sigma_{x_j}^2)}{\partial \vec{\mathbf{W}}_j} \\ &= \vec{\mathbf{W}}_j^H \Sigma_{\vec{\mathbf{y}}} - \nu \Sigma_{x_j\vec{\mathbf{y}}} = 0. \end{aligned}$$

Then, a linear system can be written as

$$\begin{cases} \vec{\mathbf{W}}_j^H \Sigma_{\vec{\mathbf{y}}} = \nu \Sigma_{x_j\vec{\mathbf{y}}} & (\text{a}) \\ \vec{\mathbf{W}}_j^H \Sigma_{\vec{\mathbf{y}}x_j} = \sigma_{x_j}^2 & (\text{b}). \end{cases} \quad (\text{C.10})$$

Multiplying both sides of (C.10b) by  $\Sigma_{x_j\vec{\mathbf{y}}}$  and isolating  $\vec{\mathbf{W}}_j^H$  yields to

$$\vec{\mathbf{W}}_j^H = \sigma_{x_j}^2 \Sigma_{x_j\vec{\mathbf{y}}} \left( \Sigma_{\vec{\mathbf{y}}x_j} \Sigma_{x_j\vec{\mathbf{y}}} \right)^{-1}, \quad (\text{C.11})$$

which is inserted in (C.10a) leading to

$$\begin{aligned} \sigma_{x_j}^2 \Sigma_{x_j\vec{\mathbf{y}}} \left( \Sigma_{\vec{\mathbf{y}}x_j} \Sigma_{x_j\vec{\mathbf{y}}} \right)^{-1} \Sigma_{\vec{\mathbf{y}}} &= \nu \Sigma_{x_j\vec{\mathbf{y}}} \\ \sigma_{x_j}^2 \Sigma_{x_j\vec{\mathbf{y}}} &= \nu \Sigma_{x_j\vec{\mathbf{y}}} \left[ \left( \Sigma_{\vec{\mathbf{y}}x_j} \Sigma_{x_j\vec{\mathbf{y}}} \right)^{-1} \Sigma_{\vec{\mathbf{y}}} \right]^{-1} \\ \sigma_{x_j}^2 \Sigma_{x_j\vec{\mathbf{y}}} &= \nu \Sigma_{x_j\vec{\mathbf{y}}} \Sigma_{\vec{\mathbf{y}}}^{-1} \Sigma_{\vec{\mathbf{y}}x_j} \Sigma_{x_j\vec{\mathbf{y}}} \\ \nu &= \frac{\sigma_{x_j}^2}{\Sigma_{x_j\vec{\mathbf{y}}} \Sigma_{\vec{\mathbf{y}}}^{-1} \Sigma_{\vec{\mathbf{y}}x_j}}. \end{aligned} \quad (\text{C.12})$$

Replacing (C.12) into (C.10a) and applying the Hermitian operator on both sides yields to

$$\vec{\mathbf{W}}_j = \frac{\sigma_{x_j}^2}{\Sigma_{x_j \vec{y}} \Sigma_{\vec{y}}^{-1} \Sigma_{\vec{y} x_j}} \Sigma_{\vec{y}}^{-1} \Sigma_{\vec{y} x_j}. \quad (\text{C.13})$$

Recalling from (A.8) that  $\vec{\mathbf{W}}_j = \Sigma_{\vec{y}}^{-1} \Sigma_{\vec{y} x_j}$ , and also considering the  $j$ th row of (4.34) and the definition of (4.36), (C.13) can be rewritten as

$$\vec{\mathbf{W}}_j = \frac{\sigma_{x_j}^2}{\Sigma_{x_j \vec{x}} \mathbf{H}^H (\mathbf{H} \Sigma_{\vec{x}}^a \mathbf{H}^H + \Sigma_{\vec{w}}^a)^{-1} \mathbf{H} \Sigma_{\vec{x} x_j}} \vec{\mathbf{W}}_{j \text{LMMSE}}, \quad (\text{C.14})$$

which, retrieving from (C.13) and (C.14), finally allows to define the CWCU-LMMSE estimator in terms of its coefficient matrix  $\mathbf{W}_c = [\vec{\mathbf{W}}_1, \vec{\mathbf{W}}_2, \dots, \vec{\mathbf{W}}_q]^H$  as

$$\begin{aligned} \mathbf{W} &= \Sigma_{\vec{x}}^a \left[ \Sigma_{\vec{x} \vec{y}} \Sigma_{\vec{y}}^{-1} \Sigma_{\vec{y} \vec{x}} \right]^{-1} \mathbf{W}_{\text{LMMSE}} \\ &= \Sigma_{\vec{x}}^a \left[ \Sigma_{\vec{x}}^a \mathbf{H}^H (\mathbf{H} \Sigma_{\vec{x}}^a \mathbf{H}^H + \Sigma_{\vec{w}}^a)^{-1} \mathbf{H} \Sigma_{\vec{x}}^a \right]^{-1} \Sigma_{\vec{x}}^a \mathbf{H}^H (\mathbf{H} \Sigma_{\vec{x}}^a \mathbf{H}^H + \Sigma_{\vec{w}}^a)^{-1} \end{aligned} \quad (\text{C.15})$$

and, from the constraint on (C.6), the offset vector as

$$\vec{\mathbf{z}} = \boldsymbol{\mu}_{\vec{x}}^a - \mathbf{W} \vec{\boldsymbol{\mu}}_{\vec{y}} \quad (\text{C.16})$$

$$= \boldsymbol{\mu}_{\vec{x}} - \mathbf{W} \mathbf{H} \boldsymbol{\mu}_{\vec{x}}^a. \quad (\text{C.17})$$

Retrieving the definition on (4.3), the CWCU-LMMSE estimator can be written as

$$\begin{aligned} \vec{\boldsymbol{\mu}}_{\vec{x}}^p &= \mathbf{W} (\vec{y} - \mathbf{H} \boldsymbol{\mu}_{\vec{x}}) + \boldsymbol{\mu}_{\vec{x}} \\ &= \Sigma_{\vec{x}}^a \left[ \Sigma_{\vec{x}}^a \mathbf{H}^H (\mathbf{H} \Sigma_{\vec{x}}^a \mathbf{H}^H + \Sigma_{\vec{w}}^a)^{-1} \mathbf{H} \Sigma_{\vec{x}}^a \right]^{-1} \Sigma_{\vec{x}}^a \mathbf{H}^H (\mathbf{H} \Sigma_{\vec{x}}^a \mathbf{H}^H + \Sigma_{\vec{w}}^a)^{-1} (\vec{y} - \mathbf{H} \boldsymbol{\mu}_{\vec{x}}) + \boldsymbol{\mu}_{\vec{x}} \end{aligned} \quad (\text{C.18})$$

The error co-variance matrix of the CWCU-LMMSE estimator, which corresponds to the minimum MSE, can be derived inserting (4.3) into  $\mathbf{E} = \mathbf{E}\{(\vec{x} - \vec{\boldsymbol{\mu}}_{\vec{x}}^p)(\vec{x} - \vec{\boldsymbol{\mu}}_{\vec{x}}^p)^H\}$ , leading to

$$\begin{aligned} \mathbf{E} &= \mathbf{E}\{(\vec{x} - \mathbf{W} \vec{y} - \vec{z})(\vec{x} - \mathbf{W} \vec{y} - \vec{z})^H\} \\ &= \mathbf{E}\{\vec{x} \vec{x}^H\} - \mathbf{E}\{\vec{x} \vec{y}^H\} \mathbf{W}^H - \mathbf{E}\{\vec{x}\} \vec{z}^H - \mathbf{W} \mathbf{E}\{\vec{y} \vec{x}^H\} + \mathbf{W} \mathbf{E}\{\vec{y} \vec{y}^H\} \mathbf{W}^H \\ &\quad + \mathbf{W} \mathbf{E}\{\vec{y}\} \vec{z}^H - \vec{z} \mathbf{E}\{\vec{x}^H\} + \vec{z} \mathbf{E}\{\vec{y}^H\} \mathbf{W}^H + \vec{z} \vec{z}^H \end{aligned} \quad (\text{C.19})$$

Inserting (C.16) into (C.19) yields

$$\begin{aligned} \mathbf{E} &= \underbrace{\mathbf{E}\{\vec{x} \vec{x}^H\}}_1 - \underbrace{\mathbf{E}\{\vec{x} \vec{y}^H\} \mathbf{W}^H}_2 - \underbrace{\mathbf{E}\{\vec{x}\} \mathbf{E}\{\vec{x}\}^H}_3 + \underbrace{\mathbf{E}\{\vec{x}\} \mathbf{E}\{\vec{y}\}^H \mathbf{W}^H}_4 - \underbrace{\mathbf{W} \mathbf{E}\{\vec{y} \vec{x}^H\}}_5 \\ &\quad + \underbrace{\mathbf{W} \mathbf{E}\{\vec{y} \vec{y}^H\} \mathbf{W}^H}_6 + \underbrace{\mathbf{W} \mathbf{E}\{\vec{y}\} \mathbf{E}\{\vec{x}\}^H}_7 - \underbrace{\mathbf{W} \mathbf{E}\{\vec{y}\} \mathbf{E}\{\vec{y}\}^H \mathbf{W}^H}_8 \\ &\quad - \underbrace{\mathbf{E}\{\vec{x}\} \mathbf{E}\{\vec{x}^H\}}_9 + \underbrace{\mathbf{W} \mathbf{E}\{\vec{y}\} \mathbf{E}\{\vec{x}^H\}}_{10} + \underbrace{\mathbf{E}\{\vec{x}\} \mathbf{E}\{\vec{y}^H\} \mathbf{W}^H}_{11} - \underbrace{\mathbf{W} \mathbf{E}\{\vec{y}\} \mathbf{E}\{\vec{y}^H\} \mathbf{W}^H}_{12} \\ &\quad + \underbrace{\mathbf{E}\{\vec{x}\} \mathbf{E}\{\vec{x}\}^H}_{13} - \underbrace{\mathbf{E}\{\vec{x}\} \mathbf{E}\{\vec{y}^H\} \mathbf{W}^H}_{14} - \underbrace{\mathbf{W} \mathbf{E}\{\vec{y}\} \mathbf{E}\{\vec{x}^H\}}_{15} + \underbrace{\mathbf{W} \mathbf{E}\{\vec{y}\} \mathbf{E}\{\vec{y}^H\} \mathbf{W}^H}_{16}. \end{aligned} \quad (\text{C.20})$$

Note that in (C.20), enumerating the terms from left to right in ascending order, the pair of terms, 9 and 13, 11 and 14, 10 and 15, 12 and 16, cancels each other. Furthermore, the remaining terms can be combined, where the 1<sup>st</sup> and 3<sup>rd</sup> terms are equivalent to  $\Sigma_{\bar{\mathbf{x}}}^a$ , the 2<sup>nd</sup> and 4<sup>th</sup> together is  $-\Sigma_{\bar{\mathbf{x}}\bar{\mathbf{y}}}\mathbf{W}^H$ , the 5<sup>th</sup> and 7<sup>th</sup> corresponds to  $-\mathbf{W}\Sigma_{\bar{\mathbf{y}}\bar{\mathbf{x}}}$  and the 6<sup>th</sup> and 8<sup>th</sup> terms are identical to  $\mathbf{W}\Sigma_{\bar{\mathbf{y}}}\mathbf{W}^H$ . Hence

$$\mathbf{E} = \Sigma_{\bar{\mathbf{x}}}^a - \Sigma_{\bar{\mathbf{x}}\bar{\mathbf{y}}}\mathbf{W}^H - \mathbf{W}\Sigma_{\bar{\mathbf{y}}\bar{\mathbf{x}}} + \mathbf{W}\Sigma_{\bar{\mathbf{y}}}\mathbf{W}^H, \quad (\text{C.21})$$

which is similar to the vector representation in (C.8), except that (C.21) extends for the matricial case. Replacing (C.15) in (C.21) finally leads to

$$\mathbf{E} = \Sigma_{\bar{\mathbf{x}}}^a \left( \Sigma_{\bar{\mathbf{x}}\bar{\mathbf{y}}}\Sigma_{\bar{\mathbf{y}}}^{-1}\Sigma_{\bar{\mathbf{y}}\bar{\mathbf{x}}} \right) \Sigma_{\bar{\mathbf{x}}}^a - \Sigma_{\bar{\mathbf{x}}}^a \left[ \mathbf{H}^H(\mathbf{H}\Sigma_{\bar{\mathbf{x}}}^a\mathbf{H}^H + \Sigma_{\bar{\mathbf{w}}}^a)^{-1}\mathbf{H} \right]^{-1} - \Sigma_{\bar{\mathbf{x}}}^a. \quad (\text{C.22})$$

## References

- 1 MATTHÉ, M.; ZHANG, D.; FETTWEIS, G. Low-Complexity Iterative MMSE-PIC Detection for MIMO-GFDM. *IEEE Transactions on Communications*, v. 66, n. 4, p. 1467–1480, 2018. [4](#), [6](#), [24](#), [25](#), [28](#), [30](#), [54](#), [57](#), [58](#), [62](#), [76](#), [80](#), [96](#), [97](#), [98](#), [100](#), [104](#), [105](#), [107](#), [108](#), [113](#), [119](#)
- 2 SEO, D. The 1G (First Generation) Mobile Communications Technology Standards. In: *Evolution and Standardization of Mobile Communications Technology*. [S.l.]: IGI Global, 2013. cap. 5, p. 54–75. [20](#)
- 3 SEO, D. The 2G (Second Generation) Mobile Communications Technology Standards. In: *Evolution and Standardization of Mobile Communications Technology*. [S.l.]: IGI Global, 2013. cap. 6, p. 76–114. [20](#)
- 4 3GPP. *Specification 23.040: Technical realization of the Short Message Service (SMS)*. [S.l.], 1999. Disponível em: <https://portal.3gpp.org/desktopmodules/Specifications/SpecificationDetails.aspx?specificationId=747>. [20](#)
- 5 SEO, D. The 3G (Third Generation) of Mobile Communications Technology Standards. In: *Evolution and Standardization of Mobile Communications Technology*. [S.l.]: IGI Global, 2013. cap. 6, p. 115–161. [20](#)
- 6 DAHLMAN, E.; PARKVALL, S.; SKOLD, J. *4G: LTE/LTE-Advanced for Mobile Broadband*. 2nd. ed. USA: Academic Press, Inc., 2013. ISBN 0124199852. [20](#)
- 7 MSHVIDOBADZE, T. Evolution Mobile Wireless Communication and LTE Networks. In: *2012 6th International Conference on Application of Information and Communication Technologies (AICT)*. [S.l.: s.n.], 2012. p. 1–7. [20](#)
- 8 SHAFI, M. et al. 5G: A Tutorial Overview of Standards, Trials, Challenges, Deployment, and Practice. *IEEE Journal on Selected Areas in Communications*, v. 35, n. 6, p. 1201–1221, 2017. [20](#)
- 9 NAVARRO-ORTIZ, J. et al. A Survey on 5G Usage Scenarios and Traffic Models. *IEEE Communications Surveys & Tutorials*, v. 22, n. 2, p. 905–929, 2020. [20](#)
- 10 CHEN, B. et al. Smart Factory of Industry 4.0: Key Technologies, Application Case, and Challenges. *IEEE Access*, v. 6, p. 6505–6519, 2018. [20](#)
- 11 STORCK, C. R.; DUARTE-FIGUEIREDO, F. A Survey of 5G Technology Evolution, Standards, and Infrastructure Associated With Vehicle-to-Everything Communications by Internet of Vehicles. *IEEE Access*, v. 8, p. 117593–117614, 2020. [20](#)
- 12 YU, W. et al. A Survey on the Edge Computing for the Internet of Things. *IEEE Access*, v. 6, p. 6900–6919, 2018. [20](#)

- 13 AYAZ, M. et al. Internet-of-Things (IoT)-Based Smart Agriculture: Toward Making the Fields Talk. *IEEE Access*, v. 7, p. 129551–129583, 2019. 20
- 14 ITU-R. *Measuring digital development - Facts and figures 2021*. [S.l.], 2021. Disponível em: <<https://www.itu.int/itu-d/reports/statistics/facts-figures-2021/>>. 20
- 15 ALSHARIF, M. H. et al. Sixth Generation (6G) Wireless Networks: Vision, Research Activities, Challenges and Potential Solutions. *Symmetry*, v. 12, n. 4, 2020. ISSN 2073-8994. Disponível em: <<https://www.mdpi.com/2073-8994/12/4/676>>. 20
- 16 VAIGANDLA, K.; BOLLA, S.; KARNE, R. A Survey on Future Generation Wireless Communications-6G: Requirements, Technologies, Challenges and Applications. *International Journal of Advanced Trends in Computer Science and Engineering*, v. 10, p. 3067–3076, 10 2021. 21
- 17 HAMPTON, J. R. *Introduction to MIMO Communications*. Cambridge University Press: [s.n.], 2013. 21, 24, 27, 90
- 18 FETTWEIS, G.; KRONDORF, M.; BITTNER, S. GFDM - Generalized Frequency Division Multiplexing. In: *VTC Spring 2009 - IEEE 69th Vehicular Technology Conference*. [S.l.: s.n.], 2009. p. 1–4. ISSN 1550-2252. 21, 25
- 19 MATTHE, M. et al. Near-ML Detection for MIMO-GFDM. In: *2015 IEEE 82nd Vehicular Technology Conference (VTC2015-Fall)*. [S.l.: s.n.], 2015. p. 1–2. 21
- 20 ALMEIDA, I. B. Franco de; MENDES, L. L. Linear GFDM: A Low Out-of-band Emission Configuration for 5G Air Interface. In: *2018 IEEE 5G World Forum (5GWF)*. [S.l.: s.n.], 2018. p. 311–316. 21
- 21 MERAJ, M.; KUMAR, S. Evolution of Mobile Wireless Technology from 0G to 5G. *International Journal of Computer Science and Information Technologies*, 2015. 21
- 22 KUMAR, B. A.; RAO, P. T. Overview of Advances in Communication Technologies. In: *2015 13th International Conference on Electromagnetic Interference and Compatibility (INCEMIC)*. [S.l.: s.n.], 2015. p. 102–106. 21
- 23 TERASAWA, D.; TIEDEMANN, E. CDMAOne(R) (IS-95) Technology Overview and Evolution. In: *1999 IEEE Radio Frequency Integrated Circuits Symposium (Cat No.99CH37001)*. [S.l.: s.n.], 1999. p. 213–216. 22
- 24 SPENCER, N. An Overview of Digital Telephony Standards. In: *IEE Colloquium on The Design of Digital Cellular Handsets (Ref. No. 1998/240)*. [S.l.: s.n.], 1998. p. 1/1–1/7. 22
- 25 SOLLENBERGER, N.; SESHADRI, N.; COX, R. The Evolution of IS-136 TDMA for Third-Generation Wireless Services. *IEEE Personal Communications*, v. 6, n. 3, p. 8–18, 1999. 22
- 26 International Telecommunication Union. *Detailed Specifications of the Terrestrial Radio Interfaces of International Mobile Telecommunications Advanced (IMT-Advanced)*. [S.l.], 2012. Disponível em: <<https://www.itu.int/rec/R-REC-M.2012/en>>. 22
- 27 COX, C. *An Introduction to LTE: LTE, LTE-Advanced, SAE, VoLTE and 4G Mobile Communications*. [S.l.]: John Wiley & Sons, 2014. 22

- 28 KOZIEROK, C. M. *The TCP/IP Guide: A Comprehensive, Illustrated Internet Protocols Reference*. San Francisco: No Starch Press, 2005. ISBN 1-59327-047-X. 22
- 29 YANG, S. *OFDMA System Analysis and Design*. Artech, 2010. ISBN 9781608070770. Disponível em: <<https://ieeexplore.ieee.org/document/9100630>>. 23
- 30 ITU-R. *Minimum Requirements Related to Technical Performance for IMT-2020 Radio Interface(s)*. [S.l.], 2016. (Rep. ITU-R M.2410-0). 23
- 31 LEI, W. et al. *5G Capability: ITU-R Submission and Performance Evaluation*. Cham: Springer International Publishing, 2021. 533–602 p. ISBN 978-3-030-73703-0. Disponível em: <[https://doi.org/10.1007/978-3-030-73703-0\\_10](https://doi.org/10.1007/978-3-030-73703-0_10)>. 23
- 32 WANG, J. et al. 3D Beamforming Technologies and Field Trials in 5G Massive MIMO Systems. *IEEE Open Journal of Vehicular Technology*, v. 1, p. 362–371, 2020. 23
- 33 OJIJO, M. O.; FALOWO, O. E. A Survey on Slice Admission Control Strategies and Optimization Schemes in 5G Network. *IEEE Access*, v. 8, p. 14977–14990, 2020. 23
- 34 CAVALCANTE, A. M. et al. 5G for Remote Areas: Challenges, Opportunities and Business Modeling for Brazil. *IEEE Access*, v. 9, p. 10829–10843, 2021. 23, 110
- 35 MENDES, L. L. et al. Enhanced Remote Areas Communications: The Missing Scenario for 5G and Beyond 5G Networks. *IEEE Access*, v. 8, p. 219859–219880, 2020. 23, 27, 30, 111, 112
- 36 FERREIRA, A. et al. 5G-RANGE Project Field Trial. In: *European Conference on Networks and Communications (EuCNC)*. [S.l.: s.n.], 2019. p. 490–494. 23
- 37 DIAS, W. et al. 5G-RANGE: A Transceiver for Remote Areas based on Software-Defined Radio. In: *European Conference on Networks and Communications (EuCNC)*. [S.l.: s.n.], 2020. p. 100–104. 23, 112
- 38 UUSITALO, M. A. et al. Hexa-X The European 6G flagship project. In: *2021 Joint European Conference on Networks and Communications 6G Summit (EuCNC/6G Summit)*. [S.l.: s.n.], 2021. p. 580–585. 23
- 39 THE 17 GOALS. United Nations - Department of Economic and Social Affairs, 2022. [Online; accessed 2022-04-02]. Disponível em: <<https://sdgs.un.org/goals>>. 23
- 40 TAPIO, V. et al. Survey on Reconfigurable Intelligent Surfaces below 10 GHz. *EURASIP Journal on Wireless Communications and Networking*, v. 2021, n. 1, p. 175, Sep 2021. ISSN 1687-1499. Disponível em: <<https://doi.org/10.1186/s13638-021-02048-5>>. 24, 27, 28
- 41 EHSANFAR, S. et al. Pilot- and CP-Aided Channel Estimation in MIMO Non-Orthogonal Multi-Carriers. *IEEE Transactions on Wireless Communications*, v. 18, n. 1, p. 650–664, 2019. 24
- 42 KHOROV, E.; LEVITSKY, I.; AKYILDIZ, I. F. Current Status and Directions of IEEE 802.11be, the Future Wi-Fi 7. *IEEE Access*, v. 8, p. 88664–88688, 2020. 24
- 43 GÓMEZ-BARQUERO, D. et al. MIMO for ATSC 3.0. *IEEE Transactions on Broadcasting*, v. 62, n. 1, p. 298–305, 2016. 24

- 44 AGRAWAL, A. V.; RAWAT, M. Green HSR Reliable Communication With LTE-R Using MIMO-DPD. *IEEE Access*, v. 9, p. 105118–105130, 2021. 24
- 45 GHOSH, A. et al. 5G Evolution: A View on 5G Cellular Technology Beyond 3GPP Release 15. *IEEE Access*, v. 7, p. 127639–127651, 2019. 24
- 46 ALAMOUTI, S. A Simple Transmit Diversity Technique for Wireless Communications. *IEEE Journal on Selected Areas in Communications*, v. 16, n. 8, p. 1451–1458, 1998. 25
- 47 TAROKH, V.; JAFARKHANI, H.; CALDERBANK, A. Space-Time Block Codes from Orthogonal Designs. *IEEE Transactions on Information Theory*, v. 45, n. 5, p. 1456–1467, 1999. 25
- 48 AL-DHAHIR, N. Single-carrier Frequency-domain Equalization for Space-Time Block-coded Transmissions over Frequency-Selective Fading Channels. *IEEE Communications Letters*, v. 5, n. 7, p. 304–306, 2001. 25
- 49 MICHAÏLOW, N. et al. Generalized Frequency Division Multiplexing: Analysis of an alternative multi-carrier technique for next generation cellular systems. In: *2012 International Symposium on Wireless Communication Systems (ISWCS)*. [S.l.: s.n.], 2012. p. 171–175. ISSN 2154-0217. 25
- 50 GERZAGUET, R. et al. The 5G Candidate Waveform Race: A Comparison of Complexity and Performance. *EURASIP Journal on Wireless Communications and Networking*, v. 2017, n. 1, p. 13, Jan 2017. ISSN 1687-1499. Disponível em: <<https://doi.org/10.1186/s13638-016-0792-0>>. 26
- 51 ZHANG, D. et al. A Study on the Link Level Performance of Advanced Multicarrier Waveforms Under MIMO Wireless Communication Channels. *IEEE Transactions on Wireless Communications*, v. 16, n. 4, p. 2350–2365, 2017. 26, 28
- 52 FERREIRA, J. S. F. A. C.; MENDES, L. L. *Definition of Performance Requirements for Applications with the Greatest Potential for Social and Economic Impact and Assessment of the Technical Feasibility of Implementing these Applications*. Santa Rita do Sapucaí, Brazil, 2019. 27
- 53 WILLHAMMAR, S. et al. Channel Hardening in Massive MIMO: Model Parameters and Experimental Assessment. *IEEE Open Journal of the Communications Society*, v. 1, p. 501–512, 2020. 27
- 54 ZHANG, J. et al. Cell-Free Massive MIMO: A New Next-Generation Paradigm. *IEEE Access*, v. 7, p. 99878–99888, 2019. 27
- 55 MICHAÏLOW, N. et al. Generalized Frequency Division Multiplexing for 5th Generation Cellular Networks. *IEEE Transactions on Communications*, v. 62, n. 9, p. 3045–3061, 2014. 27, 33, 41
- 56 ÖZTÜRK, E.; BASAR, E.; ÇIRPAN, H. A. Spatial Modulation GFDM: A Low Complexity MIMO-GFDM System for 5G Wireless Networks. In: *IEEE International Black Sea Conference on Communications and Networking (BlackSeaCom)*. [S.l.: s.n.], 2016. 27

- 57 SUGA, N.; R.SASAKI; FURUKAWA, T. Channel Estimation Using Matrix Factorization Based Interpolation for OFDM Systems. In: *IEEE 90th Vehicular Technology Conference*. [S.l.: s.n.], 2019. 28
- 58 GASPAR, D.; MENDES, L. L.; PIMENTA, T. C. A Review on Principles, Performance and Complexity of Linear Estimation and Detection Techniques for MIMO Systems. *Frontiers in Communications and Networks*, v. 4, 2023. ISSN 2673-530X. Disponível em: <<https://www.frontiersin.org/articles/10.3389/frcmn.2023.968370>>. 28, 76, 77, 96, 105
- 59 HUEMER, M.; LANG, O.; HOFBAUER, C. Component-Wise Conditionally Unbiased Widely Linear MMSE Estimation. *Signal Processing*, v. 133, p. 227 – 239, 2017. ISSN 0165-1684. Disponível em: <<http://www.sciencedirect.com/science/article/pii/S0165168416302845>>. 28, 63, 66
- 60 MATTHE, M.; ZHANG, D.; FETTWEIS, G. Iterative Detection using MMSE-PIC Demapping for MIMO-GFDM Systems. In: *European Wireless 2016; 22th European Wireless Conference*. [S.l.: s.n.], 2016. p. 1–7. 28, 58, 67, 68, 69, 70, 92, 97
- 61 STUDER, C.; FATEH, S.; SEETHALER, D. ASIC Implementation of Soft-Input Soft-Output MIMO Detection Using MMSE Parallel Interference Cancellation. *IEEE Journal of Solid-State Circuits*, v. 46, n. 7, p. 1754–1765, 2011. 28, 66, 98, 100
- 62 EHSANFAR, S. et al. Interference-Free Pilots Insertion for MIMO-GFDM Channel Estimation. In: *IEEE Wireless Communications and Networking Conference (WCNC)*. [S.l.: s.n.], 2017. p. 1–6. 29, 112
- 63 FOMINYKH, A.; FROLOV, A.; QIN, K. An Efficient Soft-Input Soft-Output Decoder for Polar Codes in MIMO Iterative Detection System. In: *IEEE Wireless Communications and Networking Conference (WCNC)*. [S.l.: s.n.], 2023. 29, 112
- 64 HUNGER, R. *Floating Point Operations in Matrix-Vector Calculus*. Munich University of Technology, Inst. for Circuit Theory and Signal Processing: [s.n.], 2007. 31
- 65 The Numerical Algorithms Group (NAG). *The NAG Library*. Oxford, United Kingdom: [s.n.], 2024. Accessed Oct. 21, 2022 [Online]. Disponível em: <<https://www.nag.com>>. 31, 68
- 66 TREFETHEN, L. N.; BAU, D. *Numerical Linear Algebra*. [S.l.]: SIAM, 1997. ISBN 0898713617. 31
- 67 Mopuri, S.; Acharyya, A. Low-Complexity Methodology for Complex Square-Root Computation. *IEEE Transactions on Very Large Scale Integration (VLSI) Systems*, v. 25, n. 11, p. 3255–3259, 2017. 31
- 68 ROSEN, K. H. *Handbook of Discrete and Combinatorial Mathematics, Second Edition*. 2nd. ed. Chapman & Hall/CRC: [s.n.], 2010. ISBN 158488780X. 32
- 69 MATTHÉ, M. et al. Generalized Frequency Division Multiplexing: A Flexible Multi-Carrier Waveform for 5G. In: XIANG, W.; ZHENG, K.; SHEN, X. (Ed.). *5G Mobile Communications*. [S.l.]: Springer International Publishing, 2016. p. 223–259. ISBN 978-3-319-34208-5. 33, 35, 43, 45

- 70 GASPAR, I. et al. GFDM - A Framework for Virtual PHY Services in 5G Networks. *ArXiv e-prints*, jul. 2015. 34
- 71 MATTHÉ, M. et al. Influence of Pulse Shaping on Bit Error Rate Performance and Out of Band Radiation of Generalized Frequency Division Multiplexing. In: *2014 IEEE International Conference on Communications Workshops (ICC)*. [S.l.: s.n.], 2014. p. 43–48. ISSN 2164-7038. 35
- 72 MICHAÏLOW, N. et al. Generalized Frequency Division Multiplexing: A Flexible Multi-Carrier Modulation Scheme for 5th Generation Cellular Networks. In: *Proceedings of the German microwave conference (GeMiC'12)*. [S.l.: s.n.], 2012. p. 1–4. 37
- 73 SHARMA, C.; TOMAR, S. K.; KUMAR, A. A Comparison of GFDM and OFDM at Same and Different Spectral Efficiency Condition. In: BALAJI, S.; ROCHA, Á.; CHUNG, Y.-N. (Ed.). *Intelligent Communication Technologies and Virtual Mobile Networks*. Cham: Springer International Publishing, 2020. p. 282–293. ISBN 978-3-030-28364-3. 46
- 74 GASPAR, D.; MENDES, L.; PIMENTA, T. GFDM BER Under Synchronization Errors. *IEEE Communications Letters*, v. 21, n. 8, p. 1743–1746, 2017. 46
- 75 ARIKAN, E. Channel Polarization: A Method for Constructing Capacity-Achieving Codes for Symmetric Binary-Input Memoryless Channels. *IEEE Journal IT*, v. 55, n. 7, 2009. 48, 112
- 76 GLAVIEUX, A.; VATON, S. *Convolutional Codes*. John Wiley & Sons, Ltd, 2007. 129-196 p. ISBN 9780470612422. Disponível em: <<https://onlinelibrary.wiley.com/doi/abs/10.1002/9780470612422.ch3>>. 48
- 77 RYAN, W.; LIN, S. *Channel Codes: Classical and Modern*. [S.l.]: Cambridge University Press, 2009. 48
- 78 BEKAS, C.; KOKIOPOULOU, E.; SAAD, Y. An Estimator for the Diagonal of a Matrix. *Applied Numerical Mathematics*, v. 57, n. 11, p. 1214–1229, 2007. ISSN 0168-9274. Numerical Algorithms, Parallelism and Applications (2). Disponível em: <<https://www.sciencedirect.com/science/article/pii/S0168927407000244>>. 58, 68
- 79 ALBREEM, M. A. et al. Low Complexity Linear Detectors for Massive MIMO: A Comparative Study. *IEEE Access*, v. 9, p. 45740–45753, 2021. 63, 70, 78
- 80 SAYED, A. *Fundamentals of Adaptive Filtering*. [s.n.], 2003. (Wiley - IEEE). ISBN 9780471461265. Disponível em: <<https://www.wiley.com/en-us/Fundamentals+of+Adaptive+Filtering+-p-9780471461265>>. 64, 123
- 81 SHEWCHUK, J. R. An Introduction to the Conjugate Gradient Method Without the Agonizing Pain. August 1994. Disponível em: <<http://www.cs.cmu.edu/~quake-papers/painless-conjugate-gradient.pdf>>. 70
- 82 YATES, R. D.; GOODMAN, D. J. *Probability and Stochastic Processes*. 2nd ed.. ed. Hoboken, NJ: John Wiley & Sons, 2005. 71, 129
- 83 ANDERSEN, H. H.; HØJBJERRE M.AND SØRENSEN, D.; ERIKSEN, P. S. The multivariate complex normal distribution. In: *Linear and Graphical Models: for the Multivariate Complex Normal Distribution*. New York, NY: Springer New York, 1995. ISBN 978-1-4612-4240-6. 72

- 84 KAY, S. M. *Fundamentals of Statistical Signal Processing: Estimation Theory*. USA: Prentice-Hall, Inc., 1993. ISBN 0133457117. 73
- 85 TREES, H. L. V.; BELL, K. L. *Bayesian Bounds for Parameter Estimation and Nonlinear Filtering/Tracking*. Wiley-IEEE Press: [s.n.], 2007. ISBN 0470120959. 73
- 86 GALLAGER, R. G. *Principles of Digital Communication*. [S.l.]: Cambridge University Press, 2008. 78, 98
- 87 ALBREEM, M. A.; JUNTTI, M.; SHAHABUDDIN, S. Massive MIMO Detection Techniques: A Survey. *IEEE Communications Surveys Tutorials*, v. 21, n. 4, p. 3109–3132, 2019. 78, 95
- 88 LARSSON, E. MIMO Detection Methods: How They Work [Lecture Notes]. *IEEE Signal Processing Magazine*, v. 26, n. 3, p. 91–95, 2009. 78, 81, 83
- 89 KOBAYASHI, R. T.; CIRIACO, F.; ABRÃO, T. Performance and complexity analysis of sub-optimum MIMO detectors under correlated channel. In: *2014 International Telecommunications Symposium (ITS)*. [S.l.: s.n.], 2014. p. 1–5. 78
- 90 JALDEN, J.; OTTERSTEN, B. On the Complexity of Sphere Decoding in Digital Communications. *IEEE Transactions on Signal Processing*, v. 53, n. 4, p. 1474–1484, 2005. 78
- 91 FOSCHINI, G. J. Layered Space-Time Architecture for Wireless Communication in a Fading Environment when using Multi-element Antennas. *Bell Labs Technical Journal*, v. 1, n. 2, p. 41–59, 1996. 78
- 92 BAI, L.; CHOI, J. *Low Complexity MIMO Detection*. Springer Publishing Company, Incorporated: [s.n.], 2014. ISBN 1489998241. 79
- 93 ALBREEM, M. A.; ALSHARIF, M. H.; KIM, S. A Low Complexity Near-Optimal Iterative Linear Detector for Massive MIMO in Realistic Radio Channels of 5G Communication Systems. *Entropy*, v. 22, n. 4, 2020. ISSN 1099-4300. Disponível em: <<https://www.mdpi.com/1099-4300/22/4/388>>. 79, 80
- 94 ERIKSSON, H. et al. A Genie-Aided Detector with a Probabilistic Description of the Side Information. In: *Proceedings of 1995 IEEE International Symposium on Information Theory*. [S.l.: s.n.], 1995. p. 332–. 80
- 95 ANASTASOPOULOS, A. Sequence Error Probability Lower Bounds for Joint Detection and Estimation. *IEEE Transactions on Communications*, v. 51, n. 3, p. 347–351, 2003. 80
- 96 FINCKE, U.; POHST, M. Improved Methods for Calculating Vectors of Short Length in a Lattice. *Mathematics of Computation*, 1985. 81
- 97 HASSIBI, B.; VIKALO, H. On the Sphere-Decoding Algorithm I. Expected Complexity. *IEEE Transactions on Signal Processing*, v. 53, n. 8, p. 2806–2818, 2005. 81, 83
- 98 SOLTANI, M. D.; ALIMADADI, M.; AMINDAVAR, H. A Hybrid Method to Reduce the Complexity of k-best Sphere Decoding Algorithm. In: *2014 22nd Iranian Conference on Electrical Engineering (ICEE)*. [S.l.: s.n.], 2014. p. 1765–1770. 81

- 99 PROAKIS. *Digital Communications 5th Edition*. McGraw Hill: [s.n.], 2007. 81
- 100 KOUDOUGNON, H.; SAADANE, R.; BELKASMI, M. Sphere decoding based on QR decomposition in STBC. In: *2011 International Conference on Multimedia Computing and Systems*. [S.l.: s.n.], 2011. p. 1–5. 81
- 101 AGRELL, E. et al. Closest point search in lattices. *IEEE Transactions on Information Theory*, v. 48, n. 8, p. 2201–2214, 2002. 81
- 102 ARFAOUI, M.-A. et al. Efficient Sphere Detector Algorithm for Massive MIMO Using GPU Hardware Accelerator. *Procedia Computer Science*, v. 80, p. 2169–2180, 2016. ISSN 1877-0509. International Conference on Computational Science 2016, ICCS 2016, 6-8 June 2016, San Diego, California, USA. Disponível em: <<https://www.sciencedirect.com/science/article/pii/S1877050916308523>>. 83
- 103 BURG, A. et al. VLSI implementation of MIMO detection using the sphere decoding algorithm. *IEEE Journal of Solid-State Circuits*, v. 40, n. 7, p. 1566–1577, 2005. 83
- 104 GASPAR, D.; MENDES, L.; PIMENTA, T. Sphere Detector with Low Complexity Euclidean Distance Computation Based on Affine Transform Modulation. *Electronics Letters*, Institution of Engineering and Technology (IET), ago. 2022. Disponível em: <<https://doi.org/10.1049/ell2.12594>>. 84, 87, 88, 96
- 105 ABDELHAMEED, D.; HUSSEIN, H. S.; MOHAMED, E. M. Affine linear transformation based sphere decoder for 1-bit ADC MIMO-constant envelope modulation. In: *2016 23rd International Conference on Telecommunications (ICT)*. [S.l.: s.n.], 2016. p. 1–6. 84
- 106 MEDRA, M.; AHMED, K. E.; DAVIDSON, T. N. MOSIC: A new ordering for OSIC MIMO detection. In: *2016 IEEE 17th International Workshop on Signal Processing Advances in Wireless Communications (SPAWC)*. [S.l.: s.n.], 2016. p. 1–5. 90
- 107 GOLDEN, G. et al. Detection Algorithm and Initial Laboratory Results using V-BLAST Space-Time Communication Architecture. *Electronics Letters*, Institution of Engineering and Technology, v. 35, p. 14–16(2), January 1999. ISSN 0013-5194. Disponível em: <[https://digital-library.theiet.org/content/journals/10.1049/el\\_19990058](https://digital-library.theiet.org/content/journals/10.1049/el_19990058)>. 90
- 108 LANG, O.; HUEMER, M. CWCU LMMSE Estimation Under Linear Model Assumptions. In: . [S.l.: s.n.], 2015. p. 537–545. ISBN 978-3-319-27339-6. 94
- 109 BAHL, L. et al. Optimal decoding of linear codes for minimizing symbol error rate (corresp.). *IEEE Transactions on Information Theory*, v. 20, n. 2, p. 284–287, 1974. 100, 103, 106, 113
- 110 COLAVOLPE, G.; FERRARI, G.; RAHELI, R. Extrinsic information in iterative decoding: a unified view. *IEEE Transactions on Communications*, v. 49, n. 12, p. 2088–2094, 2001. 100
- 111 HAGENAUER, J.; OFFER, E.; PAPKE, L. Iterative decoding of binary block and convolutional codes. *IEEE Transactions on Information Theory*, v. 42, n. 2, p. 429–445, 1996. 100

- 112 FERREIRA, J. et al. GFDM Frame Design for 5G Application Scenarios. *Journal of Communication and Information Systems*, v. 32, n. 1, Jul. 2017. Disponível em: <<https://jcis.sbrc.org.br/jcis/article/view/432>>. 106
- 113 DIAS, W. et al. Performance Analysis of a 5G Transceiver Implementation for Remote Areas Scenarios. In: *2018 European Conference on Networks and Communications (EuCNC)*. [S.l.: s.n.], 2018. p. 363–367. 106
- 114 GASPAR, D. et al. Spatial Multiplexing MIMO for Remote Areas employing MMSE Parallel Interference Cancellation for Non-Orthogonal GFDM. In: *2023 International Conference on Microelectronics (ICM)*. [S.l.: s.n.], 2023. p. 119–124. 109
- 115 3GPP. *Technical Specification Group Radio Access Network; NR; Multiplexing and channel coding*. Valbonne, França, 2019. 110
- 116 MATINMIKKO-BLUE, M. et al. *White Paper on 6G Drivers and the UN SDGs*. arXiv:2004.14695: [s.n.], 2024. Accessed Mar. 19, 2024 [Online]. Disponível em: <<http://arxiv.org/abs/2004.14695>>. 111
- 117 PESSOA, A. M. et al. CDL-based Channel Model for 5G MIMO Systems in Remote Rural Areas. In: *16th International Symposium on Wireless Communication Systems (ISWCS)*. [S.l.: s.n.], 2019. p. 21–26. 112, 113
- 118 CAMMERER, S. et al. Sparse Graphs for Belief Propagation Decoding of Polar Codes. In: *IEEE International Symposium on Information Theory (ISIT)*. [S.l.: s.n.], 2018. p. 1465–1469. 112
- 119 ETSI. *Study on Channel Model for Frequency Spectrum Above 6 GHz*. [S.l.], 2017. V14.2.0. Disponível em: <<http://www.etsi.org/standards-search>>. 113
- 120 ETSI. *Study on Channel Model for Frequencies from 0.5 to 100 GHz*. [S.l.], 2020. V16.1.0. Disponível em: <<http://www.etsi.org/standards-search>>. 114
- 121 GASPAR, D. et al. A Low-Complexity 6G Transceiver Based on the Non-Orthogonal GFDM-MIMO Signal Interference Cancellation Technique for Enhanced Communications in Remote and Rural Areas . Submitted to IEEE Transactions on Communications. 2024. 118
- 122 Danilo Gaspar, Vanessa Mendes Rennó, Luiz Guedes e Luciano Leonel Mendes. *Transceptor para Redes 6G em Áreas Remotas e Rurais*. 2024. BR1020240211715. INPI - Instituto Nacional da Propriedade Industrial. 118